IAEA-TECDOC-1696

Challenges Related to the Use of Liquid Metal and Molten Salt Coolants in Advanced Reactors

Report of the collaborative project COOL of the International Project on Innovative Nuclear Reactors and Fuel Cycles (INPRO)

IAEA
International Atomic Energy Agency

CHALLENGES RELATED TO THE USE OF LIQUID METAL AND MOLTEN SALT COOLANTS IN ADVANCED REACTORS

The following States are Members of the International Atomic Energy Agency:

AFGHANISTAN
ALBANIA
ALGERIA
ANGOLA
ARGENTINA
ARMENIA
AUSTRALIA
AUSTRIA
AZERBAIJAN
BAHRAIN
BANGLADESH
BELARUS
BELGIUM
BELIZE
BENIN
BOLIVIA
BOSNIA AND HERZEGOVINA
BOTSWANA
BRAZIL
BULGARIA
BURKINA FASO
BURUNDI
CAMBODIA
CAMEROON
CANADA
CENTRAL AFRICAN REPUBLIC
CHAD
CHILE
CHINA
COLOMBIA
CONGO
COSTA RICA
CÔTE D’IVOIRE
CROATIA
CUBA
CYPRUS
CZECH REPUBLIC
DEMOCRATIC REPUBLIC OF THE CONGO
DENMARK
DOMINICA
DOMINICAN REPUBLIC
ECUADOR
EGYPT
EL SALVADOR
ERITREA
ESTONIA
ETHIOPIA
FIJI
FINLAND
FRANCE
GABON
GEORGIA
GERMANY
GHANA
GREECE
GUATEMALA
HAITI
HOLY SEE
HONDURAS
HUNGARY
ICELAND
INDIA
INDONESIA
IRAN, ISLAMIC REPUBLIC OF
IRAQ
IRELAND
ISRAEL
ITALY
JAMAICA
JAPAN
JORDAN
KAZAKHSTAN
KENYA
KOREA, REPUBLIC OF
KUWAIT
KYRGYZSTAN
LAO PEOPLE’S DEMOCRATIC REPUBLIC
LATVIA
LEBANON
LESOTHO
LIBERIA
LIBYA
LIECHTENSTEIN
LITHUANIA
LUXEMBOURG
MADAGASCAR
MALAWI
MALAYSIA
MALI
MALTA
MARSHALL ISLANDS
MAURITANIA
MAURITIUS
MEXICO
MONACO
MONGOLIA
MONTENEGRO
MOROCCO
MOZAMBIQUE
MYANMAR
NAMIBIA
NEPAL
NETHERLANDS
NEW ZEALAND
NICARAGUA
NIGER
NIGERIA
NORWAY
OMAN
PAKISTAN
PALAU
PANAMA
PAPUA NEW GUINEA
PARAGUAY
PERU
PHILIPPINES
POLAND
PORTUGAL
QATAR
REPUBLIC OF MOLDOVA
ROMANIA
RUSSIAN FEDERATION
RWANDA
SAUDI ARABIA
SENEGAL
SERBIA
SEYCHELLES
SIERRA LEONE
SINGAPORE
SLOVAKIA
SLOVENIA
SOUTH AFRICA
SPAIN
SRI LANKA
SUDAN
SWAZILAND
SWEDEN
SWITZERLAND
SYRIAN ARAB REPUBLIC
TAJIKISTAN
THAILAND
THE FORMER YUGOSLAV REPUBLIC OF MACEDONIA
TOGO
TRINIDAD AND TOBAGO
TUNISIA
TURKEY
UGANDA
UKRAINE
UNITED ARAB EMIRATES
UNITED KINGDOM OF GREAT BRITAIN AND NORTHERN IRELAND
UNITED REPUBLIC OF TANZANIA
UNITED STATES OF AMERICA
URUGUAY
UZBEKISTAN
VENEZUELA
VIETNAM
YEMEN
ZAMBIA
ZIMBABWE

The Agency’s Statute was approved on 23 October 1956 by the Conference on the Statute of the IAEA held at United Nations Headquarters, New York; it entered into force on 29 July 1957. The Headquarters of the Agency are situated in Vienna. Its principal objective is “to accelerate and enlarge the contribution of atomic energy to peace, health and prosperity throughout the world’’.

IAEA-TECDOC-1696

CHALLENGES RELATED TO THE USE OF LIQUID METAL AND MOLTEN SALT COOLANTS IN ADVANCED REACTORS

REPORT OF THE COLLABORATIVE PROJECT COOL OF THE INTERNATIONAL PROJECT ON INNOVATIVE NUCLEAR REACTORS AND FUEL CYCLES (INPRO)

COPYRIGHT NOTICE

Marketing and Sales Unit, Publishing Section
International Atomic Energy Agency
Vienna International Centre
PO Box 100
1400 Vienna, Austria
fax: +43 1 2600 29302
tel.: +43 1 2600 22417
email: sales.publications@iaea.org
http://www.iaea.org/books

For further information on this publication, please contact:

INPRO Group, Division of Nuclear Power
International Atomic Energy Agency
Vienna International Centre
PO Box 100
1400 Vienna, Austria
Email: official.mail@iaea.org

Printed by the IAEA in Austria
May 2013

IAEA Library Cataloguing in Publication Data

Challenges related to the use of liquid metal and molten salt coolants
in advanced reactors : report of the collaborative project COOL
of the International Project on Innovative Nuclear Reactors and
Fuel Cycles (INPRO). – Vienna : International Atomic Energy
Agency, 2013.
p. ; 30 cm. – (IAEA-TECDOC series, ISSN 1011-4289
; no. 1696)
ISBN 978-92-0-139910-6
Includes bibliographical references.

1. Nuclear reactors – Cooling. 2. Liquid metal cooled reactors –
Research. 3. Molten salt reactors. I. International Atomic Energy
Agency. II. Series.

IAEAL 13-00803

FOREWORD

The International Project on Innovative Nuclear Reactors and Fuel Cycles (INPRO) was launched in 2000, based on a resolution by the IAEA General Conference (GC(44)/RES/21). INPRO aims at helping to ensure that nuclear energy is available in the twenty-first century in a sustainable manner, and seeks to bring together all interested Member States, both technology holders and technology users, to jointly consider actions to achieve desired innovations. INPRO is taking care of the specific needs of developing countries.

One of the aims of INPRO is to develop options for enhanced sustainability through promotion of technical and institutional innovations in nuclear energy technology through collaborative projects among IAEA Member States. Collaboration among INPRO members is fostered on selected innovative nuclear technologies to bridge technology gaps. Collaborative projects have been selected so that they complement other national and international R&D activities.

The INPRO Collaborative Project COOL on Investigation of Technological Challenges Related to the Removal of Heat by Liquid Metal and Molten Salt Coolants from Reactor Cores Operating at High Temperatures investigated the technological challenges of cooling reactor cores that operate at high temperatures in advanced fast reactors, high temperature reactors and accelerator driven systems by using liquid metals and molten salts as coolants. The project was initiated in 2008 and was led by India; experts from Brazil, China, Germany, India, Italy and the Republic of Korea participated and provided chapters of this report.

The INPRO Collaborative Project COOL addressed the following fields of research regarding liquid metal and molten salt coolants: (i) survey of thermophysical properties; (ii) experimental investigations and computational fluid dynamics studies on thermohydraulics, specifically pressure drop and heat transfer under different operating conditions; (iii) monitoring and control of coolant chemistry; and (iv) interaction between coolant and structure materials.

Between 2008 and 2011, four consultancy meetings were held, where the participants defined the issues to be covered and presented their research results. This publication is the final report of the INPRO Collaborative Project COOL. It summarizes the results of the participants’ work concerning the above mentioned topics, including reviews of the existing relevant literature. Since the subjects covered are not reactor specific, the document is complementary to publications on FR development and operation and can support the IAEA initiative to establish a FR knowledge base.

The report is intended for technical experts knowledgeable in the field of thermohydraulics of liquid metals and molten salts, and may also be of interest to industrial designers, producers, vendors, and utility owners and operators.

The IAEA officer responsible for this publication was L. Meyer of the Division of Nuclear Power.

CONTENTS

SUMMARY

One of the aims of the International Project on Innovative Nuclear Reactors and Fuel Cycles (INPRO) is to develop options for enhanced sustainability through promotion of technical and institutional innovations in nuclear energy technology through collaborative projects among IAEA Member States. Collaboration among INPRO members is fostered on selected innovative nuclear technologies to bridge technology gaps. Collaborative projects have been selected so that they complement other national and international R&D activities.

The INPRO Collaborative Project COOL investigated the technological challenges of cooling reactor cores that operate at high temperatures in advanced fast reactors (FR), high temperature reactors (HTR) and accelerator driven systems (ADS) by using liquid metals (LM) and molten salts (MS) as coolants. The project was initiated in 2008 and was led by India: experts from Brazil, China, Germany, India, Italy and the Republic of Korea participated.

Based on the available literature pertaining to the use of liquid metals and molten salts as reactor coolants the participants identified gaps of knowledge and defined topics to be investigated in the collaborative project. The results of their work are presented in the eight self-contained chapters of this report.

In chapter 2, the most reliable thermodynamic and transport properties of lead-bismuth eutectic (LBE) and different molten salt (MS) types are summarized, if available as a function of temperature. This comprises melting and boiling points, vapour pressure, heat of vaporization, density, specific heat, thermal conductivity, viscosity and surface tension.

A salt coolant consists of different individual salt components mixed together into a multi-component system, e.g. as binary or ternary mixtures. The melting points of each individual salt component are generally too high for coolant applications, and the mixing of several components into binary/ternary systems reduces the melting point of the resulting salt system to more practical levels. Each mixture and composition will have different physical and chemical properties, and therefore the choice of molten salt coolant depends on the type of application and related trade-offs. There are two distinct uses of molten salts in nuclear reactor (MSR) systems. For the MSR systems, molten salts are used as a fuel-carrier, in which the liquid salt acts as both fuel and coolant. For the AHTR (Advanced High Temperature Reactor) and the VHTR (Very High Temperature Reactor), the molten salt is simply a coolant in the primary or secondary circuit. In this report, the thermophysical properties of molten salt mixtures are given, which are candidates for coolants in the primary circuit, such as alkali fluorides, ZrF_4- and BeF_4-salts, and which are candidates for the heat transfer loops, such as chlorides and fluor borate salts. Also, the properties of different individual salts are given.

In chapter 3, pressure drop correlations proposed in the past for the reliable prediction of single phase pressure losses in rod bundles are reviewed and evaluated on the basis of inter-comparison to provide some advices on their utilization. The availability of experimental data for liquid metal coolants (lead-bismuth and sodium) within the framework of an international benchmark proposed by OECD/NEA or a national research programme now in progress in China, has allowed a preliminary assessment of these correlations and some interesting results on their reliability are shown.

In chapter 4, the assessment of the heat transfer correlations is described. The assessment of various correlations for liquid metal flow through tubes and rod bundle geometry is done by comparison with experimental data available in literature and by application of computational fluid dynamics (CFD) for heat transfer in liquid metal flows. The computed heat transfer coefficients for forced and natural convective flows in various geometries are compared with the correlations available in literature. Further, CFD analysis was carried out to assess the turbulence models. Various correlations for calculation of turbulent Prandtl number on the prediction of Nusselt number in CFD analysis have been used.

In chapter 5, natural convection heat transfer studies in liquid metal are presented. Three dimensional transient CFD simulation was performed to investigate the natural convection heat transfer from vertical plate and horizontal cylinder submerged in liquid metal pool. The objective of the work was to understand the effect of various parameters on heat transfer, and to generate data from parametric studies.

For natural convection heat transfer from a vertical plate, it was found that heat transfer predicted in CFD analysis matches well with the Sheriff and Davies correlation. For natural convection heat transfer from a submerged horizontal cylinder, the simulation data was validated by comparing the wall temperature predicted in CFD analysis with experimental wall temperature data reported in the literature. The simulation was performed for the bulk temperature ranging from 400 to 800^{o}C. Based on simulation data generated in the present study, a correlation is proposed for natural convection heat transfer from horizontal cylinder immersed in liquid metal. The proposed correlation matches well with previously published experimental data.

In chapter 6, different applications of CFD techniques for innovative nuclear reactors using high temperature fluids are analysed. They show promising results and confirm their usefulness for the study of complex phenomena. Nevertheless, experimental data for their validation are needed.

The simplified three dimension numerical model developed in Italy for the study of the open square lattice reactor core shows the possibility to take into account the three dimensional flow effects and therefore to reduce the design safety margins needed in the one dimensional approach. However, this computational model still needs additional and relevant efforts for an accurate evaluation of the turbulence and mixing energy exchange terms which can only be confirmed with an extended future experimental campaign.

The CFD porous media code developed in China for the simulation of the wire-wrapped sub-assembly of the China Experiment Fast Reactor (CEFR) reactor has shown results in good agreement with the experimental data for the CEFR 61-pin test.

In India, solidification and melting studies of LBE are carried out using the CFD code Anupravaha. In this code the phase change problem is solved using an enthalpy-porosity model. Melting studies show that natural circulation plays an important role in heat transfer.

In chapter 7, experimental and analytical thermohydraulic studies are presented. Experimental studies for single phase natural circulation and transient studies have been performed in the liquid metal loop “HANS” built by Bhabha Atomic Research Centre (BARC). A computer code was developed and steady state and transient analyses have been performed. Results show a good agreement between theoretical and experimental studies.

At ENEA experimental studies on enhanced circulation of heavy liquid metals (HLM) by gas injection have been performed in the LBE facility CIRCE. The possibility of enhancing the LBE circulation by gas injection has been confirmed in the CIRCE facility. Further experiments are performed in the NACIE loop, with the goal to qualify the thermal behaviour of the pins for future applications, and to obtain experimental data about natural circulation and gas enhanced circulation in an HLM loop. Different types of prototypical pins with high thermal performance were tested in a simple bundle including a spacer grid. The results allow establishing a reference experiment for the benchmark of commercial codes when employed in the HLM loop.

At Korea Maritime University, the pressure drop and heat transfer characteristics of the molten salt Flinak were experimentally investigated. By using the pressure drop data in laminar flow a correlation for the viscosity of Flinak was established. Also, it was found that the measured Nusselt number was in general agreement with the theoretical values.

In chapter 8, the development of oxygen sensors and oxygen control systems of HLM coolant chemistry is described. Two different oxygen sensors were developed to measure the dissolved oxygen level in lead-bismuth eutectic. They were successfully tested in heated pools of lead and lead-bismuth, respectively, under controlled conditions in a temperature range between 350 and 650°C.

An oxygen control system was developed and built to control the oxygen concentration in a large loop of 1000 L Pb45Bi55 inventory. A mixture of H_2 and H_2O in the gas atmosphere above the liquid lead alloy is used to control the concentration of oxygen in the liquid metal to protect the steel surface by formation of stable oxide layers.

In chapter 9, methods to improve the corrosion resistance between heavy liquid metal coolant and components, structure materials and instrumentation are presented. The alloying of steel surface with aluminium using microsecond-pulsed intense electron beams was developed and optimized in order to be used for improving the corrosion resistance and creep strength of steels, exposed to liquid Pb and Pb-Bi eutectic. The procedure consists of two steps: (i) coating the steel surface with an Al-containing alloy layer and (ii) melting the coating layer and the steel surface layer using intense pulsed electron beam.

The ternary compound Ti_3SiC_2 could be a good candidate material for some applications in the primary circuit of a lead cooled fast reactor (LFR), because it combines some of the most attractive proprieties of ceramics with those of metals. Results of corrosion tests performed in a lead loop indicated that it could even be a potential material for the pump impeller and bearing of mechanical pumps which work in lead.

Finally, the design and assessment of a prototypical heat exchanger for decay heat removal (DHR) systems in HLM pool type reactors is presented. It consists of coolers immersed in the primary coolant pool, a safety-grade decay heat removal system able to operate with water or water and/or air. The prototype cooler is made of 91 bayonet tubes, which consist of three concentric tubes, containing water and helium, respectively. This configuration avoids the risk of local freezing and excessive stresses in the walls, and monitoring of the gas pressure allows the detection of leakages.

Many of the presented activities are still ongoing and the results presented reflect the state of the art in the year 2011.

CHAPTER 1. INTRODUCTION

1.1. BACKGROUND

Next generation reactors will need to incorporate innovative approaches to further enhance their reliability and safety as needed for large scale deployment in different regions of the world. An important feature of these reactors will be the use of coolants at temperatures much higher than being used in current generation reactors. The main technological goals of high temperature nuclear reactors are improved power plant efficiency and the use of process heat for hydrogen (H_2) production. Reactor designs using gas, steam, liquid metal and molten salt coolants are considered as possible alternatives. This involves addressing a wide range of issues concerning design and safety of these reactors. Joint studies and research, involving several competent research institutes located in different countries, would offer a cost beneficial approach towards addressing these issues.

The INPRO Collaborative Project COOL “Investigation of Technological Challenges related to the Removal of Heat by Liquid Metal and Molten Salt Coolants from Reactor Cores operating at High Temperatures” investigates the technological challenges of cooling reactor cores that operate at high temperatures in advanced fast reactors (FR), high temperature reactors (HTR) and accelerator driven systems (ADS) by using liquid metals (LM) and molten salts (MS) as coolants.

The project was initiated in 2008 and was led by India: experts from Brazil, China, Germany, Hungary, India, Italy and the Republic of Korea were participating. During the kick-off meeting held in 2008, the participants discussed the current status of knowledge regarding important issues related to LM and MS based coolants, identified gaps of knowledge and defined the scope of work which needed to be carried out for higher temperature application of these coolants. The result of this discussion is shown in Table 1.1. The ensuing work was performed in the years 2008–2011, and the results were reported at three consultancy meetings held during these years.

The IAEA has a long standing programme to foster international information exchange and cooperative research and development in the field of liquid metal cooled fast reactors (LMFRs). This programme has been carried out during the past 40 years under the expert guidance of a Technical Working Group on Fast Reactors (TWG-FR), formerly International Working Group on Fast Reactors (IWG-FR). The most recent IAEA publications stemming from this initiative were the starting point of the INPRO Collaborative Project COOL, Refs [1.1–1.5]. Further, for material properties, the Handbook on Lead-Bismuth Eutectic Alloy and Lead Properties Material Compatibility, published by the OECD [1.6], and the IAEA THERPRO database [1.7], and for general information on fast reactors and ADS, the IAEA databases [1.8, 1.9], were the foundation of the investigations performed.

TABLE 1.1. LIST OF ISSUES RELATED TO THE REMOVAL OF HEAT FROM REACTOR CORES OPERATING AT TEMPERATURES UP TO 1000°C WITH FOCUS ON LIQUID METALS AND MOLTEN SALTS, REFS [1.1, 1.8]

Issue	Status	Remarks
Properties of coolants (liquid metals and molten salts) at higher temperatures	Data exist up to 650ºC for lead based alloys and 700ºC for molten salts. For temperature beyond these scattered data few properties are found (Ref. [1.3]).	Reliable data using large number of data points should be generated for temperatures up to 1000ºC.
Thermohydraulic correlations for LM and MS coolants	Correlations for LM and MS have been generated previously for tubular geometries. Some correlations are available for MS in packed bed geometries (for salts commonly used in non-nuclear industries).	Additional effort is required to generate correlations for non-tubular geometries, e.g. pebble bed geometries at higher temperatures. Additionally effect of dissolved oxides, non-ideal surface conditions, etc. need to be assessed. Estimation of pressure drop and buoyancy forces in natural circulation driven systems needs to be carried out.
CFD and neutronics studies on LM and MS	Verification of calculation models has been carried out for lower temperatures (~550ºC) for LM. These correlations have been assessed for MS commonly used in chemical industry.	Verification of calculation models in currently available codes for use in LM and MS systems needs to be assessed for higher temperatures. Verification and benchmark of chemical transport codes, such as MASKOR (IPPE, Russian Federation) is needed.
Freezing/de-freezing of LM and MS	Literature on numerical simulation of freezing and de-freezing and small experimental results is available.	Extensive studies on melting/freezing in large vessels, long pipes, pebble bed geometry, etc. is required.
On-line monitoring and chemistry	Results of research on oxygen control up to 550ºC for LM are available in literature.	Extensive research for use in LM environments at temperatures up to1000ºC is required. Similar studies for MS are also called for. Development of technologies for measurement and control of impurities (e.g. oxygen) is needed.
Components for service in intimate contact with high temperature coolants, and leakage detection, monitoring, plugging for LM and MS	No information is available on MS. Limited data on structural materials for LM is known.	Development of design guidelines for components operating at higher temperatures while being in contact with LM or MS environments is needed. These guidelines may also include the use of advanced materials and devices (e.g. composites, silicon carbide). Special attention may be paid to issues of joining, ensuring leak proof operation and mechanical design. Additional attention may be paid to development of sensors, detectors and other instruments.

1.2. OBJECTIVES AND SCOPE OF WORK

Relating to the identified gaps in knowledge the specific research objectives were defined:

(1) To review and summarize the most reliable thermophysical property data of high temperature coolants (liquid metal, molten salts).

(2) To establish their thermohydraulic relationships and investigate issues related to natural circulation of such coolants.

(3) Validation of CFD and neutronic codes and their internal models and correlations versus experimental data.

(4) Addressing various issues related to handling of high temperature coolants, such as plugging of leakages, phase change behaviours, and handling of active and non-active coolants.

(5) Research on elaboration of methodology for on-line monitoring and control of coolant chemistry under the temperature regime of interest.

(6) Addressing the compatibility of components in intimate contact with high temperature coolants for prolonged service: Special components that would perform the functions of valves, heat exchangers, pumps, fuel handling systems, level detectors, flow-meters, etc. need to ensure reliable operation while being exposed to high temperature coolants for extended durations.

The present report describes the state of the art in the respective fields and the research performed in the participating member states and presents the new results of the investigations. Since the subjects covered are not reactor specific, the document is complementary to publications on fast reactor development and operation and can contribute to the IAEA database and support the IAEA initiative to establish a fast reactor knowledge base.

1.3. STRUCTURE OF THE REPORT

This publication is the final report of the INPRO Collaborative Project COOL. It summarizes the results of the participant’s work concerning experimental investigations and computational fluid dynamics studies on thermohydraulics, data on thermophysical properties of liquid metal and molten salt coolants, and high temperature coolant chemistry monitoring and control. The results are presented in eight chapters, each written by two or three authors with one of them having had the lead for the chapter. Each chapter can be considered a self-contained report on one issue.

REFERENCES TO CHAPTER 1

[1.1] INTERNATIONAL ATOMIC ENERGY AGENCY, Comparative Assessment of Thermophysical and Thermohydraulic Characteristics of Lead, Lead-Bismuth and Sodium Coolants for Fast Reactors, IAEA-TECDOC-1289, IAEA, Vienna (2002).

[1.2] INTERNATIONAL ATOMIC ENERGY AGENCY, Power Reactors and Sub-Critical Blanket Systems with Lead and Lead-Bismuth as Coolant and/or Target Material, IAEA-TECDOC-1348, IAEA, Vienna (2003).

[1.3] INTERNATIONAL ATOMIC ENERGY AGENCY, Theoretical and Experimental Studies of Heavy Liquid Metal Thermal Hydraulics (Proc. Technical Meeting Karlsruhe, Germany, 28–31 October 2003), IAEA-TECDOC-1520, IAEA, Vienna (2006).

[1.4] INTERNATIONAL ATOMIC ENERGY AGENCY, Thermophysical Properties of Materials for Nuclear Engineering: A Tutorial and Collection of Data, IAEA-THPH, IAEA, Vienna (2008).

[1.5] INTERNATIONAL ATOMIC ENERGY AGENCY, Liquid Metal Cooled Reactors: Experience in Design and Operation, IAEA-TECDOC-1569, IAEA, Vienna (2007).

[1.6] OECD NUCLEAR ENERGY AGENCY, Handbook on Lead-Bismuth Eutectic Alloy and Lead Properties Material Compatibility, Thermal-hydraulics and Technologies, OECD/NEA Nuclear Science Committee, NEA No. 6195 (2007). http://www.oecd-nea.org/science/reports/2007/pdf/

[1.7] Thermo-physical Materials Properties Date Base, THERPRO: http://www.iaea.org/NuclearPower/THERPRO/ or http://therpro.hanyang.ac.kr/top/

[1.8] IAEA Fast Reactor Database http://www.iaea.org/inisnkm/nkm/aws/frdb/index.html

[1.9] IAEA ADS Data Base, http://www-adsdb.iaea.org/index.cfm

CHAPTER 2. THERMOPHYSICAL PROPERTIES OF COOLANTS

2.1. THERMOPHYSICAL PROPERTIES OF LEAD-BISMUTH EUTECTIC

2.1.1. Introduction

The use of lead-bismuth eutectic (LBE) alloy as a coolant in nuclear reactor systems (critical and subcritical) has been investigated for some decades. Advanced thermal and fast reactor cores and accelerator driven systems are considered to be cooled by LBE. The reactor systems are designed due to the fact that LBE has many unique nuclear, thermophysical and chemical properties. Particularly, a low melting point, very high boiling point and chemical inertness are characteristics of LBE which can offer a large flexibility to design passively safe reactors with long core life combined with low capital and operating cost.

For designing the various nuclear reactor systems operating with high temperature LBE coolant, information about main thermodynamic and transport properties of LBE such as melting and boiling points, vapour pressure, density, specific heat, thermal conductivity, viscosity and surface tension is essential. Safety analysis for postulated severe accident scenarios in nuclear reactors require thermodynamic and transport property variations over a wide range of temperatures. The relationships developed by authors for various properties of LBE as a function of temperature are summarized in the following sections.

2.1.2. Melting, boiling and critical points

The operating range of nuclear reactor systems is determined generally by coolant melting and boiling temperatures. The normal melting temperature of Pb-Bi has been mentioned in the HLMC Handbook [2.1], which is taken from different sources. It varies from 396.65 to 398.7 K due to small differences in the composition of lead and bismuth. The HLMC Handbook recommended the following value for LBE:

$$T_m = 397.7 \pm 0.6 \text{ K} \tag{2.1}$$

For Pb-Bi eutectic, the boiling point is 1943 K at the normal atmosphere pressure given in old handbooks (refer HLMC Handbook [2.1, 2.7]. The HLMC Handbook has recommended the LBE boiling point, due to uncertainty in measurement of the Bismuth boiling point, as:

$$T_b = 1943 \pm 50 \text{ K} \tag{2.2}$$

For critical temperature, there appears to be no measured values available for the critical temperature and pressure. A very large uncertainty in estimating critical parameters exists in theoretical work for LBE. Recently, Morita et al. [2.2] reported that different sources give the critical temperature in the range of $T_{C(Pb\text{-}Bi)}$ = 2411–4890 K. Morita recommended following critical parameters:

$$T_c = 4890 \text{ K},\ \ P_c = 87.8 \text{ MPa},\ \ \rho_c = 2170 \text{ kg/m}^3 \tag{2.3}$$

2.1.3. Latent heat of melting at the normal melting point

The HLMC Handbook [2.1] has recommended the following value for the latent heat of melting for LBE at normal melting point:

$$Q_m = 38.5 \pm 0.3 \tag{2.4}$$

where Q_m is in kJ/kg.

2.1.4. Heat of vaporization at the normal boiling point

The heat of vaporization for LBE as recommended by HLMC Handbook is given as:

$$Q_b = 854 \pm 2 \tag{2.5}$$

where Q_b is in kJ/kg.

2.1.5. Saturation vapour pressure

The HLMC Handbook [2.1], based on measured data from different sources, recommended the following equation for saturated vapour pressure:

$$p(Pa) = 1.11 \times 10^{10} exp\left(-\frac{22552}{T}\right) \tag{2.6}$$

The equation is valid in the temperature range 673–1943 K. The maximum deviation reported in this temperature range is ±60%.

Morita et al. [2.2] recommended the following equation for saturated vapour pressure for the temperature range 700–2000 K:

$$ln\, p = 35.773 + 2.8006 \times 10^{-4}\, T - \frac{24.053}{T} - 1.6402\, ln\, T \tag{2.7}$$

The deviation with the experimental data reported is −30%–+60%.

Figure 2.1 shows the variation in vapour pressure as a function of temperature for lead-bismuth eutectic.

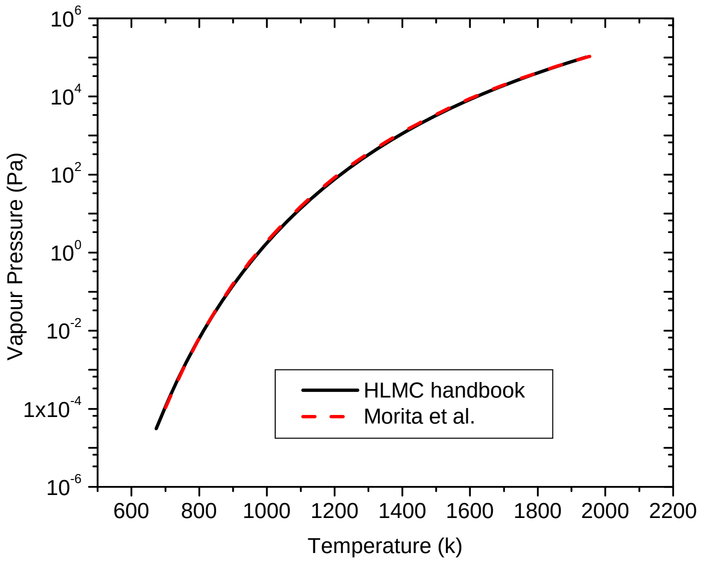

FIG. 2.1. Variation of vapour pressure with temperature for LBE.

2.1.6. Liquid density

The HLMC Handbook [2.1] has compiled data from Lyon [2.3], Kutateladze [2.4], the IAEA-TECDOC-1289 [2.5] and Alchagirov [2.6]. Based on the above data, the HLMC Handbook provided a density relationship as a function of temperature as given below:

$$\rho_{Pb\text{-}Bi} = 11096 - 1.3236\, T \tag{2.8}$$

The above equation is valid in the temperature range 403–1273 K. It was reported in the HLMC Handbook that the deviation with experimental data is 0.8%.

Alchagirov et al. [2.6] measured the density of molten LBE in the temperature range 410–726 K and proposed a linear function of temperature as given below:

$$\rho_{Pb\text{-}Bi} = (10981.7 \pm 2.3) - (1136.96 \pm 3.8)\times 10^{-3}\, T \tag{2.9}$$

They reported that the discrepancy between Eq. (2.9) and available data was within 1–2%.

Morita et al. [2.2] reported that the SIMMER-III code [2.7] uses temperature dependent liquid density in the following function forms:

$$\frac{\rho}{\rho_m} = 1 + C_1(T - T_m) + C_2(T - T_m)^2 + C_3(T - T_m)^3 \tag{2.10}$$

for $T_m \leq T \leq C_4 T_c$ and

$$\frac{\rho}{\rho_m} = 1 + C_5(T_c - T)^{1/2} + C_6(T_c - T)^2 \tag{2.11}$$

for $C_4 T_c \leq T \leq T_c$.

Following values for constants are given [2.2] for use of Eqs (2.10) and (2.11).

T_m =398.15 K ρ_m = 10529 kg/m^3

T_c = 4890 K ρ_c = 10529 kg/m^3

$c_1 = -1.07978\times 10^{-4}$ $c_2 = 0.0$ $c_3 = 0.0$

$c_4 = 6.66667\times 10^{-1}$ $c_5 = 6.35972\times 10^{-2}$ $c_6 = -8.08885\times 10^{-8}$

Figure 2.2 shows the density variation of lead-bismuth eutectic with temperature by various formulations mentioned above.

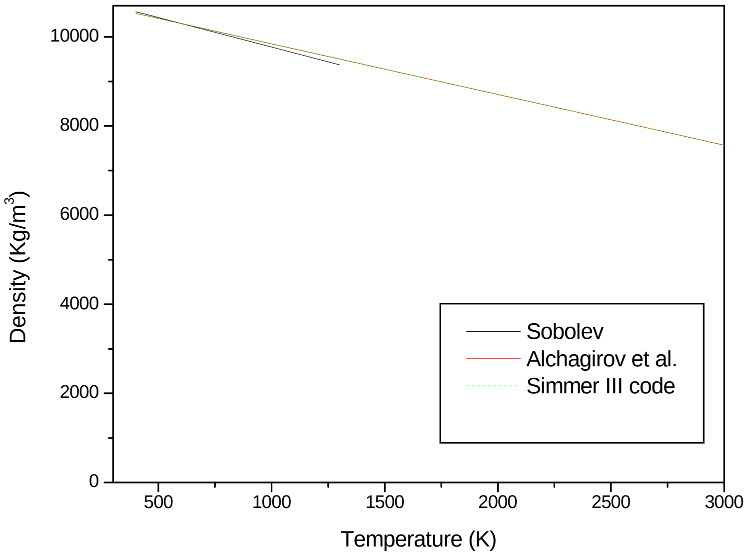

FIG. 2.2. Density variation with temperature for LBE.

2.1.7. Liquid specific heat

In the HLMC Handbook, it is reported that there are only three independent sources where heat capacity of molten LBE is given at different temperatures: Lyon [2.3], Kutateladze [2.4] and Hultgren [2.8]. Following relationship has been recommended for specific heat by the HLMC Handbook:

$$C_p = 159 - 2.72 \times 10^2 T + 7.12 \times 10^{-6} T^2 \tag{2.12}$$

where C_p is in J/kg K, and T is in K. Equation (2.12) is valid for the temperature range 400–1100 K.

2.1.8. Liquid viscosity

The temperature dependence of dynamic viscosity of liquid metals is usually described by an Arrhenius type formula. The expression for the coefficient of dynamic viscosity for lead-bismuth is that recommended by Fink [2.9] given as follows:

$$\mu = 0.490 \times exp\left(\frac{760.1}{T}\right) \tag{2.13}$$

The applicability of Eq. (2.13) is in the temperature range 400–1273 K.

The HLMC Handbook [2.1] has recommended the following relationship for dynamic viscosity in the temperature range 400–1100 K:

$$\mu = 0.494 \times exp\left(\frac{754.1}{T}\right) \tag{2.14}$$

Cevolani and Tinti [2.10] recommended the following formula:

$$\mu = 3.26 - 6.26 \times 10^{-3} T + 4.64 T^2 \tag{2.15}$$

Kaplun et al. [2.11] performed experiments and correlated dynamic viscosity with temperature by following formula:

$$\mu = 0.4656 \times exp\left(\frac{773.2}{T}\right) \tag{2.16}$$

Equations (2.15) and (2.16) were developed for the temperature range 400–1000 K. Figure 2.3 shows the viscosity variation with temperature for LBE by various equations given above.

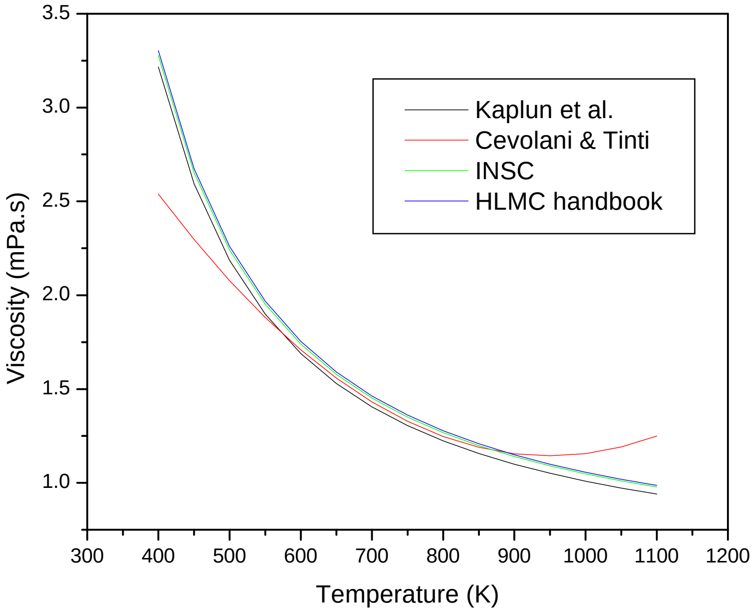

FIG. 2.3. Dynamic viscosity variation with temperature for LBE.

2.1.9. Liquid thermal conductivity

There are some reports on thermal conductivity of liquid LBE. Sobolev [2.12] used the data of Lyon [2.3], Kutateladze [2.4] and Iida [2.13] and correlated them with a parabolic function which yields the following recommended correlation:

$$k = 3.61 + 1.517 \times 10^{-2}T - 1.741 \times 10^{-6}T^2 \tag{2.17}$$

Equation (2.17) is valid for the temperature range 403–1073 K.

Plevachuk et al. [2.14] performed experiments for measuring conductivity and suggested the following formulation:

$$k = 0.7158 + 0.0233T - 8.1098 \times 10^{-6}T^2 \tag{2.18}$$

Equation (2.18) was developed for the temperature range 400–1100 K.

Sar et al. [2.15] calculated thermal conductivity from electrical resistivity and Seebeck coefficient measurements and proposed the following formulation:

$$k = 6.690 + 18.586 \times 10^{-3}T - 5.102 \times 10^{-6}T^2 \tag{2.19}$$

where T is in ^{o}C. Equation (2.19) is applicable for the temperature range 550–1225 K.

A simple theoretical relation exists for pure metals between electrical and thermal conductivities known as Wiedemann-Franz-Lorenz law. Based on this law, the following correlation for LBE for thermal conductivity is recommended by Sobolev [2.12]:

$$k = \frac{2.45T}{86.33+0.0511T} \tag{2.20}$$

Figure 2.4 depicts the variation of thermal conductivity with temperature using Eqs (2.17–2.19).

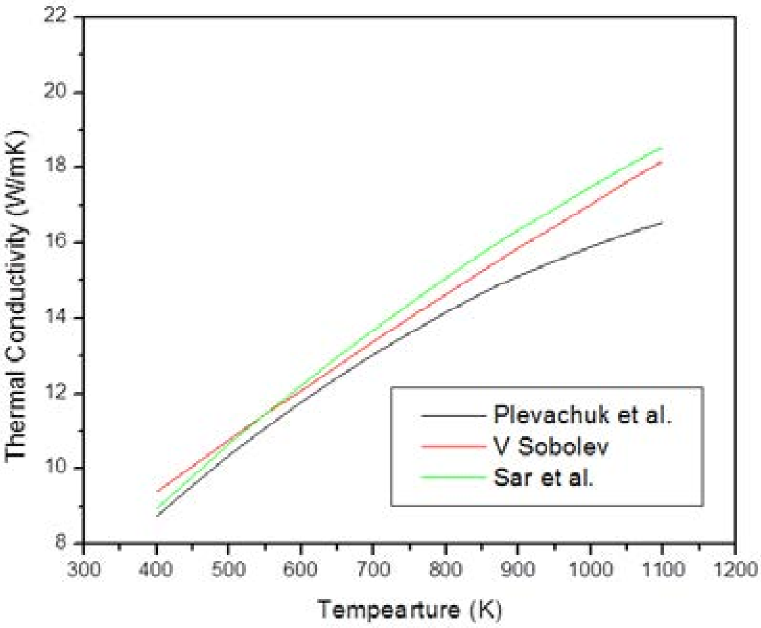

FIG. 2.4. Variation of thermal conductivity with temperature for LBE.

2.1.10. Surface tension

Surface tension of liquid surfaces is related to the tendency to minimize their surface energy. It decreases with temperature and reduces to zero at the critical temperature (Tc) where the difference disappears between liquid and gas phases. HLMC Handbook [2.1] used data from different sources and correlated the following relationship:

$$\sigma = 0.437 - 6.6 \times 10^{-5}T \tag{2.21}$$

Plevachuk et al. [2.14] performed measurements for molten eutectic $Pb_{44}Bi_{56}$ between melting point and 1000 K. The following formulation has been obtained by them as a function of temperature:

$$\sigma = 416.208 - 0.0799 \times (T - T_m) \tag{2.22}$$

where the surface tension σ is in mN/m.

Figure 2.5 shows the variation in surface tension as a function of temperature by using Eqs (2.21) and (2.22) for LBE.

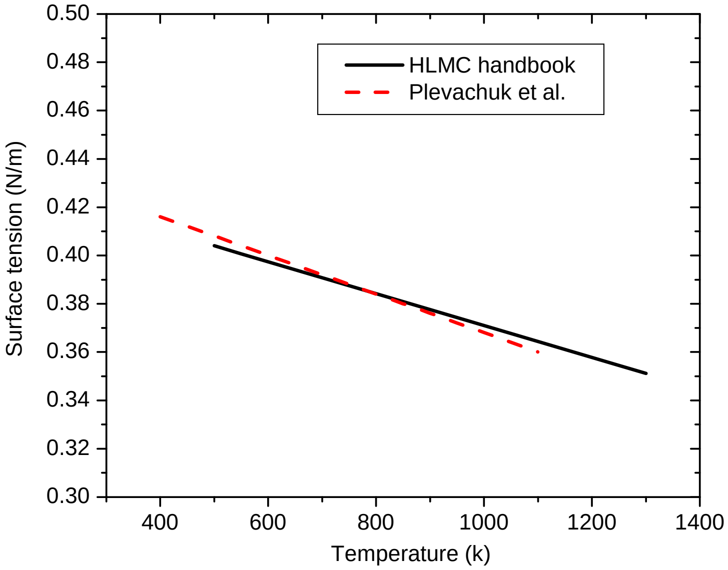

FIG. 2.5. Variation in surface tension with temperature for LBE.

2.2. THERMOPHYSICAL PROPERTIES OF MOLTEN SALTS

This section will summarize the most reliable thermophysical properties data for the different molten salt types (up to the 900–1000ºC range) from selected sources. The data tables present consolidated lists of the summarized/referenced thermophysical properties data (and/or data references). It will go through each property, commenting on the level of validation (estimation or measurement methods), summarized from the given literature sources.

2.2.1. Types of molten salts

A *salt component* or compound, such as sodium fluoride (NaF), can be written in general as M^+X^-, in which the X^- is the “anion” (i.e. F^- in NaF) and the M^+ is the “cation” (i.e. Na^+ in NaF). In general, materials compatibility properties usually govern the choice of anion (e.g. fluorides, chlorides, etc.), and the choice of cation is usually governed by other “performance issues” such as physical and nuclear properties, costs, etc. Some examples of molten salt components include BeF_2, $MgCl_2$, $NaBF_4$ and KNO_3.

A salt mixture (or coolant) consists of different individual salt components mixed together into a multicomponent system, such as the binary mixture LiF-BeF_2 or ternary mixture LiF-NaF-KF. The melting points of each individual salt component are too high for coolant applications (e.g. the melting point of NaF is 995ºC [2.16]), and the mixing of several components into binary/ternary systems reduces the melting point of the resulting salt system to more practical levels. Each mixture also has a certain composition, depending on the different proportions of each component in the mixture. For example, an optimum eutectic composition of LiF-BeF_2 is 67-33 % mol. Each mixture and composition will have different physical and chemical properties, and therefore the choice of molten salt coolant depends on the type of application and related trade-offs.

Various sources in the open literature provide an overview of the different reactor applications of molten salt coolants. Table 2.1 summarizes the different applications of molten salts and gives the reference molten salt composition for each (table adapted from [2.17] and [2.18]).

TABLE 2.1. DIFFERENT APPLICATIONS AND TYPES OF MOLTEN SALTS IN NUCLEAR REACTORS

REACTOR TYPE	NEUTRON SPECTRUM	APPLICATION	REFERENCE SALT
MSR Breeder	Thermal	Fuel	^{7}LiF-BeF$_2$-AnF$_4$
	Fast	Fuel	^{7}LiF-AnF$_4$
		Secondary coolant	NaF-NaBF$_4$
MSR Burner	Fast	Fuel	LiF-NaF-BeF$_2$-AnF$_3$
AHTR	Thermal	Primary coolant	^{7}LiF-BeF$_2$
VHTR	Thermal	Heat transfer coolant	LiF-NaF-KF
MS-FR	Fast	Primary coolant	LiCl-NaCl-MgCl$_2$
SFR	Fast	Intermediate coolant	NaNO$_3$-KNO$_3$

From Table 2.1 it is clear that there are two distinct uses of molten salts in nuclear reactor systems. For the MSR systems, molten salts are used as a fuel-carrier (or *‘fuel’* as given in the table), in which the liquid salt acts as both fuel and coolant. For the AHTR and the VHTR, the molten salt is simply a coolant; *‘primary coolant’* (AHTR) and *‘heat transfer coolant’* (for AHTR and VHTR).

The Oak Ridge National Laboratory (ORNL) report “Assessment of Candidate Molten Salt Coolants for the Advanced High Temperature Reactor (AHTR)” by Williams et al. [2.16] gives a detailed review of the molten salts considered for the primary loop of the AHTR as well as heat transfer coolant salts, assessing the physical properties, nuclear properties and chemical issues for a wide range of salts.

2.2.2. Thermophysical properties of molten salts

The Oak Ridge National Laboratory (ORNL) reports ([2.16], [2.19], [2.20]) and the Molten Salt Database [2.21] built jointly by University of Wisconsin and Shell give comprehensive collections and review of the thermophysical properties of molten salts. In this report, the main thermophysical properties of melting and boiling points, vapour pressure, density, heat capacity, dynamic viscosity and thermal conductivity are summarized in tables.

The thermophysical properties for primary coolant salts (AHTR) are given in Table 2.2, heat transfer coolant salts in Table 2.3, and individual salts in Table 2.4.

TABLE 2.2. THERMOPHYSICAL PROPERTIES OF THE CANDIDATE MOLTEN SALTS FOR THE PRIMARY AHTR COOLANT

Salt		Melting / boiling point (°C)	Vapour pressure at 900°C (mm Hg)	Density ρ (g/cm³) equation	Heat capacity C_p (cal/g-°C)		Viscosity μ (cP)		Thermal conductivity k (W/m K)	
Class	Composition (% mol)				Measured (at 700°C)	Predicted (at 700°C)	μ (at 700°C)	Equation	Measured	Predicted (at 700°)
Alkali Flourides	LiF-KF (50-50)	492 / ?	?	2.460-0.00068.T(ºC) 2.407-0.0005362.T(K) T range 1120–1340K	0.44	0.381	?	?	?	0.91
	LiF-RbF (44-56)	470 / ?	?	3.300-0.00096.T(ºC) T range 500–750°C	0.284	0.226	2.6	0.0212.exp(4678/T(K)), T range 873–1073K	?	?
	LiF-NaF-KF (46.5-11.5-42)	454 / 1570	~0.7	2.530-0.00073.T(ºC) 2.5793-0.000624.T(K) T range 940–1170K	0.45	0.387	2.9	0.04.exp(4170/T(K)), T range 873–1073K	0.6 at 500°C	0.92, 0.90
	LiF-NaF-RbF (42-6-52)	435 / ?	~0.8	3.261-0.000811.T(ºC) T range 500–700°C	?	0.236	2.6	?	?	0.62
ZrF_4 Salts	LiF-ZrF_4 (51-49)	509 / ?	77	3.739-0.000924.T(ºC)	?	0.292	> 5.1	?	?	0.48
	NaF-ZrF_4 (59.5-40.5)	500 /~1350 (extrapolated)	5	3.650-0.00088.T(ºC) T range 550–700°C	0.28	0.275	5.1	For (57-43 % mol) 0.0767.exp(3977/T(K)), T range 873–1073K	?	0.49
	RbF-ZrF_4 (58-42)	410 / ~1450 (extrapolated)	1.3	3.923-0.00100.T(ºC)	?	0.200	5.1	?	?	0.39
	KF-ZrF_4 (58-42)	390 / ~1450 (extrapolated)	1.2	3.416-0.000887.T(ºC)	?	0.251	< 5.1	0.0159.exp(3179/T(K)), T range 873–1073K	?	0.45
	LiF-NaF-ZrF_4 (26-37-37)	436 / ?	~5	3.533-0.000870.T(ºC) T range 500–650°C	?	0.296	6.9	?	?	0.53
BeF_2 Salts	LiF-BeF_2 (67-33)	460 / ~1400 (extrapolated)	1.2	2.280-0.000488.T(ºC) T range 500-650°C 2.413-0.000488.T(K) T range 800-1080K 2.4156-0.00049072.T(K) T range 732.2–4498.8K	0.577	0.566	5.6	0.0116.exp(3755/T(K)), T range 873–1073K	1 at 600°C	1.1
	NaF-BeF_2 (57-43)	340 / ~1400 (extrapolated)	1.4	2.270-0.00037.T(ºC) T range 450–550°C	0.52	0.440	7	0.0346.exp(5165/T(K)), T range 873–1073K	1.0 at T?	0.87
	LiF-NaF-BeF_2 (31-31-38)	315 / ?	1.7	2.313-0.000450.T(ºC) T range 450–550°C	?	0.489	5	?	?	0.97

TABLE 2.3. THERMOPHYSICAL PROPERTIES OF THE CANDIDATE MOLTEN SALTS FOR THE HEAT TRANSFER LOOP

Salt		Melting point / boiling point (°C)	Vapour pressure (at 900 °C)	Density ρ (g/cm³) Equation	Heat Capacity C_p (cal/g-°C)		Viscosity μ (cP)		Thermal Conductivity k (W/m K)	
Class	Composition (% mol)				Measured (at 700°C)	Predicted (at 700°C)	μ (at 700°C)	Equation	Measured	Predicted (at 700°C) (based on pure compound values)
Chlorides	LiCl-KCl (59.5-40.5)	355 / ~1400 (extrapolated)	5.8	1.8772-0.00087.T(ºC)	0.287	0.289	1.15	0.0861.exp(2517/T(K)) T range 873–1173K	0.38 at 700°C	0.42
	LiCl-RbCl (58-42)	313 / ?	?	2.7416-0.000689.T(ºC)	0.213	0.212	1.3	?	?	0.36
	NaCl-$MgCl_2$ (68-32)	445 / >1465	<2.5	2.2971-0.000507.T(ºC)	0.258	0.262	1.36	0.0286.exp(1441/T(K)) T range 973–1173K	?	0.50
	KCl-$MgCl_2$ (68-32)	426 / >1418	<2.0	2.2546-0.000474.T(ºC), 2.001-0.0004571.T(K) T range 1030–1140K	0.276	0.229	1.4	0.0146.exp(2230/T(K)) T range 900–1073K	?	0.40
Fluoroborate salts	NaF-$NaBF_4$ (8-92)	385 / 694	9500	2.2521-0.000711.T(ºC)	0.36	0.435	0.9	0.0877.exp(2240/T(K)) T range 873–1173K	0.4 at 621°C	0.40
	KF-KBF_4 (25-75)	460 / 1070	100	2.258-0.0008026.T(ºC)	0.312	0.367	0.9	0.0431.exp(3060/T(K)) T range 873–1073K	?	0.38
	RbF-$RbBF_4$ (31-69)	442 / >1070	<100	2.946-0.001047.T(ºC)	0.218	0.258	0.9	?	?	0.28

TABLE 2.4. THERMOPHYSICAL PROPERTIES OF INDIVIDUAL SALTS

Compound	Melting point (°C)	Normal boiling point (°C)	Density ρ (g/cm³)	Vapour pressure at 900°C (mm Hg)
			Equation (worked out using additive molar volume method)	
LiF	845	1681	2.3581-0.0004902.T(K) T range 1140–1310K	0.1
NaF	995	1704	2.755-0.000636.T(K) T range 1280–1370K 2.655-0.00056.T(K) T range 1270–1330K	0.07
KF	856-858	1502	2.6464-0.0006515.T(K) T range 1150–1310K	1.2
RbF	775	1408	?	0.75
BeF_2	555	1327	?	Equation (theoretical)
ZrF_4	903	600 (sublimes)	?	722
BF_3	126	100	?	NA
LiCl	610	1382	1.8842-0.0004328.T(K) T range 910–1050K	7
NaCl	808	1465	2.1393-0.0005430.T(K) T range 1080–1290K	2.5
KCl	772	1407	2.1359-0.0005831.T(K) T range 1060–1200K	2.0
RbCl	717	1381	?	3.8
$MgCl_2$	714	1418	1.976-0.000302.T(K) T range 1020–1160K	7

2.3. CONCLUSIONS

The most reliable thermodynamic and transport properties of lead-bismuth eutectic (LBE) and different molten salt types (MS) were summarized, generally up to a temperature range of 900–1000°C, and where available as a function of temperature. This comprises melting and boiling points, vapour pressure, heat of vaporization, density, specific heat, thermal conductivity, viscosity and surface tension.

Both types of molten salts in nuclear reactor systems were considered, MS used as a fuel-carrier and MS simply used as coolant in the primary or secondary circuit. The thermo-physical properties of molten salt mixtures are given, which are candidates for coolants in the primary circuit, such as Alkali Fluorides, ZrF_4- and BeF_4-salts, and which are candidates for the heat transfer loops, such as Chlorides and Fluor borate salts. Also, the properties of different individual salts are given.

List of abbreviations and symbols to Chapter 2

C_1–C_6	constants
C_p	specific heat, J/kg K
k	thermal conductivity, W/m K
P	saturation pressure, Pa
Q	heat, kJ/kg
T	temperature, K
ρ	density, kg/m^3
σ	surface tension, N/m
μ	viscosity
b	boiling
c	critical
m	melting

REFERENCES TO CHAPTER 2

[2.1] OECD NUCLEAR ENERGY AGENCY, Handbook on Lead-Bismuth Eutectic Alloy and Lead Properties Material Compatibility, Thermal-hydraulics and Technologies, OECD/NEA Nuclear Science Committee, NEA No. 6195 (2007). http://www.oecd-nea.org/science/reports/2007/pdf/

[2.2] MORITA, K., MASCHEK, W., FLAD, M., YAMANO, H., TOBITA, Y., Thermophysical Properties of Lead-Bismuth Eutectic Alloy in Reactor Safety Analyses, J. Nucl. Sci. Technol. **43** (2006) 526–536.

[2.3] LYON, R.N., “Liquid Metals”, Reactor Handbook, 2nd edn Vol. 1, Materials, Sect. F, (TIPTON, C.R. Jr., Ed.), Interscience Publishers, New York, United States of America (1960).

[2.4] KUTATELADZE, S.S., et al., Liquid-metal heat transfer media, Atom Energy, Suppl. 2 (transl. Cons. Bur. Inc., New York, 1959) (1959).

[2.5] INTERNATIONAL ATOMIC ENERGY AGENCY, Comparative Assessment of Thermophysical and Thermohydraulic Characteristics of Lead, Lead-bismuth and Sodium Coolants for Fast Reactors, IAEA-TECDOC-1289, IAEA, Vienna (2002).

[2.6] ALCHARIGOV, B.B., SHAMPAROV, T.M., MOZGOVOI, A.G., Experimental investigation of the density of molten lead-bismuth eutectic, High Temp. **41** 2 (2003) 210.

[2.7] MASCHEK, W., et al., “SIMMER-III: Code development for analysing transients and accident in an accelerator driven system (ADS)”, Proc. 2000 ANS/ENS Int. Meeting on Nuclear Applications of Accelerator Technology (AccApp00), Washington, DC, 2000.

[2.8] HULTGREN, R., et al., “Selected Values of the Thermodynamic Properties of Binary Alloys”, ASM, Metals Park, Ohio, United States of America (1973).

[2.9] INTERNATIONAL NUCLEAR SAFETY CENTER OF ARGONNE NATIONAL LABORATORY, “Pb-Bi Eutectic viscosity”, http://insc.anl.gov/(2000).

[2.10] CEVOLANI, S., TINTI, R., ENEA technical report DT.SBD.00004 (1998).

[2.11] KAPLUN, A.B., SHULAEV, V.M., P.LINKOV, S., VARTNOV, Y.D., “The viscosity of the eutectic lead-bismuth alloy”, The Thermophysical Properties of Substances and Materials, Kutateladze Institute of the Thermophysics of the USSR Academy of Sciences, Novosibirsk, 105 (1979).

[2.12] SOBOLEV, V., Thermophysical properties of lead and lead-bismuth eutectic, J. Nucl. Mater. **362** (2007) 235–247.

[2.13] IIDA, T., GUTHRIE, R.I.L., The Physical Properties of Liquid Metals, Clarendon Press, Oxford, United Kingdom (1988).

[2.14] PLEVACHUK et al., Some Physical data of the near eutectic liquid Lead-Bismuth, J. Nucl. Mater. **373** (2008) 335–342.

[2.15] SAR et al., Thermal conductivity of liquid lead-bismuth alloy, possible coolants for fourth generation spallation nuclear reactors, J. Non-Cryst. Solids **353** (2007) 3622–3627.

[2.16] WILLIAMS, D.F., TOTH, L.M., CLARNO, K.T., Assessment of candidate molten salt coolants for the Advanced High-Temperature Reactor (AHTR), ORNL/TM-2006/12 (2006) (on-line).

[2.17] BENES, O., KONINGS, R.J.M., Thermodynamic properties and phase diagrams of fluoride salts for nuclear applications, J. Fluorine Chem. **130** (2009) 22.

[2.18] KHOKHLOV, V., IGNATIEV, V., AFRONICHKIN, V., Evaluating physical properties of molten salt reactor fluoride mixtures, J. Fluorine Chem. **130** (2009) 30.
[2.19] WILLIAMS, D.F., Assessment of candidate molten salt coolants for the NGNP/NHI Heat-Transfer Loop, ORNL/TM-2006/69 (2006) (on-line).
[2.20] CANTOR, S., et al., Physical properties of Molten-Salt Reactor fuel, coolant and flush salts, ORNL/TM-2316 (1968).
[2.21] MOLTEN SALT DATABASE, Molten Salt Database Project (Joint effort University of Wisconsin-Madison and Shell) (http://allen.neep.wisc.edu/shell/).

CHAPTER 3. PRESSURE DROP CORRELATIONS FOR LM

3.1. INTRODUCTION

An accurate prediction of the core pressure drop is a relevant task in the design of LMFR (Liquid Metal Fast Reactor). From one side, the core pressure drop represents the larger contribution to the total pressure drop of the primary circuit, thus influencing the design options (e.g. type and size of the primary pump) as well as the thermohydraulic behaviour of the reactor in natural circulation conditions. From the other side, the optimization of the core design requires uniform distribution of the core outlet temperature; this outcome is usually obtained by means of a chocking scheme at the core inlet that has to be fixed on the basis of the core pressure drop. This aspect is even more critical in the design of innovative liquid metal reactors, where to meet the requirements of GEN IV the natural circulation behaviour is fundamental for the safety design and assessment.

Several investigators made efforts in the past to develop reliable correlations for predicting pressure losses in rod bundles of different geometry and size. In the next paragraph, different correlations are introduced without a classification in order of merit because the touchstone of experimental measurements has not been considered. Some judgement will be expressed, principally on the basis of intercomparison, and an advice about their utilization will be given. Some experimental work is in progress worldwide in order to assess these correlations that are used for the design purpose and introduced in the numerical tools for the safety assessment. Some interesting results of these assessment activities are also presented in the following chapters.

3.2. HYDRODYNAMIC MODELS FROM LITERATURE

This section is initially addressed to pressure losses both in a bare-rod bundle with spacer grids and in wire-wrapped rods. It has to be highlighted that the geometry of a wire-wrapped bundle is completely defined just by the lead of the wire; the grid-spaced bundles, on the contrary, are much less “categorized” in the sense that the geometry of the grid spacers is more “free” than a wire-geometry. Since spacers are accessories that can vary widely, it is more difficult to give an ‘exhaustive’ view of grid-spaced bundles.

3.2.1. Novendstern (Colebroook) model

This model [3.1] has been developed to predict pressure losses in a wire-wrapped fuel assembly but, since it is based on a bare rod correlation plus correction to take into account the effect of wire-spacers, it may be employed for a bare-rod fuel assembly as well.

The velocity V_1 in a central subchannel, formed by three rods in a triangular array, is determined from assembly dimensions and average fluid velocity V_B:

$$V_1 = X \cdot V_B \tag{3.1}$$

where the flow distribution factor X is taken as:

$$X = \frac{A_B}{N_1 A_1 + N_2 A_2 \left(D_{e_2} / D_{e_1}\right)^{0.714} + N_3 A_3 \left(D_{e_3} / D_{e_1}\right)^{0.714}} \tag{3.2}$$

Using the flow conditions for the central subchannel, the pressure drop is determined by:

$$\Delta p = M \cdot f \frac{L}{D_{e_1}} \frac{\rho V_1^{\ 2}}{2g} \tag{3.3}$$

The friction factor for flow in a smooth pipe *f* is approximated by a modified version of the Colebrook equation:

$$f = \left\{ 2\log_{10}\left[-\frac{5.028}{\mathrm{Re}_1}\log_{10}\left(\frac{16.76}{\mathrm{Re}_1}\right)\right]\right\}^{-2} \tag{3.4}$$

The multiplication factor M is used to increase the pressure drop above that calculated with the smooth tube friction factor:

$$M = \left\{ \frac{1.034}{(P/D)^{0.124}} + \frac{29.7(P/D)^{6.94}\,\mathrm{Re}_1^{\ 0.086}}{(H/D)^{2.239}} \right\}^{0.885} \tag{3.5}$$

It is clear that, in case of the pressure loss in a bare bundle, the Novendstern model simply reduces to the Colebroook (at best) or to the simplified Blasius formula. The model has been established to predict pressure losses in hexagonal arrays only. But, considering that simply it takes back to the application of the Blasius formula, it wouldn’t seem insensible if we extrapolate to square arrays as well.

The applicable range for the correlation is limited by the following values:

Number of rods	N_r	19–217
Rod diameter (mm)	D	5–12
Pitch-to-diameter ratio	P/D	1.06–1.42
Lead-to-diameter ratio	H/D	8–96
Reynolds number	Re	2600–200 000

3.2.2. Rehme model

In a first paper [3.2], Rehme proposed a simple method for the prediction of the turbulent friction factor in non-circular channels, which is suitable to be employed for calculation of the pressure loss along a bare-rod bundle. Following his method, the turbulent friction factor *f* should verify the equation:

$$\sqrt{\frac{8}{f}} = A\left[2.5\ln \mathrm{Re}\sqrt{\frac{f}{8}} + 5.5\right] - G^* \tag{3.6}$$

where A and G* should be taken from two diagrams as a function of the geometry factor K for laminar flow. The geometry factor K descends from the relationship:

$$\lambda \cdot \mathrm{Re} = K\ , \tag{3.7}$$

obviously for a channel of the same non-circular geometry. Just to be clear, K is the constant that assumes the value of 64 for laminar flow in a circular channel. If the channel is not circular, K may assume a value that is slightly different, and this is accounted for in any textbook. What is not explained (usually) is the way to derive such values for whatever channel shape occurring in practice. The original paper too does not give much detail; as a matter of fact, some references in the literature are given, that could be of help to calculate the geometry factors of laminar flow in cases of practical significance, but they are not easily attainable.

For the case of grids, the pressure drop at the spacer is just added to the pressure loss in the bare-rod bundle [3.3], whereas for the case of wires, the friction factor is determined by the following equations:

$$f=\left(\frac{64}{\mathrm{Re}_B}F^{0.5}+\frac{0.0816}{\mathrm{Re}_B^{\;0.133}}F^{0.9335}\right)\frac{N_r\cdot\pi\left(D+D_w\right)}{\left(P_b\right)_B} \tag{3.8}$$

with

$$F=\left(\frac{P}{D}\right)^{0.5}+\left[7.6\frac{\left(D+D_w\right)}{H}\left(\frac{P}{D}\right)^{2}\right]^{2.16} \tag{3.9}$$

that is, the pressure losses by the rods and by the wires are integrated in the same formulae. Concerning the geometry (hexagonal or square), with wire wraps apparently there is not a definite conclusion because the method is validated on both of them, but only a (limited) number of measurements have been carried out with rod bundles in square arrays. The applicable range for the correlation is limited by the following values:

Number of rods	N_r	7–217
Rod diameter (mm)	D	5–12
Pitch-to-diameter ratio	P/D	1.1–1.42
Lead-to-diameter ratio	H/D	8–50
Reynolds number	Re	2000–300 000

3.2.3. Engel, Markley and Bishop model

It should be considered a ‘specialized’ model [3.4] because it is particularly aimed at application to flows of very low Reynolds number, covering however laminar, transitional and turbulent regimes. Actually, it is useful only in a limited number of cases, as long as the operation to be explored is not too far from the conditions of the experiments used to fit the model; in fact:

- It is based on measurements of pressure drops carried out only across wire-wrapped hexagonal rod bundles, thus leaving out of consideration grid-spacers and square arrays.

- It is not recommended much beyond the maximum value of Reynolds number tested, which is not very high (~40,000).

- Although recommended for laminar and transitional flow, it is acknowledged that only limited wire-wrapped rod bundle laminar flow friction data are available, and, for its own range, the investigation is rather centred on a single rod bundle having a 1.08 triangular pitch-to-diameter ratio and a 10cm wire-wrap lead.

The friction factor is evaluated by the following equations:

for $\mathrm{Re_B} \leq 400$ $$f = \frac{110}{\mathrm{Re}_B} \tag{3.10}$$

for $400 \leq \mathrm{Re_B} \leq 5000$ $$f = \frac{110}{\mathrm{Re}_B}(1-\psi)^{0.5} + \frac{0.55}{\mathrm{Re}_B^{\ 0.25}}\psi^{0.5} \tag{3.11}$$

for $\mathrm{Re_B} \geq 5000$ $$f = \frac{0.55}{\mathrm{Re}_B^{\ 0.25}} \tag{3.12}$$

where the intermittency factor ψ is:

$$\psi = \frac{(\mathrm{Re}_B - 400)}{4600} \tag{3.13}$$

The equations are particularly fitted to data corresponding to the reference rod bundle tested, i.e. with a pitch-to-diameter ratio ~1.08 and a 10cm wire-wrap lead. In laminar flow however, the friction factor × Reynolds number product for a bare rod bundle having the same pitch-to-diameter ratio as the reference rod bundle tested is deduced to be ~60. Furthermore, the effects of pitch-to-diameter ratio P/D and wire-wrap lead H are assessed “for the limited wire-wrapped rod bundle laminar flow friction data available” and are correlated to the laminar flow average rod bundle friction factor f by:

$$f \cdot \mathrm{Re} = \frac{320}{\sqrt{H}}(P/D)^{1.5} \tag{3.14}$$

No mention is made of the effect of similar parameters in transitional and turbulent flow, then we must believe the equations are fitted to the reference rod bundle. The correlation is said to have been checked in laminar conditions over the ranges:

Number of rods	N_r	61–217
Pitch-to-diameter ratio	P/D	1.067–1.27
Lead (cm)	H	5–30
Reynolds number	Re	50–400

No mention again about transitional and turbulent conditions which must be deemed to be those of the reference test conditions, i.e.:

Number of rods	N_r	61
Rod diameter (mm)	D	~13
Pitch-to-diameter ratio	P/D	~1.08
Lead-to-diameter ratio	H/D	~8
Reynolds number	Re	400–25 000

3.2.4. Cheng and Todreas model

It is largely based on Rehme's method. In order to overcome the lack of knowledge about laminar results affecting the definition of the geometry factors, Cheng and Todreas [3.5] restored and integrated into their model an existing work [3.2], in which, for rod bundles in hexagonal and square arrays, laminar solutions have been elaborated by numerical integration of Poisson's equation for different types of subchannels (centre, wall and corner) and different pitch-to-diameter ratios P/D or wall distance-to-diameter ratios W/D. Thus, it is possible to know the product $\lambda \cdot \mathrm{Re}$, which is now called C'_{fL}, for any arbitrary shaped bare rod flow channel. We are still in the realm of laminar regime.

For the turbulent regime, the spirit of Rehme's method is kept (A and G*, equation above, etc.), introducing a friction factor constant C'_{fL} for turbulent flow which is equalled to the product $\lambda \cdot \mathrm{Re}^m$, where m = 0.18. In the original paper [3.4], these results are tabulated for hexagonal and square arrays, for different types of subchannel (interior, edge, corner), and for different values of pitch-to-diameter ratios (ranging from 1.0 to 1.5).

The friction factor is evaluated by equations which are formally similar to those of the previous subsection:

for $\mathrm{Re} \le \mathrm{Re}_L$

$$f = \frac{C'_{fL}}{\mathrm{Re}} \tag{3.15}$$

for $\mathrm{Re}_L \le \mathrm{Re} \le \mathrm{Re}_T$

$$f = \frac{C'_{fL}}{\mathrm{Re}}(1-\psi)^{\gamma} + \frac{C'_{fT}}{\mathrm{Re}^{0.180}}\psi^{\gamma} \tag{3.16}$$

for $\mathrm{Re} \ge \mathrm{Re}_T$

$$f = \frac{C'_{fT}}{\mathrm{Re}^{0.180}} \tag{3.17}$$

where the intermittency factor is now:

$$\psi = \frac{\log \mathrm{Re} - \log \mathrm{Re}_L}{\log \mathrm{Re}_T - \log \mathrm{Re}_L} \tag{3.18}$$

$$\log\left(\frac{\mathrm{Re}_L}{300}\right) = 1.7\left(\frac{P}{D} - 1.0\right) \tag{3.19}$$

$$\log\left(\frac{\mathrm{Re}_T}{1000}\right) = 1.7\left(\frac{P}{D} - 1.0\right) \tag{3.20}$$

The correlations for the laminar-transition Reynolds number Re_L and the transition-turbulent Reynolds number Re_T are purely empirical and stem from a log-plot of the transition Reynolds number versus P/D ratio. An intermittency factor ψ is defined from the log-plot ψ vs. Re and is used to weight the friction factor *f* between laminar and turbulent regime. The exponent γ is fitted from the data, and is found to be 1/3.

Now, it comes to the point of treating wire-wrapped rods. The treatment is different respectively for internal and external subchannels. In both cases, it is based on empirical constants. We skip the details and arrive to the final formulas. For the interior subchannel friction factor, we have now a rather impressive equation:

$$f_1 = \frac{1}{\mathrm{Re}_1^m}\left[C'_{f1}\left(\frac{P'_{b1}}{P_{b1}}\right)+W_d\left(\frac{3A_{r1}}{A'_1}\right)\left(\frac{De_1}{H}\right)\left(\frac{De_1}{D_w}\right)^m\right] \tag{3.21}$$

Please notice that the prime mark denotes bare rod values i.e. without considering wire (but complete nomenclature is given in annex); for a bare rod case $P'_{w1}/P_{w1} = 1$ and $A_{r1} = 0$, so that equation reduces to $f'_1 = C'_{f1}/\mathrm{Re}_1^m$ (as previously said).

Similarly, the exterior subchannel friction factor (edge i = 2, corner i = 3) is given by:

$$f_i = \frac{C'_{fi}}{\mathrm{Re}_i^m}\left[1+W_s\left(\frac{A_{ri}}{A'_i}\right)\tan^2\theta\right]^{(3-m)/\,2} \tag{3.22}$$

These formulas offer different solutions for laminar and turbulent regimes because of the friction factor constant C'_{fi} (the subscripts *L* or *T* have been dropped, but it has a different value from laminar to turbulent), of the exponent m (m = 1 in laminar flow and m = 0.180 in turbulent flow), and of the constants W_d and W_s.

The constants W_d and W_s have been determined in turbulent flow from Rehme and Trippe's data [3.6]:

$$W_d = \left[29.5-140(D_w/D)+401(D_w/D)^2\right](H/D)^{-0.85} \tag{3.23}$$

$$W_s = 20\log(H/D)-7 \tag{3.24}$$

and in laminar flow from Seban and Hunsbedt's data [3.7]:

$$W_d = \left[41.3-196(D_w/D)+561(D_w/D)^2\right](H/D)^{-0.85} \tag{3.25}$$

$$W_s = 6\log(H/D)-2.1 \tag{3.26}$$

In the transition region, the empirical constant, which is said to need calibration, is the exponent γ for the intermittency factor, which is calibrated from the bundle friction factor data in the transition region and is assumed to be the same for the three kinds of subchannel. By this method, γ is calibrated to be 1/3.

3.2.5. Local loss factor across grid spacers

Pressure drop correlations of a variety of spacers and grids were published by Rehme [3.3] who, on the basis of tests on several grid-type spacers, concluded that grid head loss data can be correlated by:

$$h_{grid} = C_V\varepsilon^2\frac{V_B^{\;2}}{2g} \tag{3.27}$$

where V_B is the average bundle fluid velocity, and C_V is a modified drag coefficient. It is assumed a relative plugging where A_V is the projected frontal area of the spacer, and A_B is the average flow area of the bundle.

The advantage of this equation is that the effect of the plugging ratio ε is explicitly taken into account and can be seen as a grid spacer parameter. As for C_V, the distributions of experimental results have been plotted on paper [3.3] for rod bundles installed in hexagonal and square arrays. These distributions have been linearly approximated for the purposes of our investigation. As the paper says, the modified loss coefficient appears to be $C_V = 6–7$ for Reynolds numbers in the rod bundle $Re_B = 5 \times 10^4$. Data agreement is good, taking into account that the measurements have been carried out on different grids and that a geometric similarity doesn't exist among them. If one assumes that other grid designs behave in a similar way, the head loss at the spacer grid may be expressed (by approximation) with the equation described above.

Obviously, the total pressure loss Δp of the bundle is made up of the friction pressure loss Δp_B in the bare-rod bundle and of the sum of pressure losses Δp_G at each grid spacer, that is, in case of n grids:

$$\Delta p = \Delta p_B + n \cdot \Delta p_G \tag{3.28}$$

There are no measurements for small Reynolds numbers. The equation correlates the 'average' bundle fluid velocity V_B and the 'average' head loss h_{grid}. No provision is made for single subchannels.

3.2.6. Local loss factor at bundle entrance and exit

Entrance and exit losses should be determined by experiment; nonetheless, they can be preliminarily evaluated as those due to sudden contractions and expansions. Several equations exist in literature (so-called 'minor losses'), which can be adapted to suit the situation. For instance, the entrance to the bundle can be figured as a sudden contraction in the flow path to each subchannel where, depending on the type of subchannel, the head loss is computed to be:

$$(h_{IN})_i = (\zeta_{IN})_i \frac{V_i^2}{2g} \tag{3.29}$$

where V_i is the fluid velocity through the subchannel and $(\zeta_{IN})_i$ is a coefficient given in literature directly [3.8] or through the equation $\zeta_{IN} = [(1/C_c) - 1]^2$ where C_c is the contraction coefficient [3.9], i.e. the area of the jet at the 'vena contracta' divided by the subchannel flow area.

Similarly, the exit of the bundle can be figured as a sudden expansion in the flow path from each subchannel, where the pressure drop coefficient can be computed from the Borda-Carnot formula:

$$(h_{OUT})_i = (\zeta_{OUT})_i \frac{V_i^2}{2g} = \left(1 - \frac{A_i}{A_i^0}\right)^2 \frac{V_i^2}{2g} \tag{3.30}$$

in which V_i is the fluid velocity through the subchannel and A_i, A^0_i, respectively, the restricted and unrestricted flow areas along the flow path from each subchannel.

The best resort, however, is to employ the formulae by Idelchick [3.10] which, even though a plethora of equations and graphs, remains a most reliable reference for everyone working on pressure drop coefficients. Evidently, recourse to this handbook is particularly valuable for low Reynolds number.

The handbook provides graphs for sudden contraction and sudden expansion where the curves of ζ *vs Re* are reported for a wide range of Re. The curves are parameterized by different values of the ratio A_i/A^0_i where A_i, A^0_i are, respectively, the restricted and unrestricted flow areas along the flow path to each subchannel.

3.3. ASSESSMENT OF RELAP5 PRESSURE DROP CORRELATIONS FOR HLM SYSTEMS

The correlations described in the previous paragraph are largely applied in the thermo-hydraulic design of the *Innovative Liquid Metal Reactor* as well as in the safety assessment. In particular, the *Best Estimate* system codes, that allow simulating the integral behaviour of the thermohydraulic system in forced and natural conditions, rely on these correlations for the closure relationship (for instance the wall friction). Moreover, the code users apply some correlations to develop their hydraulic model (for instance for the local pressure losses). A multinational systematic study on LBE thermohydraulic was proposed by OECD/NEA with the purpose to assess the prediction models for *Lead-Alloy Cooled Advanced Nuclear Energy System* (LACANES) via benchmarking [3.11]. Main objectives of LACANES benchmark are to validate thermohydraulic loop models and to establish guidelines for quantifying thermo-hydraulic modelling parameters related to friction and heat transfer in lead-alloy coolant systems.

To provide experimental data to LACANES benchmarking, thermohydraulic tests were conducted by using the twelve meters high LBE integral test facility HELIOS (Heavy Eutectic liquid metal Loop for Integral test of Operability and Safety of PEACER) constructed in Seoul National University of Republic of Korea in 2005 [3.12]. The layout of the facility with the indication of the main components and relevant instruments is reported in Fig. 3.1. The prediction of forced convection (Phase-I) and natural circulation behaviour (Phase-II) for a test facility are the benchmark activities initially launched [3.11].

ENEA has participated in the benchmark with a RELAP5 dedicated version to heavy liquid metal (HLM) [3.13], which is its reference tool for the safety analysis of HLM *Innovative Reactors*. The objective is to assess the closure relationships originally developed and validated for water cooled systems (e.g. Colebrook-White correlations for distributed friction losses) as well as to establish some general rules for the development of thermohydraulic models. In the first part of the benchmark concerning the forced convection, the participation has been addressed to obtain a confirmation of the suitability of the code in the distributed pressure drop calculation as well as to determine its limits in the representation of the concentrate pressure drops.

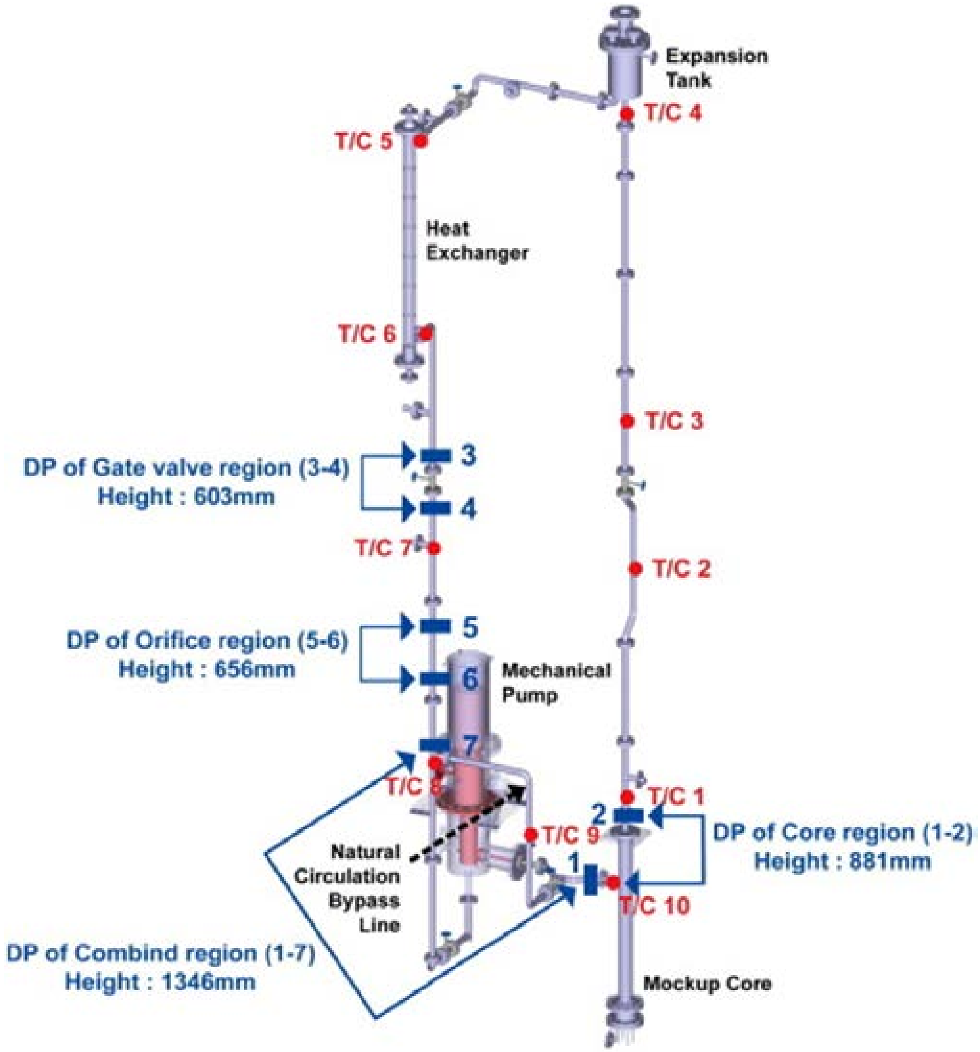

FIG. 3.1. HELIOS three dimensional drawing with instrumentation locations.

In the RELAP5 code [3.14], the distributed pressure drop inside the loop is calculated utilizing a relation of type $\Delta p = f\frac{L}{D}\rho\frac{v^2}{2}$, where the friction loss coefficients are internally calculated.

The code utilizes the different correlations reported in Table 3.1, at different flow regimes to determine the Darcy-Weisbach friction factor. Three different correlations — for laminar flow regime, for turbulent flow regime and for transition flow regime from laminar to turbulent — are used. In particular, the turbulent friction factor is given by the Zigrang-Sylvester engineering approximation to the Colebrook-White correlation.

The concentrated pressure drops due to flow area variations as well as elbows, orifices and grids are taken into account in the RELAP5 model by means of the expression $\frac{1}{2}\zeta\rho V^2$. The pressure loss coefficients are precalculated by means of correlations, mainly drawn from the Hydraulic Handbook [3.10], and introduced in the corresponding junctions of mesh elements of the RELAP5 nodalization. In the calculation of the singular pressure loss coefficient for flow area variations, the formulas are reported in the previous paragraphs and are summarized in Table 3.2.

TABLE 3.1. RELAP5 CORRELATIONS FOR FRICTION FACTORS

Laminar flow regime	$\lambda_L = \dfrac{64}{\mathrm{Re}\,\Phi_s}$	$0 \le \mathrm{Re} \le 2200$
Turbulent flow regime	$\dfrac{1}{\sqrt{\lambda_T}} = -2\log_{10}\left\{\dfrac{\varepsilon}{3{,}7D} + \dfrac{2{,}51}{\mathrm{Re}}\left[1{,}14 - 2\log_{10}\left(\dfrac{\varepsilon}{D} - \dfrac{21{,}25}{\mathrm{Re}^{0{,}9}}\right)\right]\right\}$	$\mathrm{Re} > 3000$
Transition flow regime	$\lambda_{L,T} = \left(3{,}75 - \dfrac{8250}{\mathrm{Re}}\right)\left(\lambda_{T,3000} - \lambda_{L,2200}\right) + \lambda_{L,2200}$	$2200 \le \mathrm{Re} \le 3000$

TABLE 3.2. SINGULAR PRESSURE LOSS COEFFICIENT FOR FLOW AREA VARIATION

Sudden change in flow area	$\zeta = \left(1 - \dfrac{A_0}{A_1}\right)^2$	Sudden expansion	A_0 smallest area
	$\zeta = 0.5\left(1 - \dfrac{A_0}{A_1}\right)$	Sudden contraction	A_1 biggest area
Grids	$\varsigma = C_V \varepsilon^2$	$C_V = 3{,}5 + \dfrac{73{,}5}{R_e^{0{,}264}} + \dfrac{2{,}79 * 10^{10}}{R_e^{2{,}79}}$ $\varepsilon = \dfrac{A_V}{A_S}$	A_v grid area A_s flow area without grid
Orifice	$\zeta = \left(1 + 0{,}707\sqrt{1 - \dfrac{F_0}{F_1}} - \dfrac{F_0}{F_1}\right)^2 \left(\dfrac{F_1}{F_0}\right)^2$	$R_e \ge 10^5$	F_0 smallest area F_1 biggest area

Two isothermal steady states at high (13.57 kg/s) and low (3.27 kg/s) mass flow-rates have been calculated with the RELAP5 code to assess the suitability of these correlations and formulas for HLM hydraulics. Figure 3.2 shows the accumulated pressure losses versus the accumulated length of the forced convection flow path for the high mass flow-rate case. The accumulated pressure losses start from the core inlet and go through the main components of the HELIOS loop. At a distance of 3 m, declinations are due to pressure loss of the core region, and at a distance of 9–10 m, they are due to pressure loss of the orifice region. At a distance of about 25 m, the accumulated pressure losses are compensated by head supplied by a mechanical pump. Moreover, in the diagram, the experimental pressure drops are reported measured on the core, valve and orifice as well as on the entire loop.

The calculation slightly underestimates the total pressure drop owing to an evident underestimation of the core pressure drop. The preliminary results of the benchmark derived from the comparison with the calculations of the other participants (code-to-code) and with the measurements (code-to-data) allow some conclusions like the correctness of the distributed pressure drop calculated by the code and the need of CFD simulations to evaluate pressure drops in complex geometries.

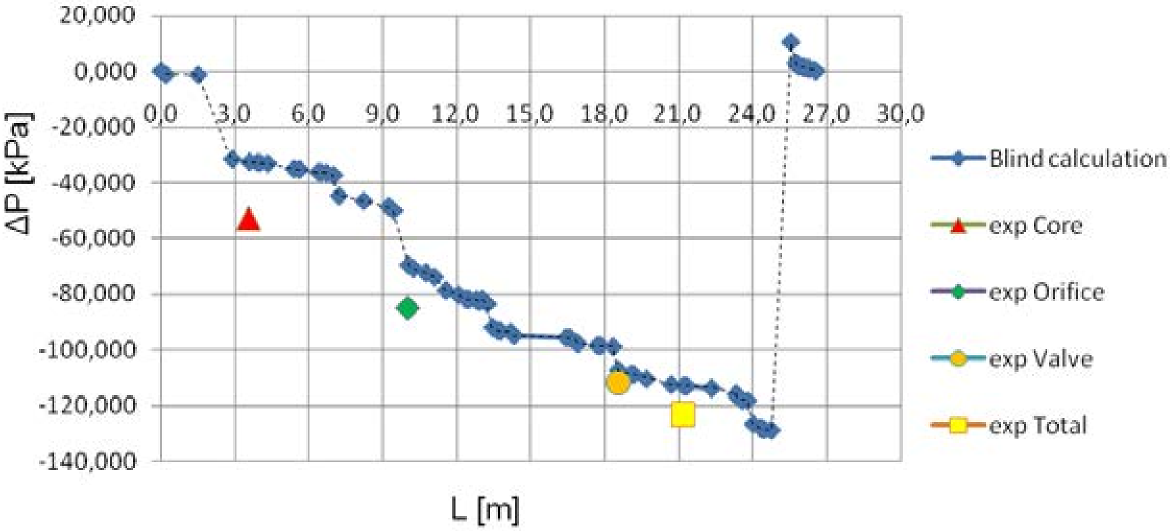

FIG. 3.2. Accumulated pressure drop along HELIOS loop.

3.4. PRESSURE DROP RESEARCH OF REACTOR CORE IN SODIUM REACTOR CEFR

CEFR (China experiment fast reactor) is an important research facility of sodium fast reactor in China. Information on the pressure drop of the reactor core research is necessary to understand the flow resistance in the loop for the natural circulation tests. The thermal conductivity of the sodium used in CEFR is about 100 times that of water, but it's dynamic viscosity is at the same level to water; for example, the dynamic viscosity of the sodium at 350°C at atmospheric pressure is 3.08×10^{-6} kg/s m, which is very close to 3.14×10^{-6} kg/s m of the dynamic viscosity of the water at 90°C at atmospheric pressure. So, for pressure drop research for the CEFR reactor core, water is a suitable fluid to be used in the hydraulics test rig.

Different from other fast reactor cores, in the CEFR there is a connected diagrid between core diagrid and the fuel subassemblies, just as shown in Fig. 3.3. So, in the primary circuit of the reactor, the total pressure drop of the reactor core includes two parts: one is due to the connected reactor diagrid and the other to the fuel subassembly. So the pressure drop of the reactor core can be given like this:

$$\Delta p_{CORE} = \Delta p_{DIAGRID} + \Delta p_{SUBASSEMBLY}$$

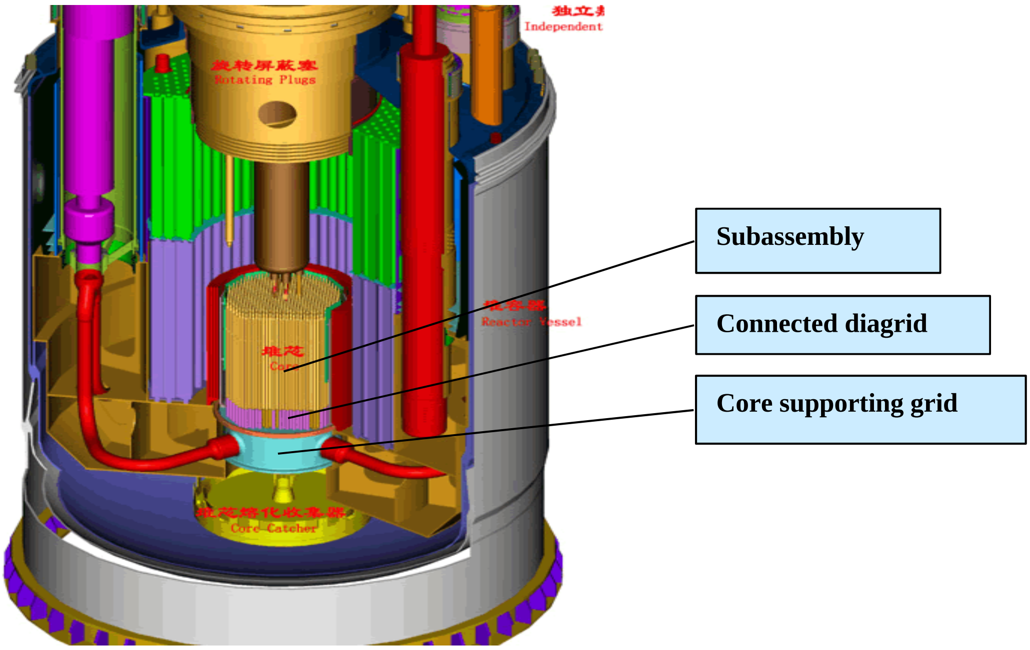

FIG. 3.3. The location of the connected diagrid in the core of CEFR.

Compared to the fuel subassembly, the pressure drop of the connected diagrid is lower than that of the subassembly, but for the complex flow path of the structure, a special test section had been set up to perform hydraulic tests. Figure 3.4 shows the detailed structure of the connected diagrid and the subassemblies, where the forced flow of the sodium from the primary pump goes through the core diagrid and then enters into the connected diagrid; finally, it is distributed into the inlet holes of the seven subassemblies and flows through the subassemblies which contain the wire-wrapped rods.

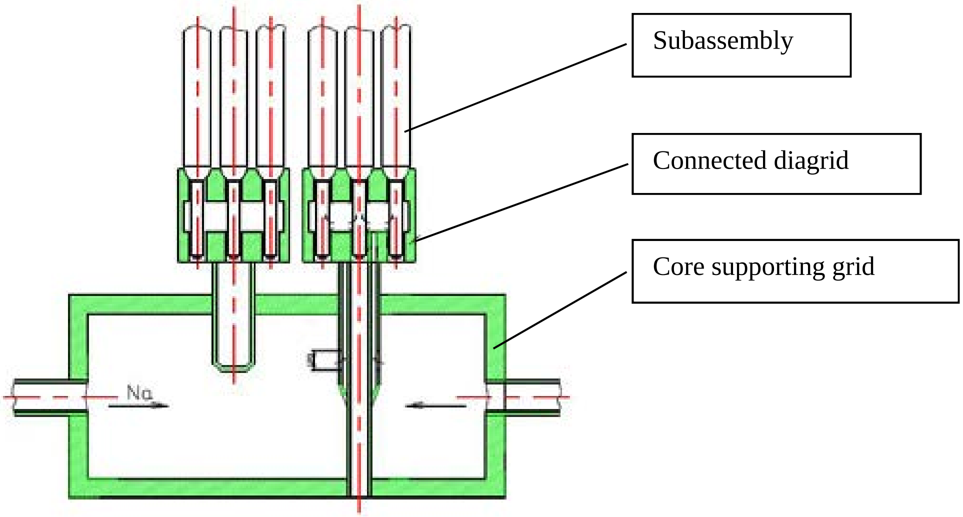

FIG. 3.4. The detail structure of the connected diagrid.

In our tests, two test sections are used for the hydraulic test, one is for the CEFR subassembly and the other is for the connected diagrid. We will describe them in the following paragraph separately.

In CEFR, wire-wrapped rods are adopted to increase the heat transfer coefficient in liquid metal reactor, but their drawback is a sensible increase of the pressure drop that makes more critical to rely on natural circulation in accident conditions. In order to characterize the pressure drop of the 61-pin sub-assembly, the hydraulic tests were performed in a test rig shown in Fig. 3.5. The water facility was built specifically for the tests of CEFR rod bundles. The mock-up of the fuel subassembly was made of stainless steel, the rod bundle has 61 simulated fuel rods in a hexagonal duct, and the parameters are the same as the fuel subassembly of the CEFR reported in Table 3.3.

TABLE 3.3. GEOMETRY PARAMETERS OF THE FUEL SUBASSEMBLY OF CEFR

Parameters	Value
Geometry	
Pitch of fuel rods	7.0 mm
Diameter of the fuel rod	6.0 mm
Height of the helix	100 mm
Length of the active part	450 mm
Thermal power	969 kW
Inlet temperature	360 ℃
Inlet flow rate	3.94 kg/s

The pressure drop of the rod bundle can be estimated by:

$$\Delta p = f\,\frac{L}{D_e}\,\frac{\rho \overline{V}^2}{2} \tag{3.31}$$

and the friction factor *f* deduced from the Colebrook formula for different flow types is shown in Table 3.4.

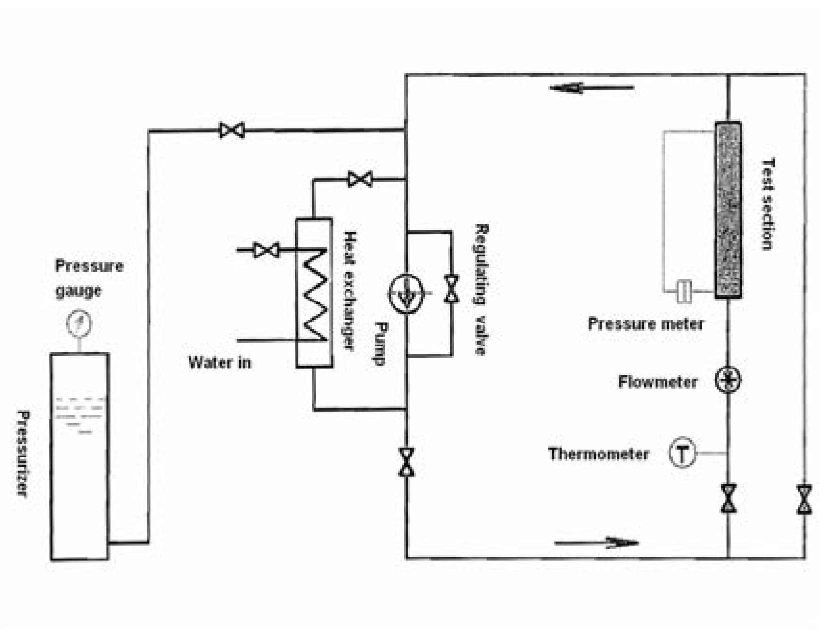

FIG. 3.5. Test rig for pressure drop.

TABLE 3.4. FLOW RESISTANCE OF THE ROD BUNDLES

Flow type	Resistance	Qualification
Turbulent	$g_1 d_1 f_{s1} M_1 X_1 + g_2 d_2 f_{s1} M_2 X_2$	$Re > 5000$
Transition	$\frac{\varphi}{Re\sqrt{H}}\left(\frac{P}{D}\right)^{1.5}(1-\psi)^{0.5} + \frac{0.3M_1}{Re^{0.25}}\psi^{0.5}$	$400 \leq Re \leq 5000$
Laminar	$\frac{\varphi}{Re\sqrt{H}}\left(\frac{P}{D}\right)^{1.5}$	$Re < 400$

The primary purpose of the tests was to measure the pressure drop through the rod bundle and entire fuel subassembly. Empirical formulas called CRT (Chiu-Rohsenow-Todreas) model [3.15] for wire-wrapped rods were assessed and the flow resistance coefficient of the entire fuel subassembly can be obtained after the tests.

Before comparing to the test result, let’s review the CRT (Chiu-Rohsenow-Todreas) model first. This model has taken into account the following two effects in the determination of the subchannel friction factor and of the subchannel flow split. One of the effects is the form pressure drop induced by the wires and the other is the effect of the transverse momentum, which can affect the determination of the friction factor. In the CRT model, pressure drop parameters are derived for channels 1 (interior) and 2 (edge) only. The results are shown below:

$$\Delta p_1 = f_{s1} \frac{L}{D_{e1}} \frac{\rho V_1^2}{2} \left[1 + C_1 \frac{A_{r1}}{A_1^{'}} \frac{D_{e1}}{H} \frac{P^2}{(\pi P)^2 + H^2} \right] \tag{3.32}$$

$$\Delta p_2 = f_{s2} \frac{L}{D_{e2}} \frac{\rho V_2^2}{2} \left\{ 1 + \left[C_2 n \left(\frac{V_T}{V_2} \right)_{GAP} \right]^2 \right\}^{1.375} \tag{3.33}$$

where Δp_1 and Δp_2 represent pressure drop in channel 1 and 2 respectively, and f_s is the friction coefficient, which is computed by the Colebrook formula:

$$\frac{1}{f^{0.5}} = -4 \lg \left[\frac{(\varepsilon / D)}{3.7} + \frac{1.255}{\left(R_e f^{0.5} \right)} \right] \tag{3.34}$$

The value of pressure drop obtained by this study was compared with the hydraulic test results (Fig. 3.6). In this figure, the results of pressure drop in the rod bundle of the four flow zones in the CEFR reactor core are shown, and compared to the CRT model. The maximum deviation is no more than 3%. Based on these comparisons, the CRT model will be adopted for a reasonable prediction of the pressure drop through the rod bundle. At the same time, the flow friction of the entire fuel subassembly can be given like this:

$$f = 96.711 \mathrm{Re}^{-0.2006} \tag{3.35}$$

The relationship of the pressure drop and the flow rate of the subassembly can be obtained by:

$$\Delta \mathrm{p} = 9.108 \times 10^7 \times \left(\frac{\nu^{0.201}}{\rho^{0.799}} \right) \times G^2 \tag{3.36}$$

The flow friction of the connected diagrid can be given by:

$$f = 2.533 - 1 \times 10^{-7} \mathrm{Re} \tag{3.37}$$

And the results of the test are shown in Fig. 3.7. From this figure, it can be seen that the flow friction of the structure almost remains the same with increasing Re-number. As a consequence, the relationship of the pressure drop and the flow rate of the connected diagrid can be obtained by:

$$\Delta \mathrm{p} = 48.532 \times G^{1.987} \tag{3.38}$$

3.5. CONCLUSIONS

The correlations proposed in the past for the reliable prediction of single phase pressure losses in rod bundles have been reviewed and evaluated on the basis of intercomparison to provide some advices on their utilization. The availability of experimental data for Liquid Metal coolants (Lead-Bismuth and Sodium) within the framework of an international benchmark (OECD/NEA LACANES) or a national research programme (CEFR) now in progress, has allowed a preliminary assessment of these correlations and some interesting results on their reliability have been shown.

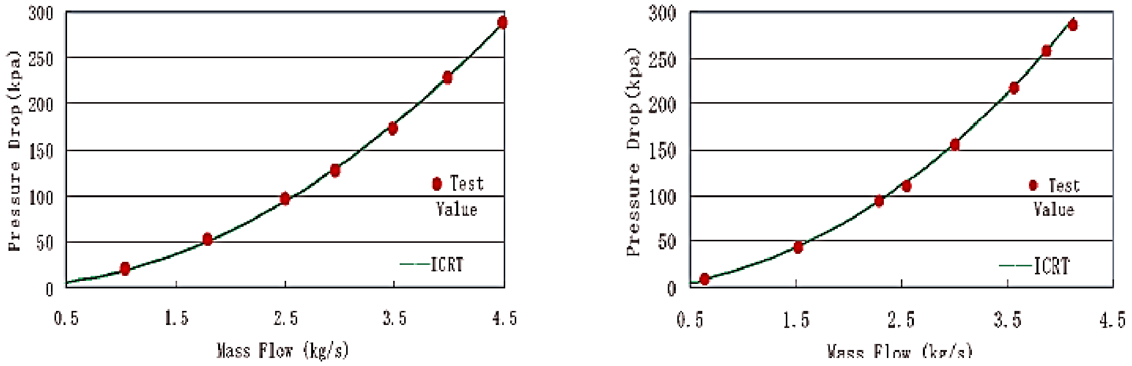

SA of No.1 Flow Zone (T water=90~95℃) **SA of No.2 Flow Zone (T water=90~95℃)**

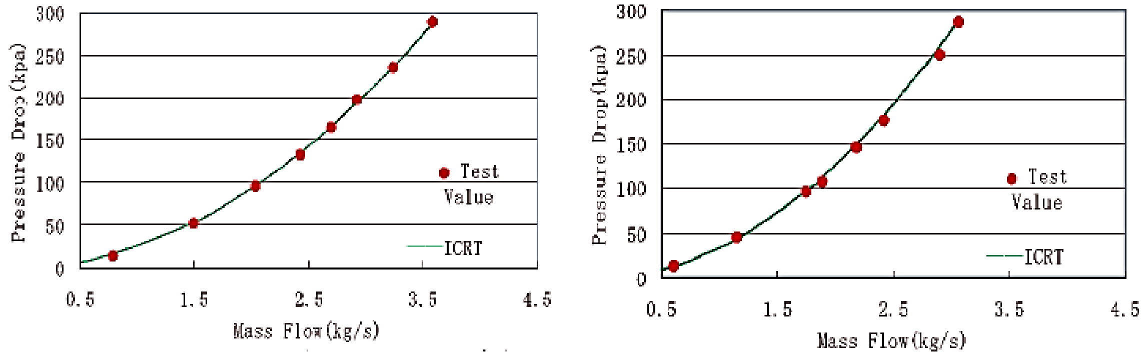

SA of No.3 Flow Zone (T water=90~95℃) **SA of No.4 Flow Zone (T water=90~95℃)**

FIG. 3.6. Pressure drop test for the SA of CEFR.

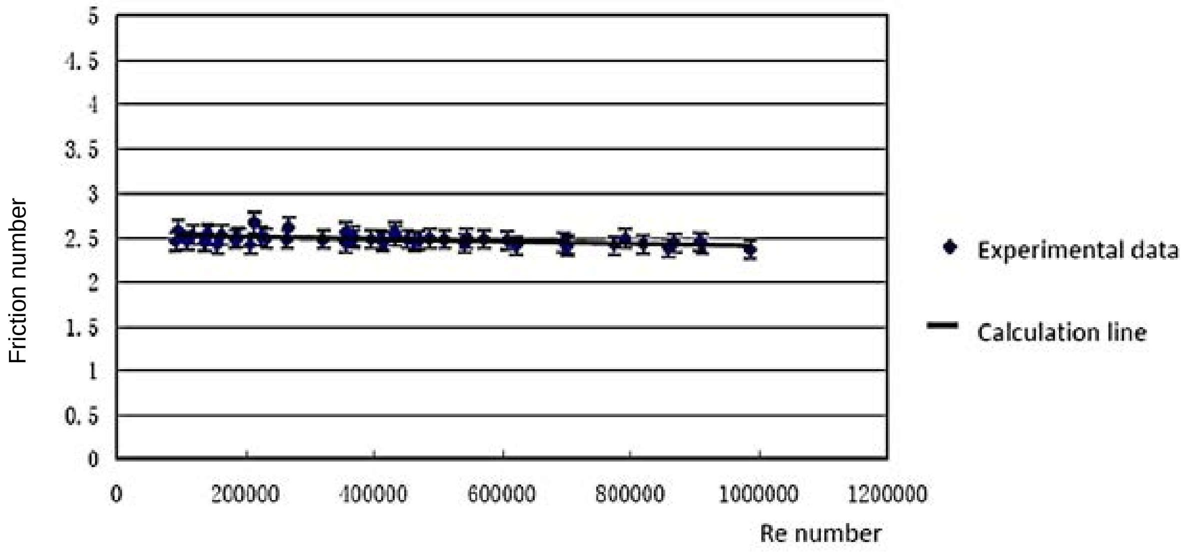

FIG. 3.7. The flow friction coefficient from the test.

List of abbreviations and symbols to Chapter 3

A	geometry factor in turbulent regime (Rehme)
A_B	bundle average flow area
A_i	flow area [subchannel i]
A_{ri}	projected frontal area of a wire [subchannel i]
A_v	projected frontal area of a grid spacer
C	friction factor constant (Cheng and Todreas)
C_c	contraction coefficient
C_v	modified drag coefficient for grids
D	rod diameter
D_{ei}	hydraulic diameter [subchannel i]
D_w	wire diameter
f, f_s	Darcy friction factor
f_i	Darcy friction factor [subchannel i]
f_{ISO}	Darcy friction factor under isothermal conditions
F	geometry factor for wire-wrapped bundle (Rehme)
g	gravity acceleration
$G*$	geometry factor in turbulent regime (Rehme)
h_{grid}	grid head loss
$(h_{in})_i$	entrance head loss [subchannel i]
$(h_{out})_i$	exit head loss [subchannel i]
H	wire lead length
K	geometry factor in laminar regime
L	axial length
m	Reynolds number exponent
M	friction factor multiplier (Novendstern)
n	number of grids
N_i	number of subchannels [type i]
N_r	number of rods
P	rod pitch
P_b	wetted perimeter
$(P_b)_B$	bundle averaged wetted perimeter
P_{bi}	wetted perimeter [subchannel i]
Re	Reynolds number
Re_B	bundle averaged Reynolds number
Re_i	Reynolds number [subchannel i]
T	temperature (absolute)
V_B	bundle average axial velocity
V_i	axial velocity [subchannel i]
W_d	wire drag constant
W_s	wire sweeping constant
X	flow distribution factor

α	mean coefficient of thermal expansion
γ	exponent
Δp	pressure drop
ε	relative plugging (for grids) or surface roughness
θ	angle formed by the wire with the vertical direction
λ	laminar friction factor
$\lambda_{L,2200}$	laminar friction factor at Re=2200
$\lambda_{L,3000}$	turbulent friction factor at Re=3000
μ	dynamic viscosity
ρ	density
ψ	intermittency factor
Φ_s	shape factor for noncircular flow channel
$(\zeta_{IN})_i$	entrance pressure drop coefficient [subchannel i]
$(\zeta_{OUT})_i$	exit pressure drop coefficient [subchannel i]

Subscripts

1	denotes interior subchannel
2	“ edge “ “
3	“ corner “ “
B	“ bundle average
f	“ friction
L	“ laminar flow region
T	“ turbulent “ “

‘	denotes equivalent bare rod values (subchannel without considering wires)
°	denotes equivalent unrestricted values (subchannel without considering rods & wire)

REFERENCES TO CHAPTER 3

[3.1] NOVENDSTERN, E.H., Turbulent flow pressure drop model for fuel rod assemblies utilizing a helical wire-wrap spacer system, Nucl. Eng. Des. **22** (1972) 19–27.

[3.2] REHME, K., Simple method of predicting friction factors of turbulent flow in non-circular channels, Int. J. Heat Mass Tran. **16** (1973) 933–950.

[3.3] REHME, K., Pressure drop correlations for fuel element spacers, Nucl. Technol. **17** (1973) 15–23.

[3.4] ENGEL, F.C., MARKLEY, R.A., BISHOP, A.A., Laminar, transition and turbulent parallel flow pressure drop across wire-wrap-spaced rod bundles, Nucl. Sci. Eng. **69** (1979) 290–296.

[3.5] CHENG, S.K., TODREAS, N.E., Hydrodynamic models and correlations for bare and wire-wrapped hexagonal rod bundles — bundle friction factors, subchannel friction factors and mixing parameters, Nucl. Eng. Des. **92** (1986) 227–251.

[3.6] REHME, K., TRIPPE, G., Pressure drop and velocity distribution in rod bundles with spacer grids, Nucl. Eng. Des. **62** (1980) 137–146.

[3.7] SEBAN, R.A., HUNSBEDT, A., Friction and heat transfer in the swirl flow of water in an annulus, Int. J. Heat Mass Tran. **16** (1973) 303–310.

[3.8] KING, W., Handbook of Hydraulics, McGraw-Hill Book Company (1976).

[3.9] WEISBACH, J., Die Experimental-Hydraulik, J.S. Engelhardt, Freiberg (1855).

[3.10] IDELCHICK, I.E., Handbook of Hydraulic Resistance, 3rd Edition, Jaico Publishing House (2003).

[3.11] OECD/NEA, “Benchmarking of Thermal-Hydraulic Loop Models for Lead-alloy Cooled Advanced Nuclear Energy Systems (LACANES) — Task Guideline for Phase 1: Characterization of HELIOS” (2007).

[3.12] JEONG, S.H., et al., “Operation Experience of LBE loop: HELIOS”, Proc. of the 2006 International Congress on Advances in Nuclear Power Plants (ICAPP ‘06), American Nuclear Society, Reno, United States of America (2006).

[3.13] MELONI, P., et al., “Implementation and preliminary verification of the RELAP5/PARCS code for Pb-Bi cooled subcritical systems”, Proc. of the International Conference on Accelerator Applications AccApp01, Nuclear American Society, Reno, United Sates of America (2001).

[3.14] SLOAN, S.M., SCHULTZ, R.R., WILSON, G.E., “RELAP5/MOD3 code manual”, Tech. Rep. NUREG/CR-5535, INEL-95/0174, Nuclear Regulatory Commission, Washington, DC, United States of America (1995).

[3.15] CHIU, C., ROSENOW, W.M., TODREAS, N.E., Flow split model for LMFBR wire wrapped assemblies, Massachusetts Institute of Technology（1978).

CHAPTER 4. HEAT TRANSFER AND RELATED CFD STUDIES FOR LIQUID METAL COOLANTS

4.1. INTRODUCTION

The renewed interest in liquid metal coolants in various nuclear energy systems is attributed to the inherent safety features of the coolant, like high boiling point, the inertness to water and air for lead, etc. Various nuclear reactor designs are being proposed to be cooled by sodium and heavy liquid metals (lead and lead-bismuth eutectic). Lead-bismuth eutectic (LBE) is also being actively considered as the main coolant for ADS.

This chapter describes the assessment of the heat transfer correlations available in literature for liquid metal flow through tube and Computational Fluid Dynamics (CFD) application for heat transfer in liquid metal flows. The computed heat transfer coefficients for forced and natural convective flows in various geometries are compared with the correlations available in literature.

4.2. LITERATURE REVIEW

4.2.1. Heat transfer in tubular geometry

A number of experimental and theoretical investigations to determine the heat transfer characteristics of liquid metals in a tubular geometry have been made by various investigators. In the literature, the results of the experimental investigations are often compared with each other and with the results of theoretical investigations. Experimental studies have been carried out on heat transfer in liquid metals, mercury, sodium, sodium-potassium and lead-bismuth, flowing through tubes, annulus geometries and bundles. A lot of work was carried out in 1950’s and 60’s. Lubarsky and Kaufman [4.1], Kutalteladze et al. [4.2] and HLMC Handbook [4.3] described in brief most of the experimental studies. Kirillov and Ushakov [4.4] gave a chronology of liquid metal studies in the former USSR from 1940 to 1975.

4.2.1.1. Fully developed heat transfer coefficient

Different correlations for convective heat transfer under fully developed single phase turbulent flow have been proposed by many researchers. Martinelli [4.5] first proposed a heat transfer theory specifically applicable to liquid metals. He applied the analogy concept of turbulent momentum and energy transfer to liquid metal taking into account molecular thermal conduction.

4.2.1.2. Correlations for uniform heat flux for tubular geometry

Lyon [4.6] proposed a simpler method and derived the following semiempirical equation for calculating heat transfer in liquid metals for the case of constant wall heat flux:

$$Nu = 7.0 + 0.025\left(\frac{Pe}{\mathrm{Pr}_t}\right)^{0.8} \tag{4.1}$$

Equation (4.1) is valid for the range $0 < \mathrm{Pr} < 0.1$ and $4000 < \mathrm{Re} < 3.2 \times 10^6$.

Lubarsky and Kaufman [4.1] proposed an empirical correlation based on the work performed by twenty researchers on various liquid metals during 1950’s. The following correlation was suggested by Lubarsky and Kaufman:

$$Nu = 0.625 Pe^{0.4} \tag{4.2}$$

Equation (4.2) is valid for the range $0 < \mathrm{Pr} < 0.1$ and $10^4 < \mathrm{Re} < 10^5$.

Notter and Sleicher [4.7] critically examined the correlations available for liquid metal heat transfer to identify the reasons behind the discrepancy among them. The correlations developed by them for constant heat flux and constant wall temperature conditions are based on numerical analysis on eddy diffusivity and the minimum error of the cloud of experimental data. Following is the empirical correlation for the case of uniform wall heat flux suggested by them:

$$Nu = 6.3 + 0.0167 Pe^{0.85} \tag{4.3}$$

Equation (4.3) is valid for the range $0.004 \leq \mathrm{Pr} \leq 0.1$ and $10^4 \leq \mathrm{Re} \leq 10^6$.

The correlation recommended by Ibragimov et al. [4.8] satisfies the experimental results which were conducted under industrial conditions (no continuous purification of the liquid metal was carried out). Following correlation was proposed by Ibragimov et al.:

$$Nu = 4.5 + 0.0147 Pe^{0.8} \tag{4.4}$$

Equation (4.4) is valid for the range $0 < \mathrm{Pr} < 0.1$ and $10^4 < \mathrm{Re} < 10^5$.

Skupinski et al. [4.9] performed experiments to determine heat transfer coefficients in a horizontal circular tube with sodium-potassium (NaK) for a constant heat flux at Reynolds numbers between 3.6×10^3 and 9.05×10^5. The Prandtl number of NaK was about 0.0153. They compared experimental data with other published experimental data and correlated these data by the following relationship:

$$Nu = 4.82 + 0.0185 Pe^{0.827} \tag{4.5}$$

Kirillov and Ushakov [4.4] recommended the following correlation for LBE flows:

$$Nu = 4.5 + 0.018 Pe^{0.8} \tag{4.6}$$

Equation (4.6) is valid for the range $0 < \mathrm{Pr} < 0.1$ and $10^4 < \mathrm{Re} < 10^5$.

Recently Cheng and Tak [4.10] carried out a review of various empirical heat transfer correlations. The best suitable correlations at different ranges of Peclet number were found and a new correlation was developed which is applicable for a wide range of Peclet numbers for molten lead-bismuth eutectic. They carried out a review and an assessment of the existing correlations. A new correlation was developed which is applicable for a wide range of Peclet number in molten LBE:

$$Nu = A + 0.018 Pe^{0.8} \tag{4.7}$$

$$A=\begin{cases}4.5 & \mathrm{Pe}\leq 1000\\ 5.4\text{-}9\times 10^{-4}Pe & 1000\leq Pe\leq 2000\\ 3.6 & Pe\geq 2000\end{cases}$$

The validity range of the above equation is $10^4 < \mathrm{Re} < 5.0 \times 10^5$.

4.2.1.3. Correlations for uniform wall temperature for tubular geometry

Seban and Shimazaki [4.11] developed a correlation for turbulent tube flow (ref. Lubarsky and Kaufman, [4.1]) with constant wall temperature which is given as:

$$Nu = 5 + 0.025Pe^{0.8} \tag{4.8}$$

Gilliland et al. [4.12] developed the following correlation for the case of constant wall temperature:

$$Nu = 3.3 + 0.025Pe^{0.8} \tag{4.9}$$

Equation (4.9) is valid for the range $0.0 < \mathrm{Pr} \leq 0.1$ and $10^4 \leq \mathrm{Re} \leq 5 \times 10^6$.

Sleicher and Tribus [4.13] developed the following correlation for the case of constant wall temperature:

$$Nu = 4.8 + 0.015Pe^{0.91}\,\mathrm{Pr}^{0.3} \tag{4.10}$$

Hartnett and Irvine [4.14] developed a correlation for the case of constant wall temperature (ref. LBE Handbook, [4.3]), which is given as:

$$Nu = 5.78 + 0.015Pe^{0.8} \tag{4.11}$$

Equation (4.11) is valid for the range $0.0 < \mathrm{Pr} \leq 0.1$ and $10^4 \leq \mathrm{Re} \leq 5 \times 10^6$.

Azer and Chao [4.15] investigated turbulent heat transfer for fully developed pipe flow for constant wall temperature. The following correlation is recommended by them:

$$Nu = 5 + 0.05Pe^{0.77}\,\mathrm{Pr}^{0.25} \tag{4.12}$$

Equation (4.12) is valid for the range $0.0 < \mathrm{Pr} \leq 0.1$ and $10^4 \leq \mathrm{Re} \leq 5 \times 10^5$.

Notter and Sleicher [4.7] developed the following semiempirical correlation for the case of constant wall temperature:

$$Nu = 4.8 + 0.0156Pe^{0.85}\,\mathrm{Pr}^{0.09} \tag{4.13}$$

Equation (4.13) is valid for the range $0.004 \leq \mathrm{Pr} \leq 0.1$ and $10^4 \leq \mathrm{Re} \leq 10^6$.

Unless special measures are taken for liquid metal purification, heat transfer coefficients inside tubes are given by the relationship:

$$Nu = 3.3 + 0.014Pe^{0.8} \tag{4.14}$$

The thermal contact resistance between the wall surface and the liquid metal mainly results from deposition of a film of liquid metal oxides in the region of the laminar sublayer. The effect of the contact resistance was confirmed by test data with different contents of oxide in heavy liquid metal (HLM) and also by time dependent data. Kirillov and Ushakov [4.4] predicted the thermal resistance between the tube wall and the liquid medium due to oxide layer. The value of the contact resistance is given by:

$$R_c \frac{k}{D} \cong 7\,\mathrm{Re}^{-0.5} \tag{4.15}$$

Where k is the thermal conductivity of the fluid and D is the hydraulic diameter. The $\mathrm{Nu_c}$ for liquid metal without special purification is given by:

$$R_c \frac{k}{D} \cong \frac{1}{Nu_c} - \frac{1}{Nu} \tag{4.16}$$

The value of Nu is obtained from the correlation suggested by Kirillov and Ushakov [4.4] by Eq. (4.6). The correlation given is based on pure molten sodium.

4.2.1.4. Correlations for entrance region of tube

Experimental data or predicted Nusselt numbers are rather limited in the entrance region. Following are the correlations for heat transfer in the entrance region.

Developing thermal region

Sleicher, Awad and Notter [4.16] proposed approximate empirical formulae for the developing thermal region:

$$Nu_x = Nu_\infty \left(1 + \frac{2}{x/D}\right) \qquad x/D > 4 \tag{4.17}$$

$$Nu_{avg} = Nu_\infty \left(1 + \frac{8}{L/D} + \frac{2}{L/D} \ln\left(\frac{L/D}{4}\right)\right) \qquad L/D > 4 \tag{4.18}$$

where Nu_∞ is the fully developed Nusselt number (Eqs (4.3) and (4.13)) developed by Notter and Sleicher [4.7] for a tube.

An analytical study adopting a modified Van Driest and Cebeci mixing length turbulence model is performed by Chen and Chiou [4.17]. The study is relevant to liquid metals. The predicted results were compared with experimental data by Awad [4.18] under constant wall heat flux and temperature conditions. They proposed the following correlations for the local and the mean Nusselt numbers

$$Nu_x = Nu_\infty \left(1 + \frac{2.4}{x/D} + \frac{1}{\left(x/D\right)^2}\right) \qquad x/D > 2 \text{ and } Pe > 500 \tag{4.19}$$

$$Nu_x = Nu_\infty \left(1 + \frac{7}{L/D} + \frac{1}{(L/D)} \ln\left(\frac{L/D}{10} \right) \right) \qquad L/D > 2 \text{ and } Pe > 500 \qquad (4.20)$$

Here again, Nu_∞ is the fully developed Nusselt number calculated from Eqs (4.3) and (4.13) developed by Notter and Sleicher [4.7] for constant heat flux and wall temperature for a tube.

Developing thermal and velocity region

Chen and Chiou [4.17] recommended the following correlation for Nusselt number in the developing thermal and velocity region:

$$Nu_x = Nu_\infty \left(0.88 + \frac{2.4}{x/D} + \frac{1.25}{(x/D)^2} - E \right) \qquad 2 \leq x/D < 35 \qquad (4.21)$$

and for average Nusselt number Nu_{avg}:

$$Nu_{avg} = Nu_\infty \left(1 + \frac{5}{L/D} + \frac{1.86}{L/D} \ln\left(\frac{L/D}{10} \right) - F \right) \qquad (4.22)$$

For constant wall temperature, $E = \frac{(40 - x/D)}{190}$, $F = 0.09$,

and for constant heat flux condition, $E = F = 0$.

4.2.1.5. Effect of variable properties

For design convenience, Chen and Chiou [4.17] provided the following relationship for accounting the temperature effect on heat transfer:

$$\frac{Nu}{Nu_0} = \left(\frac{T_b}{T_i} \right)^n \qquad (4.23)$$

The subscript zero refers to the values calculated under the assumption of constant physical properties. T_b represents the bulk temperature and T_i is the inlet temperature. The values of n for constant wall heat flux and temperature conditions are given by Chen and Chiou [4.17] for liquid metals Na and NaK.

4.2.2. Turbulent heat transfer in a concentric annulus

Heat transfer to liquid metals flowing through a concentric annulus under conditions of constant heat flux, fully established turbulent flow and heat transfer through the outer wall only is represented by the following semiempirical equation of Dwyer [4.19]:

$$Nu = \alpha_1 + \beta_1 \left(\overline{\psi} Pe \right)^n \qquad (4.24)$$

$$\alpha_1 = 5.26 + \frac{0.05}{r^*}, \quad \beta_1 = 0.01848 + \frac{0.003154}{r^*} - \frac{0.0001333}{r^{*2}}$$

$$n = 0.78 - \frac{0.01333}{r^*} + \frac{0.000833}{r^{*2}}$$

$$\overline{\psi} = 1 - \frac{1.82}{\Pr\left(\varepsilon_M/\nu\right)_{\max}^{1.4}} \quad with \quad \left(\frac{\varepsilon_M}{\nu}\right)_{\max} = \frac{1}{2}\left(\frac{\varepsilon_M}{\nu}\right)_{\max,core}$$

The radius ratio, r^*, is defined as $r^* = \frac{r_i}{r_o}$, where r_i is the radius of inner wall and r_o is the radius of outer wall of the annulus.

As mentioned in the HLMC Handbook [4.3], an expression for $\left(\varepsilon_M/\nu\right)_{\max,core}$ applicable to a circular duct ($r^*=0$) was developed by Bhatti and Shah [4.20] and is given as $\left(\varepsilon_M/\nu\right)_{\max,core} = 0.037\,\mathrm{Re}\, f^{\,0.5}$, where f is the Fanning friction factor.

For the case of heat transfer through the inner wall only, the heat transfer is represented by the following semiempirical equation of Dwyer [4.19]:

$$Nu = \alpha_1 + \beta_1\left(\overline{\psi} Pe\right)^n \tag{4.25}$$

$$\alpha_1 = 4.63 + \frac{0.686}{r^*}, \quad \beta_1 = 0.02154 - \frac{0.000043}{r^*}$$

$$n = 0.752 + \frac{0.01657}{r^*} - \frac{0.000833}{r^{*2}}$$

Rensen [4.21] developed a correlation for heat transfer in a concentric annulus, with the inner wall subjected to a uniform heat flux and the outer one thermally insulated. The experiment was conducted for liquid sodium in a Reynolds number range $6 \times 10^3 < \mathrm{Re} < 6 \times 10^4$ and the radius ratio, $r^* = 0.5409$, was maintained. Following is the correlation developed by him:

$$Nu = 5.75 + 0.022 Pe^{0.8} \tag{4.26}$$

4.2.3. Correlations for flow in rod bundles

Researchers have performed experiments to determine heat transfer to liquid metals flowing in triangular and square lattice of cylindrical rods for a wide range of Peclet numbers. Based on experimental data various correlations are reported in the literature.

Dwyer and Tu [4.22] recommended the following correlation for triangular bundle of circular rods:

$$Nu = 0.93 + 10.81\left(\frac{P}{D}\right) - 2.01\left(\frac{P}{D}\right)^2 + 0.0252\left(\frac{P}{D}\right)^{0.273}\left(\psi Pe\right)^{0.8} \tag{4.27}$$

Friedland and Bonilla [4.23] calculated Nusselt numbers for parallel liquid metal flow through infinite tube bundles and correlated them by an approximate function according to Eq. (4.28), where both terms on the right hand side are dependent from the pitch to diameter ratio (*P/D*). Ψ is the ratio of the eddy diffusivity of heat (ε_H) and the eddy diffusivity of momentum (ε_M). The function had been evaluated in the range $10 \leq \mathrm{Pe} \leq 100\,000$ and $1.375 \leq P/D \leq 10$.

$$Nu = 7 + 3.8\left(\frac{P}{D}\right)^{1.52} + 0.027\left(\frac{P}{D}\right)^{0.27}\left(\psi Pe\right)^{0.8} \tag{4.28}$$

Maresca and Dwyer [4.24] performed experiments in the Brookhaven National Laboratories on 13 pins of 13 mm OD arranged in an equilateral triangular lattice with a pitch to diameter ratio of 1.75. The working fluid was mercury (Pr ~ 0.02). The following semiempirical correlation was used to describe test data:

$$Nu = 6.66 + 3.126\left(\frac{P}{D}\right) + 1.184\left(\frac{P}{D}\right)^{2} + 0.0155\left(\psi Pe\right)^{0.86} \tag{4.29}$$

Equation (4.29) is recommended for triangular bundles in the range of Peclet numbers of 70–10 000 and a pitch to diameter ratio of 1.3–3.

The factor ψ can be correlated by an empirical equation as:

$$\psi = 1 - \frac{1.82}{\mathrm{Pr}\left(\frac{\varepsilon_M}{\nu}\right)_{\max}^{1.4}} \tag{4.30}$$

For the factor $(\varepsilon_M/\upsilon)_{\max}$, an approximation can be used as mentioned in the report by Pfrang and Struwe [4.25]:

$$\ln\left(\frac{\varepsilon_M}{\nu}\right)_{\max} = 0.864 \ln \mathrm{Re} - 0.24\left(\frac{P}{D}\right) - 2.12 \tag{4.31}$$

Subbotin et al. [4.26] recommended the following correlation for flow of liquid metal in a triangular lattice of rods with a pitch-to-diameter ratio from 1.1 to 1.5 and Peclet numbers ranging from 80 to 8000:

$$Nu = 0.58\left(\frac{D_h}{D}\right)^{0.55} Pe^{0.45} \tag{4.32}$$

where D_h and D are the hydraulic and rod diameters, respectively.

Borishanskii et al. [4.27] reported the results obtained in 7 pins of 22 mm OD arranged in equilateral triangular bundles with different values of P/D (1.1, 1.3, 1.4 and 1.5) using coolants with Pr of 0.007, 0.03 and 0.024. The following correlation was derived by Borishanskii et al.:

$$Nu = 24.15\log\left[-8.12+12.76\left(\frac{P}{D}\right)-3.65\left(\frac{P}{D}\right)^{2}\right]+0.0174\left(1-e^{6\left[\left(\frac{P}{D}\right)-1\right]}\right)B \tag{4.33}$$

where $B = \begin{cases} 0 & Pe \le 200 \\ (Pe-200)^{0.9} & Pe \ge 200 \end{cases}$

For Eq. (4.33), the experimentally qualified range for the P/D ratio is 1.1–1.5 and for Peclet number it is 60–2200.

Graber and Rigger [4.28] developed the following relationship for triangular arrays:

$$Nu = 0.25+6.2\frac{P}{D}+\left(0.32\frac{P}{D}x-0.007\right)Pe^{\left(0.8-0.024\frac{P}{D}\right)} \tag{4.34}$$

Equation (4.34) is recommended for the range $150 \le Pe \le 4000$ and $1.2 \le P/D \le 2.0$.

Calamai et al. [4.29] proposed the following relationship which does not refer to any particular lattice:

$$Nu = 4+0.16\left(\frac{P}{D}\right)^{5}+0.33\left(\frac{P}{D}\right)^{3.8}\left(\frac{Pe}{100}\right)^{0.86} \tag{4.35}$$

The validity range for above correlation is $10 \le Pe \le 5000$ and $1.1 \le P/D \le 1.4$.

Ushakov et al. (ref. Subbotin et al. [4.30]) recommended the following correlation for flow of liquid metal in a triangular lattice of rods with a pitch-to diameter ratio 1.3–2.0 and Peclet number up to 4000:

$$Nu = 7.55\left(\frac{P}{D}\right)-20\left(\frac{P}{D}\right)^{-13}+0.041\left(\frac{P}{D}\right)^{-2}\left[1-\frac{1}{\left(\frac{P}{D}\right)^{30}-1/6+\sqrt{1.15+1.24\varepsilon}}\right]Pe^{0.56+0.19\left(\frac{P}{D}\right)-0.1\left(\frac{P}{D}\right)^{-30}} \tag{4.36}$$

An experimental programme was conducted for the BREST lead-cooled reactor project to study the heat transfer to liquid metal in a square lattice of round tubes by Zhukov et al. [4.31]. The working section was comprised of 25 tubes of 12 mm outer diameter. Experiments were performed with sodium-potassium (22%Na-78%K) working fluid in four sets for pitch-to diameter ratios of 1.25, 1.28, 1.34 and 1.46. The heated length was 980 mm. Zhukov et al. correlated experimental results by the following equation for Peclet number ranging from 60 to 2000 and pitch-to-diameter ratios ranging from 1.2 to 1.5.

$$Nu = 7.55\left(\frac{P}{D}\right)-14\left(\frac{P}{D}\right)^{5}+0.007Pe^{0.64-0.246\left(\frac{P}{D}\right)} \tag{4.37}$$

Zhukov et al. [4.31] investigated the effect of spacer for square lattice of tubes on heat transfer and temperature field experimentally. The following correlation was developed for pins with one spacer grid:

$$Nu = 7.55\left(\frac{P}{D}\right) - 14\left(\frac{P}{D}\right)^5 + aPe^{0.64-0.246\left(\frac{P}{D}\right)} \tag{4.38}$$

where a = 0.01 for overlapping of passage cross-section for the coolant porosity, ε_p = 10% and a = 0.009 for porosity, ε_p = 20%.

Recently Mikityuk [4.32] reviewed four sets of experimental data for heat transfer to liquid metal obtained in triangular or square rod bundle geometry. The data used were of Maresca and Dwyer [4.24] , Borishanskii et al. [4.27] , Gräber and Rieger [4.28], and Zhukov et al. [4.31]. He developed the following correlation:

$$Nu = 0.047\left(1 - e^{-3.8\left[\left(\frac{P}{D}\right)-1\right]}\right)\left(Pe^{0.77} + 250\right) \tag{4.39}$$

Equation (4.39) is valid for the range 30 ≤ Pe ≤ 5000 and 1.1 ≤ P/D ≤ 1.95.

4.2.4. Turbulent Prandtl number

The reliability and accuracy of the CFD simulation essentially depends on the physical model used, especially, turbulence models and parameters like mesh structures and turbulent Prandtl numbers. The most widely used turbulence models are based on eddy diffusivity concepts (e.g., k–ε model), which use the turbulent Prandtl number to describe the turbulent heat transport.

In turbulent flow, the thermal eddy diffusivity (ε_H) is correlated to momentum diffusivity as below:

$$\varepsilon_H = \frac{\varepsilon_M}{\Pr_t} \tag{4.40}$$

Where $\Pr_t$ is called turbulent Prandtl number; Reynolds analogy assumes that $\varepsilon_H = \varepsilon_M$, i.e. $\Pr_t$ = 1.0. Experimental evidence indicates that $\Pr_t$ = 0.9 is correct for most of the conventional fluids, i.e. air, water, etc. (Kays et al. [4.33]). During 1950s, it was found that the experimentally determined heat transfer coefficient for liquid metal flows seemed to fall below what would be predicted using Reynolds analogy. After this, many experimental and theoretical studies were carried out to evaluate $\Pr_t$. Reynolds [4.34] assessed several studies available in literature to calculate $\Pr_t$ and divided them into several groups according to their approaches. Kays et al. [4.33] assessed the present status of the $\Pr_t$ for a wide range of Prandtl numbers. It was found that for liquid metal the turbulent Prandtl number is higher than unity. The HLMC Handbook [4.3] has also given a detailed review of the studies on $\Pr_t$ for liquid metal heat transfer based on different approaches. The value of $\Pr_t$ in a tube depends on the molecular Prandtl number Pr, radial distance from the wall and eddy diffusivity. It was emphasized that semiempirical methods are the best approach to derive the turbulent Prandtl number of fluid flow. Jischa and Reike [4.35] gave a short recapitulation of Reynolds' work [4.34].

However, for practical application, the empirical correlations are preferred for simplicity. But care should be taken while applying those correlations, because they are developed for a particular range of parameters and fluids. Some of the empirical correlations for $\mathrm{Pr_t}$ developed for liquid metal applications are discussed below.

Aoki [4.36] proposed the following correlation:

$$\mathrm{Pr}_t = X\left[1-\exp\left(\frac{-1}{X}\right)\right] \tag{4.41}$$

where $X = 0.014\,\mathrm{Re}^{0.45}\mathrm{Pr}^{0.2}$.

Reynolds [4.34] proposed the following correlation for liquid metal flows:

$$\mathrm{Pr}_t = \left(1+100Pe^{-0.5}\right)\left[\frac{1}{1+120\,\mathrm{Re}^{-0.5}}-0.15\right] \tag{4.42}$$

Gori et al. [4.37] carried out numerical analysis for low Prandtl number fluids by using a one equation (*k*) turbulence model near the wall region and a two equation (*k*-*ε*) turbulence model in the core region. From the analysis, they recommended that Eqs (4.41) and (4.42) can be used for 40 000 < Re < 170 000. For 170 000 < Re < 260 000, the following correlation is proposed:

$$\mathrm{Pr}_t = 0.85+\frac{0.005}{\mathrm{Pr}} \tag{4.43}$$

The above correlation was derived by Jischa and Rieke [4.35], based on the modelling of transport equations for turbulent kinetic energy, turbulent heat flux and turbulent mass flux. For 260 000 < Re < 400 000, $\mathrm{Pr_t} = 0.85$ is recommended.

Cheng and Tak [4.10] developed a correlation for $\mathrm{Pr_t}$, based on the evaluation of various heat transfer correlations for liquid metal flow and CFD analysis:

$$\mathrm{Pr}_t = \begin{cases} 4.12 & Pe \le 1000 \\ \dfrac{0.01Pe}{\left[0.018Pe^{0.8}-(7-A)\right]^{1.25}} & 1000 \le Pe \le 6000 \end{cases} \tag{4.44}$$

where constant A is defined in Eq. (4.7).

4.2.5. CFD studies for heat transfer

One of the main challenges in the CFD application is a reliable modelling of turbulent energy transport. Hadidy et al. [4.38] performed heat transfer analysis to low Prandtl number in pipes with constant heat flux. The turbulence model employed was of the two equations (*k*-*ε*) in the core and one equation in the near wall region. They found that temperature profiles and Nusselt numbers are in good agreement with experimental data for fully developed flow.

IAEA-TECDOC-1520 [4.39] provides a comprehensive report on the different CFD studies and highlights major hurdles in liquid metal systems. The inability of reproducing liquid metal thermohydraulic experimental results by commercial CFD software is highlighted. It was emphasized that improvement in turbulence modelling and turbulent Prandtl number formulation is essential for precession results. HLMC Handbook [4.3] also points out that careful validation of CFD codes with experimental results are necessary for liquid metal flow related analysis.

Cheng and Tak [4.10] studied various turbulence models available in the CFD code CFX. It was found that standard k-ε and RNG k-ε turbulence models give good results. But the results obtained by using a k-ω turbulence model are found to be highly dependent on the mesh sizes.

Recently, Chandra et al. [4.40] have carried out extensive studies on application of turbulence modelling in nuclear reactor liquid metal thermohydraulics. CFD studies on liquid metal flow were carried out with various geometries, like heated circular tube, flow around a heated rod in an annular cavity and flow in heated rod bundles. They found that the Baseline-Reynolds Stress Model (BSL-RSM) with Automatic Wall Treatment (AWT) available in ANSYS-CFX code can be preferred for heavy liquid metal heat transfer in complex geometries.

The Large Eddy Simulation (LES) modelling approach requires more computational effort and has been assessed by Merzari et al. [4.41] and Popov et al. [4.42]. It is considered more accurate than the Reynolds Average Navier Stokes (RANS) modelling approach.

Direct Numerical Simulation (DNS) of the flow in pipe has been performed by Redjem-Saad et al. [4.43]. Further, the DNS approach in rod-bundles has been applied by Baglietto et al. [4.44] and Ninokata and Merzari [4.45]. In this approach, time dependent flow details, including turbulent structures, are captured by the simulation. For the analysis, no turbulence model is required.

4.3. HEAT TRANSFER STUDIES PERFORMED IN BARC

Heat transfer studies have been carried out and discussed in detail. The assessment of various correlations has been carried out for tubular geometry, and the effect of various parameters on heat transfer in CFD studies has also been studied.

4.3.1. Input data for heat transfer analysis

For the heat transfer analysis, a circular tube with the conditions described in Table 4.1 is considered. First, the analysis is performed for an inlet temperature of 500°C with constant wall heat flux. Heat transfer studies have been performed using various turbulence models. The effect of turbulent Prandtl number using various correlations, the effect of different developing lengths and the effect of the dimensionless distance to wall at the first mesh, y^+, has also been studied. Further, the heat transfer analysis has been extended for LBE temperature ranging from 200°C to 900°C.

The thermophysical properties required for analysis are taken from sources as listed in Table 4.2.

TABLE 4.1. PARAMETERS FOR THE TURBULENT FLOW ANALYSIS FOR LBE COOLANT

Parameters	Values
Reynolds number	
For laminar flow analysis	800–2500
For turbulent flow analysis	5.0×10^4–4.5×10^5
Wall heat flux (W/m^2)	
For laminar flow	1.0×10^4
For turbulent flow	2.0×10^5
y^+	30–130

TABLE 4.2. THERMOPHYSICAL PROPERTIES OF LBE USED IN THE THERMOHYDRAULIC ANALYSIS

Properties	Unit	Correlation	Temperature range (K)	Reference
Density	kg/m^3	$\rho = 11096–1.3236T$	403–1100	HLMC Handbook [4.3]
Dynamic viscosity	Pa·s	$\mu = 4.94 \times 10^{-4} \exp(754.1/T)$	400–1100	
Thermal conductivity	W/mK	$k = 3.61 + 1.517 \times 10^{-2}. T-1.741 \times 10^{-6} T^2$	403–1100	
Specific heat	J/kgK	$C_p = 159–2.302 \times 10^{-2} T$	400–1100	Morita et al. [4.46]

The applicable range of the correlations for thermophysical properties of LBE is up to 827°C (1100 K). For heat transfer analysis at higher temperature, the same correlations are extrapolated beyond this temperature.

Figure 4.1 shows the 2D axis-symmetric geometry considered for the CFD analysis. A wall with thickness of 1.0 mm is considered. The boundary condition of constant heat flux or constant temperature is imposed on the outer surface of the tube wall. The velocity and thermal boundary layer is developed as the flow proceeds towards downstream.

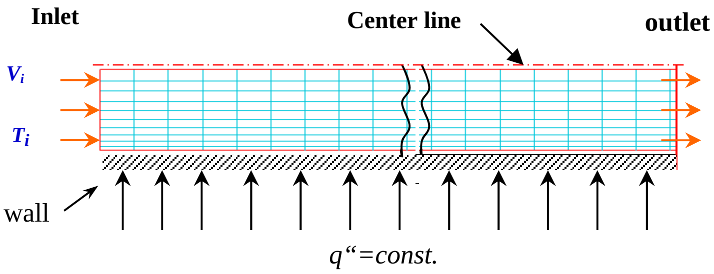

FIG. 4.1. 2D Symmetry section of tube with mesh distribution.

4.3.2. Assessment of heat transfer correlations

As discussed earlier, there are numerous heat transfer correlations available for liquid metals. Figure 4.2 depicts the Nusselt number calculated as function of Peclet number using various heat transfer correlations. The Nusselt number estimated by correlations is assessed by comparing them with experimental data of Lubarski [4.47], Seban (ref. Lubarski and Kaufman [4.1]), and Johnson et al. [4.48]. The correlation Eq. (4.1) given by Lyon [4.6] overpredicts the experimental data, with $Pr_t = 1.0$, while with $Pr_t = 3.0$ it underpredicts. So, the influence of Pr_t on heat transfer coefficients can be observed. The correlation Eq. (4.2) suggested by Lubarsky and Kaufman [4.1] underpredicts the experimental results. It should be noted that this correlation has been developed from the results from twenty experimental studies. The working fluids for these studies include sodium, lead-bismuth and mercury. Though, this is considered as a general correlation for all liquid metal coolants, it underpredicts the heat transfer in case of lead-bismuth coolant. The correlation Eq. (4.4) recommended by Ibragimov [4.8] also underpredicts the experimental results. As mentioned above, the possible reason may be that they have no control of impurity and oxygen in the liquid metal during the experiments. The objective of the experiments was to study the heat transfer performance of liquid metal in industrial environment. The correlation Eq. (4.6) of Kirillov and Ushakov [4.4] overpredicts the experimental results. It may be noted that the correlation of Kirillov and Ushakov has been developed from the results of experimental studies for pure sodium, whose thermophysical properties are different from lead-bismuth eutectic. The correlation Eq. (4.3) of Notter & Sleicher [4.7] predicts well the experimental data which is also being used in the HLMC Handbook [4.3] for assessment of other correlations for liquid metal applications. The correlation Eq. (4.7) from Cheng and Tak [4.10] proposed recently also gives closer results to experimental data. This correlation is based on the careful assessment of different correlations for liquid metal applications. Another interesting prediction is the heat transfer in presence of thermal resistance due to oxide layer formation at the heat transfer surface. The estimation of Nusselt number correlation Eq. (4.6) of Kirillov and Ushakov [4.4] with the thermal resistance term as given in Eq. (4.16) is also shown in Fig. 4.2. As expected, this underpredicts the heat transfer compared to experimental results and well confirms the correlation Eq. (4.4) recommended by Ibragimov [4.8].

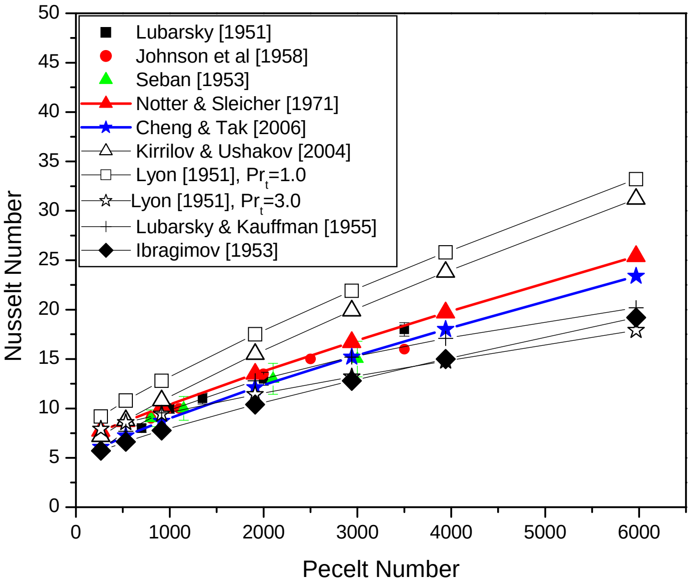

FIG. 4.2. Assessment of liquid metal heat transfer correlations.

4.3.3. Turbulent Prandtl number effect

The turbulent Prandtl number varies with flow rate of the liquid metal. The correlations for Pr_t given by Aoki [4.36], Reynolds [4.34], Jischa and Rieke [4.35] and Cheng and Tak [4.10] (Eqs (4.41–4.44)) have been used for analysis. Figure 4.3 shows the variation of turbulent Prandtl number with Peclet number by the above mentioned correlations. The correlation proposed by Cheng and Tak [4.10] is applicable to the entire range of Peclet numbers covered in Fig. 4.3, while as per by Gori et al. [4.37], Reynolds [4.34] and Aoki [4.36] correlations are valid up to Peclet number 2000. Beyond Pe = 2000, the correlation of Jischa and Rieke [4.35] is valid. It can be seen that, for low Pe, the value of Pr_t , as estimated by Chen and Tak [4.10], is higher than the predictions by other correlations. The correlation was derived from empirical heat transfer correlations for Pr_t and results obtained from CFD analysis. Further, the non-linear values of the coefficient *A* make the Pr_t variation not so smooth as the other two correlations. The variation of Pr_t given by Aoki [4.36] and Reynolds [4.34] correlations varies in similar fashion. The prediction by correlation of Jischa and Rieke [4.35] does not vary significantly with Pe. This correlation is suggested by Gori et al. [4.37] for high Pe range because at high Pe turbulence plays the dominant role in heat transfer as compared to molecular conduction. So the variation of Pr_t with Pe is not significant.

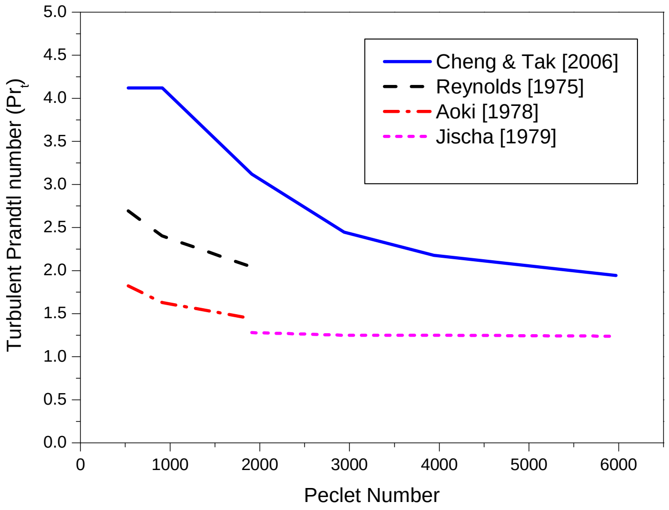

FIG. 4.3. Variation of turbulent Prandtl number with Peclet number for liquid metal.

To study the effect of turbulent Prandtl number on the heat transfer prediction using CFD, the Nusselt number for fully developed flow has been depicted in Fig. 4.4 for different Peclet numbers. The values of turbulent Prandtl number estimated by Eqs (4.41–4.44) are incorporated in the standard *k-ε* turbulence model in the PHOENICS code [4.49]. For comparison purpose, the Nusselt number estimated by correlation of Notter and Sleicher (Eq. (4.3)) and Cheng and Tak (Eq. (4.7)) is also given in Fig. 4.4. It can be seen from Fig. 4.4 that, with $Pr_t = 1.0$, the CFD analysis overpredicts the Nusselt number. In case of liquid metal, the thermal conductivity is much higher than that of air or water. The molecular conduction is much higher near the wall compared to convection heat transfer. The turbulent thermal diffusivity plays a lesser role here. It can also be seen from Eq. (4.40), when $Pr_t = 1.0$, $\varepsilon_H = \varepsilon_M$, which means ε_H is overestimated in case of liquid metals. This results in higher prediction of heat transfer. Further, from Fig. 4.4 it can be seen that Pr_t calculated from Aoki and Reynolds correlations give best confirmation with correlations for heat transfer. The analysis performed with Pr_t using the Cheng and Tak correlation for Pr_t underpredicts. This may be due to the fact that the value of Pr_t, calculated by the equation, is high, which suppresses ε_H as per Eq. (4.40).

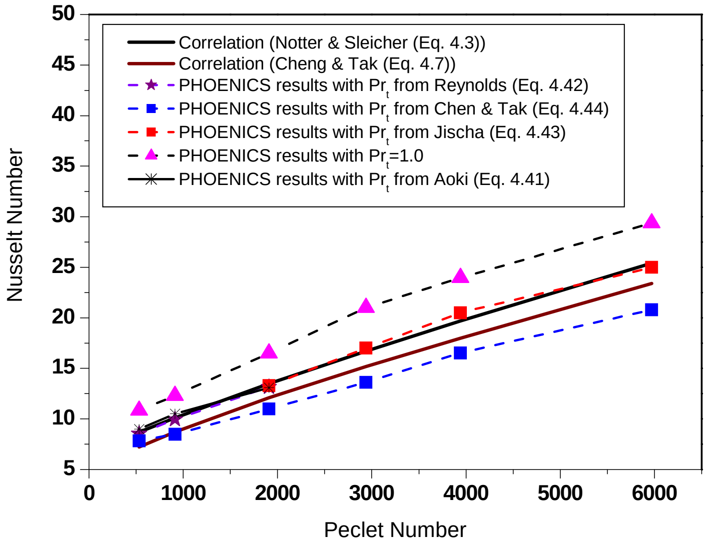

FIG. 4.4. Comparison of CFD prediction using standard k-ε model for different Pr_t with experimental and empirical correlations for Nusselt number.

4.3.4. Effect of mesh size

The geometry is discretized with structured mesh as shown in Fig. 4.1. As per PHOENICS user manual [4.49], for k-ε based turbulence model application, the value of y^+ should be maintained between 30 and 500. However, as the log-law wall function is used for turbulence modelling, y^+ is maintained between 30 and 120. Figure 4.5 shows the variation of Nusselt number with y^+ for inlet velocity 2 m/s. Standard k-ε model is used for the analysis. It can be seen that the prediction of Nu is unaffected by variation of y^+ in the range between 40 and 80. For further analysis, the range of y^+ is kept from 40 to 80 for all flow velocities by changing the mesh size near the wall.

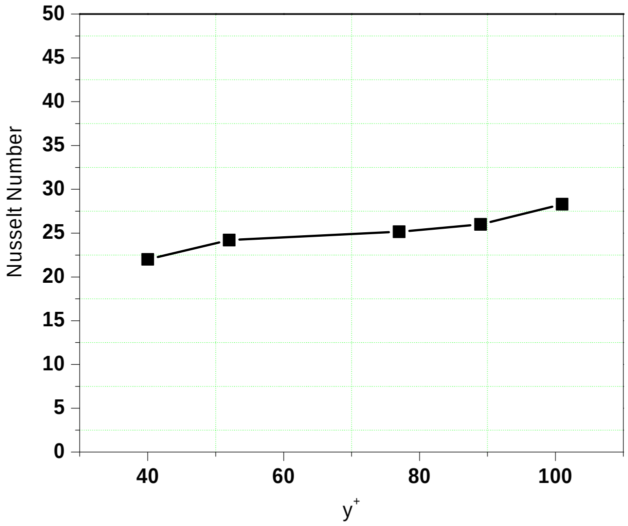

FIG. 4.5. Variation of fully developed Nusselt number with y^+ with k-ε turbulence model.

4.3.5. Developing length effect

It is well known that the local Nusselt number varies in the entry length due to the developing boundary layer. As shown in Fig. 4.6, up to 0.5 m of the upstream length the Nu variation is very clear. Beyond this length, the Nusselt number becomes steady, which means that the flow is fully developed. It can be seen that at 0.1 m length the local Nusselt number is 1.7 times higher than in developed flow. It can further be seen that the CFD prediction is in good agreement with the Eq. (4.21) for the whole length of the tube. The calculation is carried out with the inlet velocity of 2 m/s and with k-ε model and Pr_t calculated from Reynolds [4.34] and Jischa and Rieke [4.35] correlations, Eqs (4.42) and (4.43).

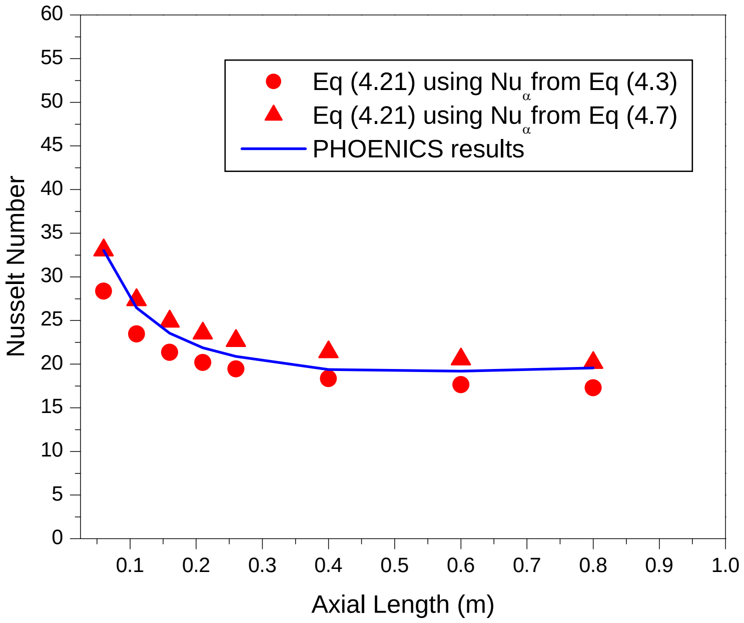

FIG. 4.6. Variation of local Nusselt number with axial distance.

4.3.6. Heat transfer studies using various turbulence models

The selection of turbulence model is also important for prediction of heat transfer flow. Four turbulence models have been selected for the analysis. Figure 4.7 shows the prediction of the Nusselt number using various turbulence models. The Pr_t values for this analysis are calculated from Reynolds [4.34] and Jischa and Rieke [4.35] correlations, Eqs (4.42) and (4.43). The values of Pr_t are incorporated in all the turbulence models except for RNG k-ε model. In RNG k-ε model, the turbulent heat transfer is accounted by an effective Prandtl number, which in turn varies with turbulent viscosity and molecular Prandtl number (HLMC Handbook [4.3]). For comparison purpose, the Nusselt number estimated by the correlation of Notter and Sleicher, Eq. (4.3), and Cheng and Tak, Eq. (4.7), is also given in Fig. 4.7. The analysis using the RNG k-ε model overpredicts the Nusselt number by 10% compared to that estimated by the heat transfer correlation of Notter and Sleicher at a Peclet number of 6000.

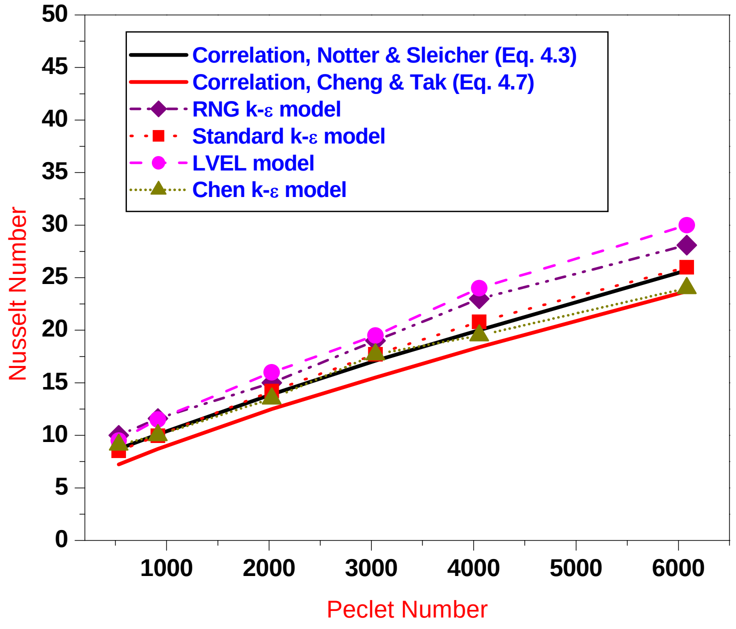

FIG. 4.7. Comparison of Nusselt numbers predicted by CFD using different turbulence models and estimated by correlations.

4.3.7. Effect of fluid temperature

The thermophysical properties of fluids change with temperature. For LBE, the variations in properties are calculated from the equations given in Table 4.2. The change in the properties affects the heat transfer rate in the fluid medium. High temperature reactors proposed for future generation will operate at high temperature for hydrogen production. Hence, it is important to note that prediction of heat transfer using CFD is affected by change in operating range of fluid temperature. In this analysis, turbulent flow with different inlet temperature is imposed and the Nusselt number in fully developed flow was calculated. It is seen from Fig. 4.8(a) that, at 200°C inlet temperature, the prediction of the heat transfer coefficient is little lower than that estimated by the Notter and Sleicher correlation, Eq. (4.3). With T = 500°C and 700°C, the predictions are in good agreement with the correlations and are shown in Figs 4.8(b) and 4.8(c). Figure 4.8(d) shows the prediction of Nusselt number for LBE inlet temperature 900°C. With 900°C as inlet temperature, the heat transfer rate is overpredicted in CFD studies as compared to that estimated by the correlation. This may be due to non-linear behaviour of the properties in this temperature zone. The other reason may be that the correlations are not tested at higher temperatures. Hence, experimental studies and evaluation of thermophysical properties are essential for this zone.

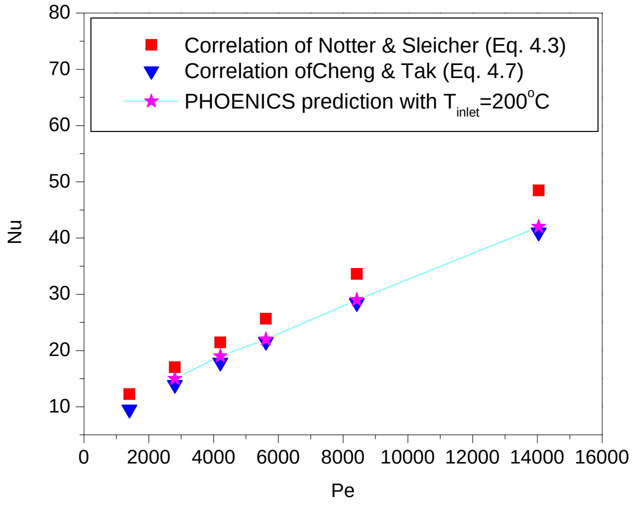

FIG. 4.8(a). Comparison of CFD prediction with correlations for bulk tube inlet temperature 200°C.

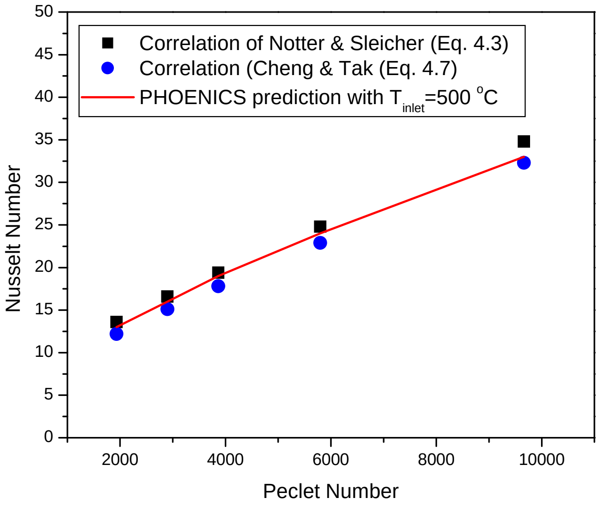

FIG. 4.8(b). Comparison of CFD prediction with correlations for bulk tube inlet temperature 500°C.

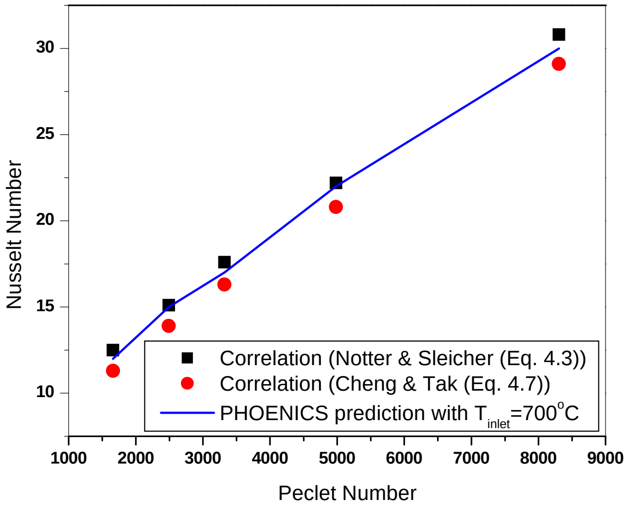

FIG. 4.8(c). Comparison of CFD prediction with correlations for bulk tube inlet temperature 700°C.

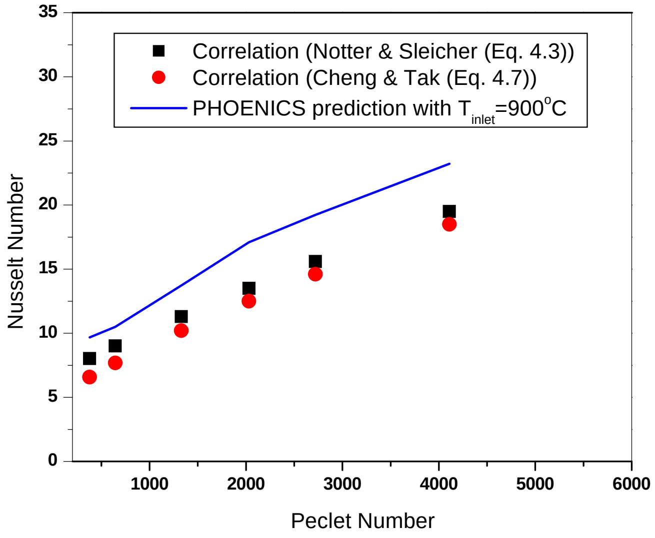

FIG. 4.8(d). Comparison of CFD prediction with correlations for bulk tube inlet temperature 900°C.

4.3.8. Heat transfer with constant wall temperature

Further, analysis was also carried out with constant wall temperature conditions for different Peclet numbers. The results are compared with the correlations available in literature for constant wall temperature. The wall outer surface is maintained at 800°C and LBE inlet temperature is 500°C. It can be seen from Fig. 4.9 that the PHOENICS prediction agrees well with the correlations for constant wall temperature.

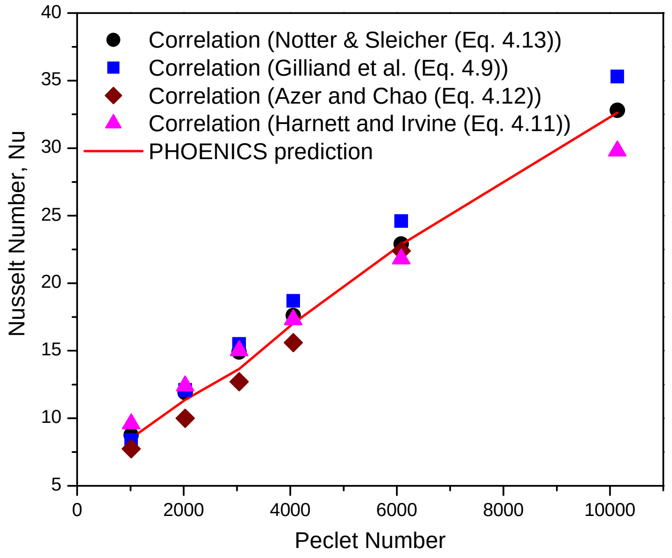

FIG. 4.9. Comparison of CFD prediction with heat transfer correlations for constant wall temperature conditions.

4.4. HEAT TRANSFER STUDIES ON HEAVY LIQUID METAL IN ENEA

4.4.1. Assessment of heat transfer correlations

Within the framework of national and international research programmes, experimental and numerical activities are in progress in ENEA to establish a proper set of heat transfer correlations for the thermohydraulic analysis of heavy liquid metal (HLM) cooled reactors with a particular interest for the core bundle geometry. The first part concerned a comparative assessment of the empirical correlations already available. Most of these correlations derive from the good experience gained in the Russian Federation with lead-bismuth eutectic alloys used as reactor coolant (Antonucci et al. [4.50]). The more promising correlations, which resulted from comparison with available experimental data and some calculations performed with commercial CFD (Computational Fluid Dynamic) codes, have been implemented in a HLM dedicated version of the system code RELAP5. Their validation on experimental data from HLM facilities is in progress at present.

This work is focused on the heat transfer correlation for fully developed turbulent flows with constant heat flux. Laminar flow (Re < 2000) would never be encountered during any normal operating situation and, therefore, this regime has been ruled out. Hypothetical accident conditions, where this regime can be found, are not considered in this investigation.

Usually, the single phase turbulent heat transfer coefficients of an external flow along a tube bank are estimated using the same correlations as for the inside of tubes. Although we are precisely interested in seeing what happens in case of an external flow parallel to a tube bank, and in the effect of lattice geometry upon heat transfer coefficients, it might be worthwhile remembering that our primary source of knowledge relies on flow inside, not outside tubes. We refer specifically to results reported in the comparative assessment (IAEA-TECDOC-1289 [4.51]), which in turn are drawn from studies available in the open literature (Kirillov [4.52–4.54], Kutateladze et al. [4.2], Talanov et al. [4.55]). Considering nature and date of printing of Ref. [4.51], we believe its contents may be taken as an authoritative reference. Similar results are reported however by other reports, e.g. Kirillov [4.52], [4.53], without remarkable contradiction.

In order to point out the effect of the liquid metal purification on the heat transfer, a comparison of the related parameters computed through correlations Eqs (4.14) and (4.8) is shown in Table 4.3.

TABLE 4.3. COMPARISON OF HEAT TRANSFER COEFFICIENTS FOR PB AT 400°C, D_H = 10 mm

Re	Pe	Nu Eq. (4.14)	Nu Eq. (4.8)	α_1 (W/m^{2}K) Eq. (4.14)	α_2(W/m^{2}K) Eq. (4.8)
10000	174	4.168	6.550	7136	11 214
20000	348	4.811	7.699	8236	13 181
50000	870	6.446	10.618	11 036	18 178
100000	1740	8.773	14.781	15 019	25 305

There is an increase in the heat transfer coefficient with purification that should not be lower than ~60%. Usually, lower heat transfer coefficients obtained without careful purification are assumed to be caused by thermal contact resistance at the wall liquid boundary. Without being involved with issues of chemistry and oxide deposition, we simply stand by the fact that the contact resistance was confirmed by test data with different content of oxide in heavy liquid metals (Kirillov [4.54]).

As discussed earlier, a number of relationships are recommended for computation of the heat transfer from a rod bundle, where the rods are cooled by liquid metal flowing along their external surfaces, in a direction noticeably parallel to the axes. The fuel rods are considered to be arranged in a triangular or square lattice with a definite pitch-to-diameter ratio (x = P/D), whose value explicitly appears in all relevant formulas.

To our knowledge, a frequently used correlation is that of Ushakov (co-author of ref. Subbotin et al. [4.30]) (for P/D > 1.3), which has been implemented in RELAP5/PARCS for the analysis of a Pb-Bi cooled ADS (Meloni et al. [4.56]), and in the subchannel code MATRA for the preparation of the KALLA experiment at FZK (Karlsruhe) (Litfin et al., [4.57]). Interestingly enough, it is acknowledged in Ref. [4.30] that the Nusselt values calculated with the correlation are much higher than the ones used for heat transfer of LBE in circular tubes, but there is no account for that.

Results provided by various correlations have been compared. We consider a flow of lead (or LBE, whose physical properties are quite similar) in typical reactor conditions, that is:

Temperature	T	= 400°C
Prandtl number	Pr	= 0.0225
Lattice pitch	p	= 1.36 cm
Rod diameter	d	= 0.85 cm
Cross-section	s	= 1.28 cm^2
Hydraulic diameter	D_h	= 1.92 cm

The rods have been considered arranged in a square lattice, also for the first two correlations (Borishanski [4.27], Graber [4.28]) which, for what we know, are for triangular arrays. We have chosen to preserve the geometry which is candidate for the core design within the framework of the European Lead-cooled System (ELSY) project (ELSY Work Program-Technical Report [4.58]), even if this may cast a shadow on the overall consistency of the comparison. In actual facts, however, there is no difference of practical significance. On the other hand, we get freed of any problem about which parameter should be maintained if it is to pass from square to triangular array, i.e. section or volumic fraction. We are faced to one parameter only, effectively the subchannel flow velocity, which we get ranging from 0.9 to 1.4 m/s (corresponding to the Pe values shown at top of each column).

TABLE 4.4. COMPARISON OF NUSSELT NUMBERS ACCORDING TO DIFFERENT CORRELATIONS

Pb at 400°C, p = 13.6 mm, D = 8.5 mm, D_h = 19.2 mm, Pr = 0.0225

Peclet =	1636	1818	2000	2181	2363	2545
Borishanski	23.1	24.4	25.7	27.0	28.3	29.6
Graber	22.6	23.6	24.6	25.6	26.6	27.5
Calamai	27.5	29.5	31.6	33.6	35.6	37.5
Zhukov (bare rods)	28.9	31.1	33.2	35.4	37.6	-
Zhukov (spacers)	34.1	36.9	39.7	42.5	45.3	-
Ushakov	21.6	22.5	23.4	24.3	25.1	26.0
Cheng and Tak	10.6	11.1	11.5	12.0	12.6	13.1
Lubarski	12.1	12.6	13.1	13.5	14.0	14.4

We distinguish a first group of results coming from the correlations recommended by IAEA (Borishanski, Graber, Calamai, and Zukov, [4.51]). Then, we have results by Subbotin [4.26], by Cheng and Tak [4.10], and by Lubarski [4.1].

It is evident that the correlations recommended by IAEA and the Ushakov correlation (Eq. (4.36)) are less conservative. The correlations by Zhukov, which apply specifically to the square arrangement, are even more favorable.

In the thermal hydraulic design of an HLM core, the most important figure of merit to evaluate the margin in respect to the safety limits is the peak cladding temperature; this is due to the erosive/corrosive characteristics of the coolant. In Fig. 4.10, the effect of the different correlations on this parameter for a lead-cooled square lattice core is shown. The temperature drop with respect to the bulk temperature of the coolant varies from 25°C to 100°C for "clean" lead. This fact gives an idea of the negative economic impact in using too conservative correlations. In fact, to guarantee an adequate safety margin in nominal conditions could require an excessive reduction of the linear power in the pin.

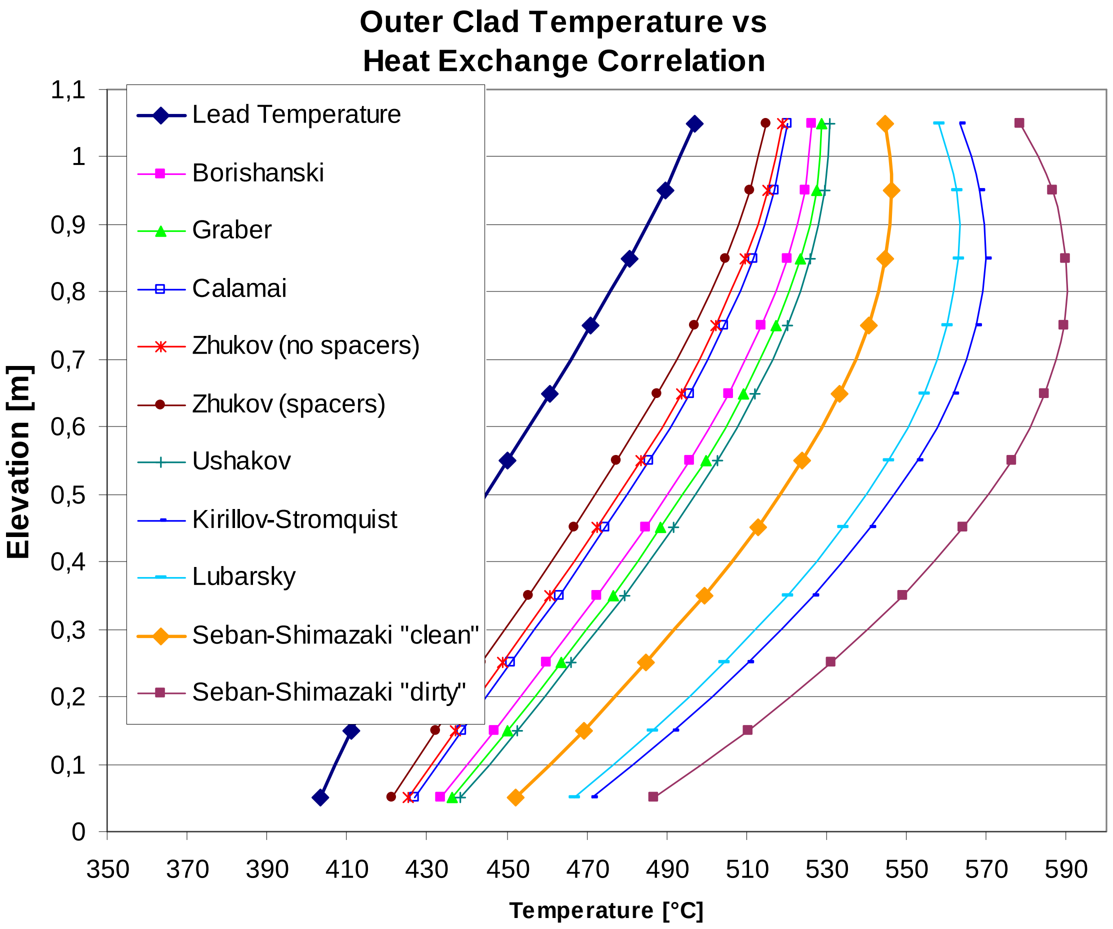

FIG. 4.10. Cladding temperature along core channel.

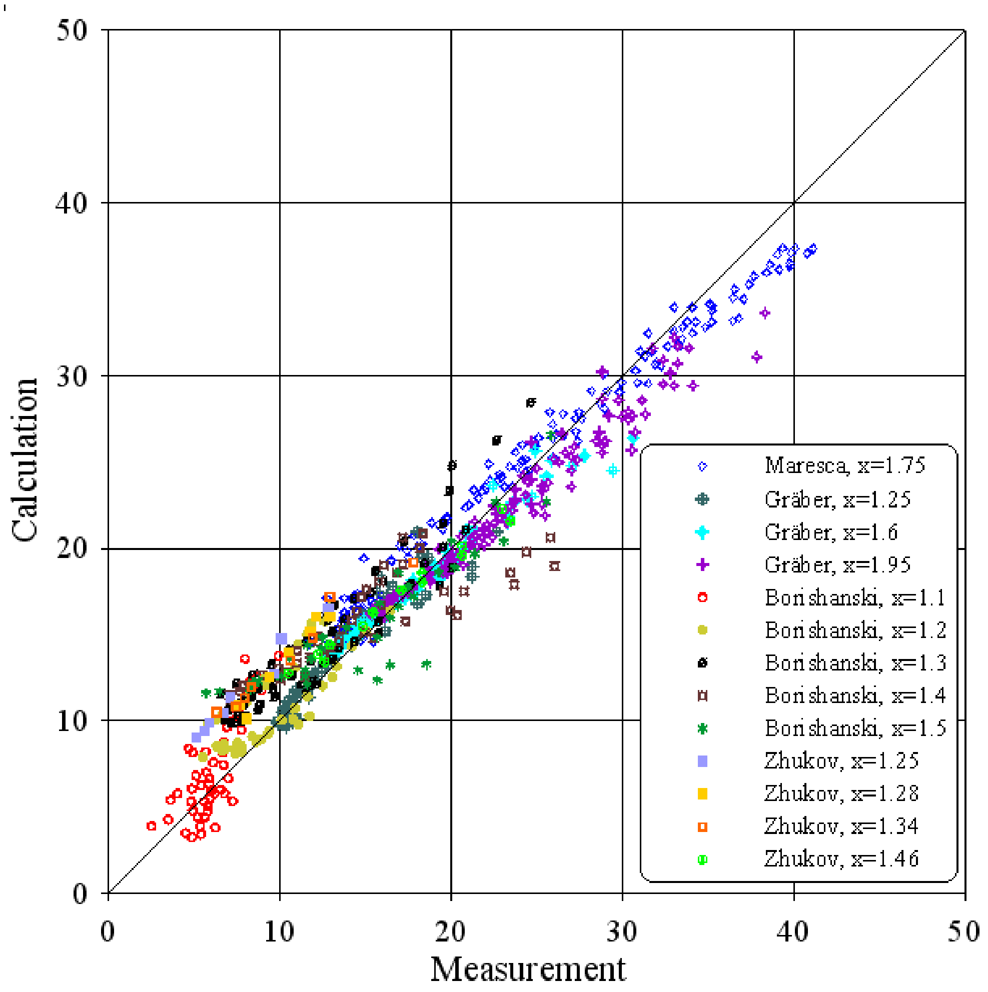

FIG. 4.11. Cladding temperature along core channel.

Within the framework of the ELSY Project, the different correlations for liquid metal flowing in tube bundles were evaluated on the basis of four sets of experimental data for heat transfer to liquid metals (NaK of different compositions and Hg) flowing in a triangular or square lattice of cylindrical rods with pitch-to-diameter ratios of 1.1 up to 1.95 for a wide range of Peclet numbers (30–5000) (Mikityuk [4.32]). The correlation, Eq. (4.36), by Ushakov (Fig. 4.11) was found to have the highest quality (among the correlations considered) in predicting the results of the experiments for the triangular tube bundles. The correlation could be used over the whole region of the data (x = 1.1–1.95 and Pe = 30–5000). The Zhukov correlation, Eq.(4.37), is recommended for heat exchange in the square tube bundle as the only experimentally supported correlation. Some calculations performed with commercial CFD (Computational Fluid Dynamic) codes presented have confirmed these conclusions.

As a conclusion of the activity, the heat transfer correlations, namely Seban-Shimazaki correlation for convective heat transfer inside pipe, Eq. (4.8), Subbotin-Ushakov correlation in simplified form (P/D > 1.2) for convective heat transfer in triangular bundle geometry, Eq. (4.36), and the Zhukov correlation without spacers for convective heat transfer in square bundle geometry, Eq. (4.37), have been implemented in the RELAP5 code for the thermohydraulic and transient analysis of the HLM reactors.

4.4.2. CFD simulation of square core channel

In order to support the selection of proper heat exchange correlations for thermohydraulic design of HLM core and safety analysis, CFD simulations of a square core channel have been performed with the FLUENT commercial code [4.59]. The activity has been carried out in two steps. First the results provided by the code have been assessed for simple geometries, calibrating the main parameters of the CFD model and selecting the more appropriate turbulence models. Then, the model has been applied to evaluate the heat transfer characteristics of a pin bundle.

The first step referred to the experimental studies on cylindrical tube and was reported by Cheng and Tak in Ref. [4.10]. The computational domain has been limited to a quarter of tube imposing the symmetry condition on the lateral surface and a wall condition on the curvilinear surface (Fig. 4.12). This choice has allowed using a very fine meshing, thus optimizing the computational resources without affecting the accuracy of the results. The tube considered has a length of 1 m with a diameter of 10 mm. The fluid simulated is lead-bismuth with a velocity of 1 m/s and inlet temperature of 400°C. The heat generation along the wall is constant with a heat flux of 7.5×10^5 W/m^2.

A fundamental parameter for this simulation is the turbulent Prandtl number. Its importance in this study derives from the high Reynolds number considered, as this dimensionless number quantifies the thermal exchange connected with the turbulence influencing the turbulent conductivity:

$$k_t = \frac{\mu_t c_p}{\mathrm{Pr}_t} \tag{4.45}$$

That, added to the conductivity of the material, increases the thermal exchange performance in case of liquid metals. In the simulations, two values have been considered for $\mathrm{Pr}_t = 0.9$ and 3.

Another important parameter for the evaluation of the convective thermal exchange is the meshing of the thermal layer near the wall. Two kinds of mesh have been considered, characterized by a fine grid ($y^+ = 0.6$) and a coarse grid ($y^+ = 60$).

Three different turbulence models have been tested with a different combination of the previous parameters: standard (S) k-ε model, Shear Stress Transport (SST) k-ω model and Large Eddy Simulation (LES) model.

In Fig. 4.12, the influence of the two parameters on the thermal exchange, which is quantified by the Nusselt number, can be seen clearly. The use of coarse meshes along with a low value for Pr_t leads to an overestimation of the thermal exchange. The value of 3 for Pr_t is in line with the correlation of Cheng and Tak [4.10]. As this correlation has been developed explicitly for LBE, it has been considered more correct to use this correlation for the determination of the Pr_t for the turbulent models.

In order to assess the correctness of the FLUENT predictions, two experimental correlations, those by Lyon, Eq. (4.1), and by Kirillov-Ushakov, Eq. (4.6), developed for liquid metal flow in cylindrical pipes, have been considered. The Nusselt numbers obtained with the three turbulence models for different Reynolds number are compared to the values obtained with the experimental correlations in Fig. 4.13. It can be noticed that the two isotropic models, Standard k-ε and SST k-ω, have a similar trend as the experimental correlations, although the thermal exchange results are overestimated by 35–40%. On the contrary, the anisotropic LES models predict a trend that is inconsistent with the experimental correlations and non-physical, as the thermal exchange is higher at lower velocities.

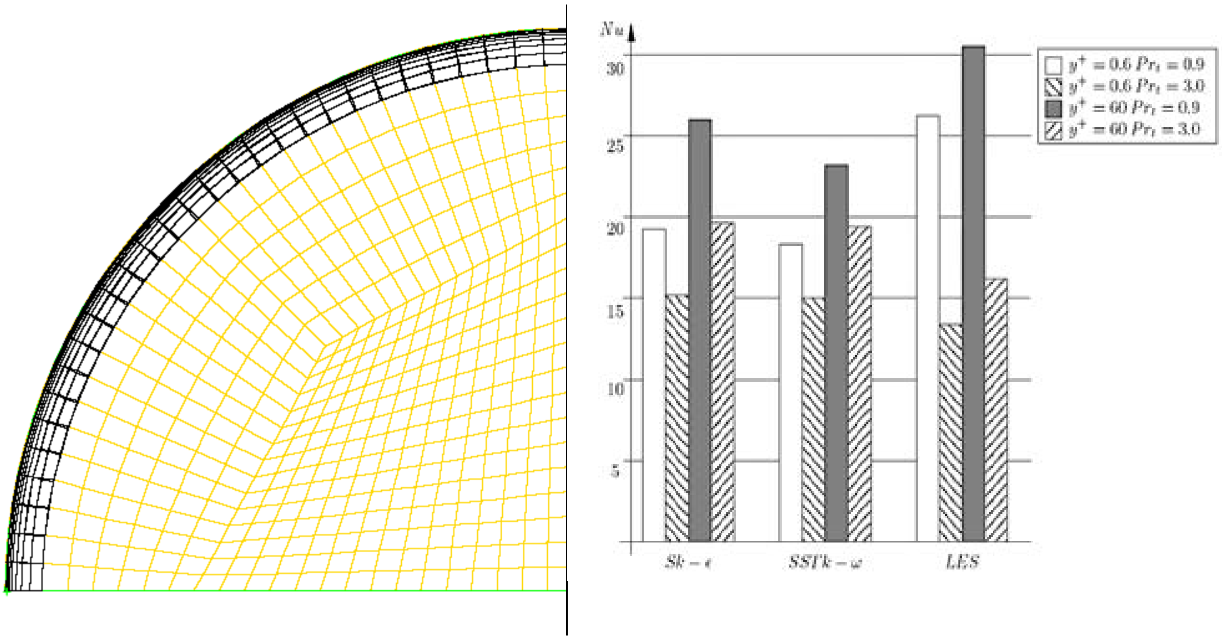

FIG. 4.12. Variability of Nusselt number with y^+ and Pr_t in different turbulence models.

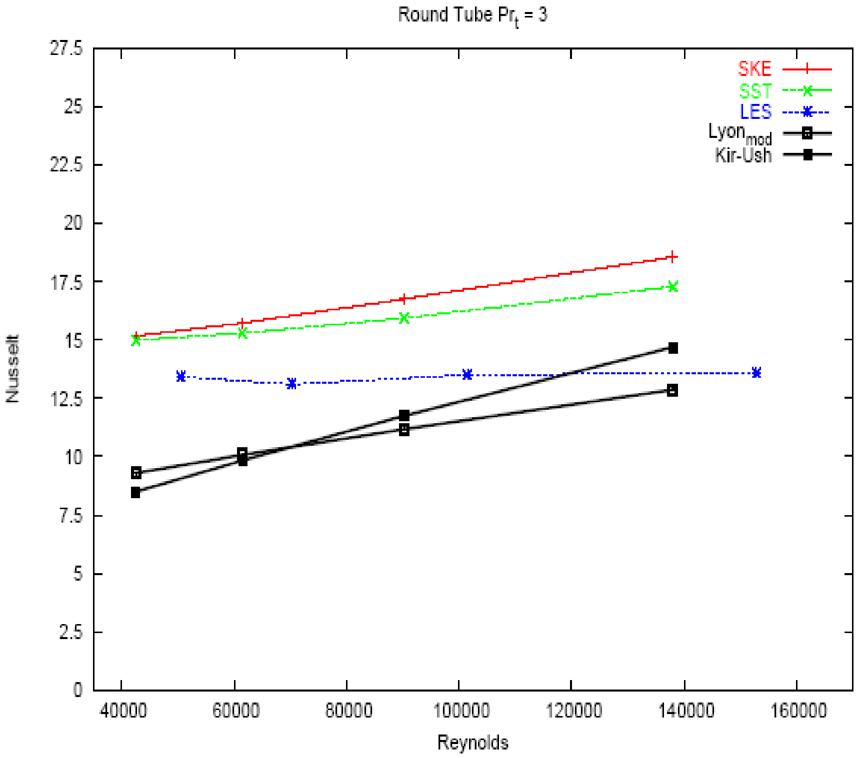

FIG. 4.13. Thermal exchange performance at different fluid velocities.

Once the main parameters and the turbulence model were settled based on experimental data, a CFD simulation was performed for the square core bundle of the European Lead Fast Reactor studied within the framework of the EU VII Framework Program (ELSY Work Program [4.58]). The simulation domain has been related to a single channel with symmetric boundary conditions (Fig.4.14). The comparison of the calculation results with semiempirical correlations from existing literature (Fig.4.14) has allowed a preliminary evaluation of these correlations for thermal exchange in a square bundle. The results indicate, in accordance with the conclusion of the analysis in earlier section, that the Zhukov correlation, Eq. (4.37), seems the most suitable for this kind of applications.

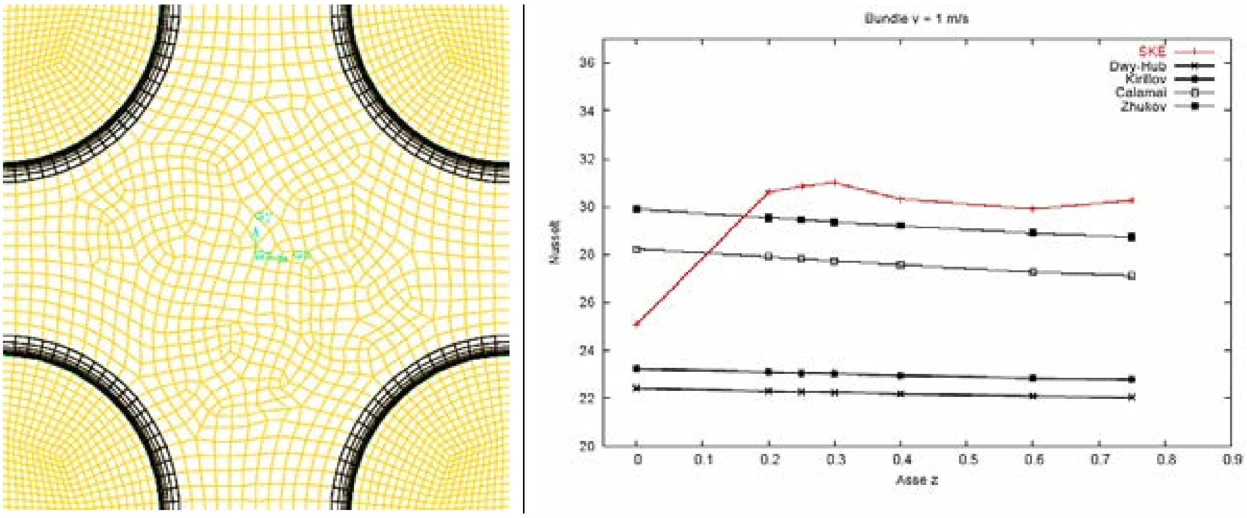

FIG. 4.14. FLUENT computation of Nusselt number in a square channel.

4.5. CONCLUSIONS

The design of LBE based nuclear reactor systems requires reliable physical models for heat transfer and CFD studies. Assessments of various correlations with experimental data available in literature have been carried out for tube and rod bundle geometry. CFD analysis is carried out to assess the turbulence models. Various correlations for calculation of turbulent Prandtl number (Pr_t) on the prediction of Nusselt number in CFD analysis have been used.

List of abbreviations and symbols to Chapter 4

a, A	coefficients
b, B	coefficients
c	constant
C_p	specific heat (J/kgK)
D	tube diameter (m)
E	coefficient
f	friction factor
F	coefficient
k	thermal conductivity (W/mK)
L	length (m)
N	exponent
Nu	Nusselt number, $\left(\frac{\alpha D}{k}\right)$
P	pitch between the tube, m
Pe	Peclet number, *(Re Pr)*
Pr	Prandtl number, $\left(\frac{c_p \mu}{k}\right)$
Pr_t	turbulent Prandtl number, $\left(\frac{\varepsilon_M}{\varepsilon_H}\right)$
R	radius, m
R_c	contact resistance
Re	Reynolds number, $\left(\frac{\rho u D}{\mu}\right)$
u, v	averaged velocity respectively, m/s
T	temperature, K
x	axial distance, m, pitch to diameter ratio (P/D)
y	radial distance from the tube wall (m)
y^+	dimensionless distance to wall at the first mesh, $y^+ = \frac{y}{\nu}\frac{u}{\left(\tau_s/\rho\right)^{1/2}}$

α	heat transfer coefficient (W/m^{2}K)
α_1	parameter defined in Eq. (4.24)
β_1	parameter defined in Eq. (4.25)
ε_H	eddy diffusivity of heat transfer (m^2/s)
ε_M	eddy diffusivity of momentum transfer (m^2/s)
ε_p	porosity
μ	dynamic viscosity, Pa·s
τ_s	shear stress (N/m^2)
ν	kinematic viscosity (m^2/s)
ψ	($\varepsilon_H/\varepsilon_M$), dimensionless
$\overline{\psi}$	average value of ψ

Subscripts

avg.	average
b	bulk
c	without special purification
i	inner, inlet
o	outer
h	hydraulic
x	local
∞	fully developed

REFERENCES TO CHAPTER 4

[4.1] LUBARSKI, B., KAUFMAN, S.J., Review of Experimental Investigations of Liquid Metal Heat Transfer, NACA Technical Note, TN-3336 (1955).

[4.2] KUTALTELADZE, S.S., BORISHANSKII, V.M., NOVIKOV, I.I., FEDYNSKII, O.S., Liquid Metal Heat Transfer Media, Atomic Press (1958).

[4.3] OECD/NEA NUCLEAR SCIENCE COMMITTEE, Handbook on Lead-bismuth Eutectic Alloy and Lead Properties, Materials Compatibility, Thermal-hydraulics and Technologies, NEA No. 6195, 2007 Edition.

[4.4] KIRILLOV, P.L., USHAKOV, P.A., Heat transfer to liquid metals: specific features, methods of investigation, and main relationships. Therm. Eng. **48** 1 (2001) 50–59.

[4.5] MARTINELLI, R.C., Heat transfer to molten metals, Trans. ASME **69** 8 (1953) 947–950.

[4.6] LYON, R.N., Liquid metal heat transfer coefficients, Chem. Eng. Prog. **47** 2 (1951) 75–79.

[4.7] NOTTER, R.H., SLEICHER, C.H., A solution to the turbulent Graetz-Problem III fully developed and entrance region heat transfer rates, Chem. Eng. Sci. **27** (1972) 2073–2093.

[4.8] IBRAGIMOV, M., SUBBOTIN, V.I., USHAKOV, P.A., Investigation of heat transfer in the turbulent flow of liquid metals in tubes, Atomnaya Energiya **8** 1 (1960) 54–56.

[4.9] SKUPINSKI, E., TORTEL, J., VAUTREY, L., Détermination des coefficients de convection d’un alliage sodium-potassium dans un tube circulaire, Int. J. Heat Mass Tran. **8** (1965) 937–951.

[4.10] CHENG, X., TAK, NAM-IL, Investigation on turbulent heat transfer to lead-bismuth eutectic flows in circular tubes for nuclear applications, Nucl. Eng. Des. **236** (2006) 385–393.

[4.11] SEBAN, R.A., SHIMAZAKI, T.T., Heat transfer to a fluid flowing turbulently in a smooth pipe with wall at constant temperature, Trans. ASME **73** (1951) 803–809.

[4.12] GILLILAND, E.R., MUSSER, R.J., PAGE, W.R., Heat transfer to Mercury, Gen. Disc. Heat Transfer, Inst. Mech. Eng. ASME, London (1951) 402–404.

[4.13] SLEICHER, C.A., TRIBUS Jr., M., Heat transfer in a pipe with turbulent flow and arbitrary wall temperature distribution, Trans. ASME **79** (1957) 789–797.

[4.14] HARTNETT, J.P., IRVINE, T.F., Nusselt values for estimating liquid metal heat transfer in non-circular ducts, AIChE J. **3** (1957) 313–317.

[4.15] AZER, N.T., CHAO, B.T., Turbulent heat transfer in liquid metals — fully developed pipe flow with constant wall temperature, Int. J. Heat Mass Tran. **3** (1961) 77–83.

[4.16] SLEICHER, C.A., AWAD, A.S., NOTTER, R.H., Temperature and eddy diffusivity profiles in NaK, Int. J. Heat Mass Tran. **16** 8 (1973) 1565–1575.

[4.17] CHEN, C.J., CHIOU, J.S., Laminar and turbulent heat transfer in the pipe entrance region for liquid metals, Int. J. Heat Mass Tran. **24** (1981) 1179–1189.

[4.18] AWAD, A.S., Heat transfer and eddy diffusivity in NaK in pipes at uniform wall temperature, PhD Thesis, University of Washington, Seattle (1965).

[4.19] DWYER, O.E., Eddy transport in liquid metal teat transfer, AIChE J. **9** (1963) 261–268.

[4.20] BHATTI, M.S., SHAH, R.K., “Turbulent and transition flow, convective heat transfer in ducts”, Chapter 4, Handbook of single-phase convective heat transfer, (KAKAC, SHAH, AUNG, Eds.), John Wiley and Sons, New York, 1987.

[4.21] RENSEN, Q., Experimental investigation of the turbulent heat transfer to liquid sodium in the thermal entrance region of an annulus, Nucl. Eng. Des. **68** (1981) 397–404.

[4.22] DWYER, O.E., TU, P.S., “Analytical study of heat transfer rates for parallel flow of liquid metals through tube bundles”, Part I. Chemical Engineering Progress Symposium Series **56** 30 (1960) 183–193.

[4.23] FRIEDLAND, A.F., BONILLA, C.F., Analytical study of heat transfer rates for parallel flow of liquid metals through tube bundles, AIChE J. **7** 1 (1961) 107–112.

[4.24] MARESCA, M.W., DWYER, O.E., Heat transfer to mercury flowing in-line through a bundle of circular rods, J. Heat Trans.-T ASME **86** (1964) 180–186.

[4.25] PFRANG, W., STRUWE, D., Assessment of correlations for heat transfer to the coolant for heavy liquid metal cooled core designs, Report FZKA 7352, Forschungszentrum Karlsruhe, Germany (2007).

[4.26] SUBBOTIN, V.I., et al. “Heat transfer from fuel elements of liquid metal-cooled reactors”, Proc. Third Int. Conf. Peaceful Uses of Atomic Energy, Geneva, NY, United Nations, 8 (1965) 192–203.

[4.27] BORISHANSKII, V.M., GOTOVSKI, M.A., FIRSOVA, É.V., Heat transfer to liquid metals in longitudinally wetted bundles of rods, Sov. Atom. Energy **27** (1969) 1347–1350; translated from Atomnaya Énergiya, **27** 6 (1969) 549–552.

[4.28] GRABER, H., RIEGER, M., Experimentelle Untersuchung des Wärmeübergangs an Flüssigmetallen in Parallel Durchströmten Rohrbündeln bei Konstanter und Exponentieller Wärmeflussdichtverteilung, Atomkernenergie **19** 1 (1972) 23.

[4.29] CALAMAI, G.J., et al., “Steady state thermal and hydraulic characteristics of the FFTF fuel assemblies”, FRT-1582 (1974), (cit. by A.E.Waltar, A.B. Reynolds, Fast Breeder Reactors, Perg. Press., N.Y. 1981).

[4.30] SUBBOTIN, V.I., et al., “Heat Transfer in Cores and Blankets of Fast Breeder Reactors — a Collection of Reports”, (Proc. Symp. of CMEA Countries: present and future work on creating AES with fast reactors), vol. 2., Obninsk 1975.

[4.31] ZHUKOV, A.V., et al., An experimental study of heat transfer in the core of a BREST-OD-300 reactor with lead cooling on models, Therm. Eng. **49** 3 (2002) 175–184; translated from Teploenergetika.

[4.32] MIKITYUK, K., Heat transfer to liquid metal: Review of data and correlations for tube bundles, Nucl. Eng. Des. **239** (2009) 680–687.

[4.33] KAYS, W.M., Turbulent Prandtl number — where are we, J. Heat Trans.-T ASME **116** (1994) 284–295.

[4.34] REYNOLDS, A.J., The prediction of turbulent Prandtl and Schmidt numbers, Int. J. Heat Mass Tran. **18** (1975) 1055–1069.

[4.35] JISCHA, M., REIKE, H.B., About the prediction of turbulent Prandtl and Schmidt numbers, Int. J. Heat Mass Tran. **22** (1979) 1547–1555.

[4.36] AOKI, S., A consideration on heat transfer of liquid metal, Bulletin Tokyo Institute of Technology **54** (1963) 63–73.

[4.37] GORI, F., EL HADIDY, M.A., SPALDING, D.B., Numerical prediction of heat transfer to low-Prandtl number fluids, Numer. Heat Transfer **2** (1979) 441–454.

[4.38] EL HADIDY, M.A., GORI, F., SPALDING, D.B., Further results on the heat transfer to low-Prandtl number fluids in pipes, Numer. Heat Transfer **2** (1982) 441–454.

[4.39] INTERNATIONAL ATOMIC ENERGY AGENCY, Theoretical and Experimental Studies of Heavy Liquid Metal Thermal Hydraulics, IAEA-TECDOC-1520, IAEA, Vienna (2006).

[4.40] CHANDRA, L., ROELOFS, F., HOUKEMA, M., JONKER, B., A stepwise development and validation of a RANS based CFD modeling approach for the hydraulic and thermal-hydraulic analyses of liquid metal flow in a fuel assembly, Nucl. Eng. Des. **239** (2009) 1988–2003.

[4.41] MERZARI, E., NINOKATA, H., BAGLIETTO, E., Numerical simulation of flow in tight lattice fuel bundles, Nucl. Eng. Des. **238** (2008) 1703–1719.

[4.42] POPOV, M., TZANOS, C.P., MENDONCA, F., "Large Eddy Simulation of turbulent flow in a rod cluster", CAANS Annual meeting 2008, USA., Trans. Am. Nucl. Soc. **98** (2008).

[4.43] REDJEM-SAAD, L., OULD-ROUISS, M., LAURIAT, G., Direct Numerical Simulation of turbulent heat transfer in pipe flows: Effect of Prandtl number, Int. J. Heat Fluid Flow **28** (2007) 847–861.

[4.44] BAGLIETTO, E., NINOKATA, H., MISAWA, T., CFD and DNS methodologies developed for fuel bundle simulations, Nucl. Eng. Des. **236** (2006) 1503–1510.

[4.45] NINOKATA, H., MERZARI, E., "Computational fluid dynamics and simulation-based design approach for tight lattice nuclear fuel lattice fuel pin subassemblies", NURETH-12, Pittsburgh, USA, 2007.

[4.46] MORITA, K., MASCHEK, W., FLAD, M., YAMANO, H., TOBITA, Y., Thermophysical properties of Lead-Bismuth Eutectic Alloy in reactor safety analysis, J. Nucl. Sci. Technol. **43** 5 (2008) 526–536.

[4.47] LUBARSKI, B., Experimental investigations of forced convection heat transfer characteristic of Lead-Bismuth Eutectic, NACA RM E51G02 (1951).

[4.48] JOHNSON, H.A., HARNETT, J.P., CALBAUGH, W.J., Heat transfer to Lead-Bismuth and Mercury in laminar and transition pipe flow, Trans. ASME (1954).

[4.49] PHOENICS Online Information System, Version 3.6.1, CHAM Ltd., 2006.

[4.50] ANTONUCCI, C.M., Comparative assessment of empirical correlations for single-phase heat transfer in rod bundles of HLM cooled reactors, ENEA-FPN-P9IX-001 (2007).

[4.51] INTERNATIONAL ATOMIC ENERGY AGENCY, Comparative Assessment of Thermophysical and Thermohydraulic Characteristics of Lead, Lead-Bismuth and Sodium Coolants for Fast Reactors, IAEA-TECDOC-1289, IAEA, Vienna (2002).

[4.52] KIRILLOV, P.L., Atomnaja Energia **13** 5 (1962) 481–484.

[4.53] KIRILLOV, P.L., Preprint FEI-284 (1971).

[4.54] KIRILLOV, P.L, Report presented to Int. Conf. Heavy Liquid Metal Coolants, Obninsk, USSR, Oct. 5–9, 1971.

[4.55] TALANOV, V.D., et al., 'Liquid Metals', pp. 9–15, Moscow, Atomizdat. 1967.

[4.56] MELONI, P., et al., "Implementation and preliminary verification of the RELAP5/ PARCS code for Pb-Bi cooled subcritical systems", Proc. Int. Conf. Accelerator Applications AccApp01, Nuclear American Society, Reno, United States of America, 2001.

[4.57] LITFIN, K., STIEGLITZ, R., "Subchannel Analysis of Heavy Liquid Metal Cooled Fuel Assemblies", Jahrestagung Kerntechnik, Aachen, Germany, 2006.

[4.58] ELSY Work Program, European Lead-cooled System (ELSY) Project, Technical Report, EURATOM, Management of Radioactive Waste, 2006.

[4.59] Fluent 6.1 User's Guide, Fluent Inc., Lebanon, NH, 2001.

CHAPTER 5. NATURAL CONVECTION HEAT TRANSFER STUDIES IN LIQUID METAL USING CFD

5.1. INTRODUCTION

The knowledge of natural convection heat transfer in liquid metal is important considering that liquid metal acts as a very effective coolant owing to its high conductivity. In advanced nuclear reactors, liquid metal is being proposed to be used as a coolant. When the forced flow of coolant is suddenly lost (due to loss of power to coolant pumps), the natural convection flow may get established. It is important to understand the heat transfer characteristics of the system under natural convection flow conditions. Study of natural convection heat transfer in various geometries has been performed. In this chapter, the study of heat transfer from a heated vertical plate and over a horizontal heated cylinder is described.

5.2. REVIEW OF PREVIOUS WORK

5.2.1. Vertical heated plate

The vertical plate is the simplest of the considered configurations and the fluid flow and heat transfer from a vertical flat plate depends on the structure of boundary layer adjacent to it. In case of the vertical plate, the boundary layer subjected to *natural convection* flow is much different than that in *forced* flow. A hot vertical plate induces buoyant flow around it. At any elevation, the velocity is zero at the plate due to no-slip conditions. The velocity increases with distance from plate in direction normal to plate. This is due to the buoyancy force. In this region, the buoyancy force overcomes gravity force. Further away from plate, due to reducing influence of buoyancy force, the velocity begins to decrease. At a certain distance, called velocity boundary layer thickness, the velocity reduces to zero. The thermal boundary layer thickness, which is zero at the leading edge, gradually increases. The relative rate of development of velocity and thermal boundary layer depends on Prandtl number. For liquid metals which have $Pr << 1$, the thermal boundary layer develops much faster than the velocity boundary layer.

The initial laminar boundary layer turns to turbulent with rise in elevation. The transition to turbulent takes place at critical Rayleigh number which is the product of Grashof number and Prandtl number. The critical Rayleigh number is 10^9 [5.1] for non-metallic liquids. As per Churchill and Chu [5.2], for liquid metals also, the critical Rayleigh number is taken to be 10^9. Sheriff and Davies [5.3] also mentioned that the critical Rayleigh number may be almost independent of the Prandtl number.

5.2.1.1. Correlations for laminar region for vertical plate

In laminar region, analytical methods have been used for obtaining heat transfer correlations. Integral, similarity and perturbation methods [5.3] are useful for this purpose. In integral and similarity methods, the boundary layer approximations are invoked. For integral method, the shapes of the velocity and thermal boundary layers have to be assumed which is a drawback. In similarity method, the equations, simplified using boundary layer approximations, are transformed to obtain the ordinary differential equations which are then solved analytically. Further, in obtaining similarity solution, it is assumed that the density and molecular viscosity is not dependent on the temperature. With this assumption, the momentum and continuity equation no longer remains coupled with energy equation and can be solved independently. However, the assumption of constant properties reduces the accuracy of the results drawn from the similarity solution method. In the perturbation method, the boundary layer assumptions are not required.

For *isothermal* vertical plates, for laminar region, the correlation proposed by Sparrow and Gregg [5.4] for low Prandtl number fluid, based on similarity method, is given by the following equation:

$$\mathrm{Nu}_\mathrm{x} = 0.5765\left(Gr_x \,\mathrm{Pr}^2\right)^{1/4} \tag{5.1}$$

The constants in the above equation are applicable to sodium. For other fluids, the constant to be used in place of 0.5765 is given in following table:

TABLE 5.1. CONSTANT IN SPARROW AND GREGG CORRELATION [5.4]

Pr	Constant
0.03	0.5497
0.02	0.5582
0.008	0.5729
0.003	0.5827
0.0	0.6

For getting a mean value, following form is used:

$$\overline{Nu} = 1.33 Nu_l \tag{5.2}$$

where subscript *l* is the length of the plate.

For *uniform heat flux conditions*, for sodium, Chang et al. [5.5] proposed the following correlation:

$$\mathrm{Nu}_\mathrm{x} = 0.732\left(Gr_x^* \,\mathrm{Pr}^2\right)^{1/5} \tag{5.3}$$

Mean Nusselt number is obtained using the following expression:

$$\overline{\mathrm{Nu}} = 1.2 Nu_l \tag{5.4}$$

Sheriff and Davies [5.3] proposed the following correlation, based on experimental investigation:

$$\mathrm{Nu}_\mathrm{x} = 0.674\left(Gr_x^* \,\mathrm{Pr}^2\right)^{0.213} \tag{5.5}$$

Equation (5.5) is applicable for $10^6 \le Gr^* \le 3\times10^{11}$.

The correlation is applicable to *uniform heat flux boundary conditions* and the constant is applicable to sodium. The form of the correlation is very close to the one analytically derived by Chang et al [5.5]. Based on curve fitting to experimental data of various researchers, Churchill and Chu [5.2] prescribed the following correlation for laminar natural convection from vertical isothermal plate:

$$\overline{Nu} = 0.68 + \frac{0.67 Ra^{1/4}}{\left[1+\left(0.492/\mathrm{Pr}\right)^{9/16}\right]^{4/9}} \tag{5.6}$$

The equation is applicable to the entire laminar range, i.e. up to Ra < 10^9. It is prescribed for any Prandtl number thus including metallic as well as non-metallic fluids. For uniform heat flux boundary condition, the following form is proposed:

$$\overline{Nu} = 0.68 + \frac{0.67 Ra^{1/4}}{\left[1 + \left(0.437/\mathrm{Pr}\right)^{9/16}\right]^{4/9}} \tag{5.7}$$

The form introduced by Churchill and Chu [5.2] ensures that, as Rayleigh number tends to zero, the Nusselt number reaches the asymptotic value of 0.68.

For non-metallic liquids, the form generally used is $Nu = c(Gr\,\mathrm{Pr})^n$. For metallic liquids, the form generally used is $Nu = c\left(Gr\,\mathrm{Pr}^2\right)^n$. In other words, the experimental data for metallic liquids correlates more with $Gr\,\mathrm{Pr}^2$ rather than with $Gr\,\mathrm{Pr}$. Though Churchill and Chu [5.2] tried to propose a general correlation applicable to metallic as well as non-metallic liquids, their correlation is based on experimental data mostly pertaining to air. Only one data set pertaining to mercury was used. Hence, the accuracy of their correlation for liquid metals may be questionable.

5.2.1.2. Correlations for turbulent region

For turbulent flow over vertical flat plate, following correlation by Kato et al. [5.6] is used:

$$\mathrm{Nu_x} = 0.176 Gr_x^{1/3}\,\mathrm{Pr}^{0.55} \tag{5.8}$$

The constant in the correlation is applicable to sodium. The correlation is obtained by an improved integral method.

Churchill and Chu [5.2] proposed following correlation for the entire laminar and turbulent range for all Prandtl number fluids for *isothermal conditions*.

$$\overline{Nu}^{1/2} = 0.825 + \frac{0.387 Ra^{1/6}}{\left[1 + \left(0.492/\mathrm{Pr}\right)^{9/16}\right]^{8/27}} \tag{5.9}$$

For *uniform heat flux* boundary condition, Churchill and Chu [5.2] proposed following form:

$$\overline{Nu}^{1/2} = 0.825 + \frac{0.387 Ra^{1/6}}{\left[1 + \left(0.437/\mathrm{Pr}\right)^{9/16}\right]^{8/27}} \tag{5.10}$$

In all the correlations proposed by Churchill and Chu [5.2] for uniform heat flux boundary condition, the temperature difference to be used is the difference between temperature at mid-point of the vertical plate and surrounding. The use of mid-point temperature is found to be more accurate than the mean area averaged surface temperature.

5.2.2. Heat transfer from an inclined surface

5.2.2.1. Correlations for laminar regime

For an inclined surface, under laminar conditions, the correlation for vertical plate would be used provided that, for calculation of the Grashof number, the component of gravitational force parallel to the plate, i.e. $(g \cdot \cos\theta)$ is used (where θ is inclination from vertical). Thus, for uniform heat flux conditions in laminar region, following form is to be used:

$$\mathrm{Nu}_\mathrm{x} = \left(0.732 Gr_x^* \cos\theta \, \mathrm{Pr}^2\right)^{1/5} \tag{5.11}$$

Incropera and Dewitt [5.1] noted that, for the heated inclined plate, above discussion is applicable for the lower surface only. For upper surface of the inclined surface, a highly complex three dimensional flow pattern is obtained. The three dimensional flow enhances the heat transfer rate and the increased heat transfer rate from the upper surface may offset the reduced heat transfer rate from bottom surface. Equation (5.11) is not applicable to top surface of the heated plate.

5.2.2.2. Correlations for turbulent regime

For inclined plates, Vliet [5.7] observed that transition to turbulence occurs at lower Rayleigh number compared to vertical plate. He recommended that the use of gravitational force parallel to the plate should be done only in laminar regime. For turbulent regime, appropriate form of correlation should be used with '*g*' and not '*g·cosθ*'.

5.2.3. Heat transfer from horizontal surfaces

In this case, there are two orientations possible, i.e. (i) downward facing and (ii) upward facing.

5.2.3.1. Downward facing surface

In case of downward facing horizontal plate, the boundary layer structure is very different from that on vertical flat plate. However, for the downward facing horizontal plate, the velocity boundary layer thickness is maximum at the center. A stagnation zone is formed at the centre. The thickness reduces towards the edge and is minimum at the edge. The thermal boundary layer shape is similar to the velocity boundary layer. This is observed in various experiments by various techniques (such as thermocouples and Schlieren technique). For similarity method to be applicable, the boundary layer has to grow in the downstream direction. Hence, the similarity method is not applicable in this case, even in laminar region. Based on approximate integral method, Clifton and Chapman [5.8] have given the following correlation for laminar region (constants in the equation are applicable to sodium under *isothermal* boundary conditions):

$$\overline{Nu} = 0.5212\left(Gr_a \, \mathrm{Pr}^2\right)^{1/5} \tag{5.12}$$

where subscript '*a*' is the half-width of the surface.

Fujii et al. [5.9] has carried out theoretical work for estimating the boundary layer characteristics like boundary layer thickness, local and average Nusselt number for laminar flow over a heated horizontal plate facing downwards. The results are generated by approximate integral method for various Prandtl numbers. The analysis is done for uniform heat flux boundary condition. He found that the velocity and thermal boundary layer thickness is maximum at centre and is minimum at the edge. With rise in Prandtl number, the boundary layer thickness at centre reduces. At the edge, velocity boundary layer thickness reduces to zero as Prandtl number rises above 100. The thermal boundary layer thickness at the edge reaches a constant value. It was concluded that the local Nusselt number is proportional to one sixth power of modified Grashof number. Further, the average Nusselt number is proportional to one fifth power of modified Grashof number.

For *uniform heat flux* boundary condition, following form, proposed by Fujii et al. [5.9], should be used (for sodium):

$$\overline{Nu} = 0.189\left(Gr_a^* \Pr^2\right)^{1/5} \tag{5.13}$$

5.2.3.2. Upward facing surface

This is the most difficult configuration for analysis as well as measurements. This is due to the fact that it is a naturally unstable configuration for natural convection flow. The flow tends to become turbulent at low Grashof number. In turbulent conditions, the flow is not amenable to analysis. Even the turbulent flow correlations based on experiments do not agree well with each other due to difficulty in measurements in turbulent conditions.

Pera and Gebhart [5.10] have carried out experimental and theoretical investigation of laminar natural convection flow over rectangular horizontal surface. For theoretical work, governing equations of mass, momentum and energy conservation, simplified using boundary layer assumptions, constant property assumption and using Boussinesq approximation, were solved by similarity method. The authors indicated that the flow and heat transfer of a horizontal surface with single leading edge is much different from that of a double leading edge. For a surface losing heat from both surfaces, the flow induced at the bottom side entrains the boundary layer at the top surface from edges. For a horizontal surface perfectly insulated from bottom, the flow is induced from the free-stream (ambient outside the edge). Thus, the energy and momentum content of fluid is different for single leading edge and double leading edge. In their experiments, single leading edge conditions were generated by insulating the bottom surface. In their experiments, uniform heat flux as well as isothermal conditions were taken. For generating uniform surface temperature conditions, multiple independent strip heaters were used and input to each heater was adjusted. A two dimensional flow at the top surface was generated by putting glass windows on both sides of the heated surface. Theoretical solution of two dimensional distribution of velocity and temperature over the surface was obtained. It was found that the thermal and velocity boundary layers were thinning with rise in Prandtl number. However, the analysis was limited to Prandtl number of 0.1.

For laminar regime, at Pr = 1, Pera and Gebhart [5.10] have given following form of the correlation for isothermal boundary conditions:

$$Nu_x = 0.5013\left(Gr_x \Pr^2\right)^{1/5} \tag{5.14}$$

For uniform heat flux, Pera and Gebhart [5.10] proposed the following form:

$$Nu_x = 0.394\left(Gr_x^* \Pr^2\right)^{1/5} \tag{5.15}$$

Appropriate constants for Prandtl number different than unity are also reported.

For turbulent conditions, Fujii et al. [5.9] experimentally observed that the heat transfer characteristics are similar to that of vertical plate (in turbulent conditions) and hence Eq. (5.8) is applicable. Other correlations based on experiments are summarized in following table:

TABLE 5.2. CORRELATIONS FOR UPWARD FACING HORIZONTAL SURFACES

McDonalds et al. [5.11]	$\overline{Nu} = 0.262\left(Gr_D \Pr^2\right)^{0.35}$	$6 \times 10^8 < Gr_D < 5 \times 10^9$
Kudryatsev[1]et al. [5.12]	$\overline{Nu} = 0.67\left(\frac{Gr_D \Pr^2}{1+\Pr}\right)^{1/4}$	$Gr_D < 10^8$ - *laminar*
Kudryatsev et al. [5.12]	$\overline{Nu} = 0.38\left(Gr_D \Pr^2\right)^{1/3}$	$Gr_D > 10^8$ - *turbulent*

5.2.4. Heat transfer from horizontal cylinders

In case of natural convection flow over horizontal cylinder, the boundary layer is very complex. From bottom of cylinder, the boundary layer starts to develop in the peripheral direction, but due to short curvature, in upper half, the boundary layer gets separated. The recirculating flow near the wall of cylinder in the upper half is formed. The wall adjacent velocity in lower half increases, but in upper half, it reduces. The wall temperature increases from bottom to top. Due to the complex shape of boundary layer, the boundary layer assumptions are no longer applicable. The survey of literature for this configuration shows that researchers have resorted to experimental and computational techniques for investigating this geometry.

Hata et al. [5.13] performed experimental investigation of natural convection heat transfer over a horizontal cylinder placed in a sodium pool. The investigation was performed for two cylinder sizes, i.e. outer diameters of 7.6 mm and 10.7 mm. For studying the effect of pool bulk temperature, experiments are carried out at 400^{o}C, 500^{o}C and 600^{o}C. At each bulk temperature and cylinder diameter, the heat flux is varied. The heat transfer characteristics of the system were represented by variation of Nu against $Gr^*Pr^2/(1+Pr)$. The modified Grashof number (Gr^*) based on heat flux was used for the calculations. They found that the two cylinders give the same heat transfer characteristics. Also it was found that the variation of Nu against $GrPr^2/(1+Pr)$ is same for all the three bulk temperatures. This may be due to the small variation of thermophysical properties over the given temperature range. The authors compared their experimental data with the experimental data of Kovalev and Zhukov [5.15] and also those of Fedynskii et al. [5.14]. The heater diameter in these works was 2–3 times larger than that in the Hata et al. [5.13] case. The experimental data of Kovalev and Zhukov

---

[1] Kudryatsev used a very small 38 mm diameter circular plate for his experiment.

were found to be higher than the Hata et al. data. The experimental data of Fedynskii et al. were found to be slightly lower.

Hyman et al. [5.16] presented the following empirical correlation based on several experimental data including those for liquid metals:

$$Nu = 0.53\left(Gr\,\mathrm{Pr}^2\right)^{0.25} \tag{5.16}$$

Kutateladze et al. [5.17] presented the following correlation for a cylinder with a uniform surface temperature in liquid metals. It was based on the boundary layer approximations:

$$Nu = 0.67\left(\frac{Gr\,\mathrm{Pr}^2}{1+\mathrm{Pr}}\right)^{0.25} \tag{5.17}$$

Churchill and Chu [5.18] compiled the heat transfer data of various researchers. The variation of Nusselt number with $Ra\Big/\left(1+\left(0.559/\mathrm{Pr}\right)^{9/16}\right)^{16/9}$ was plotted on a graph and various correlations were proposed. For the laminar range of 10^{-6} < Ra < 10^{9}, the following expression was proposed:

$$\overline{Nu}^{1/2} = 0.36 + 0.518\left[\frac{Ra}{\left[1+\left(0.559/\mathrm{Pr}\right)^{9/16}\right]^{16/9}}\right]^{1/4} \tag{5.18}$$

For even a wider range, i.e. 10^{-6} < Ra < 10^{13}, the following expression was proposed:

$$\overline{Nu}^{1/2} = 0.6 + 0.387\left[\frac{Ra}{\left[1+\left(0.559/\mathrm{Pr}\right)^{9/16}\right]^{16/9}}\right]^{1/6} \tag{5.19}$$

The correlations proposed by Churchuill and Chu [5.18] are applicable to uniform surface temperature boundary conditions and, for uniform heat flux condition (which is more relevant for practical applications), specific recommendations were not given by them.

5.3. COMPUTATIONAL INVESTIGATION OF HEAT TRANSFER OVER HORIZONTAL SURFACES

Sugiyama et al. [5.19] presented the results of their computational investigation on the liquid metal heat transfer in natural convection mode from horizontal submerged in liquid metal pool. They first obtained Boussinesq approximated equations by putting linearized property relations in the governing equations and neglecting certain insignificant terms. They mentioned that these forms of equations are valid for liquid metals because the various properties of liquid metals are nearly linear with respect to temperature. These Boussinesq approximated equations were then transformed to stream function-vorticity based equations and then solved using finite difference technique. In this technique, the diffusion terms were approximated using central difference technique and convection terms were approximated using first order upwind technique. The code was validated by comparing its results for air with existing correlations. The variation of Nusselt number with GrPr^2 was generated using the code for different Prandtl numbers. Based on best fit to the simulation data, following correlation was proposed:

$$\mathrm{Nu} = 1.11\left(Gr\,\mathrm{Pr}^2\right)^{0.196} \tag{5.20}$$

Hata et al. [5.20] performed numerical simulation of flow of sodium over a horizontal cylinder by natural convection. For the simulation, stream function-vorticity formulation in cylindrical polar coordinates was employed. The simulation is two dimensional transient simulation. The authors have performed simulations with two types of boundary conditions, namely constant heat flux and constant surface temperature. The simulation result was compared with their experimental data. They found that the simulation data with constant heat flux condition matches well with experimental data. The following correlation was proposed based on simulation data:

$$\mathrm{Nu} = 10^z \tag{5.21}$$

where

$$z = 0.193 + 0.145 \log R_f + 0.66 \times 10^{-2}\left(\log R_f\right)^2 - 0.2 \times 10^{-3}\left(\log R_f\right)^3 - 0.2 \times 10^{-4}\left(\log R_f\right)^4$$

$$R_f = Gr^* \,\mathrm{Pr}^2 \Big/ \left(4 + 9\,\mathrm{Pr}^{1/2} + 10\,\mathrm{Pr}\right)$$

Hata et al. [5.20] also found that the correlation of Kutateladze [5.17], which employs boundary layer approximations, underestimates the value of heat transfer coefficient. They also found that the correlation of Sugiyama, which is based on Sugiyama’s simulation data, predicts well within its range of applicability. But beyond that, Sugiyama’s correlation [5.19] underpredicts heat transfer coefficients.

Vaidya et al. [5.21] performed three dimensional simulation of natural convection flow over horizontal cylinder. The data for sodium as well as lead-bismuth eutectic were generated from their simulations. The effect of cylinder diameter and bulk temperature on heat transfer was studied. They found that the bulk temperature does not have much impact on heat transfer coefficient. But they found that the cylinder diameter has significant impact on heat transfer.

5.4. HEAT TRANSFER FROM HEATED VERTICAL PLATE

Computational investigation was performed for heat transfer studies from a vertical heated plate immersed in Pb-Bi alloy pool using a computer code PHOENICS [5.22]. The dimension of heated plate and Pb-Bi pool taken for the CFD analysis was same as used by UOTANI [5.23] for their experimentally investigation. Figure 5.1 shows the geometry analysed. The vertical heated plate is a 3 mm thick stainless steel plate. One side of the plate was provided with thermal insulation of 40 mm to avoid heat transfer from rear side of the plate. The heat transfer from the front side of the plate was only taking place to the liquid pool. Natural convection heat transfer study was performed under uniform heat flux conditions, applied on the vertical plate. The heat flux taken for the analysis were 1.8E4 and 2.2E4 W/m^2. The heat transfer from the surface of the heated plate induces natural convection in the surrounding Pb-Bi alloy pool. Figure 5.2 shows the variation of Nusselt number as a function of Grashof number, including a comparison with the Sheriff and Davies correlation [5.3].

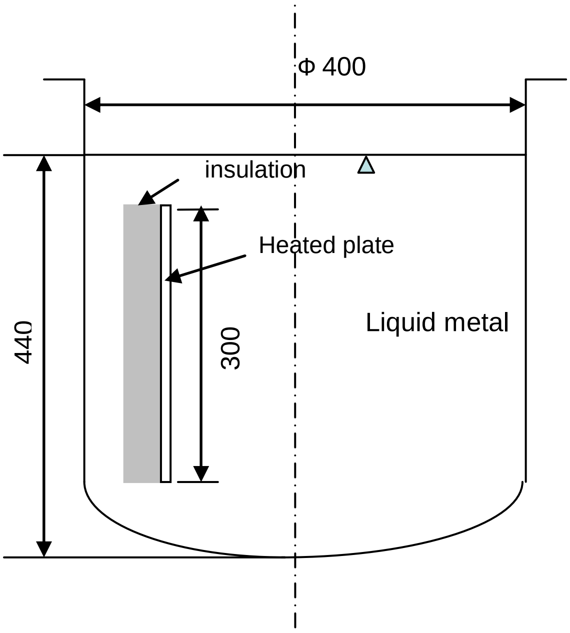

FIG. 5.1. Geometry for analysis for natural convection from heated vertical plate.

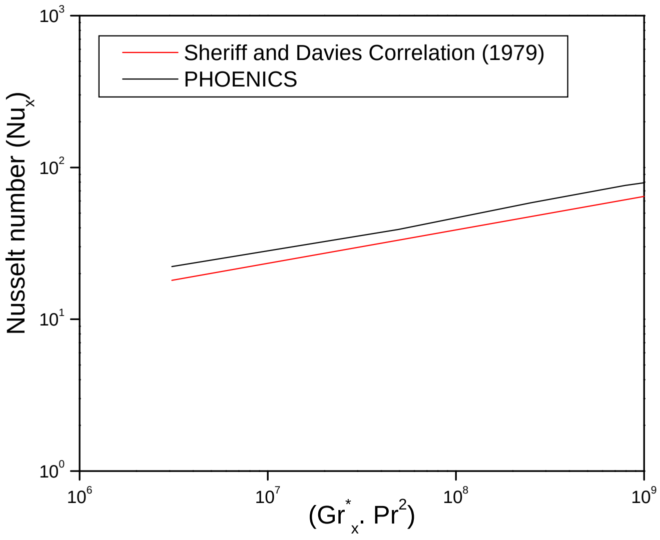

FIG. 5.2. Variation of local Nusselt numbers as a function of $Gr^* \times Pr^2$.

5.5. HEAT TRANSFER STUDIES ON HORIZONTAL CYLINDER

The geometry adopted for simulation was similar to that taken by Hata et al. [5.13] for their experiments. A schematic diagram of the system is shown in Fig. 5.3. The system consisted of a horizontal cylinder with a central heated portion (of 50 mm length) and unheated portions (250 mm each) at both ends. The heat was transferred to the sodium which surrounded the cylinder. The bulk temperature of the pool was maintained at different levels (e.g. 400°C–800°C). The investigation was performed for different bulk liquid temperatures as well as for different cylinder diameters (e.g. 7.6 mm, 10.7 mm and 25 mm). In each case, the surface heat flux was varied over a wide range (50 kW/m^2–2660 kW/m^2). In the experiments of Hata et al., heating was performed for 40 s and the outer surface temperature of the heated portion of the horizontal cylinder was measured. Hence, in the present CFD simulation, a transient study was performed for 40 s. At the final time step, values of surface temperature obtained from CFD were compared with experimental data.

5.5.1. Computational model

The simulation was performed using the PHOENICS CFD code [5.22]. The model is shown in Fig. 5.4. Owing to symmetry, half of the physical domain was modelled. Thus, the computational model shown in Fig. 5.4 represents half of the total domain shown in Fig. 5.3. The domain was discretized using body fitted grid. Heat flux boundary condition was given on the surface of the cylinder. The LVEL (i.e. the Length scale and VELocity) model, which was a zero equation turbulence model, was used. The results were also generated with k-ε turbulence model, but it was found to give same results as LVEL model. The transient simulation for 40 s was performed with the time step of 4 s. The analysis was repeated for different time steps. Thus, presented results are time step independent and also turbulence model independent (Vaidya et al. [5.21]). Boussinesq approximation for density was invoked for modelling the buoyancy driven flow. Initial condition for transient simulation was uniform bulk fluid temperature and stagnant flow field. Conductivity, viscosity and specific heat of sodium were considered as function of temperature and taken from Incropera and DeWitt [5.1]. The reference density was 860.2 kg/m^3 at 372°C and the thermal expansion coefficient was 2.866×10^{-4} K^{-1}.

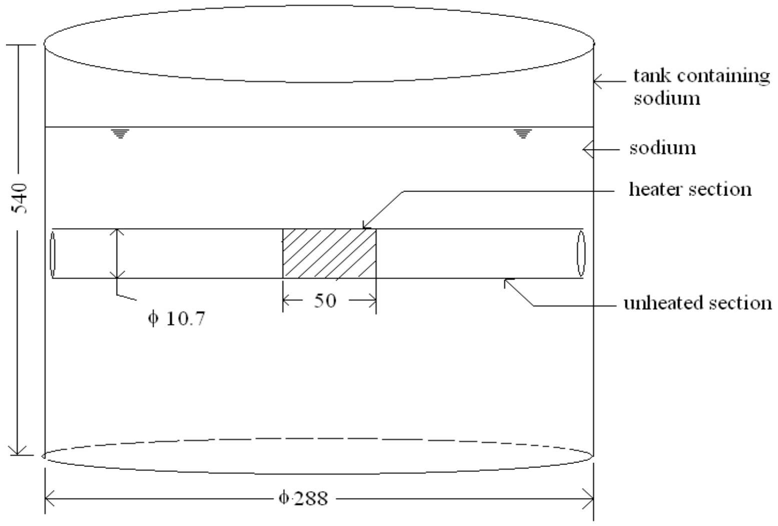

FIG. 5.3. Schematic diagram of the system (Dimensions are in mm).

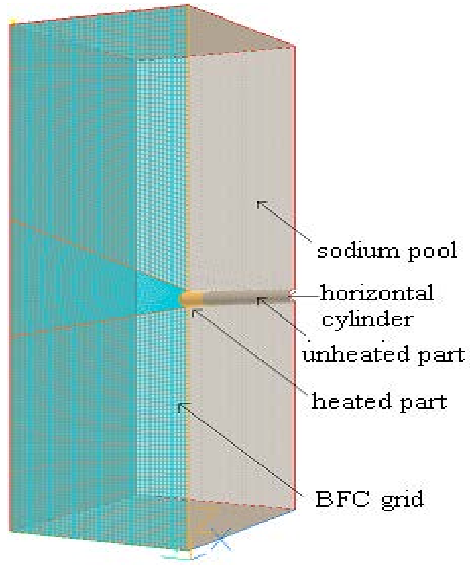

FIG. 5.4. Geometry and body fitted mesh generated in PHOENICS.

For cylinder diameter of 10.7 mm, and bulk liquid temperature of 400°C, Hata et al. [5.13] have given the surface temperature variation for various heat fluxes. This data was used for validating PHOENICS results. Figure 5.5 shows the comparison of experimental and computed temperature difference (surface temp–bulk temp) for heat flux of 10^5 W/m^2 and 5×10^5 W/m^2. Figure 5.6 shows the comparison for heat flux of 10^6 W/m^2 and 2.66×10^6 W/m^2. It can be seen that PHOENICS results match well with the experimental results at various heat fluxes.

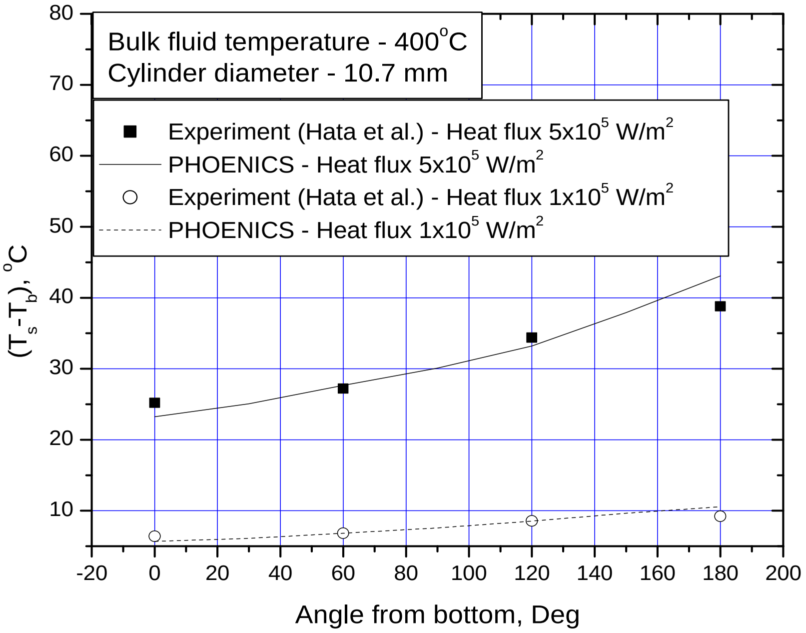

FIG. 5.5. Comparison of experimental and computed temperature difference (surface temp–bulk temp) for heat flux of 1 × 10^5 W/m^2 and 5 × 10^5 W/m^2.

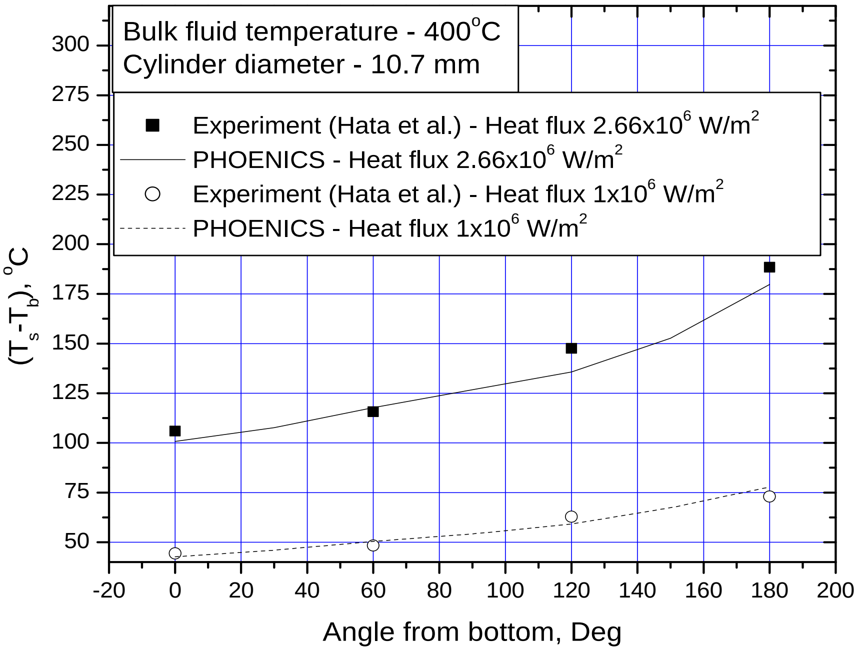

FIG. 5.6. Comparison of experimental and computed temperature difference (surface temp–bulk temp) for heat flux of 2.66 × 10^6 W/m^2 and 1 × 10^6 W/m^2.

5.6. RESULTS AND DISCUSSIONS

In present work, the heat and fluid flow was computed for following conditions: (i) Cylinder diameter — 7.6 mm, 10.7 mm and 25 mm; (ii) Bulk temperature — 400°C, 500°C, 600°C and 800°C; (iii) Heat flux — 1 kW/m^2–2600 kW/m^2. For each case, average wall temperature was computed. Based on averaged wall temperature and bulk fluid temperature, the average heat transfer coefficient was computed. Heat transfer characteristics were expressed in the form of variation of Nu with $Gr\,Pr^2/(1+Pr)$. Detailed explanation of results is given in forthcoming sections. All these results were generated for sodium as well as lead-bismuth eutectic. The results for lead-bismuth eutectic were qualitatively the same as sodium and hence are not reproduced for brevity. For obtaining a correlation, however, all data of sodium as well as lead-bismuth are included, as is explained later.

5.6.1. Effect of bulk fluid temperature on heat transfer characteristics

FIG. 5.7 shows the variation of Nusselt number against $Gr\,Pr^2/(1+Pr)$ for different bulk fluid temperatures. The heater diameter was 7.6 in all these cases. It can be seen that, with rise in bulk fluid temperature, the Nusselt number at a given $Gr\,Pr^2/(1+Pr)$ very slightly increased. Same study was conducted for heater diameter of 10.7 mm. The result is shown in FIG. 5.8. In this case, the Nusselt number was found to increase by 5% for a rise in bulk temperature by 200°C. Thus, the heat transfer characteristics were not significantly affected by bulk temperature.

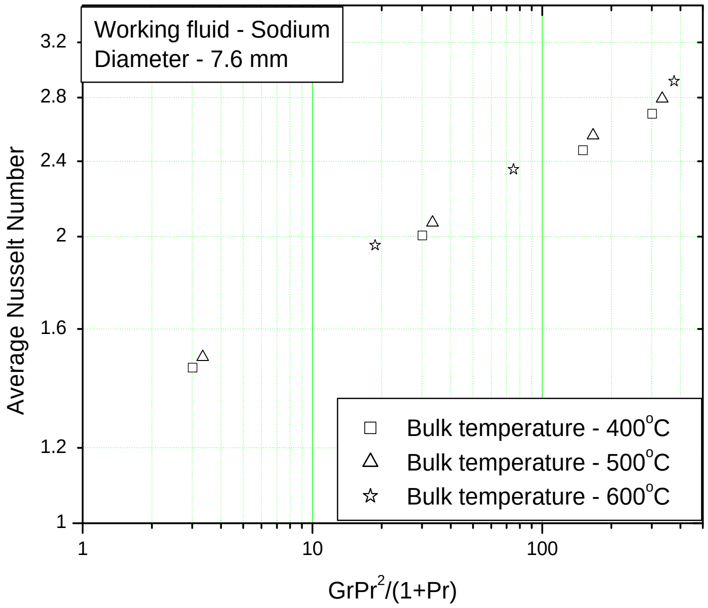

FIG. 5.7. Variation of Nu with $GrPr^2/(1+Pr)$ for different bulk temperatures for heater diameter of 7.6 mm.

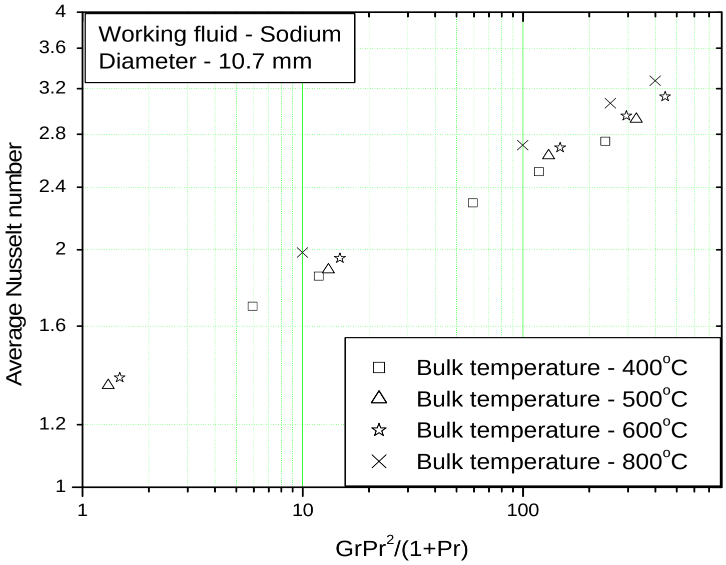

FIG. 5.8. Variation of Nu with $GrPr^2/(1+Pr)$ for various bulk temperatures for heater diameter of 10.7 mm.

5.6.2. Effect of cylinder diameter

The variation of average Nusselt number with $GrPr^2/(1+Pr)$ is plotted for different diameters. Figure 5.9 shows the change in Nusselt number due to change in diameter from 7.6 mm to 10.7 mm. It is seen that, with rise in diameter from 7.6 mm to 10.7 mm, the Nusselt number increased by about 5%. Similarly, the change in Nusselt number due to change in diameter from 10.7 mm to 25 mm is also studied as shown in Fig. 5.10. It is found that, with rise in

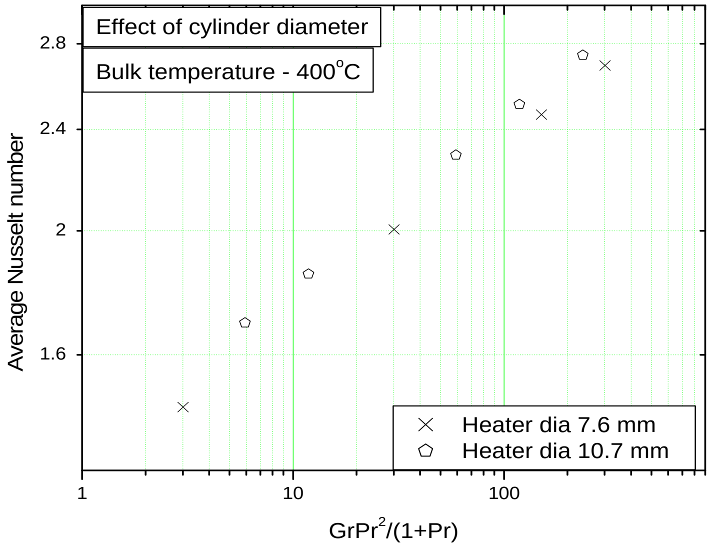

FIG. 5.9. Variation of Nu with $GrPr^2/(1+Pr)$ for heater diameters of 7.6 mm and 10.7 mm.

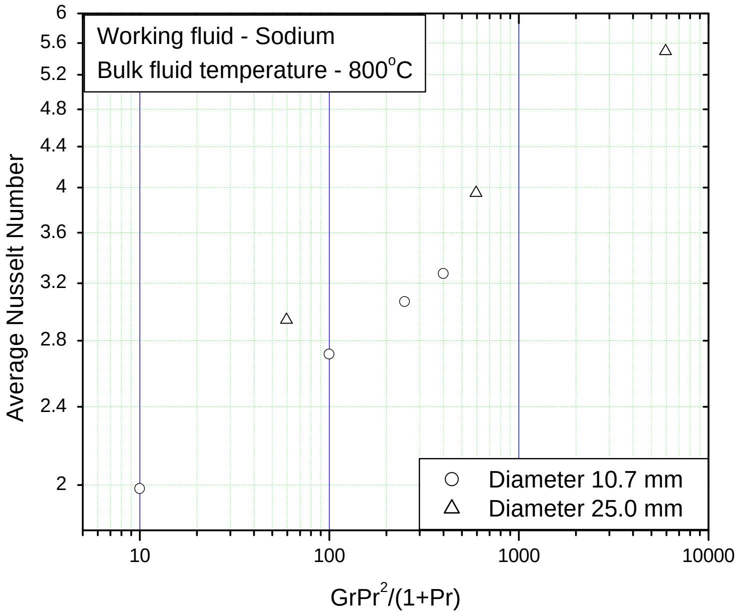

FIG. 5.10. Variation of Nu with $GrPr^2/(1+Pr)$ for heater diameters of 10.7 mm and 25 mm.

diameter from 10.7 mm to 25 mm, the Nusselt number increased by about 15%. Thus, the cylinder diameter was found to have a significant impact on Nusselt number.

While proposing a correlation for the heat transfer coefficient for this configuration, it is important that the correlation should be based on the data which is generated for various diameters covering a wide range.

All the above mentioned studies given for sodium were also repeated for lead-bismuth eutectic. Thus, heater diameter was varied from 7.6 mm to 25 mm, bulk temperature was varied from 400°C to 800°C and heat flux was varied to achieve a range of $GrPr^2/(1+Pr)$. Even for lead-bismuth eutectic, it was found that the heat transfer is insignificantly affected by bulk temperature and the effect of cylinder diameter is more pronounced.

The data from all above cases, which include data obtained by varying heat flux, cylinder diameter, bulk fluid temperature and working fluid, are compiled to give a single plot of Nu against $GrPr^2/(1+Pr)$. The resulting plot is shown in Fig. 5.11. A linear fit to the entire data is also shown in the figure. The following correlation is proposed based on simulation data:

$$Nu = 1.246 \times \left(\frac{Gr \Pr^2}{1+\Pr} \right)^{0.15732} \tag{5.22}$$

5.6.3. Comparison of present simulation data with previous correlations and experimental data

The simulation data generated are compared with the previously proposed correlations (viz. Hyman, Kutateladse, Churchill, Sugiyama correlations). They are also compared with experimental data of Hata et al. [5.13] and Fedynskii [5.14]. Figure 5.12 shows the comparison of proposed correlation and other previously proposed correlations with experimental data of Hata et al. Figure 5.13 shows the comparison of the proposed correlation and other previously proposed correlations with experimental data of Fedynskii. In both figures, it can be seen that the proposed correlation agree well with both experimental data sets. The previously proposed correlations, except Sugiyama's correlation (Eq. (5.20)) [5.19], underpredict, especially at lower range.

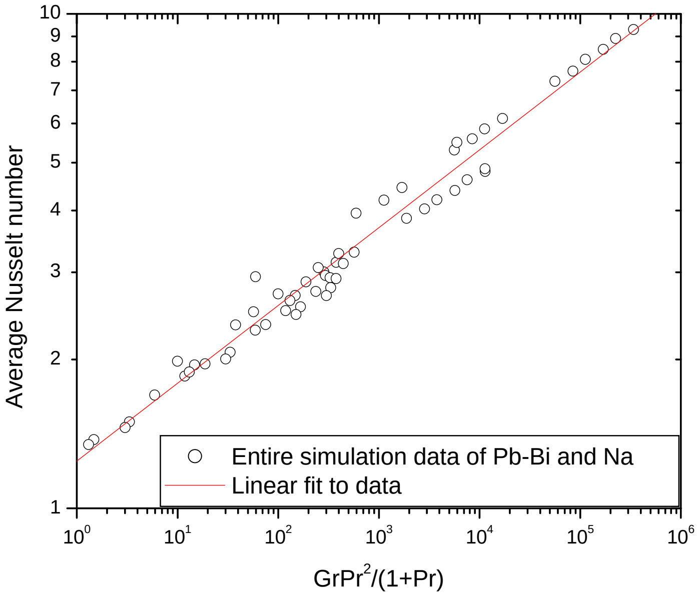

FIG. 5.11. Variation of Nu with $GrPr^2/(1+Pr)$ for heater diameters of 7.6 mm, 10.7 mm and 25 mm and for bulk fluid temperatures of 400°C, 500°C, 600°C and 800°C.

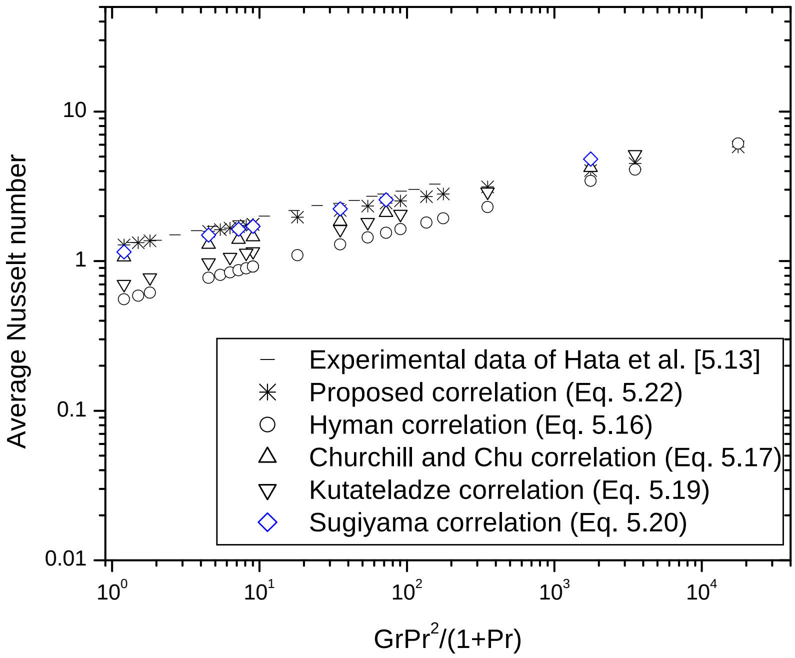

FIG. 5.12. Comparison of proposed correlation and previously proposed correlations with experimental data of Hata et al. [5.13].

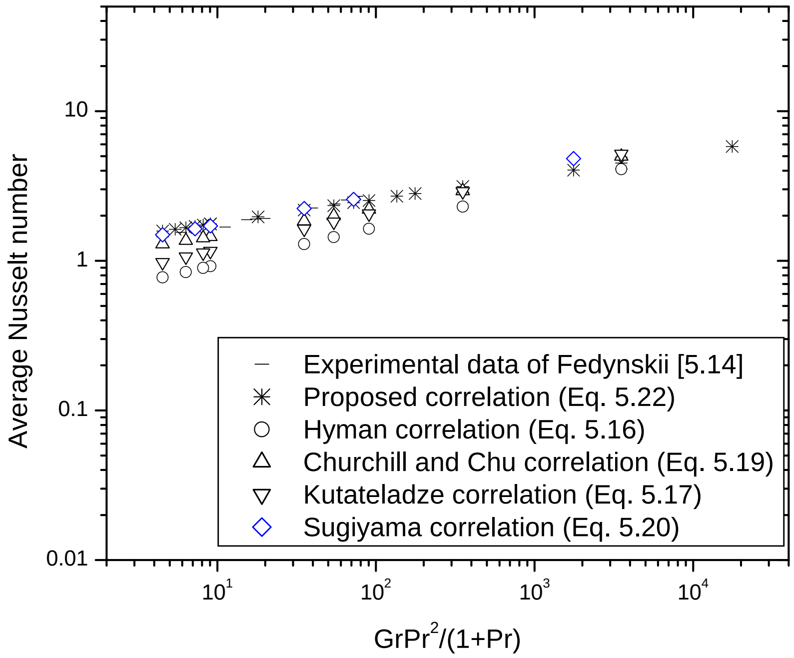

FIG. 5.13. Comparison of proposed correlation and previous correlations with experimental data of Fedynskii [5.14].

5.7. SUMMARY AND CONCLUSIONS

Three dimensional transient CFD simulation was performed to investigate the natural convection heat transfer from vertical plate and horizontal cylinder submerged in liquid metal pool. The objective of the work was to understand the effect of various parameters on heat transfer and to generate data from parametric studies.

For natural convection heat transfer from vertical plate, it was found that heat transfer predicted in CFD analysis matches well with Sheriff and Davies correlation. For natural convection heat transfer from submerged horizontal cylinder, the simulation data was validated by comparing the wall temperature predicted in CFD analysis with experimental wall temperature data reported by Hata et al. [5.13]. The simulation was performed for the bulk temperature ranging from 400^{o}C to 800^{o}C. Based on simulation data generated in the present study, a correlation, Eq. (5.22), was proposed for natural convection heat transfer from a horizontal cylinder immersed in liquid metal. The proposed correlation matches well with previously published experimental data.

List of abbreviations and symbols to Chapter 5

g	gravitational acceleration, m/s^2
Gr	Grashof number, (defined as $\frac{g\beta\Delta T l^3}{\nu^2}$)
Gr*	modified Grashof number, (defined as $\frac{g\beta q l^4}{k\nu^2}$)
k	conductivity, W/m K
l	length, m
Nu	Nusselt number, $\left(\frac{hl}{k}\right)$
Pr	Prandtl number, $\left(\frac{\mu c_p}{k}\right)$
Ra	Rayleigh number, $(Gr \times \mathrm{Pr})$
q	heat flux, W/m^2
ν	kinematic viscosity, m/s^2
β	thermal expansion coefficient, K^{-1}
θ	angle of plate from vertical
a	half-width/radius
x	local value

REFERENCES TO CHAPTER 5

[5.1] INCROPERA, F.P., DEWITT, D.P., Fundamentals of Heat and Mass Transfer, 5th Ed, John Wiles and Sons, 2002.

[5.2] CHURCHILL, S.W., CHU, H.H.S., Correlating equations for laminar and turbulent free convection from a vertical plate, Int. J. Heat Mass Tran. **18** (1975) 1323–1329.

[5.3] SHERIFF, N., DAVIES, N.W., Liquid metal natural convection from plane surfaces: a review including recent sodium measurements, Int. J. Heat Fluid Flow, **1** 4 (1979) 149–154.

[5.4] SPARROW, E.M., GREGG, J.L., Laminar free convection from a vertical plate with uniform surface heat flux, Trans. ASME **78** (1956) 435–440.

[5.5] CHANG, K.C., AKINS, R.G., BURRIS, L., BANKOFF, S.G., Free convection of a low Prandtl number fluid in contact with a uniformly heated vertical plate, Argonne National Laboratory, ANL-6835 (1964).

[5.6] KATO, H., NISHIWAKI, N., HIRATA, M., On the turbulent heat transfer by free convection from a vertical plate, Int. J. Heat Mass Tran. **11** (1968) 1117.

[5.7] VLIET, G.C., Natural convection local heat transfer on constant-heat-flux inclined surfaces, J. Heat Trans.-T ASME **91C** (1969) 511–516.

[5.8] CLIFTON, J.V., CHAPMAN, A.J., Natural convection on a finite size horizontal plate, Int. J. Heat Mass Tran. **12** (1969) 1573–1584.

[5.9] FUJII, T., HONDA, H., MORIOKA, I., A theoretical study of natural convection heat transfer from downward facing horizontal surfaces with uniform heat flux, Int. J. Heat Mass Tran. **16** (1973) 611–627.

[5.10] PERA, L., GEBHART, B., Natural convection boundary layer flow over horizontal and slightly inclined surfaces, Int. J. Heat Mass Tran. **16** (1973) 1131–1146.

[5.11] MCDONALDS, J.S., CONNOLLY, T.J., Investigation of natural convection heat transfer in liquid sodium, Nucl. Sci. Eng. **8 (**1960) 369–377.

[5.12] KUDRYATSEV, A.P., OVECHKIN, D.M., SOROKIN, D.N., SUBBOTIN, V.I., TSYGANOK, A.A., Experimental study of heat transfer from a flat horizontal surface to sodium by free convection, in ‘Zhidkic Metally’, P.L. Kirillov (Ed.), Atomizdat. (1967).

[5.13] HATA, K., TAKEUCHI, Y., SHIOTSU, M., SAKURAI, A., Natural convection heat transfer from a horizontal cylinder in liquid sodium, Part 2: Generalised correlation for laminar natural convection heat transfer, Nucl. Eng. Des. **194** (1999) 185–196.

[5.14] FEDYNSKII, O.S., Heat Transfer and Thermal Modeling, AN, USSR, p. 107 (1958).

[5.15] KOVALEV, S.A., ZHUKOV, V.M., Experimental study of heat transfer during sodium boiling under conditions of low pressures and natural convection, Prog. Heat Mass Transfer **7** (1973) 347–354.

[5.16] HYMAN, S.C., BONILLA, C.F., EHRLICH, S.W., Natural-convection transfer processes: I. Heat transfer to liquid metals and nonmetals at horizontal cylinders, Chem. Eng. Prog. Symp. Ser. **49** (1953) 21–31.

[5.17] KUTATELADZE, S.S., BORISHANSKII, V.M., NOVIKOV, I.I., FEDYNSKII, O.S., Zhidkometallitcheskye Teplonositeli (Liquid Metal Heat Transfer Agents), Atomizdat, Moscow (1958).

[5.18] CHURCHILL, S.W., CHU, H.H.S., Correlating equations for laminar and turbulent free convection from a horizontal cylinder, Int. J. Heat Mass Tran. **18** (1975) 1049–1053.

[5.19] SUGIYAMA, K., MA, Y., ISHIGURO, R., Laminar natural convection heat transfer from a horizontal circular cylinder to liquid metals, J. Heat Trans.-T. ASME **113** (1991) 91–96.

[5.20] HATA, K., TAKEUCHI, Y., SHIOTSU, M., SAKURAI, A., Natural convection heat transfer from a horizontal cylinder in liquid sodium, Part 2: Generalized correlation for laminar natural convection heat transfer, Nucl. Eng. Des. **194** (1999) 185–196.

[5.21] VAIDYA, A.M., MAHESHWARI, N.K., VIJAYAN, P.K., SAHA, D., Liquid metal natural convection heat transfer over a horizontal cylinder, Proc. 37th National and 4th International Fluid Mechanics and Fluid Power Conference, Chennai, Dec 16–18, 2010.

[5.22] PHOENICS Online Information System, Version 3.6.1, CHAM Ltd., 2006.

[5.23] UOTANI, M., Natural convection heat in thermally stratifies liquid metal, J. Nucl. Sci. Technol. **24** 6 (1987) 442–451.

This page has been left intentionally blank.

CHAPTER 6. VARIOUS APPLICATIONS OF CFD AND REACTOR KINETICS STUDIES

6.1. INTRODUCTION

The use of the Computational Fluid Dynamics (CFD) techniques is getting more and more widespread in the study of the nuclear power systems. In the present generation of LWR, the CFD applications range from the simulation of the heat and moment transport in complex geometries to the multiscale and multiphysics modelling of the reactor core.

The innovative nuclear reactors envisage high temperature coolants like liquid metal, gas and molten salt for which usually experiments are very expensive and accurate measurements are complex or even impossible. Therefore, application of CFD for predictions of various flow characteristics becomes an attractive and complementary practice used in the design and evaluation of the innovative reactors, for instance to simulate the three dimensional mixing effects in the core of metal reactors, as shown in Italy and China studies here described.

Other CFD applications concern specific items related to the characteristics of the coolant used in the reactor, like the solidification and melting studies of LBE in natural circulation conditions performed in India.

Finally, in the design of innovative reactors like ADS (accelerator driven systems), the need is recognized to provide an accurate simulation of the reactor dynamics for both the safety study and the core design optimization. For this reason, the coupling of three dimensional thermohydraulic modules with reactor kinetics modules is pursued in many research programmes. The study carried out in Brazil on the reactor kinetics in ADS reactors is located in this line of research.

6.2. CFD MODEL OF AN OPEN SQUARE LATTICE CORE OF A LEAD COOLED REACTOR

The open assembly core option studied within the framework of the European project ELSY (European lead cooled system) [6.1] is supposed to bring quite relevant advantages to meet the requirements of nuclear sustainability, non-proliferation and energy production characterizing the Generation IV reactors [6.2]. The reduction of the weight inside the vessel structure impacts positively the economics allowing compacting of the pool. Fewer absorbers and the coolant characteristics lead to an improvement in the neutronic balance increasing the minor actinide burning capability required to meet sustainability. From the point of view of safety, the risk of severe consequences for the fuel assembly blockage is reduced, the high pitch-to-diameter ratio allows having less core pressure drop enhancing the natural circulation; furthermore, the mixing effects between assembly flows could promote the reduction of the hot-spot temperature on the pin cladding.

However, this design solution requires an accurate assessment of the cladding peak temperature that is considered the most critical parameter in order to meet safety limits, due to the corrosion/erosion lead physical properties. For this purpose, a one dimensional RELAP5 [6.3] model for independent channel analysis of the core thermohydraulics has been developed with particular attention to the heat transfer correlations used for the rod bundle coolant-cladding temperature and pressure drops. This model has provided a conservative assessment for the preliminary core design of the 1500 MW lead fast reactor with an open square lattice and three radial zones at different levels of fuel enrichment.

After this preliminary assessment of the thermohydraulics and safety of the ELSY open square core design, we have developed a dedicated full three dimensional CFD code for the analysis of the whole core behaviour which may take into account mixing and multi-dimensional effects among assembly flows. The numerical simulations, based on the full three dimensional incompressible Navier-Stokes and energy equations, take place at a coarse, assembly length level and are linked to the fine, subchannel level state through transfer operators based on parametric coefficients that summarize local fluctuations (Fig. 6.1). The overall effects among assembly flows are evaluated by using average assembly turbulent viscosity and energy exchange coefficients that are estimated with CFD simulations over limited subassembly regions.

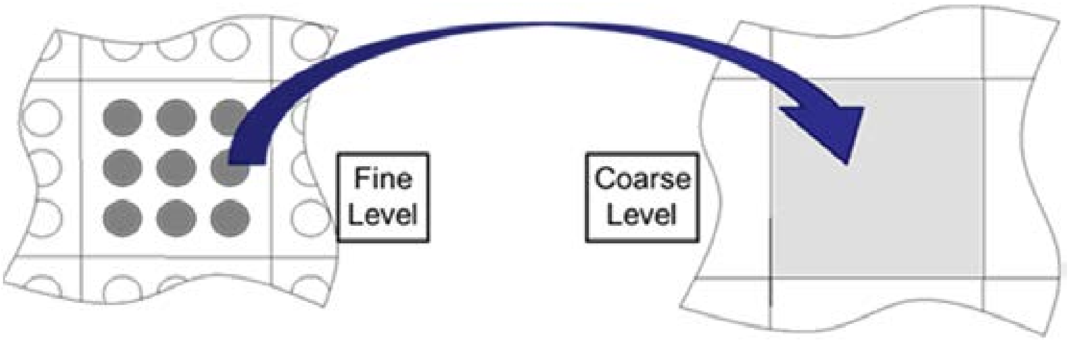

FIG. 6.1. Two level approach for CFD simulation of lead square unwrapped lattice core.

The model of the ELSY core has been set up and benchmarked with the RELAP5 model with separated channels (Fig. 6.2). Some simplifying assumptions have been introduced:

- Any core assembly is considered as a homogeneous and continuous lattice of fuel pins.
- The radial exchange of momentum and energy is modelled with empirical coefficients [6.4].
- Turbulence effects are modelled with a simple LES approach.
- Pressure losses are modelled by using standard monodimensional correlations; the dummy/reflector region and control rod assemblies are not simulated.

The three dimensional code solves the Navier-Stokes equations coupled with the incompressibility constraint and the energy equation in the reactor domain, where lumped coefficients are used to model the subgrid structures and forces. The values of these coefficients are still an open question and standard generic correlations are used in this computation for momentum and energy exchange coefficients [6.5], [6.6].

The power source and the pressure losses are introduced element-wise in order to reproduce the values computed by the neutronic reactor model and by the geometric configuration with accidental and distributed pressure losses used in the REALP5 model. The boundary conditions for the velocity fields are set to full slip along the side of the reactor and inflow and outflow conditions at the top and bottom. The pressure distribution, which can be not uniform, is set at the inlet and outlet of the reactor. Constant temperature profile, the inlet temperature profile, is imposed uniformly on the bottom surface. On the symmetry planes, symmetric boundary conditions are used. The solution is computed by means of a coupled multigrid solver over two levels [6.7] and is fully determined by the imposed inlet

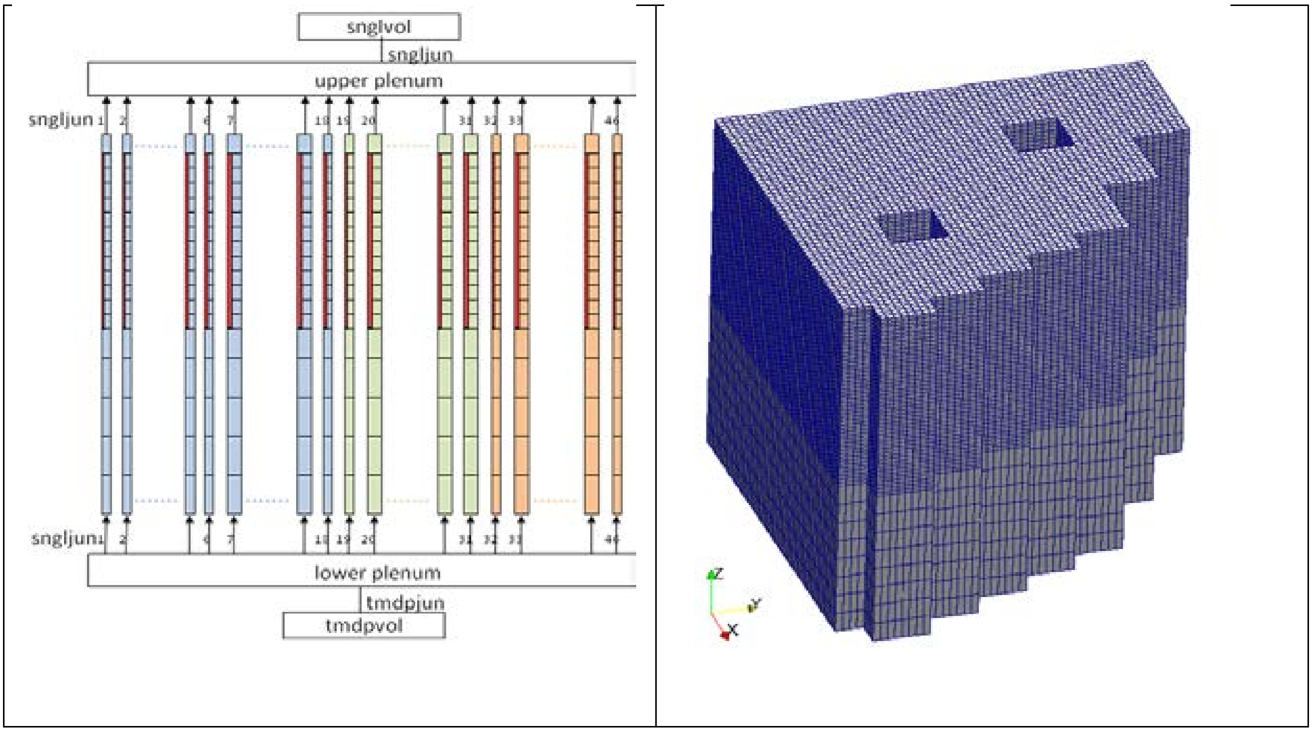

FIG. 6.2. Independent channel models (RELAP5) and three dimensional model of ELSY core.

temperature and pressure distributions. The inlet and outlet pressure values are chosen in order to reproduce the same inlet flow rate as the RELAP5 model.

The meshes for the full reactor and for the computational domain are shown in Fig. 6.2. Each assembly is represented by 4 × 4 × 20 Hex27 finite elements. For the quarter reactor, the number of nodes is 11 6481, resulting in 481 485 DOFs (velocity, pressure and temperature) and 15 561 elements. In this case, the domain is discretized with standard Lagrangian finite element families. In order to assure the solution stability, piecewise linear elements are used for pressure, while piecewise quadratic elements are used for velocity and temperature variables [6.8].

The three dimensional simulation of the ELSY open core has been initially carried out without taking into account the turbulent viscosity and with constant boundary conditions at core inlet and outlet. In this configuration, the model provides almost the monodimensional solution, since the effect of momentum and energy exchange among assemblies is negligible. The lead temperature field presented in Fig. 6.3 shows that the core outlet temperature distribution reproduces the profile of the power distribution, as in the RELAP5 separate channel model. In fact, the temperature jump across the core calculated with the two models differs only by less than two degrees.

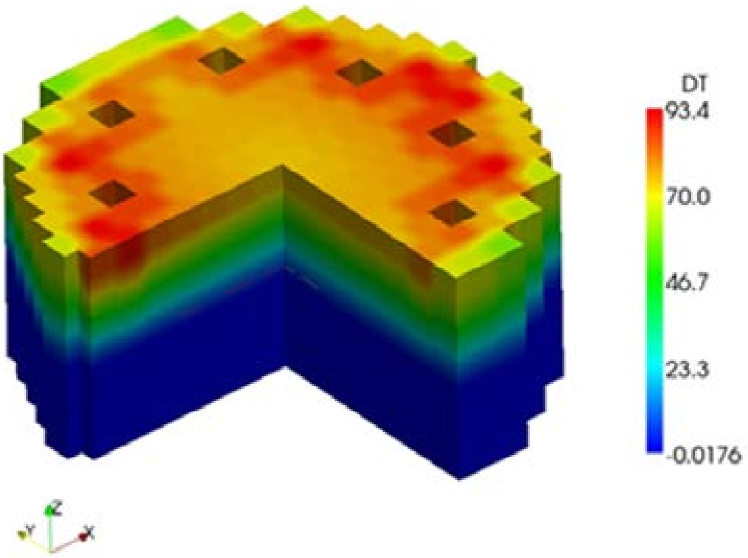

FIG. 6.3. *Temperature jump over the reactor core.*

A preliminary assessment of the CFD model for the three dimensional simulation of the ELSY core thermohydraulics has been carried out comparing the results obtained for a simple test with those obtained with the RELAP5 one dimensional independent channels approach [6.9]. The fully three dimensional temperature distributions are generated in case non-uniform pressure boundary conditions are imposed at core outlet, in order to promote the mixing effects among assembly flows.

A parabolic axisymmetric outlet pressure distribution has been assumed to take into account the pumps locations and the upper plenum structure. An outlet profile of pressure is not uniform as in the case where the pressure pumps are in precise locations at the top of the reactor, then the computations become fully three dimensional. If we consider a simulation with a parabolic axisymmetric outlet pressure distribution, then the velocity field changes direction and magnitude inside the core, and the outflow temperature profile differs substantially from the RELAP5 model, as shown in Fig. 6.4. In this figure, one can see that temperatures computed with the three dimensional code are substantial lower in the inner zone and higher in the outer zone than those computed by using the RELAP5 model.

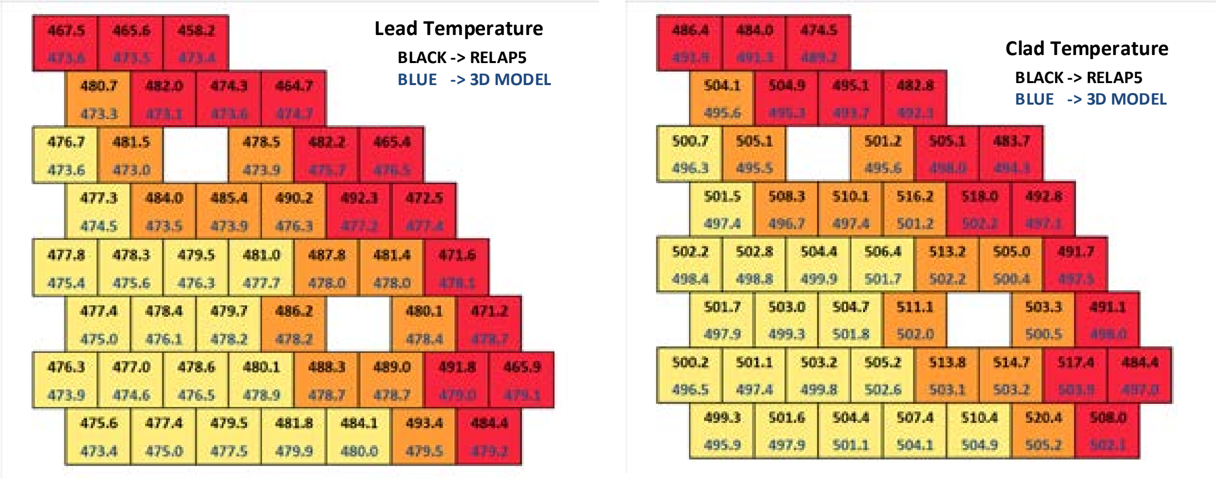

Lead Temperature

BLACK -> RELAP5
BLUE -> 3D MODEL

467.5 473.6	465.6 473.5	458.2 473.4					
480.7 473.3	482.0 473.1	474.3 473.6	464.7 474.7				
476.7 473.6	481.5 473.0		478.5 473.9	482.2 475.7	465.4 476.5		
477.3 474.5	484.0 473.5	485.4 473.9	490.2 476.3	492.3 477.2	472.5 477.4		
477.8 475.4	478.3 475.6	479.5 476.3	481.0 477.7	487.8 478.0	481.4 478.0	471.6 478.1	
477.4 475.0	478.4 476.1	479.7 478.2	486.2 478.2		480.1 478.4	471.2 478.7	
476.3 473.9	477.0 474.6	478.6 476.5	480.1 478.9	488.3 478.7	489.0 478.7	491.8 479.0	465.9 479.1
475.6 473.4	477.4 475.0	479.5 477.5	481.8 479.9	484.1 480.0	493.4 479.5	484.4 479.2	

Clad Temperature

BLACK -> RELAP5
BLUE -> 3D MODEL

486.4 491.9	484.0 491.3	474.5 489.2					
504.1 495.6	504.9 495.3	495.1 493.7	482.8 492.1				
500.7 496.3	505.1 495.5		501.2 495.6	505.1 498.0	483.7 494.3		
501.5 497.4	508.3 496.7	510.1 497.4	516.2 501.2	518.0 502.2	492.8 497.1		
502.2 498.4	502.8 498.8	504.4 499.9	506.4 501.7	513.2 502.2	505.0 500.4	491.7 497.5	
501.7 497.9	503.0 499.3	504.7 501.8	511.1 502.0		503.3 500.5	491.1 498.0	
500.2 496.5	501.1 497.4	503.2 499.8	505.2 502.6	513.8 503.1	514.7 503.2	517.4 503.9	484.4 497.0
499.3 495.9	501.6 497.9	504.4 501.1	507.4 504.1	510.4 504.9	520.4 505.2	508.0 502.1	

FIG. 6.4. *Effect of outlet pressure distribution.*

6.3. CFD APPLICATION TO A FUEL SUBASSEMBLY (SA) OF CEFR IN CHINA

It is important to know the distribution of the velocity and temperature fields in the fuel subassembly for the design and analysis of the thermohydraulics of the CEFR (China Experiment Fast Reactor). Although the subchannel analysis is a very useful tool for the thermal calculation of the hot channel, the CFD method and the Porous Media Model are other important analysis methods in this field. In the following part, two methods are given with a brief introduction.

6.3.1. CFD simulation in the CEFR fuel subassembly

Figure 6.5 is a schematic of a CEFR fuel subassembly. Each fuel subassembly has 61 fuel rods with 6mm diameter fuelled with UO_2, and there are wire-wraps located on the surface of each fuel rod. It is shown that the structure of the fuel rod bundles is very complex, which makes the numerical simulation of the CFD work difficult if we don't make any simplification. Sometimes, it will even be an impossible task. So, in order to complete this analysis, a series of simplifications of the structure and in the hypothesis of analysis are necessary.

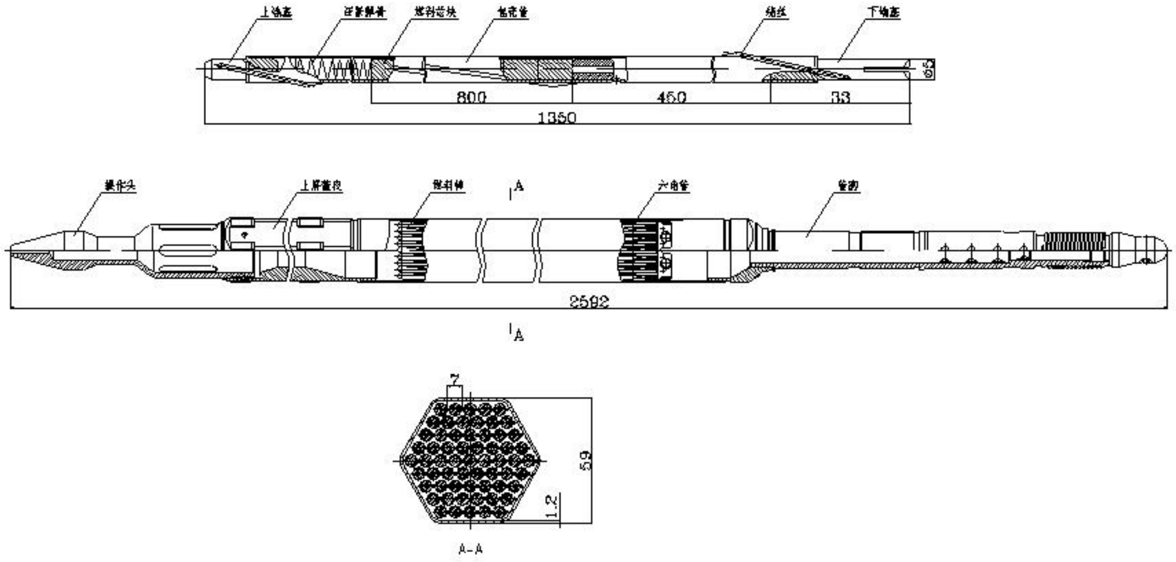

FIG. 6.5. Fuel subassembly of CEFR.

TABLE 6.1. GEOMETRY PARAMETERS OF THE FUEL SA OF CEFR

Parameters	Value
Geometry	
Pitch of fuel rods	7.0 mm
Diameter of the fuel rod	6.0 mm
Height of the helix	100 mm
Length of the active part	450 mm
Thermal power (max)	969 kW
Inlet temperature	360°C
Inlet flow rate	3.94 kg/s

Table 6.1 shows the geometry parameters of the subassembly with the maximal thermal power.

In our analysis work, The CFD code CFX is used to model the inner region of a fuel SA of CEFR. Considering the calculation capacity and operational CPU time of the computer, only the fluid region is simulated. At the same time, in order to form the fine grids, the wire wraps around the fuel pins are simplified, the finial structure is shown in Fig. 6.6.

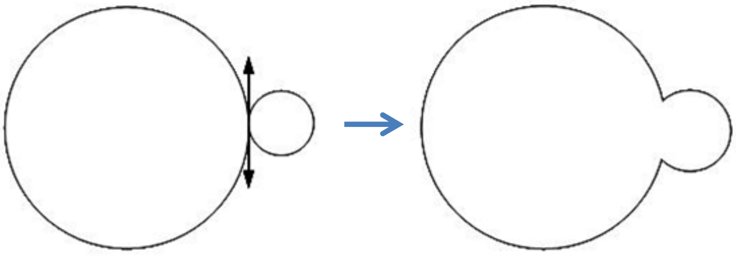

FIG. 6.6. Geometry simplification.

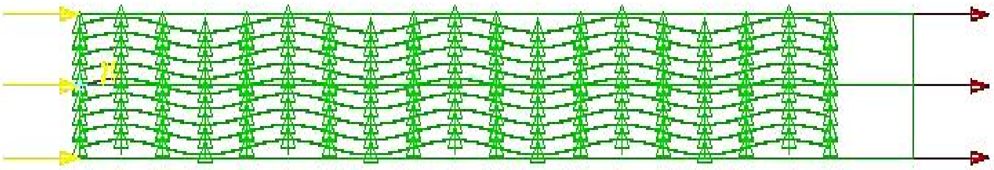

FIG. 6.7. Active part of fuel SA.

For the boundary conditions, heat flux was adopted on the surface of the adiabatic hexagonal sheath. Fig. 6.7 shows the inlet and outlet boundaries of the simulation part of CEFR fuel SA.

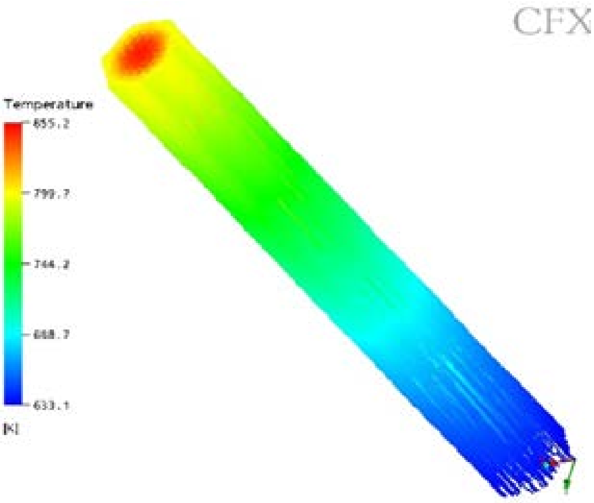

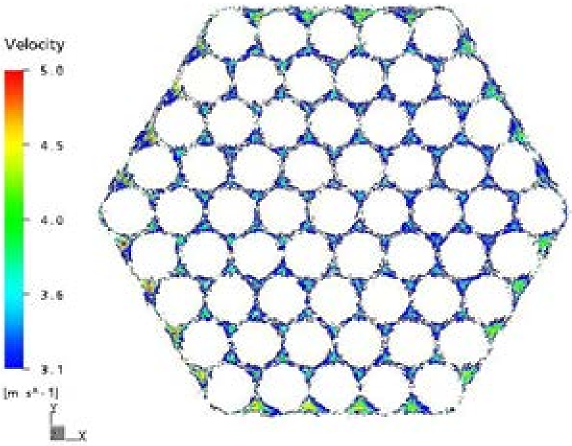

FIG. 6.8. Temperature distribution.
FIG. 6.9. Velocity distribution.

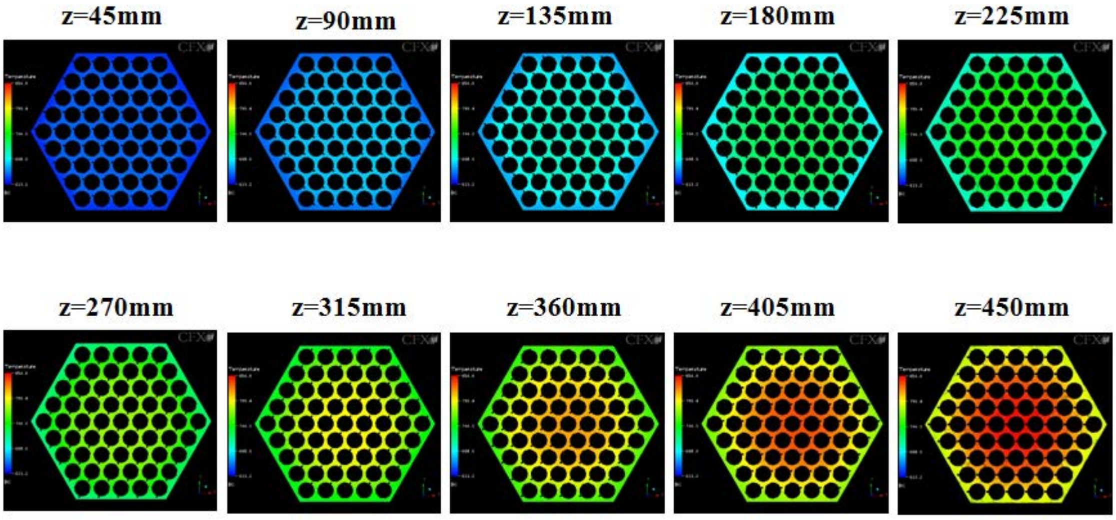

FIG. 6.10. Temperature distribution at 10 cross-sections.

Some calculation results showed that the numerical results were in good agreement with CRT model [6.10], ICRT (Improved CRT) correlation (cf. chapter 3.4) and the improved SUPERENERGY code. Secondary swirls induced by the spacer wires were observed in the rod bundle, which promoted the mixing of the coolant. Figs. 6.8 and 6.9 show the temperature and velocity distribution in the rod bundles and Fig. 6.10 shows the temperature distribution in the different cross-sections.

6.3.2. Porous media model

In order to simulate the coolant flow, mixing and heat transfer characteristics in a fuel SA with a few meshes, a porous model is adopted, which is a generalization of both the Navier-Stokes equations and the Darcy's law. In this model, volume porosity, surface porosity, distributed resistance and distributed heat source are defined respectively. With some empirical data, the Chiu-Rohsenow-Todreas model and an effective eddy diffusivity are employed. By using this model, the steady and transient behaviour can be evaluated with a few nodes. As an example, the flow and heat transfer characteristics in a fuel subassembly of CEFR are simulated.

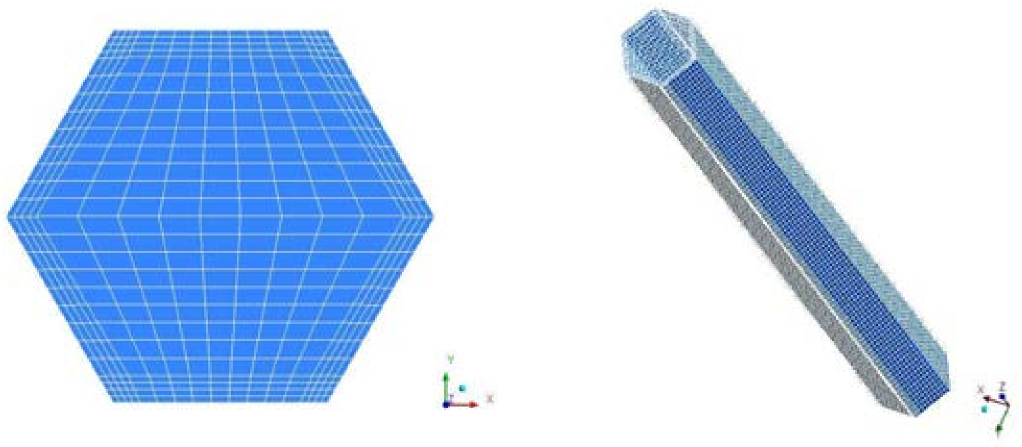

FIG. 6.11. Meshes of the active part.

In the CRT model, pressure drop parameters are derived for channels 1 (interior) and 2 (edge) only. The results are shown below:

$$\Delta p_1 = f_{s1} \frac{L}{D_{e1}} \frac{\rho V_1^2}{2} \left[1 + C_1 \frac{A_{r1}}{A_1^{'}} \frac{D_{e1}}{H} \frac{P^2}{(\pi P)^2 + H^2} \right] \tag{6.1}$$

$$\Delta p_2 = f_{s2} \frac{L}{D_{e2}} \frac{\rho V_2^2}{2} \left\{ 1 + \left[C_2 n \left(\frac{V_T}{V_2} \right)_{GAP} \right]^2 \right\}^{1.375} \tag{6.2}$$

where Δp_1 and Δp_2 represent pressure drop in channel 1 and 2 respectively, and f_s is the friction coefficient which is computed by the Colebrook formula:

$$\frac{1}{f^{0.5}} = -4 \lg \left[\frac{(\varepsilon / D)}{3.7} + \frac{1.255}{(R_e f^{0.5})} \right] \tag{6.3}$$

In the interior region of the rod bundle, the flow mixing through the gaps between fuel rods results from turbulent flow exchange, sweeping cross-flow and pressure-induced cross-flow. In the peripheral region, a transverse flow called a swirl flow runs parallel with the duct wall. The spacer wires enhance the coolant mixing in the rod bundle obviously. An effective eddy diffusivity ε is adopted in the energy conservation equation to simulate the effect of spacer wire, which is similar to the approach of SUPERENERGY code. Then the equations for conservation of energy are transformed to:

$$\frac{\partial}{\partial t}\left(\gamma\rho H\right)+\nabla\cdot\left(\rho K\cdot UH\right)-\nabla\cdot\left(\left(\rho C_p\varepsilon+\Gamma_e K\right)\cdot\nabla H\right)=\gamma S^H \tag{6.4}$$

where ε is a function of the rod bundle parameters, Γ_e is an effective thermal diffusivity and S^H contains a heat source or sink to or from the porous medium. These parameters have been implemented in the SUPERENERGY code.

The geometry and boundary conditions have the same parameters as mentioned before.

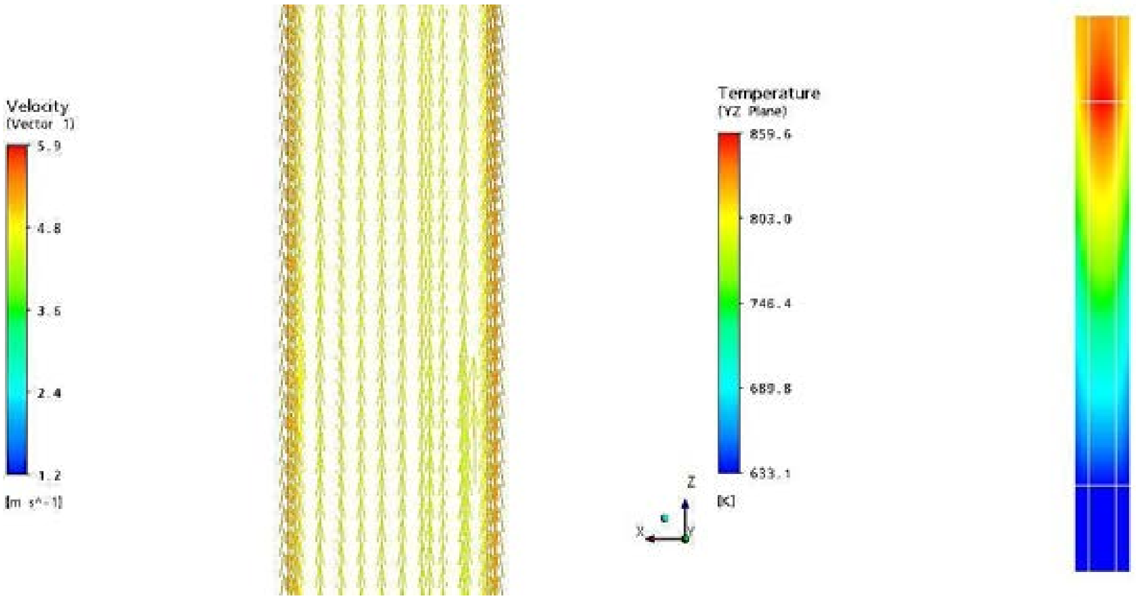

FIG. 6.12. Axial velocity and temperature distribution in the rod bundle.

The comparison of results for a CEFR 61-pin test showed that there was good agreement between this porous code calculation and the experimental data. The differences in temperature were found between this porous code and SUPERENERGY code because of the pressure drop, induced by different pressure models, but these differences are small.

6.4. MELTING AND SOLIDIFICATION STUDIES ON LEAD-BISMUTH EUTECTIC

Heavy liquid metals (HLM), lead (Pb) and three alloys of lead — lead-bismuth eutectic (LBE) 44.5 wt. % Pb + 55.5 wt. % Bi, lead-lithium eutectic 99.32 wt. % Pb + 0.68 wt. % Li, and lead-magnesium eutectic 97.5 wt. % Pb-2.5 wt. % Mg, are considered at present as potential candidates for the coolant of new generation reactors (critical and subcritical) and for liquid spallation neutron sources and accelerated driven systems (ADS). LBE is expected to be used in most of ADS projects, mainly due to its low melting temperature of 397 K (~124°C), resulting in lower corrosion rates and easier maintenance. Freezing-solidification processes with a lead-bismuth alloy have been studied to assess computational fluid dynamics codes commercially developed. The present work briefly describes the experiments and CFD analysis performed on melting and solidification process with LBE.

Several methods have been proposed to deal with melting and solidification problems with natural convection. The most popular method is the enthalpy-porosity technique proposed by Voller and coworkers [6.11][6.13]. It is a fixed grid numerical solution method for solving phase change problems. Instead of explicitly defining the phase front location in the governing energy equation, the model implicitly specifies the phase front location by introducing the concept of porosity.

Sanyal et al. [6.14] studied the effect of natural convection phenomena in a transportation cask enthalpy porosity method. They also performed separate analyses in which natural convection was neglected. They concluded that conduction analysis alone (neglecting natural convection) is not adequate to accurately model the phase change problems.

Duan et al. [6.15] performed a numerical study of solidification of n-hexadecane in an enclosure based on the enthalpy formulation. They concluded that the solidification process is more affected by natural convection at an early stage of solidification than at the later stage.

The solidification of pure tin and 90/10% wt. tin-bismuth has been analysed experimentally with different cooling rates by Quillet et al. [6.16]. They observed differences between the two cases and interpreted them in terms of differences in natural convection. In the alloy case, convection was due to both solution and buoyancy, but former was significantly greater.

Melting and solidification experiments are performed in the melt tank of Heavy Metal Alloy Natural Circulation Study (HANS) Loop [6.17]. All the components and piping are made of SS316. The melt tank is provided with adequate thermal insulation in order to reduce heat loss to the environment. The LBE is melted in the melt tank (12” SCH 80) by three band heaters of equal capacity. For the present melting study, only two band heaters (heater HT1 and HT2 as shown in Fig.6.13) were put into operation. Adequate care has been taken to prevent contact of air with the molten LBE. The total power given to heaters was 4 kW. Three thermocouples were placed along the centre line of the melt tank as shown in Fig. 6.13. Melting and solidification experiments were performed with LBE initial level in the melt tank at 470 mm.

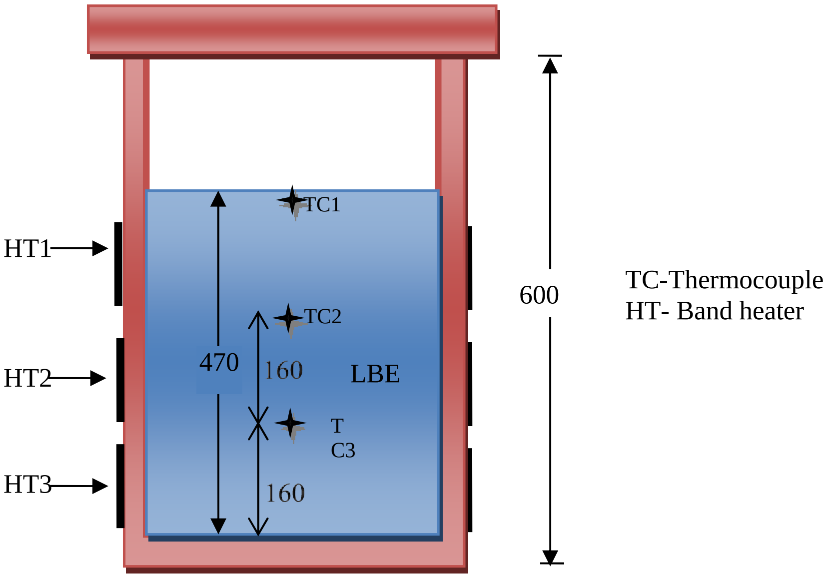

FIG. 6.13. Melt tank with heater and thermocouples arrangements.

Melting and solidification analysis of LBE material was performed with a two dimensional axisymmetric model. Numerical simulation was done using the CFD code Anupravaha. Anupravaha is a multiblock finite volume solver for non-orthogonal hexahedral structured grids. It reads grids in CGNS format and solves the Navier-Stokes, continuity, temperature and species transport equations, and writes the results in CGNS files to be read and displayed by any post-processing software. The grids are generated by the grid-generation code GridZ. To model phase change, enthalpy-porosity technique is used in the CFD code Anupravaha. To account for the phase change of a metal/alloy, three distinct regions are considered: a solid region, a totally liquid region and a mushy region.

The melting experiments were performed by heating lead-bismuth eutectic in the melt tank with electrical band heaters as shown in Fig. 6.13. Heaters 1 and 2 are kept operating for a period of one and half hour. The total power of the heaters was maintained at 4 kW. Figure 6.14 shows the variation of temperature as a function of time at one of the thermocouple locations, TC1, during the melting experiment. A comparison of CFD results with experimental data is also shown in Fig. 6.14 for a transient rise in temperature. It can be observed that, after melting point has been reached, the temperature jumps by about 43°C within 40 s in the experiment. In the CFD analysis, this jump is about 13°C within 50 s. This steep jump in temperature may be due to the fact that hot fluid near the heater starts circulating towards the thermocouple location, where it is completely melted. After that, the temperature is steadily raising. Figure 6.15 shows the contour plot at different times. The slope of the curve decreases after melting occurs at that location. This is because of the liquid sensible heat is higher compared to solid sensible heat.

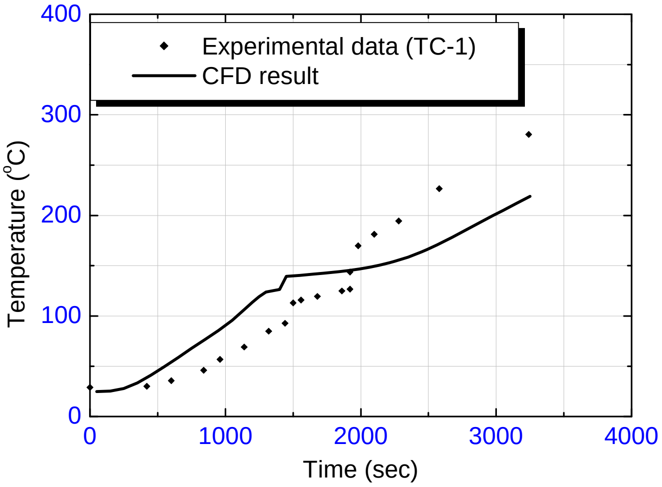

FIG. 6.14. Variation of temperature with time during melting of LBE.

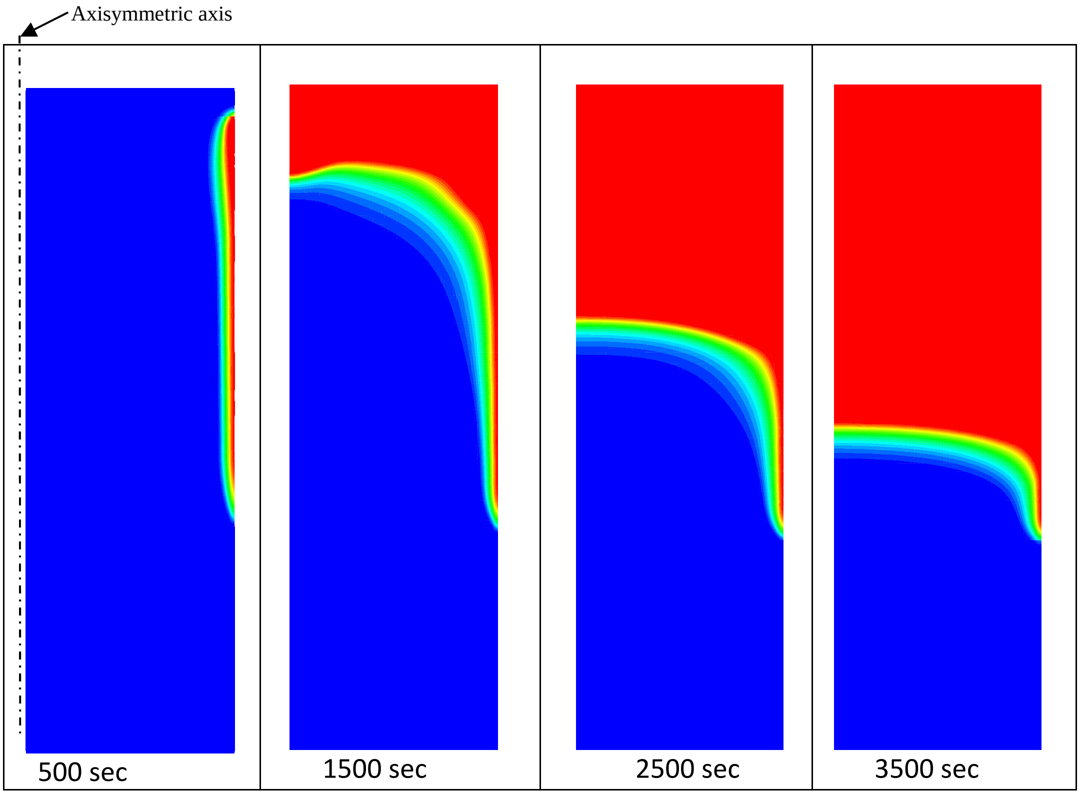

FIG. 6.15. Progression of melt front in the melt tank.

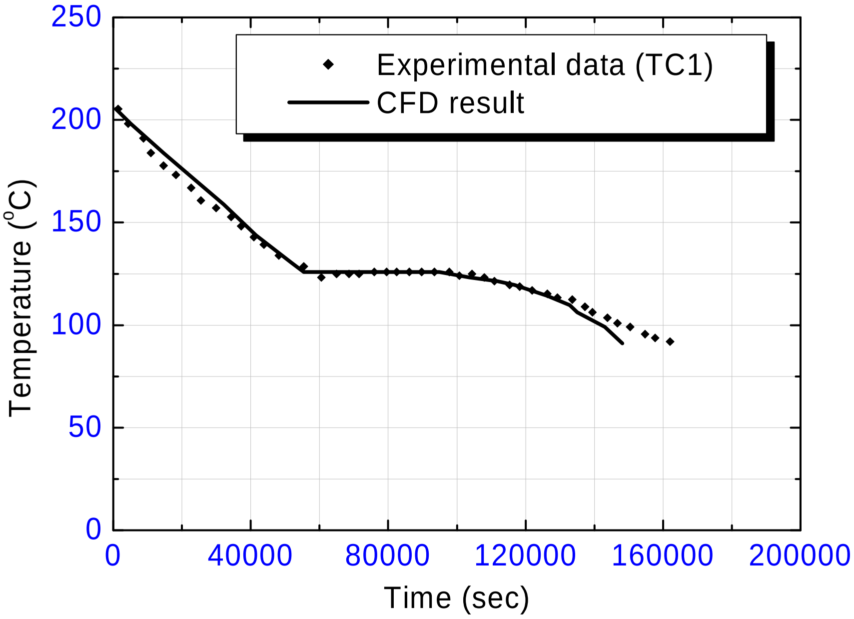

FIG. 6.16. Variation in temperature with time during solidification of LBE.

After the investigations on melting, solidification studies were performed in the same melt tank. Heaters were switched off and LBE was allowed to cool due to the heat loss to the surrounding through natural convection. CFD analysis has also been performed for solidification. Figure 6.16 shows the comparison between experimental data and CFD results. A good agreement was found between the experimental data and CFD results. It was found that about 45 000 s are required before the phase change starts under natural cooling. After solidification, the cooling rate is decreasing due decrease in natural convective heat transfer rate. Figure 6.17 shows contour plots at various time levels. It can be seen that solidification is rapidly progressing from top and side surfaces towards centre. During the solidification process, all the thermocouples follow almost the same trend of temperature. This indicates that the temperature of the whole system is not decreasing until the whole liquid LBE solidifies.

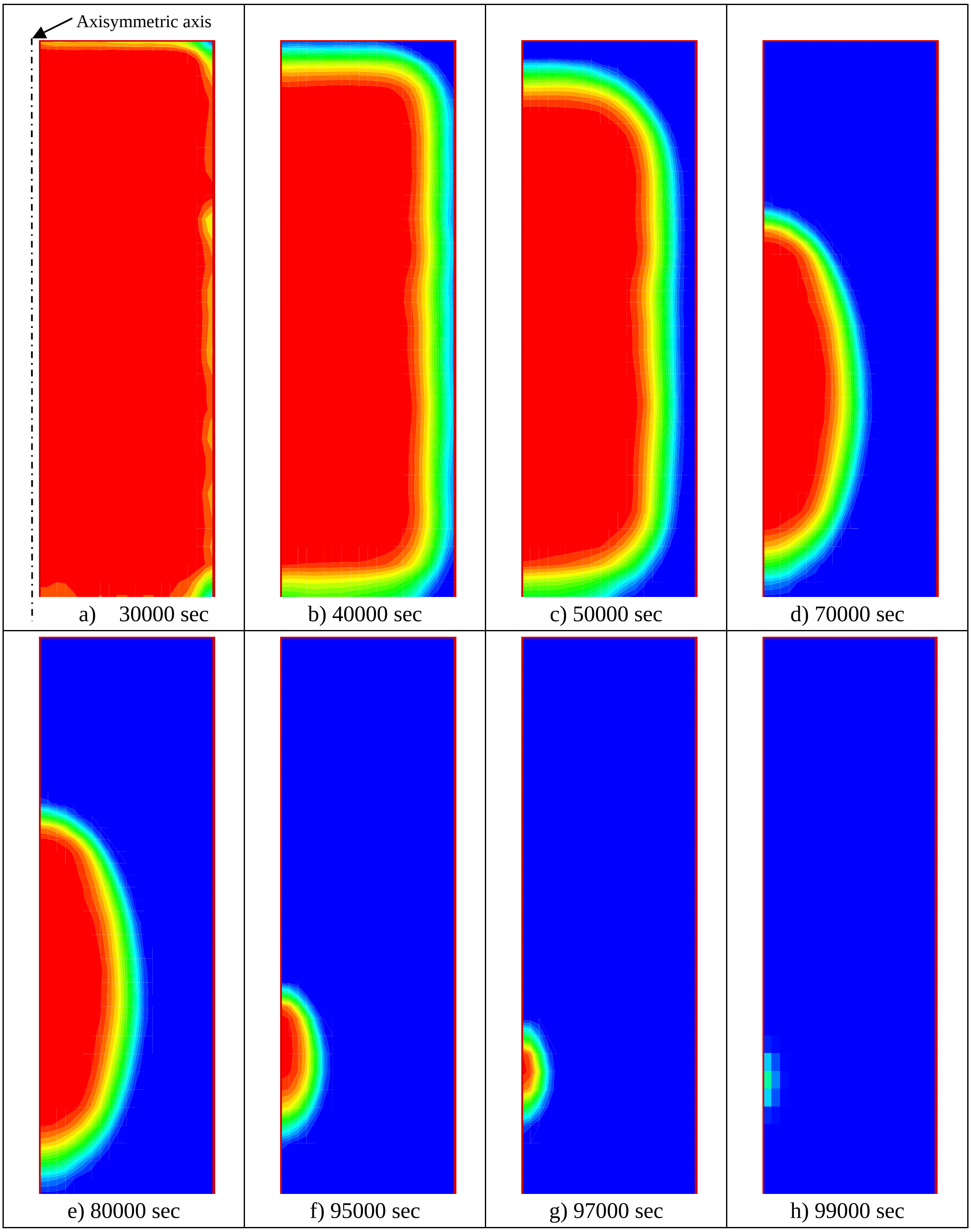

a) 30000 sec

b) 40000 sec

c) 50000 sec

d) 70000 sec

e) 80000 sec

f) 95000 sec

g) 97000 sec

h) 99000 sec

FIG. 6.17. Progression of solidification process under natural cooling.

6.5. REACTOR KINETICS APPLICATIONS IN AN ADS IN BRAZIL

Because fast neutrons have more long mean path length than thermal ones, neutron fluxes are more decoupled in such reactors. Thus, an accelerator driven system, that ultimately is a fast one, usually needs many energy groups in core calculations to capture resonance cross-sections. That is because resonance cross-sections have a strong influence on the effective multiplication factor.

Resonance cross-sections vary with temperature, not only in the fuel region, but also in the coolant one. In this way, two transients are analysed: beam interruption and startup transients. These transients are useful to analyse the feedback effect on power of the accelerator driven systems, since they cover a wide range of temperature variations, be it a beam interruption in power or a startup one, when the ADS are powered up from zero power to power operation.

Beam interruption and startup transients were carried out, taking into account the LBE correlations proposed in the COOL Project (Chapter 2 of this report). The results were compared with those calculated with correlations from a Benchmark of NEA [6.18]. For that, use was made of the SIRER-ADS code, a programme based on a point kinetic model [6.19]. In the code, the fuel temperature, cladding and channel are solved numerically, after space and time discretization. Figure 6.18 shows the temperature distribution. In the following figures, COOL project means that thermal properties and correlations are based on Table 6.2, while NEA means that the thermal properties and correlations are based on Table 6.3.

TABLE 6.2. NEA BENCHMARK 2004 [6.19]

$$\rho_{LBE}(kg/m^3) = 11112 - 1.375T_{TBE}(K)$$

$$k_{LBE}(W/mK) = 3.9021 + 0.0123T_{TBE}(K)$$

$$\mu_{LBE}(Pa\cdot s) = 0.00537 - 8.92\times10^{-6}T_{TBE}(K) + 4.71\times10^{-9}T_{LBE}^2(K)$$

$$c_{LBE}(J/kgK) = 146.5$$

$$Nu = 4.0 + 0.16(P/D)^5 + 0.33(P/D)^{3.8}\left[(P/D)/100\right]^{0.86}$$

TABLE 6.3. COOL PROJECT HANDBOOK OCDE 2007 [6.20]

$$\rho_{LBE}(kg/m^3) = 11096 - 1.3236T_{TBE}(K)$$

$$k_{LBE}(W/mK) = 3.61 + 1.517\times10^{-2}T_{TBE}(K) - 1.741\times10^{-6}T_{LBE}^2(K)$$

$$\mu_{LBE}(Pa\cdot s) = 4.94\times10^{-4}\exp(754.1/T_{TBE}(K)$$

$$c_{LBE}(J/kgK) = 148$$

$$Nu = 7.55(P/D) - 20(P/D)^{-13} + 0.040778(P/D)^{-2}Pe^{[0.56+0.19(P/D)]}$$

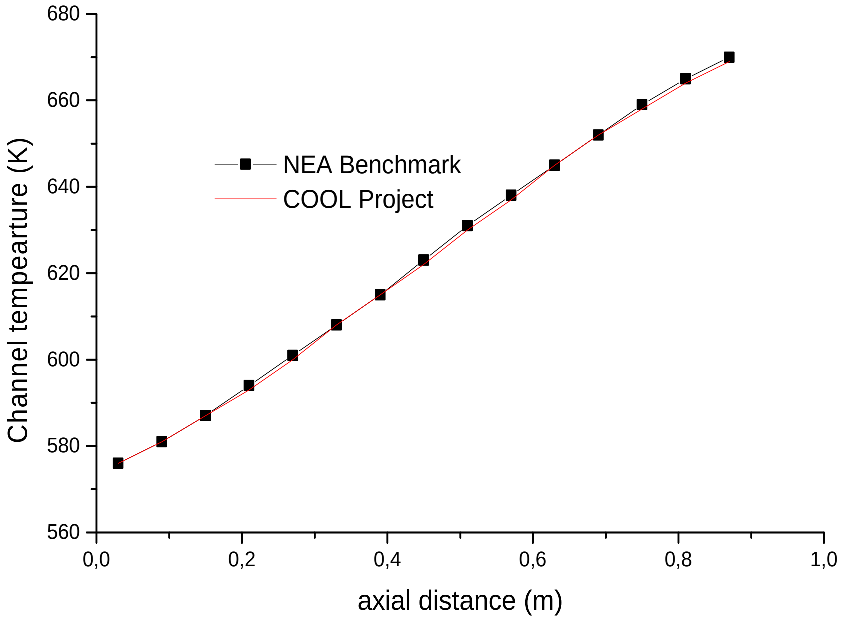

FIG. 6.18. Fuel temperature distribution.

6.5.1. Beam interruption

This transient simulates an interruption of the beam in an ADS, supposedly designed to operate in a continuous mode to generate energy, to burn actinides or to transmute long lived fission products. The beam is interrupted for 1 s from steady state. Figure 6.19 shows the power variation and Fig. 6.20 the temperature at channel exit.

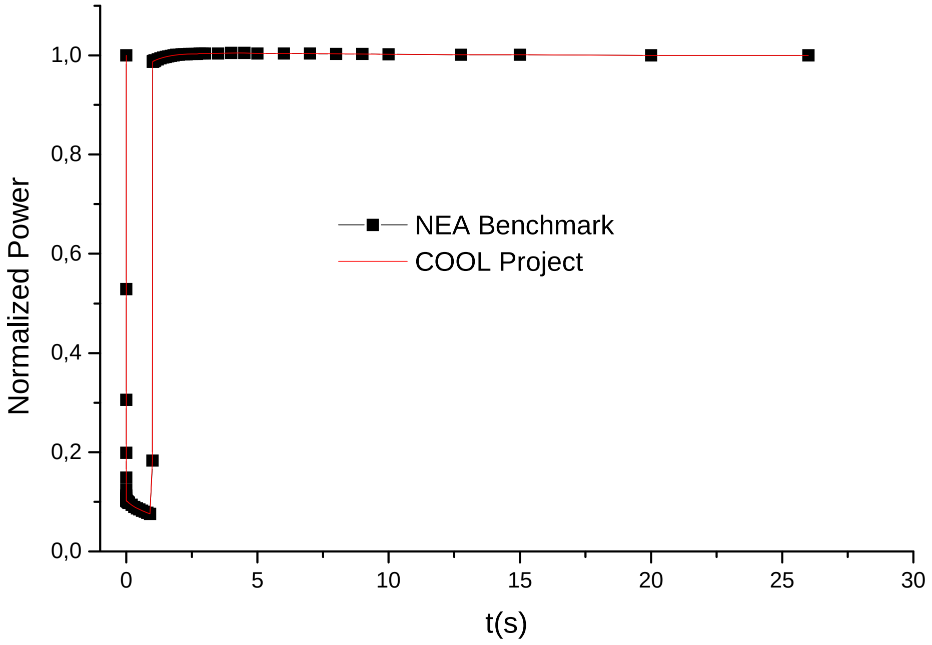

FIG. 6.19. Normalized power during a beam interruption.

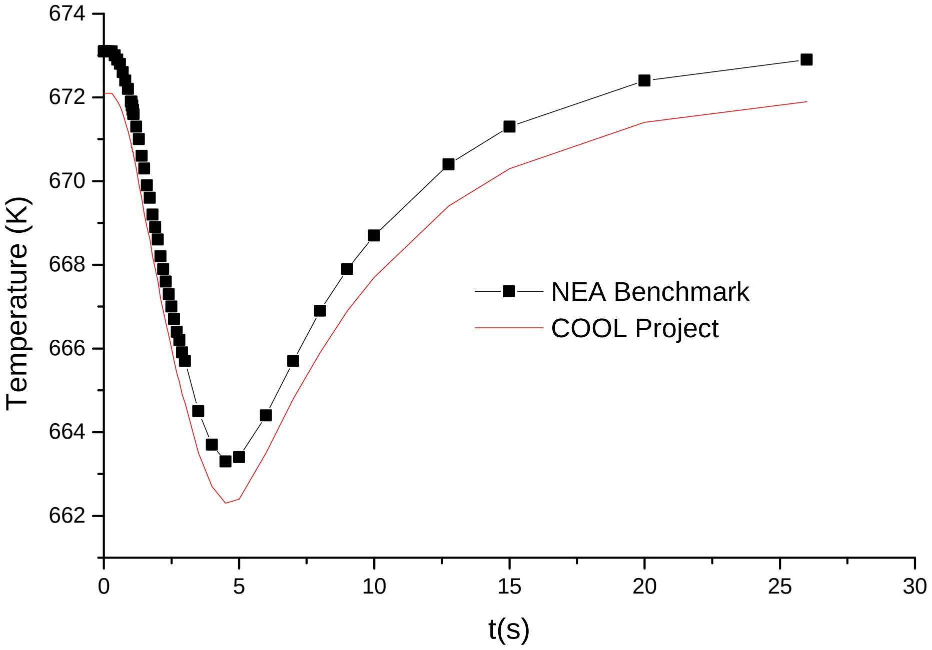

FIG. 6.20. Channel exit temperature for beam interruption.

6.5.2. Startup transient

This transient simulates the power up-rate of an ADS core for 26 s. It covers a long range of variation of the thermal properties. Starting at standby condition, the temperatures increase until nominal power is reached. Figures 6.21 and 6.22 show the pin centre line temperature and the channel exit temperature, respectively.

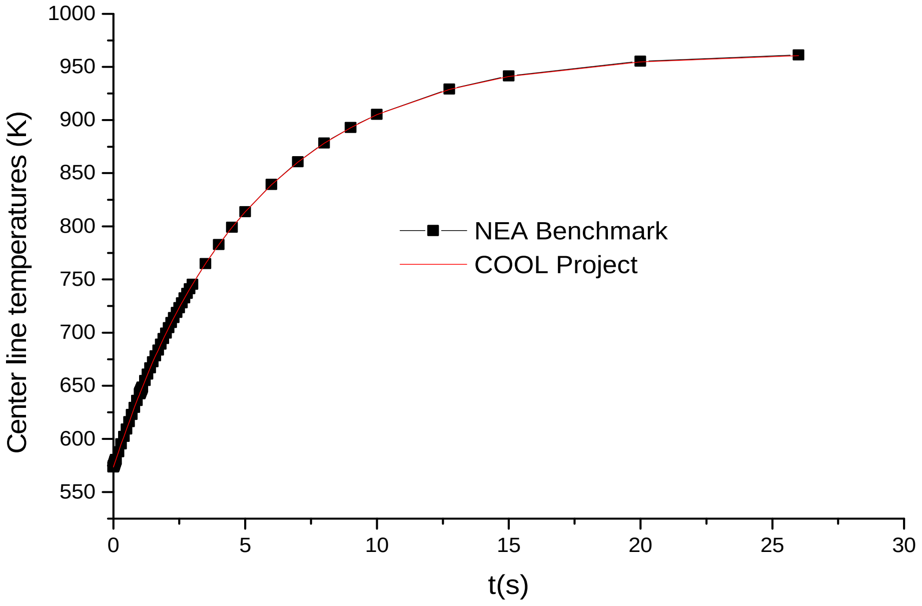

FIG. 6.21. Fuel centre line temperature.

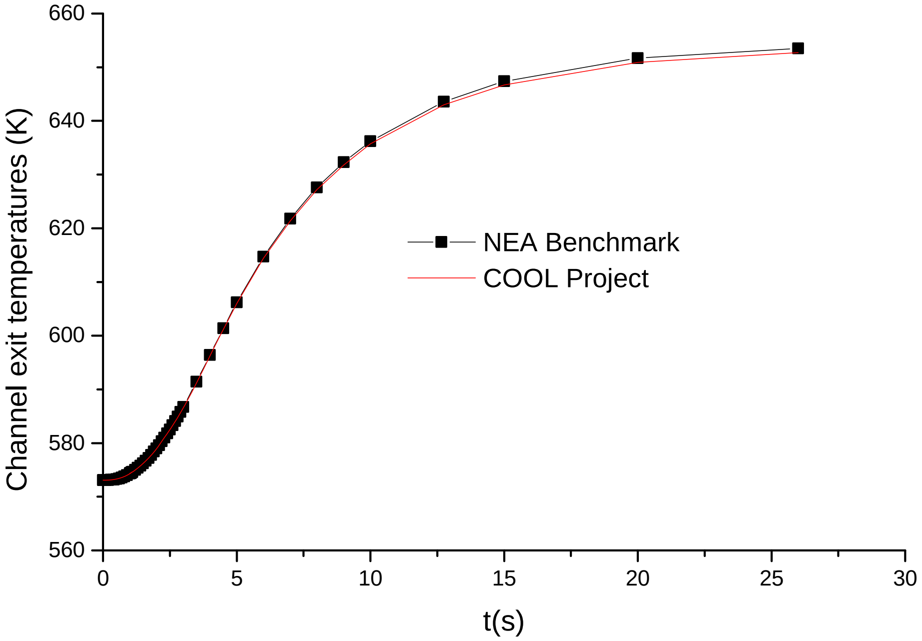

FIG. 6.22. Channel exit temperature.

6.5.3. Comments

The results have shown good concordance between NEA and COOL correlations. In Fig. 6.22, if the end of the transient is enlarged, the difference between NEA and COOL is consistent with the channel temperature behaviour, exhibited in Fig. 6.20, which shows the NEA channel temperature exit is slightly over the COOL result.

6.6. CONCLUSIONS

Different applications of CFD techniques for innovative nuclear reactors using high temperature fluids show promising results and confirm their usefulness for the study of complex phenomena. Nevertheless, experimental data for their validation are needed.

The simplified three dimension numerical model developed in Italy for the study of the open square lattice reactor core shows the possibility to take into account the three dimensional flow effects and therefore to reduce the design safety margins needed in the one dimensional approach. However, this computational model still needs additional and relevant efforts for an accurate evaluation of the turbulence and mixing energy exchange terms which can only be confirmed with an extended future experimental campaign.

The CFD porous media code developed in China for the simulation of the wire-wrapped subassembly of the CEFR reactor has showed results in good agreement with the experimental data for the CEFR 61-pin test.

In India, solidification and melting studies of LBE are carried out using the CFD code Anupravaha. In this code, the phase change problem is solved using an enthalpy-porosity model. Melting studies show that natural circulation plays an important role in heat transfer.

List of abbreviations and symbols to Chapter 6

f_{s1}	friction factor
L	flow length
D_{e1}	diameter of the rod
V	velocity of the flow
C_1, C_2	non-dimensional value, determined by the experiment
A_{r1}	wire wrap projection area in a helix distance in Channel 1
A_1	flow area without wire wrap in Channel 1
H	distance of the helix
p	pin pitch
ε	roughness in a pipe
γ	volume porosity
H	enthalpy of the fluid

REFERENCES TO CHAPTER 6

[6.1] EURATOM, ELSY Work Program, European Lead-cooled System (ELSY) Project, Technical report, Management of Radioactive Waste (2006).

[6.2] UNITED STATES DEPARTMENT OF ENERGY, Nuclear Energy Research Advisory Committee and the Generation IV International Forum, A Technology Roadmap for Generation IV Nuclear Energy Systems, Technical Report GIF-002-00 (2002).

[6.3] SLOAN, S.M., SCHULTZ, R.R., WILSON, G.E., RELAP5/MOD3 code manual, Tech. Rep. NUREG/CR-5535, INEL-95/0174, NRC, Washington, DC, (1995).

[6.4] KIRILLOV, P.L., USHAKOV, P.A., Heat transfer to liquid metals: specific features, methods of investigation, and main relationships, Thermal Eng. **48** 1 (1993) 50–59.

[6.5] KIRILLOV, P.L., Experience in operating reactors indicates the need for new thermohydraulic studies, At. Tekh. Rubezh. **9** (2003) 3–9.

[6.6] YUDOV, Y.V., VOLKOVA, S.N., MIGROV, Y.A., Closure relations for thermohydraulic model of the KORSAR computer code, Teploénergetika **11**, (2002) 22–29.

[6.7] GIRAULT, V., RAVIART, P., The Finite Element Method for Navier-Stokes Equations: Theory and Algorithms, Springer, New York (1986).

[6.8] BRAMBLE, J.H., Multigrid method, Pitman Research Notes in Math, Longman, London, Vol. 294 (1993).

[6.9] MELONI, P., BANDINI, G., POLIDORI, M., MANSERVISI, S., CERVONE, A., A two-step approach for the preliminary evaluation of the thermal-hydraulics and safety of the ELSY open square core design, NURETH-13, Kanazawa, Japan, September 27 October 2 (2009).

[6.10] CHIU, C., ROHSENOW, W.M., TODREAS, N.E., Flow split model for LMFBR wire wrapped assemblies, COO-2245-56TR, MIT, Cambridge, 1978.

[6.11] VOLLER, V.R., PRAKASH, C., A fixed grid numerical modeling methodology for convection diffusion mushy region phase change problems, Int. J. Heat Mass Tran. **30** 8 (1987) 1709–1719.

[6.12] BRENT, A.D., VOLLER, V.R., REID, K.J., Enthalpy porosity technique for modeling convection diffusion phase change: application to the melting of a pure metal, Numer. Heat Transfer **13** (1988) 297–318.

[6.13] VOLLER, V.R., SWAMINATHAN, C.R., Generalized source based method for solidification phase change, Numer. Heat Transfer B **19** 2 (1991) 175–189.

[6.14] SANYAL, D., GOYAL, P., VERMA, V., CHAKRABORTY, A., A CFD analysis of thermal behaviour of transportation cask under fire test conditions, Nucl. Eng. Des. **241** 8 (2011) 3178–3189.

[6.15] DUAN, Q., TAN, F.L., LEONG, K.C., A numerical study of solidification of n-hexadecane based on the enthalpy formulation, J. Mater. Process. Tech. **120** (2002) 249–258.

[6.16] QUILLET, G., CIOBANAS, A., LEHMANN, P., FAUTRELLE, Y., A benchmark solidification experiment on a Sn–10 wt% Bi alloy, Int. J. Heat Mass Tran. **50** (2006) 654–666.

[6.17] BORGOHAIN, A., et al., Natural circulation studies in a lead bismuth eutectic loop, Prog. Nucl. Energy **53** (2011) 308–319.

[6.18] OECD NUCLEAR ENERGY AGENCY, Benchmark on Beam Interruptions in an Accelerator-driven System: Final Report on Phase II Calculations, NEA No. 5422 (2004). http://www.nea.fr/html/science/docs/2004/nsc-doc2004-7.pdf

[6.19] SANTOS, R.S., MAIORINO, J.R., On the application of SIRER-ADS in the simulation of transients in Accelerator Driven System (ADS), International Nuclear Atlantic Conference — INAC2007, Santos, SP, Brazil (2007).

[6.20] OECD NUCLEAR ENERGY AGENCY, Handbook on Lead-Bismuth Eutectic Alloy and Lead Properties Material Compatibility, Thermal-hydraulics and Technologies, OECD/NEA Nuclear Science Committee, NEA No. 6195 (2007). http://www.oecd-nea.org/science/reports/2007/pdf/

CHAPTER 7. EXPERIMENTAL AND ANALYTICAL THERMOHYDRAULIC STUDIES

7.1. INTRODUCTION

The high boiling point of heavy liquid metal (lead-bismuth eutectic (LBE) and lead (Pb)) ensures that the coolant can be operated at high temperatures without the risk of coolant boiling, which improves the thermal efficiency. It also improves the plant safety by reducing the risk of leakage at high temperatures as pressurization is not required. Heavy liquid metal does not react readily with air or water and, thus, an intermediate coolant is not essential in the reactor. Many reactor designs based on heavy liquid metal as coolant have been envisaged by various countries for high temperature process heat applications such as hydrogen production by thermochemical processes. Heavy liquid metal systems are also excellent choices as spallation targets for accelerator driven systems (ADS) [7.1]. Scientific and technological activities focused on materials compatibility, thermal fluid dynamics characterization and technology issues have been performed by many researchers. Efforts have been made to build and operate heavy liquid metal (HLM) test facilities in support to the previously mentioned applications. This chapter mainly describes the tests facilities built by BARC and ENEA and thermal hydraulic experiments conducted.

7.2. LITERATURE REVIEW

Takahashi et al. [7.2] performed Pb-Bi single phase natural circulation studies in a test facility made for the development of 45w% Pb-55w% Bi cooled direct contact boiling water small fast reactor (PBWFR). They emphasized that for stable startup of the boiling flow operation, Pb-Bi single phase natural circulation must be realized in a Pb-Bi flow system of the loop before water injection into Pb-Bi. The test facility was designed for maximum power 133.2 kW and 7 MPa pressure. The natural circulation flow was simulated analytically using one dimensional flow model.

Ma et al. [7.3] carried out experimental studies in the TALL facility with forced flow and natural circulation of LBE for ADS systems. TALL is an experimental facility constructed at KTH, to study the steady state and transient thermohydraulics performance of LBE cooled reactors, with the primary purpose of supporting the European Transmutation Demonstration (ETD) programme using LBE cooled accelerator driven systems (ADS). The transient experiments performed include the loss of heat sink, the loss of pump, the loss of both primary and secondary flows, overpower, overcooling, heater trip, and the operational transients of startup and shutdown. The numerical results from RELAP5 and TRAC/AAA analyses were compared with the experimental results by Ma et al. [7.3, 7.4].

Lee et al. [7.5] described a large scale test loop HELIOS (Heavy Eutectic Loop Integrated Operability and Safety) to support the PEACER (Proliferation resistant, Environmental friendly, Accident tolerant, Continual energy, Economical reactor) analysis results for thermohydraulic and corrosive behaviour of Pb-Bi.

Tarantino et al. [7.6] carried out steady state pretest analysis of an LBE loop, NACIE. The objective of the NACIE loop facility is to carry out experimental tests needed to characterize the natural and gas enhanced circulation flow regimes, and to qualify components for HLM applications, especially in support of the ICE (Integral Circulation Experiment) activities. They performed steady state one dimensional analytical as well as three dimensional CFD studies and compared the results.

Coccoluto et al. [7.7] reported a detailed description of the NACIE loop and the main experimental results obtained from the natural circulation tests performed. They performed post-test calculations in collaboration with the University of Pisa, adopting the RELAP5/Mod 3.3 system code modified to allow for LBE as a cooling fluid.

Cho et al. [7.8] performed experiments on direct-contact heat exchange between molten metal and water for steam production. These experiments involved the injection of water into molten lead-bismuth eutectic for heat transfer measurements in one dimensional geometry. They discussed the results of the effects of the water flow rate and the molten metal superheat on the volumetric heat transfer coefficient.

Takahashi et al. [7.9] carried out experimental studies in LBE-water two-phase loop discussed above. The Pb-Bi and steam flows were simulated analytically using one dimensional models of frictional and form losses and a drag force.

Satyamurthy et al. [7.10] performed tests in a mercury facility to study two-phase nitrogen and mercury flows at ambient temperature. The flow circulation was achieved by creating two-phase flow in the riser. The mercury facility was set up for gas driven circulating spallation targets and reactor coolants based on high density molten liquid metals like lead and LBE. Both single beam and 7- beam gamma ray systems have been used for void fraction measurement based on high energy gamma rays.

Benamati et al. [7.11] described the results of an experimental campaign concerning the possibility of achieving a steady state circulation by gas injection in a pool containing LBE as working fluid. They performed experiments in the CIRCE large scale facility, installed at the ENEA Brasimone Centre for studying the fluid dynamic and operating behaviour of ADS reactor plants cooled by LBE. A characteristic curve was generated for the system and the void fraction distribution along the riser path by means of differential pressure measurements was evaluated.

Also, analytical studies are carried out for LBE cooled reactor systems. Wu and Sienichi [7.12] carried out a one dimensional linear stability analysis for a uniform diameter rectangular natural circulation LBE loop. It was found that single phase LBE could be unstable in a high Reynolds number region and any increase in loop friction makes the forward circulation more stable.

A 2-D MASKA-LM computer code was developed for numerical calculations of lead coolant flows, temperatures and transport of impurities in integral system of BREST-type reactors (Kumayev et al. [7.13]). Heat and mass transfer in liquid metal systems were modelled, for the coupled simulation of thermohydraulic, physical and chemical processes in the real configuration of the reactor circuit.

Abanadesa and Pena [7.14] carried out natural circulation studies in a 2-D axisymmetric geometry of a LBE cooled ADS design, using a CFD code. It was found from the analysis that the ADS design based on lead-bismuth eutectic natural convection cooling will operate safely, even if the gas injection mechanism to enhance fluid motion fails.

Cheng et al. [7.1] carried out dynamic behaviour analysis of an accelerator driven test facility using SAS-4A, a code developed by Idaho National Laboratory. Five different systems with different types of fuel and different types of coolant (LBE and sodium) were evaluated. Analysis for various transient scenarios was carried out.

Davis [7.15] evaluated a pool type LBE cooled reactor design that relies on forced circulation of the primary coolant, a conventional steam power conversion system and a passive decay heat removal system. The ATHENA computer code was used to simulate transients during various postulated accidents.

Lee and Suh [7.16] carried out natural circulation studies on lead bismuth cooled PEACER-300 and PEACER-550 (proliferation resistant, environmentfriendly, accidenttolerant, continually energy, economical reactor). The capabilities of the heat removal by natural circulation of LBE were estimated.

7.3. THERMOHYDRAULIC STUDIES CARRIED OUT IN BARC

Natural circulation studies have been carried out by Bhabha Atomic Research Centre (BARC) in a heavy liquid metal loop HANS (Heavy metal Alloy Natural circulation Study loop). The purpose of the studies is to assess natural circulation of lead-bismuth eutectic coolant and other associated phenomena for the Compact High Temperature Reactor (CHTR), which is being designed in BARC and is also cooled by LBE natural circulation (Dulera and Sinha, [7.17]). The following sections describe the test facility, steady state and transient experiments performed, and a comparison of theoretical results with experimental results.

7.3.1. Lead-bismuth test loop, HANS

The LBE test loop mainly consists of a heated section, air heat exchanger, valves, various tanks and an argon gas control system (Fig. 7.1). All the components and piping are made of SS316L. The LBE ingots are melted in a melt tank and then transferred to the sump tank. The LBE coolant in the sump tank is then pressurized by the argon gas system. Due to pressurization, molten LBE flows into the loop and subsequently fills up the loop. After filling, the loop is isolated from the sump tank by a valve. Natural circulation of the coolant takes place in the loop due to heating of the coolant in the heated section and cooling in the heat exchanger. Air is used as the secondary side coolant in the heat exchanger. After losing heat in the heat exchanger, LBE enters the heated section through a 15 mm Nominal Bore (NB) pipeline. During the operation of the loop, high purity argon (Ar) gas was used as cover gas in the vessels. Electrochemical oxygen sensor is used for monitoring the oxygen level in the lead-bismuth eutectic. Intermittently, argon plus hydrogen gas is used to maintain the chemistry of the LBE coolant in the loop.

All the vessels and piping of the loop are equipped with band heaters respectively with trace heaters. The loop is provided with adequate thermal insulation in order to reduce heat loss to the environment. In the main heated section of the loop, heat is generated by electrical heaters and transferred to the liquid metal coolant as sensible heat. It mainly consists of ‘U’ shaped mineral insulated immersion type heater elements mounted on a stainless steel flange. The expansion and contraction in the liquid metal due to heating and cooling is accommodated with the help of an expansion tank which was partially filled with molten LBE. It is located between the heated section and the heat exchanger. The cover gas provided over the surface of the LBE in the expansion tank acts as a cushion. The cover gas pressure was maintained with the help of a regulating valve provided in the cover gas system.

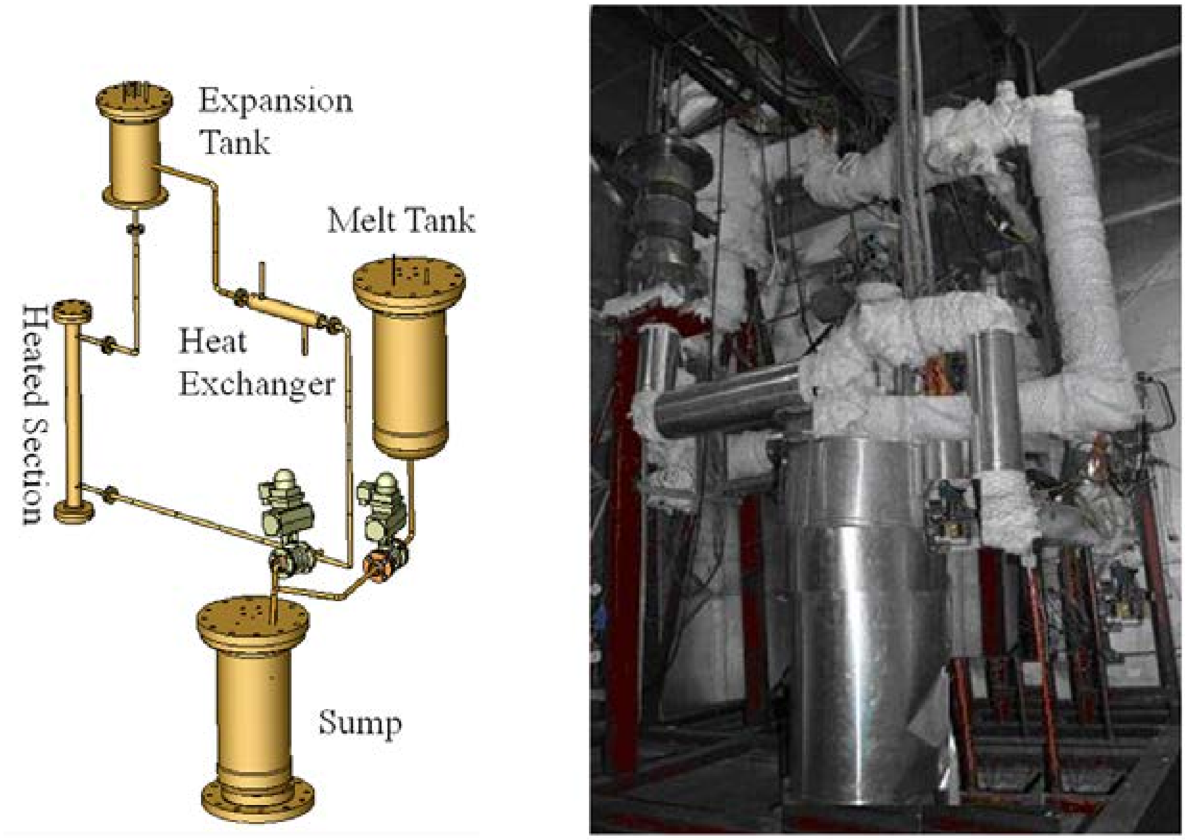

FIG. 7.1. 3-D view of the main loop and photo of heavy liquid metal loop, HANS.

The instrumentation and control of the LBE loop was realized by means of a Programmable Logic Controller (PLC) based Data Acquisition and Control System (DACS). Monitoring of various parameters like pressure, temperature, levels in different components of the loop, valve positions, etc. is done through DACS. Different sensors of the loop provide inputs to the DACS. All operational and safety conditions are built into the programme. Levels in the tanks, temperatures in the loop, cover gas pressure, flow and other parameters are measured. Warnings, alarms and automatic trips are incorporated into the programme for safe operation of the loop. The instrumentation of the loop was designed to control the loop parameters in the event of postulated accidents. High temperature pneumatically operated Control Valves (CV) and Pressure Regulating Valves (PRV) are used for the control and operation of the loop. Besides these, pressure relief valves are used to relieve argon gas in case of high system pressure. Non-return valves are used to prevent ingress of liquid metal into the impulse lines from the main loop, during any event. All the valves are made of SS316L and are PLC controlled.

High temperature pressure transmitters are used to measure the fluid pressure and gas pressure in the main loop. Fifty-six ungrounded K-type, SS (Stainless Steel) sheathed thermocouples are installed in the loop. Most of the thermocouples are installed on the surface and some are inserted into the piping and vessels through special fittings. Thermocouple readings are to be read through analogue input modules of the PLC. Since the LBE level measurement was a very important requirement of the loop, two types of level sensors are used: discrete type and continuous type. The discrete type is based on electrical conduction principle, where the electrical circuit is closed when the liquid LBE surface touches a metallic rod hanging from the top flange of expansion tank. The continuous type is based on gas bubbling technique. Here, inert gas is bubbled by injecting via a SS tube into the liquid. While measuring the differential gas pressure between the bubble tube and the cover gas in the tank, the level of

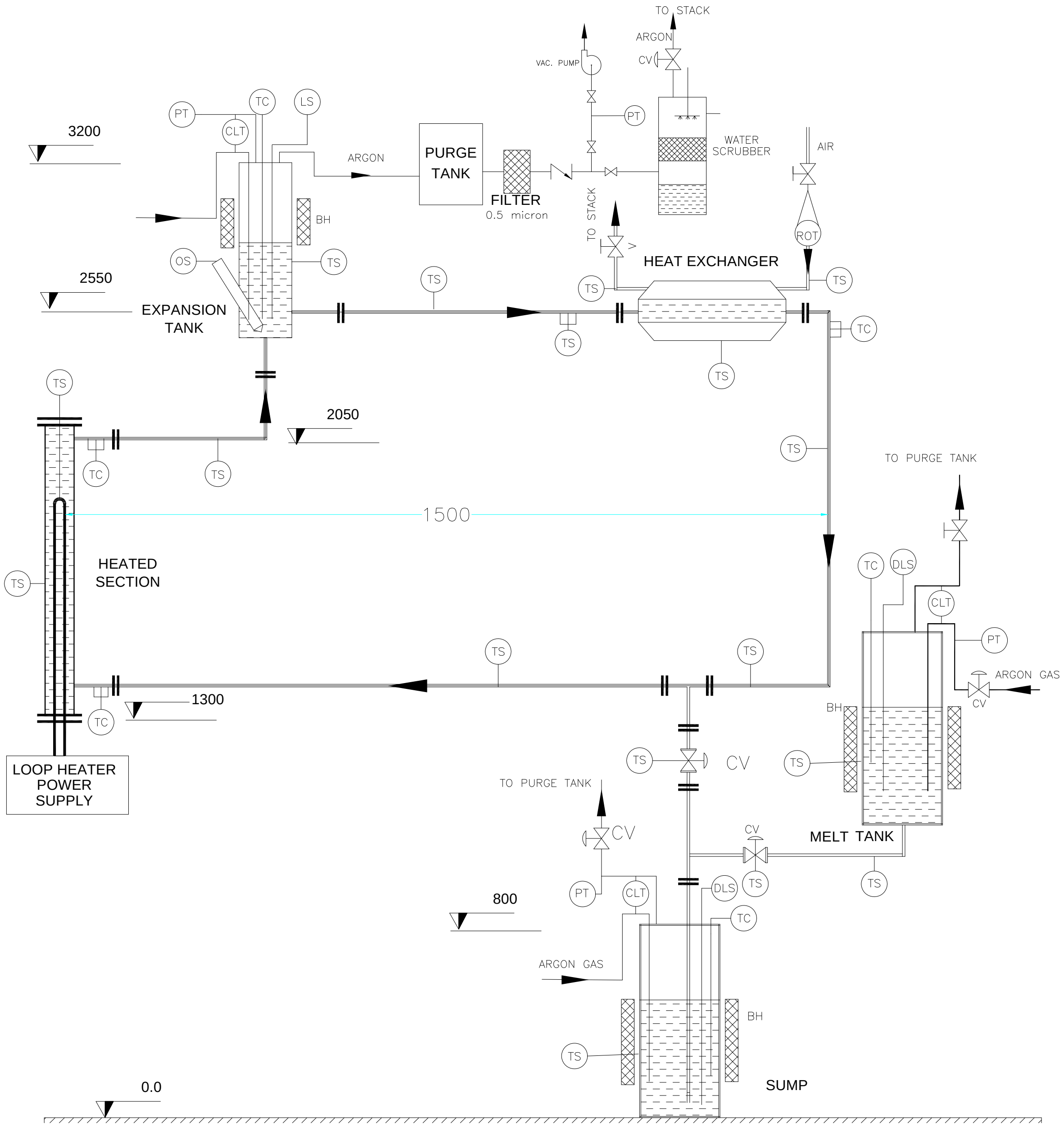

BH: Band heater

CLT: Continuous level transducer

CV: Control valve

DLS: Discrete level switch

OS: Oxygen sensor

PT: Pressure transducer

TC: Temperature sensor in coolant

TS: Temperature sensor on the piping surface

FIG. 7.2. Flow sheet of lead bismuth loop facility.

LBE can be recorded continuously. Figure 7.2 shows the flow diagram of the loop with the cover gas system. Table 7.1 gives detailed specifications of the loop.

TABLE 7.1. DESIGN PARAMETERS OF THE LOOP

Sl. No.	Parameters	Values
1.	Fluid used	Lead-bismuth eutectic
2.	Fluid circulation mode	Natural circulation
3.	Line size	15 mm NB(1/2”) Sch 80
4.	Centre line elevation difference between heat exchanger and heated section	750 mm
5.	Total circulation length	5500 mm
6.	Loop material	SS 316L
7.	Design pressure of the loop	5 bar
8.	Coolant inventory	500 kg
9.	Maximum main heater power during experiments	2.5 kW
10.	Maximum operating temperature	500°C
11.	LBE mass flow rate	0.09–0.15 kg/s

7.3.2. Numerical code, LeBENC

A code named TRANCO, (Vijayan et al. [7.18]) was available to study steady state and stability (transient) behaviour of natural circulation rectangular loops of uniform diameter for various orientations of heated section and heat exchanger. This code has been modified to predict the behaviour of liquid metal loop under natural circulation. The major modifications include extension of code applicability to: (a) handle non-uniform diameter loops, (b) different working fluid in primary and secondary side of the loop, (c) handle trace heating and surface heat loss from the walls to ambient and (d) axial conduction through liquid metal and the pipe wall. These modifications led to a computer code, LeBENC (Lead Bismuth Eutectic Natural Circulation). LeBENC is a one dimensional finite difference code, developed to study the steady state and transient behaviour of liquid metal natural circulation loop. The code is validated with single phase water loop natural circulation data (Jaiswal et al. [7.19]).

7.3.2.1. Mathematical formulation of LeBENC code

This section provides an overview of the theoretical formulation and solution procedure used in the code LeBENC. The one dimensional governing equations are discussed below. Wall and fluid axial conduction are considered in the energy equation as it might play an important role in LBE loop. From the 1-D continuity equation for incompressible fluid we obtain that the mass flow rate is independent of the locations in the loop and is only a function of time.

7.3.2.2. Momentum equation for fluid

Assuming Boussinesq approximation to be valid, the momentum equation, for 1-D incompressible flow neglecting viscous dissipation, for 'ith' pipe section can be written as:

$$\frac{\Delta x_i}{A_{in}}\frac{dW}{dt} = \rho g \Delta z_i - \frac{f_i \Delta x_i}{D_{in.i}}\left(\frac{W}{2\rho_0 A_{in,i}{}^2}\right) - k_i\left(\frac{W^2}{2\rho_0 A_{in,i}{}^2}\right) - \Delta p_i - \Delta p_{acc,i} \tag{7.1}$$

In the buoyancy term, the density ρ is given by the following equation which is valid over small temperature ranges:

$$\rho = \rho_0\left[1-\beta(T-T_0)\right] \tag{7.2}$$

The summation of acceleration pressure drop and static pressure drop in a closed loop becomes zero. Therefore, Eq. (7.1) can be written as:

$$\sum_i \frac{\Delta x_i}{A_i}\frac{dW}{dt} = \rho_0 g\beta\sum_{i=1}^{N} T_i \Delta z_i - \sum_{i=1}^{N}\frac{f_i \Delta x_i}{D_i}\left(\frac{W^2}{2\rho_0 A_i^2}\right) - \sum_{i=1}^{N} k_i\left(\frac{W^2}{2\rho_0 A_i^2}\right) \tag{7.3}$$

7.3.2.3. Energy equation for fluid

$$\frac{\partial T}{\partial t} - \alpha\frac{\partial^2 T}{\partial x^2} + \frac{W}{A\rho_0}\left(\frac{\partial T}{\partial x}\right) = \begin{cases} \dfrac{-4h_{in}(T-T_w)}{\rho_0 D\ Cp} + \dfrac{\mathrm{qA_h}}{\rho \mathrm{C_p} A_f} & \text{heated section} \\[2ex] \dfrac{-4h_{in}(T-T_w)}{\rho_0 D\ Cp} & \text{pipe and heat exchanger} \end{cases} \tag{7.4}$$

It can be noted that the second term of the right hand side of the equation is for the heat source (immersion heater) in the heated section of the loop.

7.3.2.4. Conduction equation for the wall

Heat loss from the pipe wall is considered in writing conduction equation for the pipe wall:

$$\frac{\partial T_w}{\partial t} - \alpha_w\frac{\partial^2 T_w}{\partial x^2} = -\frac{4h_i(T_w - T_i)}{\rho_w C_{p_w}}\left(\frac{D_i}{(D_0{}^2 - D_i^2)}\right) - \frac{4h_0(T_w - T_o)}{\rho_w C_{p_w}}\left(\frac{D_i}{(D_0{}^2 - D_i^2)}\right) \tag{7.5}$$

where

for cold leg and hot leg piping, $T_o = T_a$ and $h_o = h_a$,

for heat exchanger, $T_o = T_s$ and $h_o = h_s$,

for heater, $T_o = T_a$ and $h_o = h_a$ are specified.

7.3.3. Discretization of the governing equations

Out of several possible ways to discretize the governing equations, the implicit method for discretizing the momentum equation and the explicit method for discretizing energy equation for fluid as well as conduction equation for wall are used.

7.3.3.1. Discretization of momentum equation

The implicit scheme for discretizing momentum equation is used as shown below:

$$\sum_{i=1}^{N}\frac{\Delta x_i}{A_{in,i}}\frac{W^{n+1}-W^{n}}{\Delta t} = \rho_0 g\beta\sum_{i=1}^{N}T_i^{n+1}\Delta z_i - \sum_{i=1}^{N}\left(\frac{f_i\Delta x_i}{D_{in,i}}+k_i\right)\left(\frac{W^{{n+1}^2}}{2\rho_0 A_{in,i}^{2}}\right) \tag{7.6}$$

Temperature integral $\sum_{i=1}^{N}T_i^{n+1}\Delta z_i$ in the above equation is evaluated by using the Trapezoidal rule. Eq. (7.6) can be written after simplification as:

$$W^{n+1} = W^{n} - \left(\frac{C_2}{C_1}\Delta t\right)W^{n+1}\left|W^{n+1}\right| + \left(\frac{C_3}{C_1}\Delta t\right)\sum_{i=1}^{N}T_i^{n+1}\Delta z_i \tag{7.7}$$

where C_1, C_2 and C_3 are given by:

$$\left.\begin{aligned} C_1 &= \sum_{i=1}^{N}\frac{\Delta x_i}{A_{in,i}} \\ C_2 &= \sum_{i=1}^{N}\left(\frac{f_i\Delta x_i}{D_{in}}+k_i\right)\left(\frac{1}{2\rho_0 A_{in}^{2}}\right) \\ C_3 &= \rho_0 g\beta \end{aligned}\right\} \tag{7.8}$$

For solving the momentum equation, T_i^{n+1} is taken from the energy equation.

7.3.3.2. Discretization of energy equation

For the energy equation, first order explicit upwind scheme and central difference scheme is used to discretize the convective term and the diffusion term respectively. The discretized energy balance equation for 'i^{th}' node of the fluid can be written as follows:

$$\left(\frac{T_i^{n+1}-T_i^{n}}{\Delta t}\right) = \alpha\left(\frac{T_{i+1}^{n}-2T_i^{n}+T_{i-1}^{n}}{\Delta x_i^{2}}\right) - \frac{W}{\rho_0 A_{in,i}}\left(\frac{T_i^{n}-T_{i-1}^{n}}{\Delta x_i}\right) - \frac{4h_{in,i}}{D_{in,i}\rho_0 Cp}(T_i^{n}-T_{w,i}^{n+1}) + \frac{\mathrm{qA_{h,i}}}{\rho \mathrm{C_p} A_{f,i}} \tag{7.9}$$

After some algebraic manipulations, the above equation can be written as:

$$T_i^{n+1} = a_{i+1}^{n}T_{i+1}^{n} + a_i^{n}T_i^{n} + a_{i-1}^{n}T_{i-1}^{n} + b_i^{n+1} \tag{7.10}$$

The values of coefficients in Eq. (7.10) are given in Table 7.2.

Again, the coefficients of T_i^{n+1}, T_{i-1}^{n} and T_{i+1}^{n} are all positive but that of T_i^{n} may be negative. Therefore, the limiting time step to keep the coefficient positive is expressed as:

for *W>0*

$$\Delta t = \frac{1}{\left(\frac{2\alpha}{\Delta x_i^2} + \frac{W^n}{\rho_0 A_{in,i} \Delta x_i} + \frac{4h_{in.i}}{\rho_0 Cp D_{in,i}} \right)} \tag{7.11}$$

for W<0

$$\Delta t = \frac{1}{\left(\frac{2\alpha}{\Delta x_i^2} - \frac{W^n}{\rho_0 A_{in,i} \Delta x_i} + \frac{4h_{in,i}}{\rho_0 Cp D_{in,i}} \right)} \tag{7.12}$$

It is to be noted that the time step is a function of mass flow rate. Therefore, the time step is to be recalculated for each new time level.

7.3.3.3. Discretization of conduction equation for the wall

Discretized energy balance equation for 'i^{th}' node of wall can be written as:

$$\left(\frac{T_{w,i}^{n+1} - T_{w,i}^{n}}{\Delta t} \right) = \alpha_w \frac{(T_{w,i+1}^{n} - 2T_{w,i}^{n} + T_{w,i-1}^{n})}{\Delta x_i^2} - \frac{4h_{in,i}(T_{w,i}^{n} - T_i^{n})}{\rho_w Cp_w} \left(\frac{D_{in,i}}{D_{o,i}^2 - D_{in,i}^2} \right) - \frac{4h_o(T_{w,i}^{n} - T_o^{n})}{\rho_w Cp_w} \left(\frac{D_{in,i}}{D_{o,i}^2 - D_{in,i}^2} \right) \tag{7.13}$$

After some algebraic simplifications, Eq. (7.13) can be written as:

$$T_{w,i}^{n+1} = a_{w,i+1}^{n} T_{w,i+1}^{n} + a_{w,i}^{n} T_{w,i}^{n} + a_{w,i-1}^{n} T_{w,i-1}^{n} + b_{w,i}^{n} \tag{7.14}$$

The values of coefficients in Eq. (7.14) are given in Table 7.2.

The coefficients of $T_{w,i}^{n+1}, T_{w,i-1}^{n}$ and $T_{w,i+1}^{n}$ are all positive but that of $T_{w,i}^{n}$ may be negative. Therefore, the limiting time step to keep the coefficient positive is expressed as:

$$\Delta t = \left(2\frac{\alpha_w}{\Delta s_i^2} + \frac{4h_{in,i}}{\rho_w Cp_w} \frac{D_{in,i}}{(D_{o,i}^2 - D_{in,i}^2)} + \frac{4h_o}{\rho_w Cp_w} \frac{D_{in,i}}{(D_{o,i}^2 - D_{in,i}^2)} \right)^{-1} \tag{7.15}$$

The minimum of the time steps, as calculated by Eqs (7.11, 7.12 and 7.15), is taken for calculation in each time level.

TABLE 7.2. VALUES OF THE COEFFICIENTS IN EQS (7.10, 7.14)

Coefficients	Energy Equation [Eq. (7.10)]		Wall conduction Equation [Eq. (7.14)]
	W > 0	W < 0	
a_{i+1}^n , $a_{w,i+1}^n$ *	Fo_i^n	$Fo_i^n - Co_i^n$	$Fo_{w,i}^n$
a_i^n , $a_{w,i}^n$ *	$1-2Fo_i^n - Co_i^n - \frac{4h_{in,i}\Delta t}{\rho_0 CpD_{in,i}} + \frac{\mathrm{qA_h}}{\rho \mathrm{C_p} A_f}$	$\left(1-2Fo_i^n + Co_i^n - \frac{4h_{in,i}\Delta t}{\rho_0 CpD_{in,i}} + \frac{\mathrm{qA_h}}{\rho \mathrm{C_p} A_f}\right)$	$\left\{1-2Fo_{w,i}^n - \frac{4h_{in,i}}{\rho_w Cp_w}\frac{D_{in,i}\Delta t}{(D_{o,i}^2 - D_{in,i}^2)} - \frac{4h_o}{\rho_w Cp_w}\frac{D_{in,i}\Delta t}{(D_{o,i}^2 - D_{in,i}^2)}\right\}$
a_{i-1}^n , $a_{w,i-1}^n$ *	$Fo_i^n + Co_i^n$	Fo_i^n	$Fo_{w,i}^n$
b_i^n , $b_{w,i}^{n+1}$ *	$\frac{4h_{in,i}\Delta t T_{w,i+1}^{n+1}}{\rho_0 CpD_{in,i}} - \frac{\mathrm{qA_h}}{\rho \mathrm{C_p} A_f}$	$\frac{4h_{in,i}\Delta t T_{w,i+1}^{n}}{\rho_0 CpD_{in,i}} - \frac{\mathrm{qA_h}}{\rho \mathrm{C_p} A_f}$	$\left\{\frac{4h_{in,i}}{\rho_w Cp_w}\frac{D_{in,i}}{(D_{o,i}^2 - D_{in,i}^2)}T_i^n + \frac{4h_o}{\rho_w Cp_w}\frac{D_{in,i}}{(D_{o,i}^2 - D_{in,i}^2)}T_{o,i}^n\right\}$

*coefficients for Eq. (7.14)

Fo_i^n and Co_i^n are Fourier number and Courant number respectively calculated at n^{th} time level and are given by:

$$Fo_i^n = \frac{\alpha\ \Delta t}{\Delta x_i^2}\ ,\ Fo_{w,i}^n = \frac{\alpha_w \Delta t}{\Delta x_i^2}, Co_i^n = \frac{W^n \Delta t}{\rho_0 A_{in,i}\Delta x_i} \tag{7.16}$$

7.4. CODE VALIDATION

The code has been validated with the data generated in-house in a single phase rectangular loop with water, both as primary and secondary working fluid. Vijayan et al. [7.18] has given dimensional details of the rectangular loop with heater and cooler. They performed experiments for various orientations of heater and cooler in the rectangular loop. The code validation was performed with experiment data for vertical heater and horizontal cooler (VHHC) orientation. The code was also used to predict steady state behaviour of vertical heater vertical cooler (VHVC) orientation of the rectangular geometry loop. The various steady state parameters thus obtained for each power level are compared with experimentally observed data. Figure 7.3 depicts the steady state mass flow rate as a function of heater power predicted by LeBENC. The mass flow rate thus predicted is compared with experimental data in Fig. 7.3. The effect of ambient temperature variation was also studied and is given in this figure. This is to accommodate variation in ambient temperature during the experimentation.

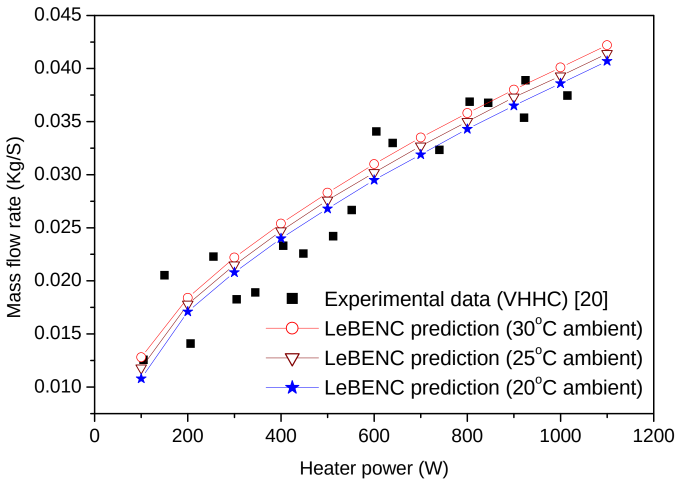

FIG. 7.3. Variation of mass flow rate with heater power at steady state for VHHC orientation.

Figure 7.4 shows steady state mean fluid temperature as a function of heater power predicted by LeBENC. Comparison of mean fluid temperature predicted by LeBENC with experimental data is also given in Fig. 7.4. Figure 7.5 shows the rise in fluid temperature in the heater section as a function of heater power.

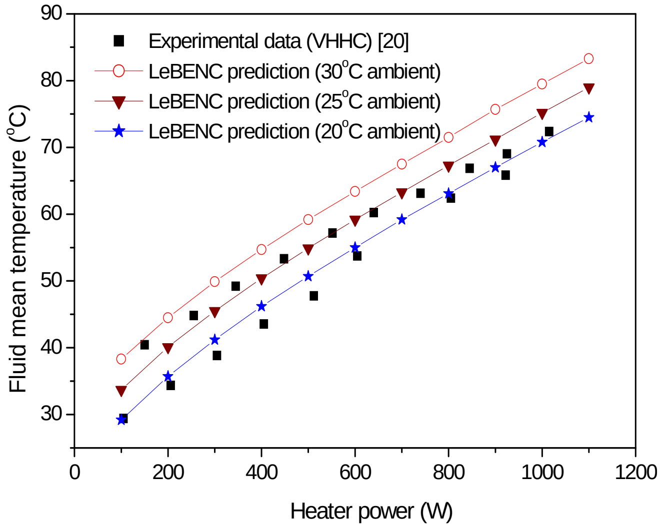

FIG. 7.4. Variation of fluid mean temperature with heater power at various steady states for VHHC orientation.

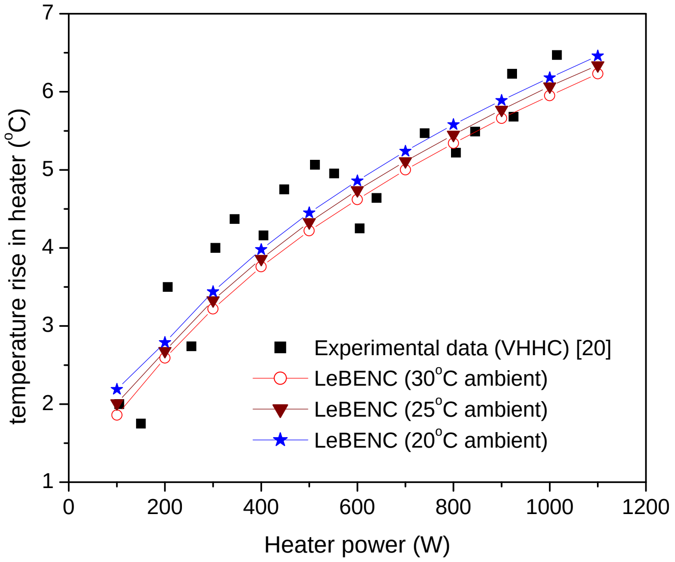

FIG. 7.5. Temperature rise in heater section vs. heater power at various steady states for VHHC orientation.

Figures 7.6–7.8 compare steady state results obtained by LeBENC with experimental data for VHVC orientation for mass flow rate, mean fluid temperature and fluid temperature rise in the heater section respectively.

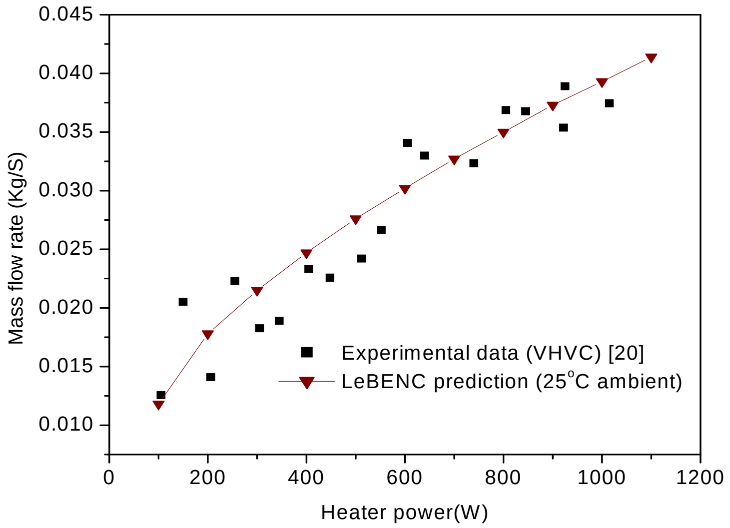

FIG. 7.6. Variation of mass flow rate with heater power at various steady states for VHVC orientation.

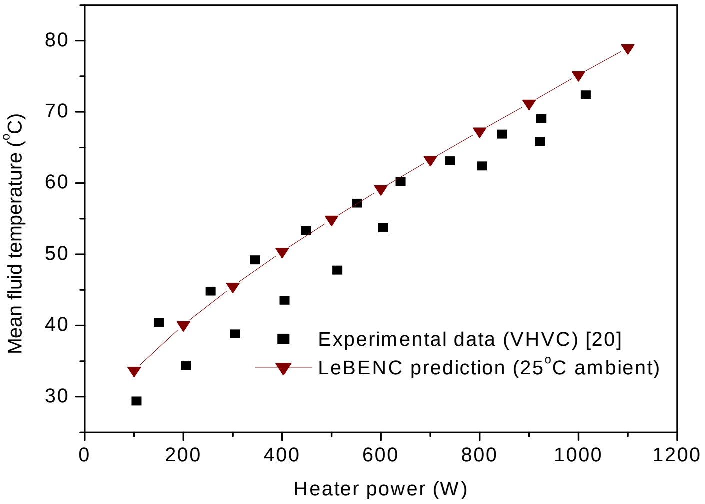

FIG. 7.7. Variation of fluid mean temperature with heater power at various steady states for VHVC orientation.

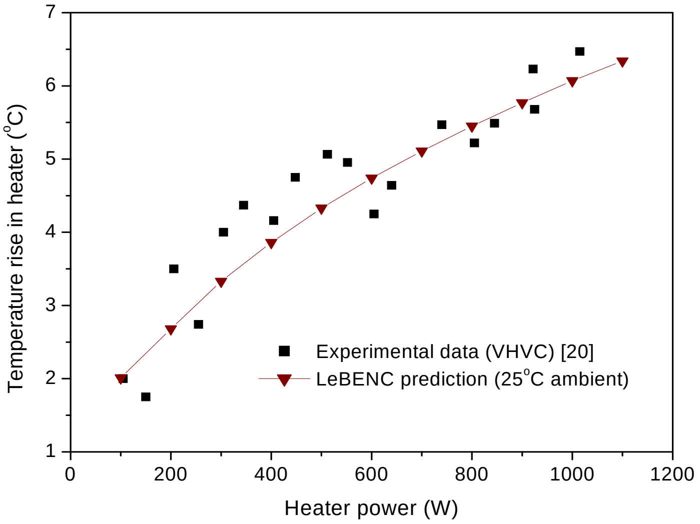

FIG. 7.8. Temperature rise in heater section vs. heater power at various steady states for VHVC orientation.

Vijayan [7.20] showed that steady state flow in single phase uniform or non-uniform diameter natural circulation loops can be expressed as:

$$\mathrm{Re}_{ss} = c\left(\frac{Gr_m}{N_G}\right)^r \qquad (7.17)$$

where the constants *'c'* and *'r'* depend on the nature of flow (i.e., laminar or turbulent). Parameter NG depends on geometry of the loop; and the detailed derivation of Eq. (7.17) can be found in [7.20]. A reference diameter of the whole loop is calculated considering the geometry and flow condition in each section of the loop. Re_{ss} and Gr_m are based on the reference diameter. The constants *c* and *r* are given as:

$$c = \left(\frac{2}{p}\right)^{\frac{1}{(3-b)}} \quad and \quad r = \frac{1}{(3-b)} \tag{7.18}$$

Thus, for a given Grashof number, Eq. (7.17) becomes a non-linear equation in Reynolds number. This equation is solved iteratively to obtain Re_{ss}. Vijayan [7.20] has not considered axial conduction in the loop, while deriving Eq. (7.17).

A comparison of theoretical analysis is made with experimental data for both orientations. It is to be noted that the centre line elevation difference between heater and cooler is taken for loop height in the calculation of Grashof number.

Figure 7.9 shows the comparison of the results obtained in terms of non-dimensional numbers using Eq. (7.17) (for theoretical analysis and experiment data) for VHHC orientation. Figure 7.10 provides a similar comparison for VHVC orientation. It is to be noted that the spatial average fluid temperature, as given by LeBENC, was used to evaluate the fluid properties. Considering the scatter in experimental data, the prediction by the code is found to be acceptable. Further, transient behaviour following the initiation of heating, with 1000 W heater power, in VHVC was predicted and the result was compared with that obtained by computer code TRANCO (see Fig. 7.11) [7.18] developed earlier.

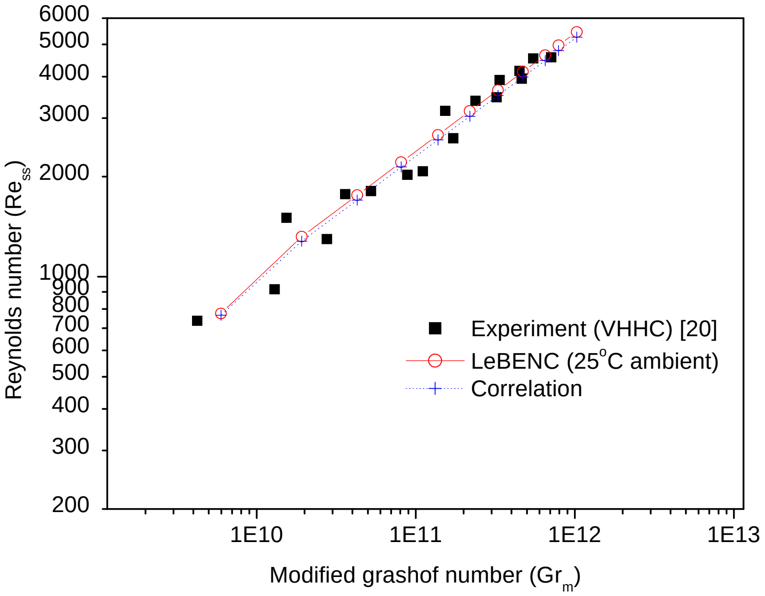

FIG. 7.9. Grashof number vs. Reynolds number at steady state for VHHC orientation.

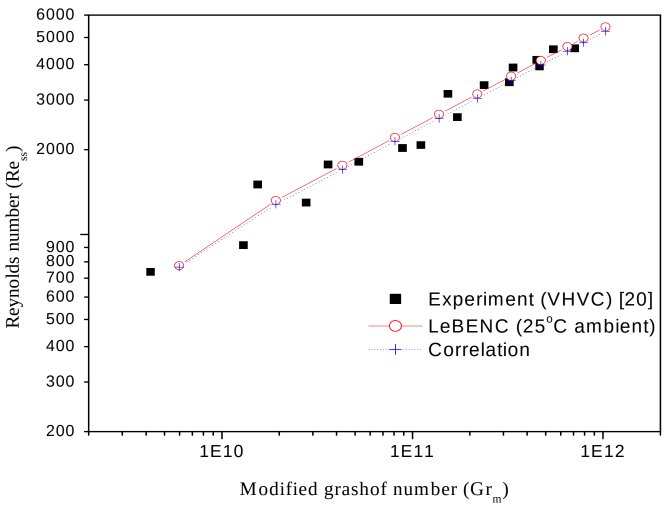

FIG. 7.10. Grashof number vs. Reynolds number at steady state for VHVC orientation.

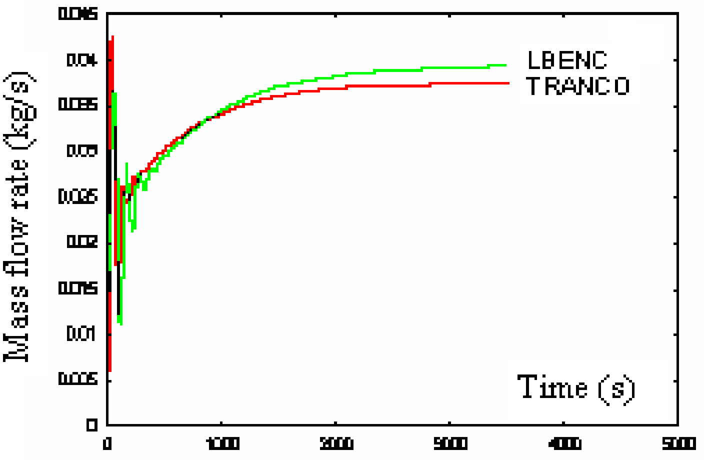

FIG. 7.11. Mass flow rate transient following initiation of heating for VHVC orientation.

7.5. EXPERIMENTS WITH LIQUID METAL

The loop was operated to study the steady state and transient behaviour of the LBE. For all the experiments, the computer code was run with the same inputs as initial conditions in the test loop and results obtained were plotted for comparison.

7.5.1. Steady state analysis

In this experiment, the test loop was allowed to reach steady state conditions at different input powers. The temperatures at inlet and outlet of the heated section were recorded. The mass flow rate in the loop was estimated from the heater power and the temperature difference calculated from temperatures at inlet and outlet of the heated section. The LBE flow rate at 2500 W was found to be 0.15 kg/s. The corresponding velocity in the 15 mm NB pipe line is

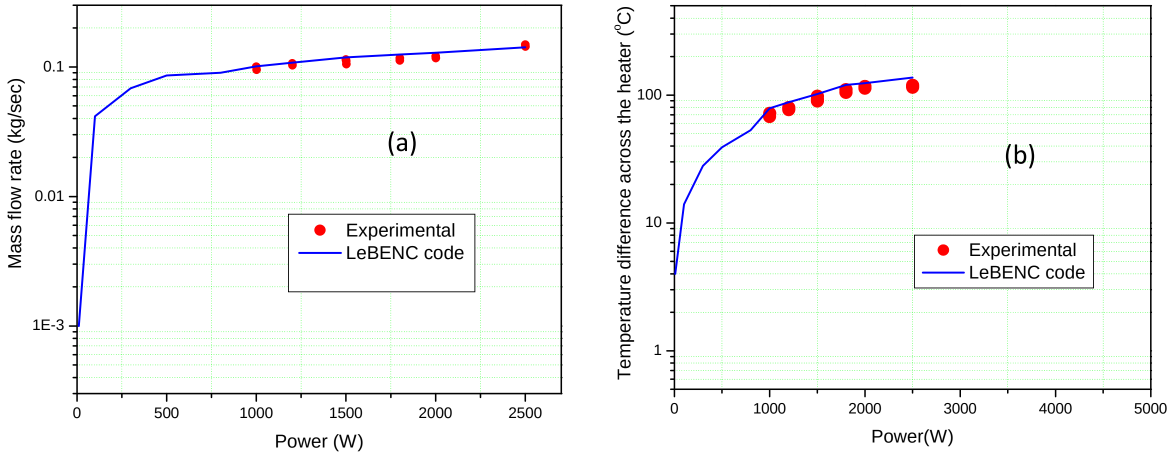

(a) Mass flow rate (b) Temperature rise across heated section

FIG. 7.12. Steady state natural circulation results at different power levels.

0.01m/s. LeBENC code was run for different power levels starting from 10 W to 2500 W. The results obtained from the test loop and those obtained from the code are plotted in Fig. 7.12. It was found that the maximum difference in experimental data and code prediction is 20% for temperature difference across the heated section for above mentioned power levels.

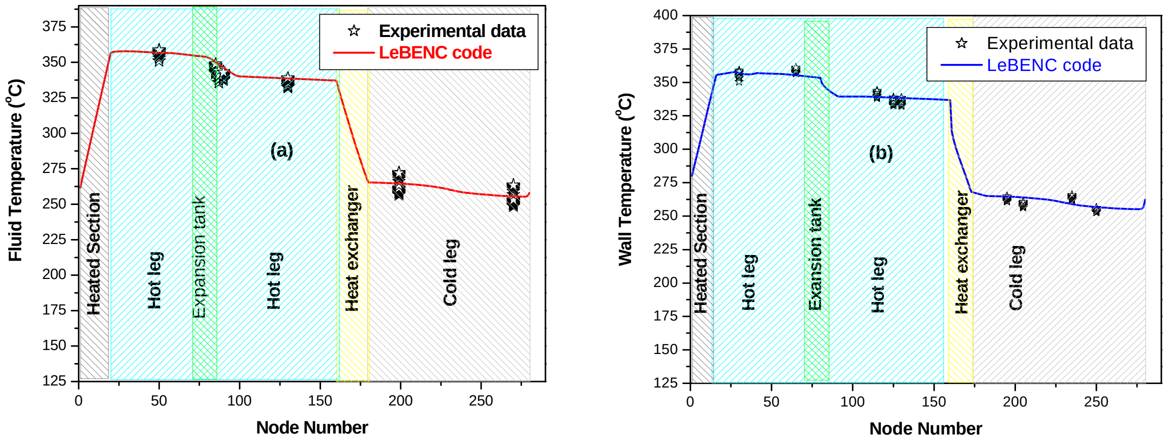

(a) (b)

FIG. 7.13. Temperature distribution along the length of the loop at steady state: (a) fluid temperature; (b) wall temperature, Power = 1500W.

The temperature distribution over the whole length of the loop is shown in Fig. 7.13. The comparison of LeBENC code prediction with the experimental values, plotted in Fig. 7.13(a), shows the fluid temperature distribution in the loop; and Fig. 7.13(b) shows the heater surface temperature. In both figures, steady rise in temperature could be seen in the heated section of the loop. There is small temperature drop in the piping due to heat loss through the insulation. This heat loss could not be avoided even with thick insulation on the pipe outside surface. Due to low heat capacity of the LBE, the temperature drop is significant even at small heat loss. The heat loss through the insulation in the 15 mm NB piping was found to be 50 W/m for a typical steady state run with 1800 W loop power. This results in LBE temperature drop of about 4^{o}C/meter along the piping. The temperature drop in the expansion tank, as can be seen from Fig.7.13, was due to the heat loss from vessel wall, flanges, gas purging lines, oxygen sensor fittings, etc. In the heat exchanger, the temperature decreases steadily as expected.

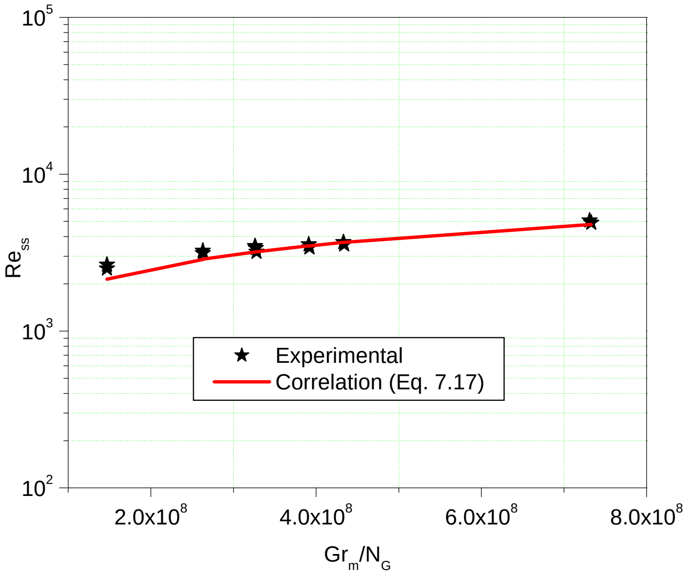

FIG. 7.14. Variation of Reynolds number for steady state flow in HANS loop.

Figure 7.14 shows the comparison of the results obtained from LeBENC with that obtained by correlation and experiments. The correlation conforms to the experimental results. So, it can be concluded that, in spite of high thermal conductivity of LBE, the role of axial conduction of LBE in natural circulation is not considerable.

7.5.2. Transient studies

Transient studies were carried out to simulate some postulated accident scenario in the reactor. The main objective was to observe the LBE coolant behaviour during various transient conditions. The transient experimental studies include startup of the loop from stagnation conditions, loss of heat sink and step power change.

7.5.2.1. Startup operation

Startup operation from zero flow condition for various power levels was carried out. The startup operation for main heater power levels of 1200 W and 1800 W has been discussed. Initially, the loop was running at steady state by natural circulation of LBE. The main heater was put off and secondary side air flow in the heat exchanger was stopped. The cold leg temperature was slowly increased to the hot leg temperature by starting the trace heaters in the cold leg. In this way, no flow condition was ensured by reducing the LBE temperature differences across the heated section and heat exchanger near to zero. During zero flow condition, the average temperature of the loop was around 270^{o}C for 1200 W case. For 1800 W main heater power, the average temperature of the LBE was around 300^{o}C. After achieving zero flow condition, all the trace heaters were put off and main heater was put on. The secondary side air flow in the heat exchanger was started. The temperature variation in the heated section outlet and heat exchanger outlet was observed till steady state condition was achieved. Fig.7.15(a) shows the variation of heated section outlet and heat exchanger outlet temperatures with time for 1200 W power. Here, the driving force (DF) of the LBE circulation is the thermal buoyancy. At initial stage, the coolant starts to flow from stagnant. Due to initial low flow, temperature at the heated section outlet rises. As the flow approaches steady state, the temperature reduces and stabilizes. The peak temperature achieved during this startup experiment is 318^{o}C, which is 10.1% higher than the steady state temperature (~290^{o}C) with 1200 W main heater power.

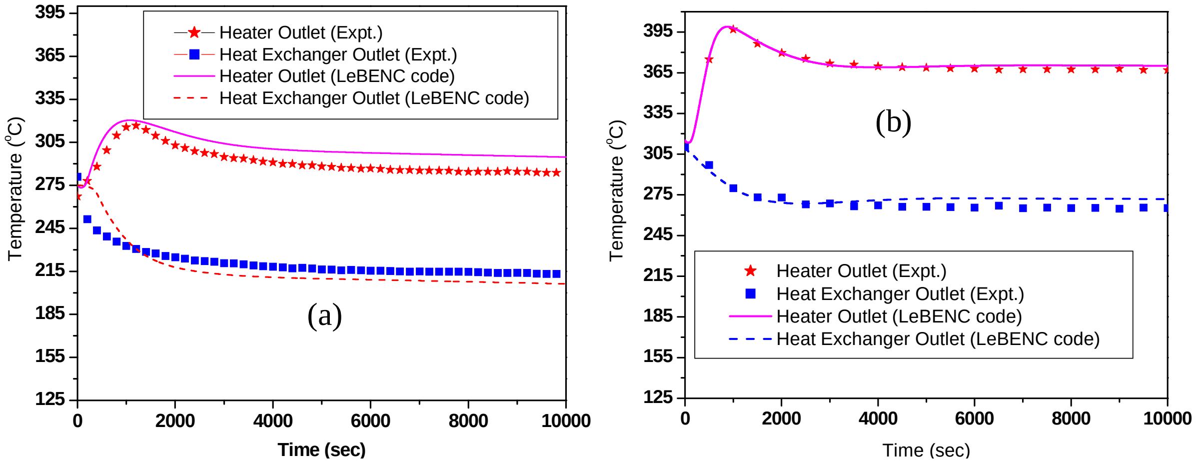

FIG. 7.15. *Startup of the loop from stagnation condition, Power: (a) 1200 W, (b) 1800 W.*

Further, from Fig. 7.15(a) it can be seen that the heat exchanger outlet temperature decreases rapidly and stabilizes after some time. Due to initial low flow of LBE, there is a drastic decrease in temperature of the LBE in the heat exchanger. But as the flow increases, the further drop in the temperature is smaller. It can be seen that the temperature stabilizes smoothly during this transient. Fig. 7.15(b) shows the startup of the loop at higher power (1800 W) level. Here again, a similar trend as in the earlier case can be seen. In this case, the temperature rise at the outlet of heater section is higher due to the higher power level. The peak temperature reached in this case is 400°C, which is 9.3% higher than the steady state temperature (~366°C). In both cases, no fluctuation in LBE temperature was found during natural circulation startup, and steady flow was achieved smoothly from stagnant condition.

Theoretical analyses for the both above mentioned cases were carried out using LeBENC code and the results were compared with the experimental results. It turned out that the prediction by LeBENC code is better at higher power level. At lower power, the part of heat loss from the piping is considerable as compared to the heat removal from the heat exchanger. This is the uncertainty in the prediction of the loop behaviour. The time of achieving steady state in both cases is almost the same in theoretical and experimental studies.

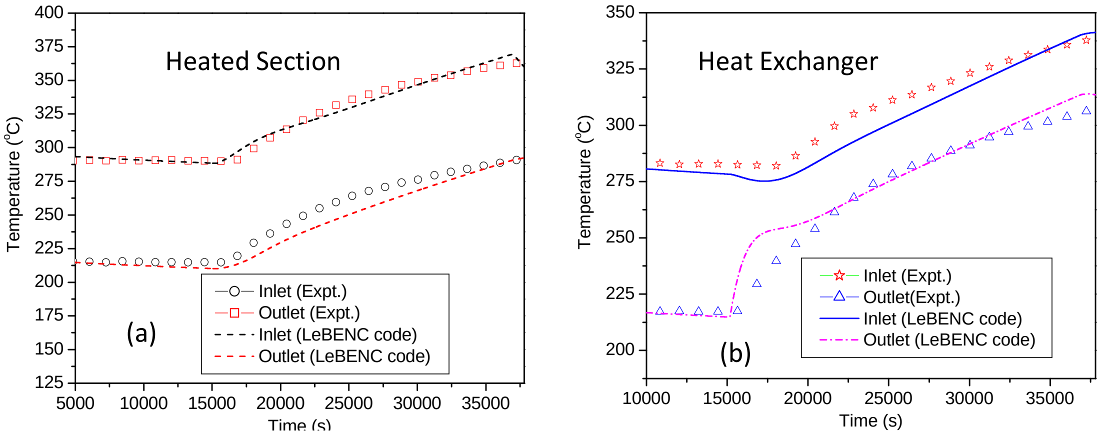

FIG. 7.16. *Variation of inlet and outlet temperature of (a) heated section and (b) heat exchanger, during the simulation of loss of heat sink.*

7.5.2.2. Loss of heat sink

The loss of heat sink is considered in the safety analysis of reactors and a good prediction is necessary to ensure safe plant operation. This experiment was carried out at 1200 W power level. The loop was started and a steady state was established. After achieving steady state, secondary flow in the heat exchanger was stopped completely at *t = 16 100 s*. Due to the inability of the liquid metal to dispense its heat, the steady state was disturbed and the temperatures of the loop began rising. From Fig.7.16(a) it can be seen that the LBE temperature at the heat exchanger outlet starts rising as soon as the air flow was stopped. The heated section outlet temperature starts rising with a delay of 380 s after stoppage of secondary side flow in the heat exchanger. This delay was due to the time taken by hot LBE to travel through downcomer to the heated section. At *t = 37 500 s*, the heater was switched off. This transient was simulated in using LeBENC code and the comparisons of the results are shown in Fig. 7.16. As can be seen in Fig. 7.16(a), the LeBENC prediction of heated section outlet temperature conforms well to the experimental data. During this experiment, it was expected that the temperature difference between heat exchanger inlet and outlet should reduce drastically, as heat exchanger was not removing heat. But a temperature difference of 30^{o}C was observed across the heat exchanger, as shown in Fig.7.16(b), during this experiment. This may be due to the heat absorbed by the heat exchanger structures while temperature rises and to the local air circulation from hot zone to the cold section in the secondary side piping. So there was heat loss in the heat exchanger. This heat loss was considered in LeBENC code for simulating this transient experiment. The predicted values of heat exchanger outlet and heated section inlet temperature initially rose more rapidly than the experimental results. This may be due to the absorption of heat by the flanges and the piping structural supports, which could not be simulated properly in the LeBENC code.

7.5.2.3. Step change of heater power

The effect of step change in main heater power has been studied in the loop. Initially, the loop is operated at 1500 W power level. The power was increased to 1800 W for some time and stepped back to 1500 W. The effect of this power change is shown in Fig. 7.17 in terms of change in temperature. In Fig. 7.17(a), at the heated section outlet, the step change can be clearly seen. At the heat exchanger outlet, the step change is not clearly visible. This is due to the large inventory of coolant in the expansion tank, which causes mixing. Fig. 7.17(b) shows the temperature differences across the heated section and heat exchanger. There was no significant change in temperature difference across the heat exchanger. This may be due to the fact that heat removal capability of the heat exchanger is controlled by the secondary side heat transfer coefficient. The prediction of LeBENC code is also shown in the figures.

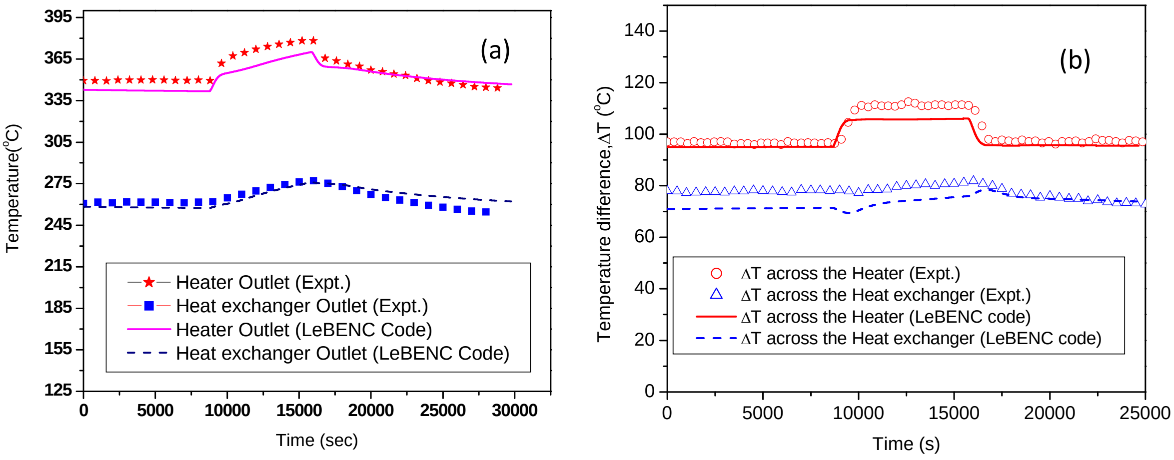

FIG. 7.17. Variation of (a) outlet temperature of heated section and heat exchanger and (b) ΔT across the heated section and heat exchanger, during step change in power of loop.

7.6. EXPERIMENTAL STUDIES ON ENHANCED CIRCULATION OF HLM BY GAS INJECTION IN CIRCE FACILITY

The possibility to enhance the circulation of heavy liquid metal (HLM) by gas injection is an important design option for both normal operation and accident conditions (operating the decay heat removal system) of an ADS or LFR prototype. This technique allows the primary coolant circulation with a plant simplification in respect to the use of mechanical pumps. The reliability of this technique has been proved on significant scale in the ENEA LBE facility CIRCE located at CR Brasimone.

Several experimental campaigns at isothermal conditions and different LBE temperatures have allowed correlating the LBE mass flow rate in the facility with the injected Argon mass flow rate; moreover, the experimental data have used for the assessment of the RELAP5 pressure drop correlations. The present experimental campaign on NACIE loop (see chapter 7.7) will provide further data for the assessment of pressure drop and heat transfer correlations in gas enhanced circulation conditions.

CIRCE (circulation experiment) is a large scale test facility designed for studying key operating principles of the 80 MW Experimental Accelerator-Driven System (XADS) proposed by ANSALDO [7.21, 7.22]. One of CIRCE’s main goals was to investigate and confirm the possibility of using the lift-pump technique to obtain a steady flow of liquid metal in representative pool configuration. For this reason, experimental activities were performed in order to characterize the gas enhanced circulation technique and analyse the fluid dynamic behaviour of the system.

In Fig. 7.18, an isometric view of the CIRCE facility is shown. The facility can be considered in two parts: the LBE containment and the auxiliary systems. Regarding the first part, the main components are the vessel S100 with a height of 8500 mm and a diameter of 1200 mm, the storage tank S200 and the intermediate vessel S300, used during the handling of the LBE between the two other vessels.

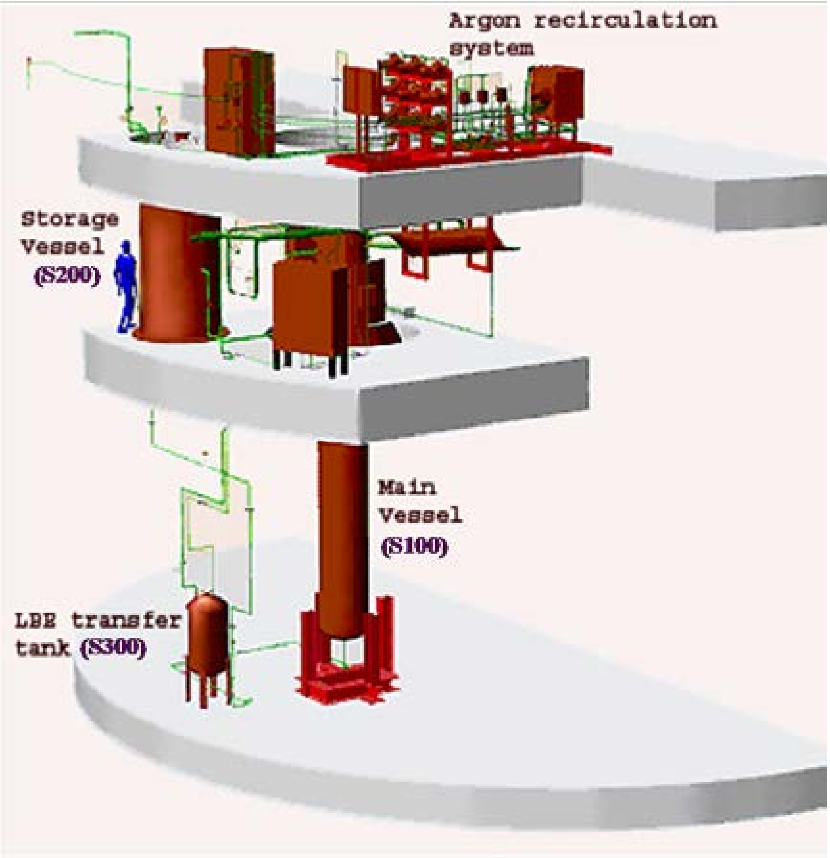

FIG. 7.18. *View of the CIRCE facility.*

A sketch of the test section used to carry out the experiments herein discussed is shown in Fig. 7.19.

It consists of different components described in the following.

Riser: It consists of only one pipe (diameter = 202.7 mm, height = 3854 mm) of the 22 pipes that form the reference XADS plant riser. Since this element is scaled 1:1, the flow mapping achievable by tests will be easily applicable to the full scale reference plant. Inside the riser, the gas injection pipe is housed, ending with the injector.

Dead volume: It is delimited by the cover head (where it is welded) on the top and by the fitting volume in the bottom; it maintains the real height of the full scale dead volume, whereas the cross-section is scaled 1:22. At present, the dead volume does not take part actively in the test run; it is filled with argon and directly connected to the cover gas in thermal equilibrium with it.

Fitting volume: It consists of a cylindrical volume delimited by two circular plates (diameter = 982 mm), 225 mm spaced. It joints the feeding conduit to the riser. This element is designed and scaled to represent the upper plenum of the core, fitting the core outlet to the riser inlet.

Feeding conduit: It is the lower part of the test section, immersed in the lower plenum of S100; a Venturi-Nozzle flow meter is installed on the conduit, as well as a drilled disk, downstream the flowmeter. The hole manufactured on this disk was calculated to provide a pressure loss suitable to simulate the one relevant to the full scale core, as defined in the ANSALDO XADS concept [7.21].

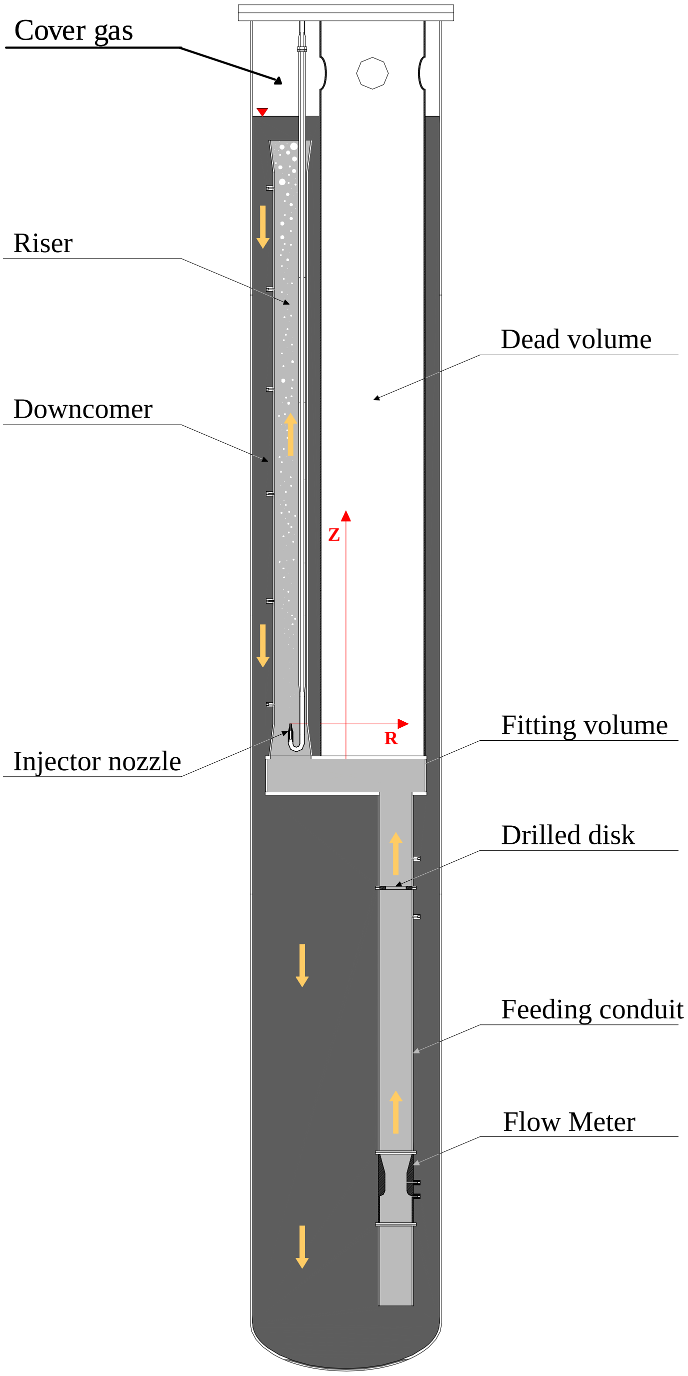

FIG. 7.19. Main vessel housing the test section (the flow path obtained during the test is shown by the arrows). In this configuration, the dead volume does not take part in the experiments, remaining in communication with the cover gas only.

Downcomer: It is the outer side of the test section where the downward LBE flow takes place during the test. It is scaled to represent 1/17 of the full scale downcomer, so it is characterized by a cross-section of around 0.7 m^2 (see Fig.7.20).

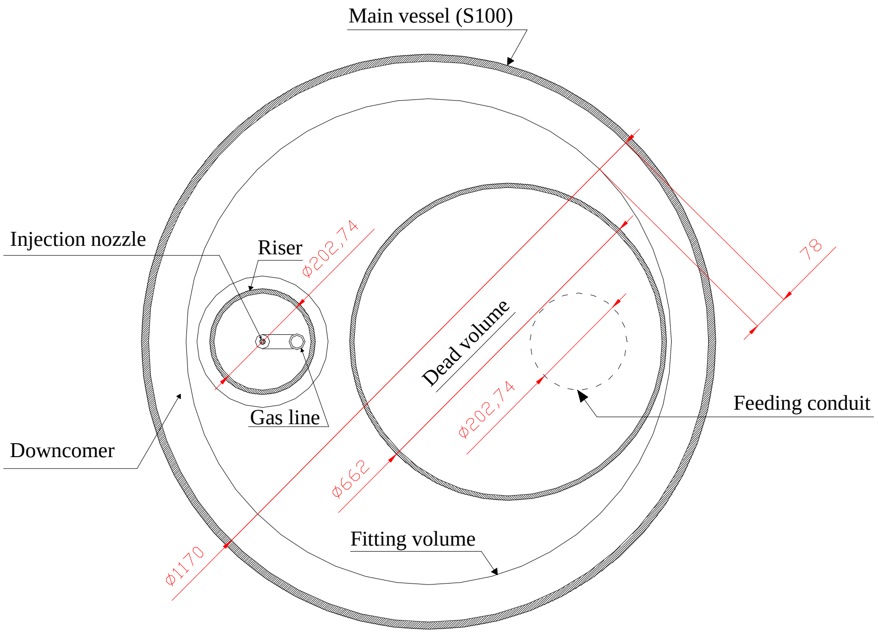

FIG. 7.20. Cross-section of the main vessel housing the test section.

The test section is equipped with all the instrumentation suitable for performing the required measurements, like thermocouples (±1 K) differential pressure meters (±0.2% FSO) and level meters (±1 mm LBE). Bubble tubes have been installed on the test section to transfer pressure signals from the LBE to differential pressure cells operating with gas at room temperature. In particular, the level measurement system (LMS) and the differential pressure measurement system (DPMS) make use of the above instruments to perform their tasks (see Fig. 7.21). Both the DMPS and the LMS, as well as the flowmeter, have been qualified and calibrated during dedicated experimental campaigns [7.23, 7.24].

The tests have been performed under isothermal conditions at different temperatures from 200 to 320°C; it should be noted that 200°C is the cold shutdown temperature in the Ansaldo XADS concept [7.21].

During the test, a gas flow rate is injected by means of the injector located in the bottom of the riser. The argon recirculation system (ARS) includes three gas flow meters (accuracy 2%) installed on the gas injection line, outside the test section, with different measurement ranges. So, switching on the suitable one, it is possible to measure a gas flow rate in the range of 0.056 to 22 Nl/s. The output signal from the selected flow meter is corrected by the data acquisition system (DAS), in order to take into account the differences between the calibration conditions and the operating conditions in terms of pressure and temperature, and is then stored. The gas flow rate range from 0.5 to 7.0 Nl/s has been covered.

For each injected gas flow rate an entrained LBE flow rate has been measured, and several steady states have been obtained. Each steady state has been maintained for 20–25 minutes, then the gas injected flow rate has been changed. The steady state condition was defined considering the average of the LBE flow rates on a span of five seconds: since the variation of this parameter during the time window of each test (20–25 min. as previously reported) is

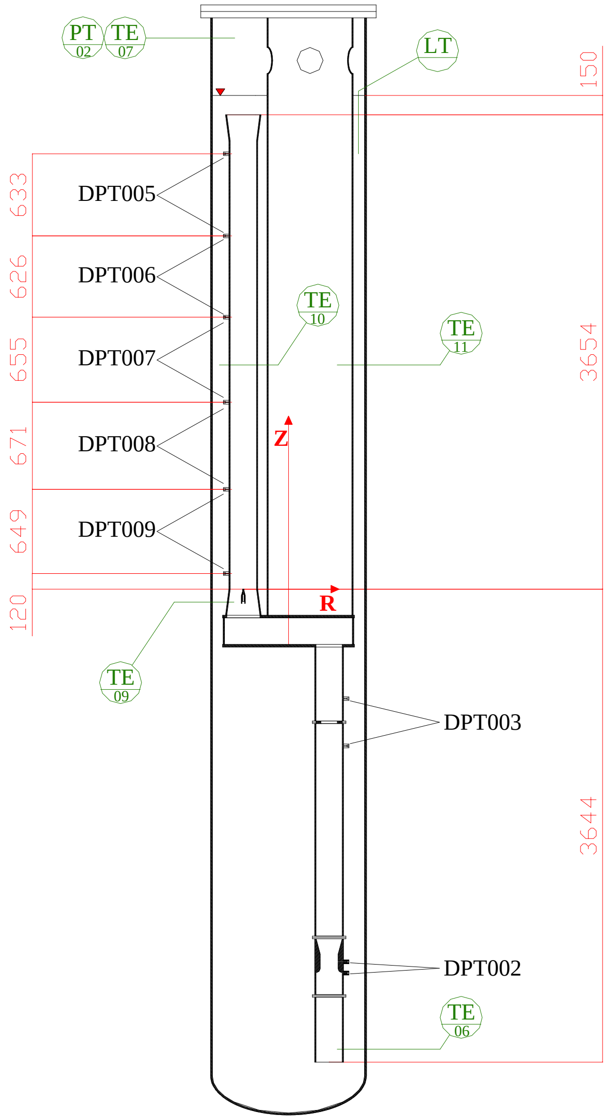

FIG. 7.21. Locations of the measurement point for the thermocouples (TE), differential pressure meters (DPT), level meters (LT) and pressure meters (PT). The main axial dimensions of the test section are given in mm. The gas line inside the riser has not been reported, as well as its own instrumentation.

within a range of ±5%, a steady state condition is assumed. The LBE flow rates have been measured by the Venturi-Nozzle flowmeter installed on the feeding conduit, using the equation carried out for the flowmeter during the calibration tests, previously performed [7.23, 7.24].

Concerning the chemical control of the LBE, only a pretreatment of the ingots has been performed, scraping off the oxides from the ingots surface before melting. Then, the ingots were melted under argon atmosphere in a removable container connected by gate valves to the top of the S200 storage vessel. The melt was finally filtered by means of a mechanical filter during its transfer in S200.

None-active chemical control nor oxygen measurement in the liquid LBE were performed during the tests because corrosion investigations and chemical control were not primary targets for these experimental activities. However, the plugging of the internals of the test section never occurred (bubble tubes included). Moreover, post-test inspection revealed as the internal surfaces of the test section (such as the inner walls of the feeding conduit or the fitting volume) were still quite clean and smooth. Nevertheless, the presence of floating slugs was detected on the surface of the liquid metal during the tests by visual inspection.

An impurity control system based on the use of chemical and mechanical filters (on the gas recirculation lines) as well as the bubbling of Ar-H_2 mixtures in the melt is going to be implemented in the facility and will be operative during the future tests planned on CIRCE in the frame of the IP-Eurotrans programme.

The tests have been performed under isothermal conditions, at different LBE temperatures (from 200°C to 320°C); for each test temperature, several steady states of circulation have been obtained by injecting different gas flow rates, each state is characterized by a different LBE flow rate. The gas injections have been realized in the range from 0.5 to 7.0 Nl/s, in order to investigate a wide range of entrained liquid metal flow rate, up to 200 kg/s. When the isothermal conditions at the selected temperature are reached, a gas flow rate is injected from the bottom of the riser, by an appropriate nozzle of 6 mm inner diameter, with a pressure of about 5 bar, needed to override the backpressure static pressure of the LBE column. Then, after a quick transient, a steady flow condition for the liquid metal is obtained. The separation between the two phases takes place on the free level, 150 mm above the riser, where the argon reaches the cover gas. Moreover, due to the high difference of density between the phases as well as to the very low LBE velocity in the downcomer (always less than 0.04 m/s), it is reasonable to assume a full separation between the gas and the liquid metal (for the thermophysical properties of the LBE, see Ref. [7.25]).

The obtained results confirm the possibility of inducing a steady circulation of LBE by injecting a controlled flow rate of gas, at least for argon flow rate higher than 1 Nl/s. However, the system shows a different behaviour at a low injected flow rate, since the occurrence of instability phenomena have been noted at gas flow rates lower than 1Nl/s.

In fact, notwithstanding the gas lift principle is valid even at low gas flow rates, the experimental occurrence of oscillatory phenomena has been observed since the gas flow rate was lower than 1 Nl/s. In this case, it was not possible to obtain a steady state condition.

When gas flow rates lower than 1 Nl/s are injected, the system shows a “pulsed” behaviour, with both flow rates characterized by periodical oscillations. Figure 7.22 shows this pulsed behaviour for the test carried out at 320°C, with an initial injected flow rate of 0.5 Nl/s.

After a short transient, both flow rates undergo a periodical and quite regular oscillation, with a frequency of about 30 mHz; the LBE flow rate also shows high magnitude oscillations, with a delay of about 10 s. The delay has to be related to the interaction between the phases during the upward flow of the bubble in the riser, to the evolution of the void fraction along the riser and to the fluid-dynamics inertia of the LBE along the flow path. This behaviour is probably related to the bubble growth and to the detachment mechanism, where a partial refilling of the injection line by LBE could take place at low gas flow rates, as indirectly suggested by the pressure evolution inside the injection line (see Figs 7.22 and 7.23).

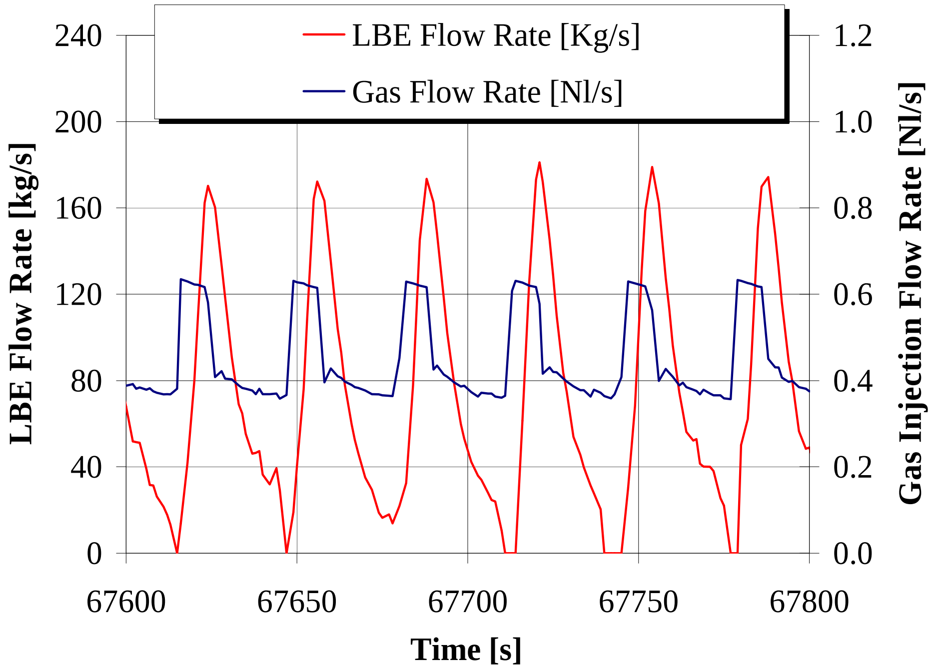

FIG. 7.22. Pulsed behaviour showed by the system for injected flow rates lower than 1 Nl/s.

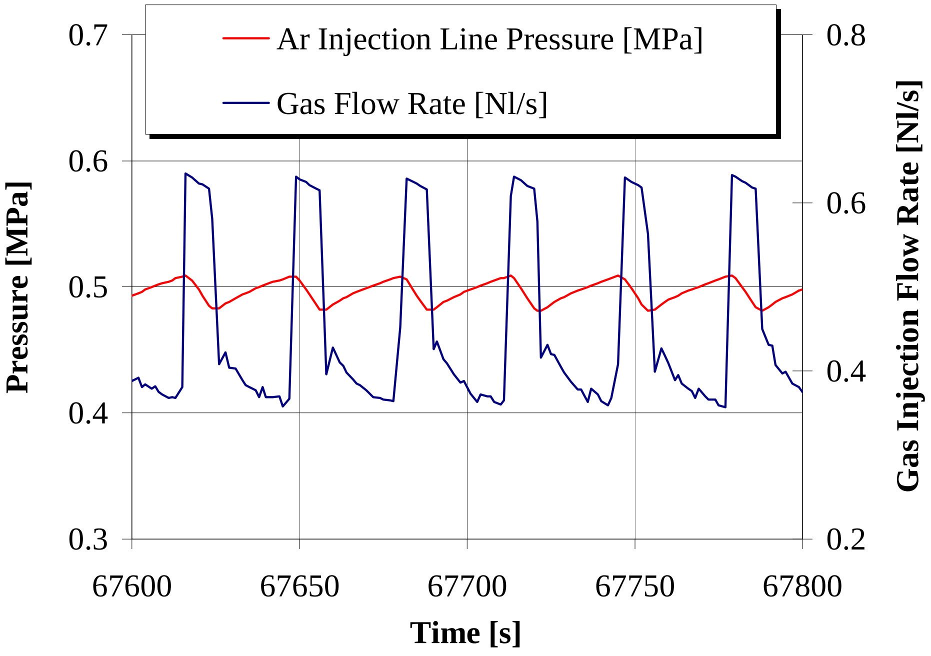

FIG. 7.23. Pressure evolution inside the gas injection line during the test reported in Fig. 7.22.

In fact, the detachment of gas corresponds to the peaks detected measuring the pressure in the injection line, downstream the gas flowmeter. When the release of gas occurs, the pressure in the line decreases rather quickly, as far as the gas flow rate; this suggests an entry of liquid metal inside the injector. Then, the pressure increases slowly and the liquid metal is pushed outside the injector until the next release of gas. So, when the pressure of the gas in the injection line reaches a value high enough to push out the liquid from the nozzle and a new release of gas takes place, the dynamic effect of the previous train of bubbles is already expired. In this case, a different geometry of the nozzle could help to override this problem.

At gas flow rate higher than 1Nl/s, a steady circulation of LBE has been achieved, in all the tests performed. Figure 7.24 shows the results obtained at 220°C; the entrained LBE flow rate was in the range of 150–230 kg/s when a gas flow rate of 2–7 Nl/s was injected. Both steady states and transient are clearly recognizable, the two flow rates are roughly constant during the steady states. However, the transient behaviour of the systems is very quick (less than 30 s), indicating a low mechanical inertia of the system.

Figure 7.25 shows the LBE flow rate versus the Ar flow rate for the same test, while in Fig. 7.26 the results obtained at different temperatures are compared. The points represent the average of the measured values for each steady state obtained. The liquid flow rate increases as the gas flow rate increases and the two quantities seem to be related by a power low like the following:

$$\dot{m}_l = A \cdot \left(\dot{m}_g\right)^b \qquad (7.19)$$

where the exponent b is close to 0.33. This behaviour can be explained as follows:

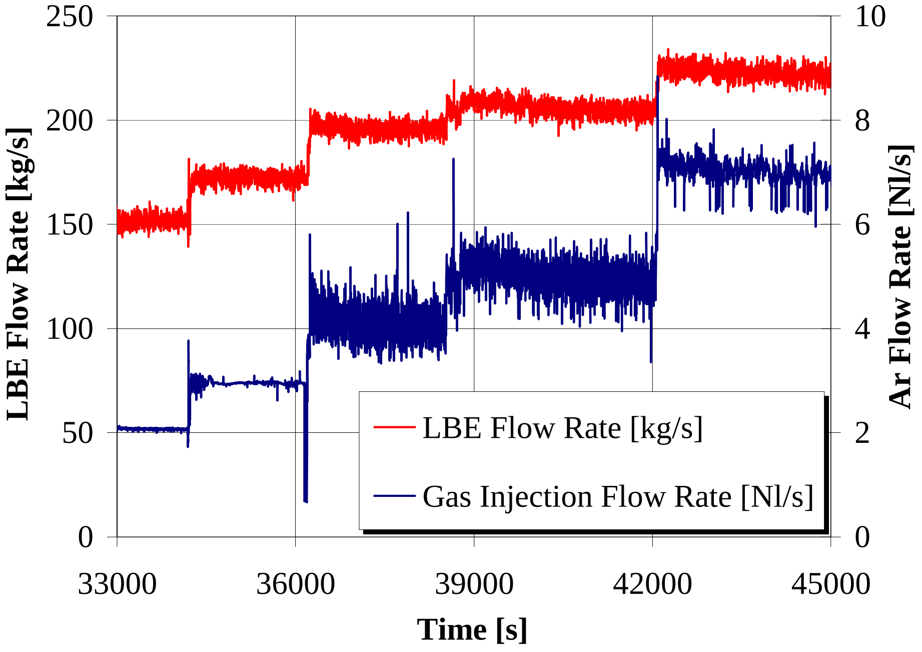

FIG. 7.24. Trend of the LBE flow rate as a function of the gas flow rate, for tests performed at 220°C. The different amplitudes in the gas flow rate measurement come from the use of flowmeters with different measurement ranges.

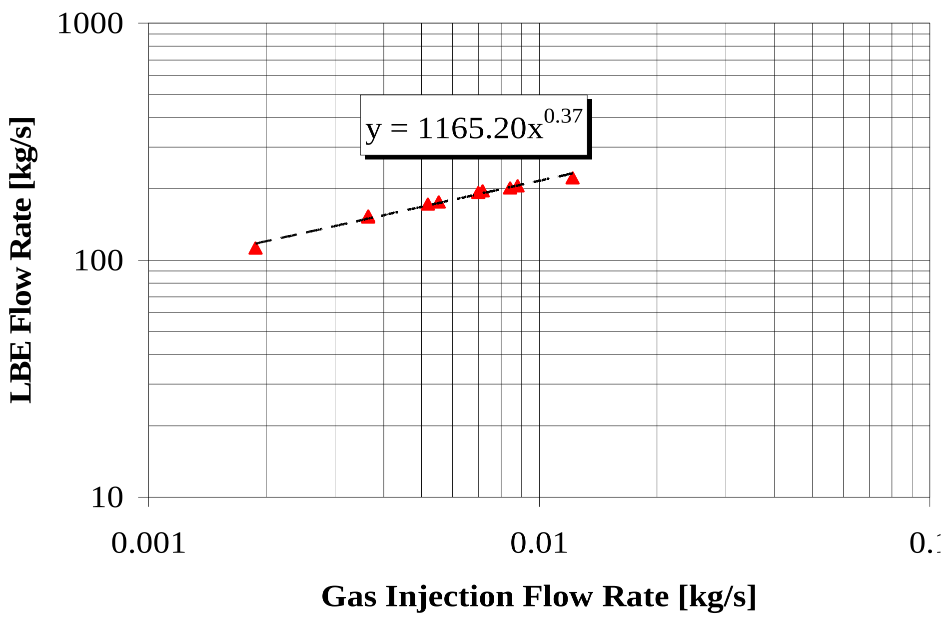

FIG. 7.25. LBE flow rate as a function of the argon flow rate, for tests performed at 220°C.

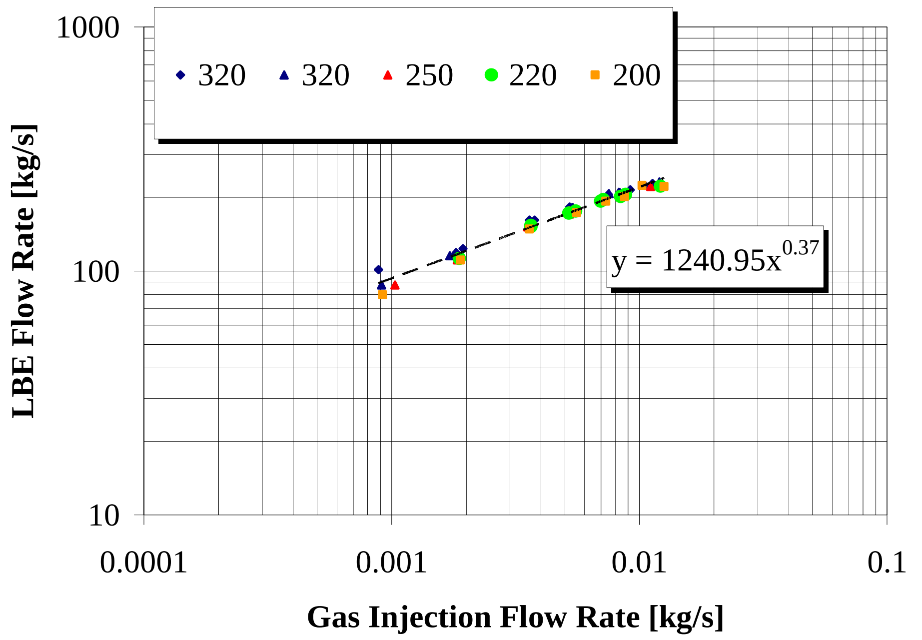

FIG. 7.26. LBE flow rate as a function of the argon flow rate, for all the performed tests.

Since the system is under steady state conditions, the momentum equation, integrated along the flow path, gives:

$$\Delta p_{DF} = \Delta p_{fric} \tag{7.20}$$

where Δp_{DF} is the DF, while Δp_f represents the total pressure drop along the flow path.

The DF can also be written as:

$$\Delta p_{DF} = H \cdot g \cdot \Delta\rho \tag{7.21}$$

where H is the hydrostatic height above the nozzle exit and $\Delta\rho$ is the density difference between the liquid in the downcomer and the fluid flowing in the riser.

The density difference can be expressed as:

$$\Delta\rho = \rho_l - \rho_m = \rho_l - \left[\rho_l \cdot (1-\alpha) + \alpha \cdot \rho_g \right] \tag{7.22}$$

where ρ_l is the density of the LBE in the downcomer, while ρ_m is the average density of the two phase mixture in the riser, defined by the void fraction, α, and ρ_g is the gas density.

The gas density is strongly dependent on pressure that is a function of position along the riser. Then, it will change as the gas rises up in the riser. Since the gas injection line runs all along inside the riser, driving the gas to its bottom part, it is reasonable to assume the rising gas in thermal equilibrium with the liquid metal. Under this hypothesis, we can express the gas density by the ideal gas law as:

$$\rho_g(z) = \frac{p(z)}{R^* \cdot T} \tag{7.23}$$

In Eq. (7.23), *z* is the curvilinear coordinate along the riser axis (*z* = 0 is the injection point), while *R** is the argon gas constant (208.21 J/kg K).

In order to simplify the model, it is useful to define an average gas density $\bar{\rho}_g$, as the density calculated at the average pressure in the riser, that means the pressure at *z* = *H*/2. Since the void fraction is small, the average pressure can be estimated as:

$$\bar{p} = p_0 + \rho_l \cdot g \cdot \frac{H}{2} \tag{7.24}$$

where p_0 is the cover gas pressure. Equation (7.22) becomes:

$$\Delta\rho = \rho_l - \bar{\rho}_m = \alpha \cdot (\rho_l - \bar{\rho}_g) \tag{7.25}$$

and is possible to write:

$$\Delta p_{DF} = \alpha \cdot (\rho_l - \bar{\rho}_g) \cdot g \cdot H \tag{7.26}$$

Now, introducing the flow quality *x* and the slip ratio *S*, defined respectively as:

$$x = \frac{\dot{m}_g}{\dot{m}_g + \dot{m}_l}, \quad S = \frac{u_g}{u_l} = \frac{1-\alpha}{\alpha} \cdot \frac{x}{1-x} \cdot \frac{\rho_l}{\rho_g} \tag{7.27}$$

the previous equation can be written as:

$$\Delta p_{DF} = \frac{(\rho_l - \bar{\rho}_g)\cdot g \cdot H}{1 + S \cdot \frac{1-x}{x} \cdot \frac{\bar{\rho}_g}{\rho_l}} \tag{7.28}$$

Let's now consider the right side of Eq. (7.20); Δp_{fric} represents the total pressure drop along the flow path. Since the localized loss of head in the two phase region is negligible, it can be written as:

$$\Delta p_{fric} = \frac{1}{2}\left[\sum f_{l0}\frac{L}{D_e}\rho_l \bar{v}^2 + \sum K \rho_l \bar{v}^2 + \Phi_{l0}^2 \cdot f_{l0}\frac{L_r}{D_{e,r}}\rho_l \cdot \bar{v}^2\right] \tag{7.29}$$

where the first term represents the distributed loss of head by friction through the single phase region, the second term represents the loss localized in singularities (such as the effect of sudden expansion or contraction, valves, orifices, etc.) and the third represents the loss of head by distributed friction along the two phase region.

The first and the third terms are characterized by a specific characteristic length, equivalent diameter, flow pattern and then friction coefficient.

Introducing the liquid flow rate, Eq. (7.29) can be written as:

$$\Delta p_{fric} = \left(\sum f_{l0}\frac{L}{D_e} + \sum K + \Phi_{l0}^2 f_{l0}\frac{L_r}{D_{e,r}}\right)\frac{\dot{m}_l^2}{2\rho_l A_r^2} = K_t \frac{\dot{m}_l^2}{2\rho_l A_r^2} \tag{7.30}$$

where A_r is the riser cross-section.

Since the single phase as well as the two phase distributed pressure losses are negligible in comparison to the singular pressure drops along the path, K_t is independent of the flow rate.

Moreover, under the tested condition, it can be assumed that:

$$1 + S \cdot \frac{\dot{m}_l}{\dot{m}_g} \cdot \frac{\bar{\rho}_g}{\rho_l} = S \cdot \frac{\dot{m}_l}{\dot{m}_g} \cdot \frac{\bar{\rho}_g}{\rho_l} \tag{7.31}$$

and it is possible to write:

$$\frac{(\rho_l - \bar{\rho}_g)\cdot g \cdot H}{S \cdot \frac{\dot{m}_l}{\dot{m}_g} \cdot \frac{\bar{\rho}_g}{\rho_l}} = K_t \cdot \frac{\dot{m}_l^2}{2 \cdot \rho_l \cdot A_r^2} \tag{7.32}$$

Rearranging the previous equation we have:

$$\frac{2 \cdot (\rho_l - \bar{\rho}_g)\cdot g \cdot H \cdot \rho_l^2 \cdot A_r^2}{S \cdot K_t \cdot \bar{\rho}_g} \cdot \dot{m}_g = \dot{m}_l^3 \tag{7.33}$$

and then:

$$\dot{m}_l = A \cdot \left(\dot{m}_g\right)^{0.33} \tag{7.34}$$

where

$$A = \frac{2 \cdot (\rho_l - \bar{\rho}_g) \cdot g \cdot H \cdot \rho_l^2 \cdot A_r^2}{S \cdot K_t \cdot \bar{\rho}_g} \tag{7.35}$$

can be considered as a constant.

For each steady state achieved, the void fraction distribution along the riser has been evaluated by the "manometric method", measuring the loss of pressure across the riser by means of five differential pressure transducers (DPTs) at different levels.

The measured loss of pressure along each part in which the riser is divided can be expressed as:

$$\Delta p_m = \Delta p_{fric} + \Delta p_{acc} + \Delta p_{grav} \tag{7.36}$$

Equation (7.36) expresses the pressure drop in the channel as the sum of three components — acceleration, friction and gravity; for all the investigated two phase flow conditions, both the friction and the acceleration pressure drops in each part of the riser have been evaluated according to Lockhart and Martinelli [26] and Todreas and Kazimi [27].

As a first approximation, it is possible to write:

$$\Delta p_{grav} >> \Delta p_{fric} + \Delta p_{acc} \tag{7.37}$$

and so:

$$\Delta p_m = p_{grav} = \bar{\rho}_m g h \tag{7.38}$$

where h is the height of the considered branch. Then, it is possible to estimate the average void fraction in each part of the riser by the following equations:

$$\bar{\alpha} = \frac{\rho_{LBE} - \bar{\rho}_m}{\rho_{LBE} - \bar{\rho}_g} \tag{7.39}$$

where

$$\bar{\rho}_m = \frac{\Delta p_m}{g h} \tag{7.40}$$

and $\bar{\rho}_g$ is the average gas density in the considered part of the riser.

Figure 7.27 shows the void fraction trends as a function of the injected argon flow rate in the riser for the test performed at 200°C. As can be noted, for the same gas flow rate, the void fraction increases along the riser as the pressure decreases. Moreover, the void fraction trend as a function of the gas injection flow rate is quite similar for any considered rate (isolevel curve).

Concerning the influence of the temperature, the liquid flow rate increases with temperature, as shown in Fig. 7.28.

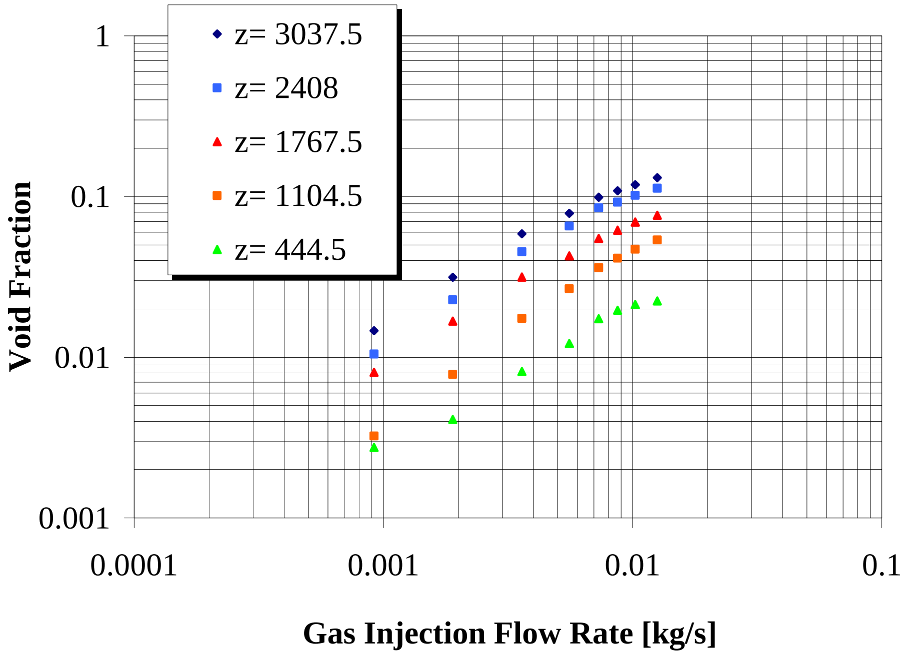

FIG. 7.27. Void fraction measured along the riser as a function of the gas flow rate for the tests performed at 200°C.

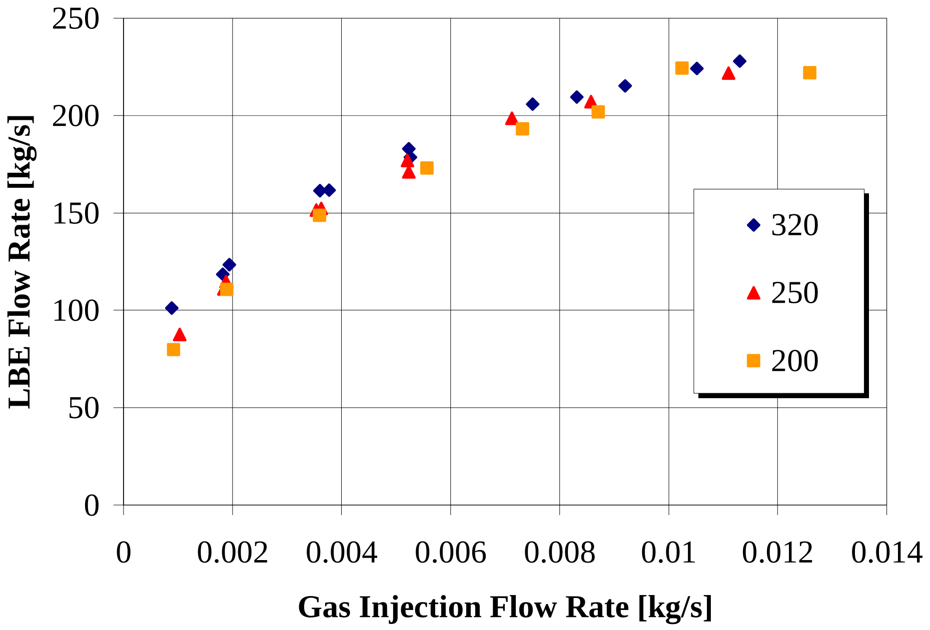

FIG. 7.28. LBE flow rate as a function of the argon flow rate for three different LBE temperatures.

Actually, as the temperature increases, the dynamic viscosity of the LBE decreases and the viscous pressure losses decrease too. However, as can be noted in Fig. 7.28, the dependence on the temperature is rather weak, and this behaviour suggests that the viscous pressure losses are small in comparison to the singular pressure drops (at the drilled disk installed along the feeding conduit). In fact, increasing the temperature from 200°C to 320°C, the dynamic viscosity of the LBE undergoes a reduction of about 30%; so, for the same DF in the systems (that means the same void fraction distribution along the riser), a little increment in the flow rate should be expected. By the way, this increment can be expected to be lower since the singularities play a key role in the system.

Concerning the void fraction, for the same gas flow rate, as the temperature increases, the void fraction in the riser increases too (see Fig. 7.29).This is because the argon undergoes a stronger isothermal expansion in the riser, the specific volume of the gas increasing with the temperature.

This behaviour suggests that, if the temperature of the system increases, the DF available for the circulation will increase (see Eq. (7.26)).

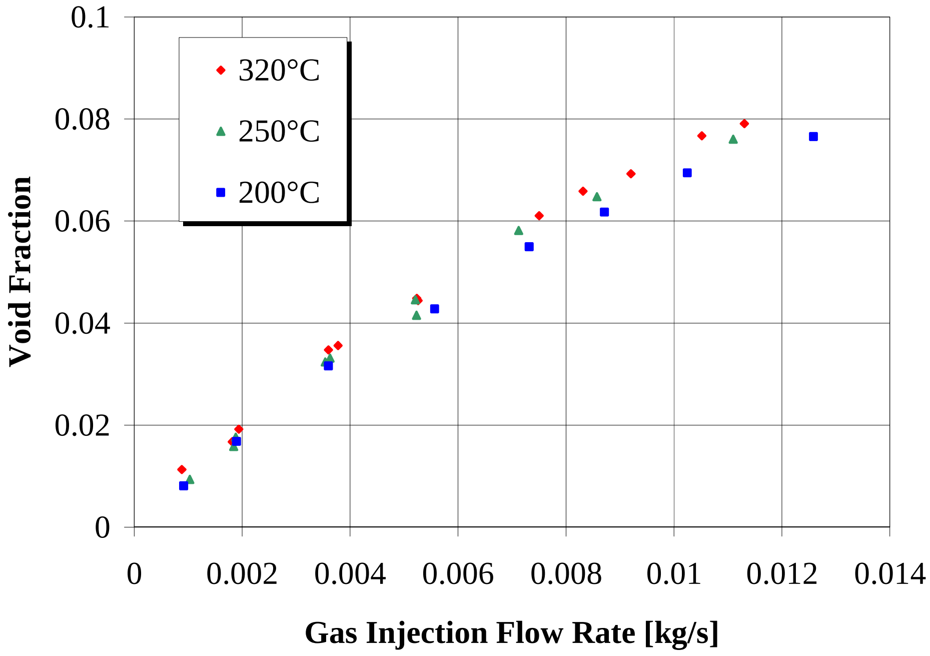

FIG. 7.29. Steady state void fraction in the central branch of the riser, as a function of the injected gas flow rate, for three different LBE temperatures.

The possibility of enhancing the LBE circulation by gas injection has been confirmed in the CIRCE facility. The obtained results show that, for argon flow rate injections higher than 1 Nl/s, it is possible to reach a steady flow of LBE through the adopted test section, that is able to reproduce the velocity fields expected for the reference ADS plant. A relation between the entrained liquid metal flow rate and the injected one has been carried out by curve fitting of the experimental data. This relation follows a power law justified by theoretical considerations.

The void fraction distribution along the riser has been evaluated by the application of the "*manometric method*"; the obtained results confirm that a strong dependency exists between the DF available for the circulation and the void buoyancy generated in the riser by the injected gas.

Finally, in the analysed range of temperatures, the circulation of the liquid metal is weakly dependent on the system temperature.

7.7. NATURAL AND GAS ENHANCED CIRCULATION TESTS IN THE NACIE LOOP

An experimental campaign is in progress on the NACIE loop, located at the CR ENEA Brasimone and depicted in Fig. 7.30.

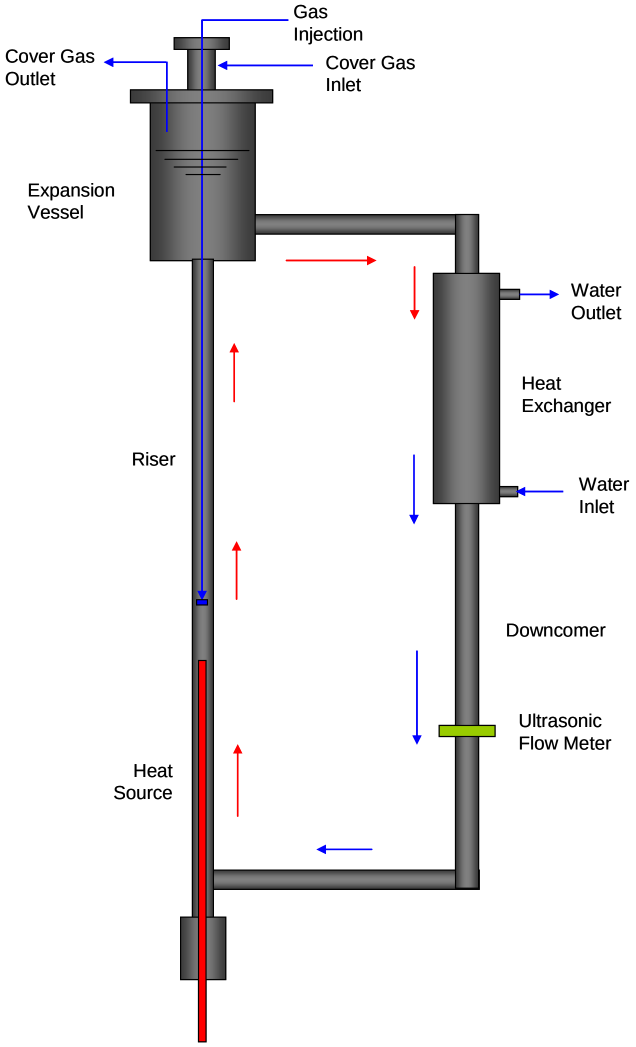

FIG. 7.30. NACE loop layout.

The NACIE loop was set up as a support facility able to qualify and characterize components, systems and procedures relevant for HLM nuclear technologies. In particular, at the NACIE loop, it will be possible to run experimental activities aiming to address the convection phenomena influenced by buoyancy. In fact, the single phase mixed convection is a common issue encountered in all innovative nuclear systems. Heat transfer from fuel to coolant is strongly affected by buoyancy, which may lead to undesired behaviour of flow and heat transfer, such as flow instability and heat transfer deterioration.

This activity will make available experimental data also for the assessment of heat transfer correlations in a rod bundle assembly in natural and gas enhanced circulation flows.

The NACIE loop was prepared to house different kinds of fuel bundles, characterized by different geometries, pin heat flux and power density.

TABLE 7.3. NACIE BUNDLE CHARACTERISTICS

Number of active pins		2
Diameter	[mm]	8.2
Active length	[mm]	850
Total length	[mm]	1400
Heat flux	[W/cm^2]	100
Thermal power	[kW]	22
Flux distribution		Uniform

The NACIE bundle consists of two high thermal performance electrical pins and two dummy pins to support the bundle itself; the characteristics of the active pins are reported in Table 7.3. The total installed power is about 45 kW, although during the tests only one pin is active. In Fig. 7.31, a sketch of the bundle is shown.

In the middle section of the active length, an appropriate spacer grid is installed to allow the thermal expansion of the pins, keeping constant the flow area of the subchannel which could be affected by the bowing of the pins itself.

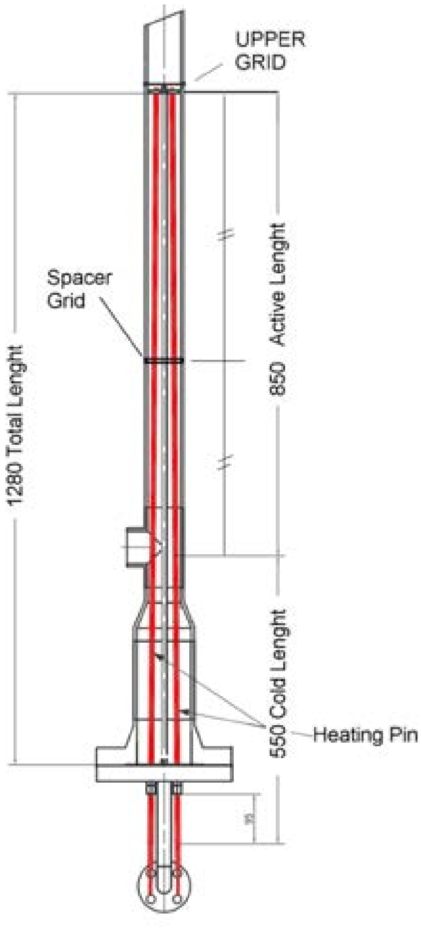

FIG. 7.31. Sketch of the NACIE bundle.

In Fig. 7.32, a cross-section of the spacer grid is shown, while in Fig. 7.33 the photo of the bundle shows the spacer grid, active and dummy pins, and a thermocouple installed close to the grid on the pin cladding.

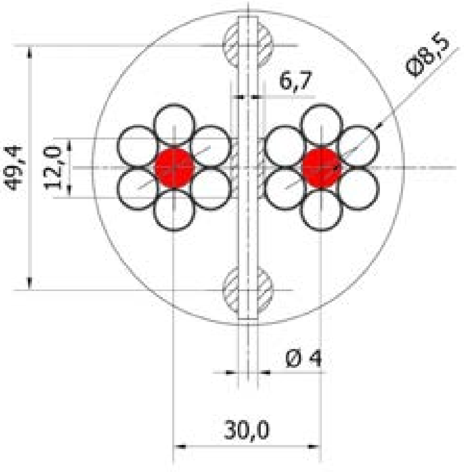

FIG. 7.32. Cross-section of the NACIE bundle.

FIG. 7.33. View of the NACIE bundle.

At each active pin, seven thermocouples have been installed, in order to monitor the trend of the cladding temperature during the test in different positions. Table 7.4 reports the height (x-position starting from the bottom) along the active length, as well the azimuthal position of the thermocouples installed on each active pin.

In the following paragraph, the abbreviations TC1X and TC2X will be used to indicate the thermocouples in the x-position (see Table 7.4) on the active pin n.1 and n.2, respectively. As can be noted, the TCs installed allow to make a rough evaluation of the hot spot factor on the pins due to the spacer grid installation, as well as to draw the axial temperature profile along the active pin.

TABLE 7.4. HEIGHT AND AZIMUTHAL POSITION OF TCs INSTALLED ALONG THE ACTIVE LENGTH OF THE PINS

TC	Active pin n.1	Active pin n.2
1	50 mm (0°)	50 mm (0°)
2	410 mm (0°)	410 mm (0°)
3	425 mm (0°)	425 mm (0°)
4	425 mm (120°)	425 mm (120°)
5	425 mm (240°)	425 mm (240°)
6	440 mm (0°)	440 mm (0°)
7	800 mm (0°)	800 mm (0°)

To promote the LBE circulation along the loop, a gas lift technique is adopted [7.11, 7.28–7.30]. A pipe having an inner diameter of 10 mm is housed inside the riser, connected through the top flange of the expansion tank to the argon feeding system. At the other end of the pipe, the injection nozzle is mounted, located just downstream the heating section (HS). The gas is injected in the riser through the nozzle, enhancing the liquid metal circulation.

In the expansion tank, the separation between the phases takes place. In this way, the risk is avoided to have a two phase mixture flowing through the heat source. The gas injection system is able to supply an argon flow rate in the range of 1–75 Nl/min, with a maximum injection pressure of 5.5 bar.

The heat exchanger (HX) designed for the NACIE loop is a ‘tube in tube’ counter-flow type; the secondary fluid is water at low pressure (about 1.5 bar). The HX is made of three coaxial tubes with different thicknesses.

The experimental activity performed on the NACIE facility included several tests concerning natural circulation (NC) and gas enhanced circulation (GEC). In particular, each test has been performed with only one pin activated inside the HS, with a nominal power of 22.5 kW. In Table 7.5, the adopted test matrix is reported, highlighting the flow regime investigated, the gas injection flow rate in the case of gas enhanced circulation test, the total power supplied to the system through the HS as well as the ramp time imposed at the power supply system to obtain the chosen value.

TABLE 7.5. NACIE ACTIVITY TEST MATRIX

Test	Flow regime	Gas injection flow rate [Nl/min]	Power ramp time [min]	Supplied power [kW]	Heating section average temperature [°C]
1	NC	-	30	18	300
2	NC	-	30	20.2	320
3	NC	-	30	22.5	340
4	NC	-	30	18	310
5	NC	-	30	20.2	340
6	NC	-	30	22.5	cancelled
7	GEC	5	1	13.5	cancelled
8	GEC	5	1	18	280
9	GEC	5	1	22.5	300
10	GEC	5	1	13.5	270
11	GEC	5	1	18	300
12	GEC	5	1	22.5	330
13	GEC	5–10	1	22.5	330
14	GEC	10–20	1	22.5	330
15	GEC	10–25	1	22.5	330
16	GEC NC	5–15	1	22.5	320
17	GEC NC	5–15	1	22.5	345
18	NC	-	1	18	280
19	NC	-	1	22.5	315
20	NC	-	1	18	315
21	NC	-	1	22.5	350
22	NC	-	1	22.5	390
23	GEC	5–10	1	22.5	380

Finally, also the average temperature of the HS has been indicated, because it is one of the main parameter which has to be taken into account when the behaviour of the system is investigated. For this aim, different boundary conditions have been applied on the secondary side of the HX, in terms of water flow rate as well as water inlet temperature. The range of LBE average temperatures considered in our experimental campaign is 270–345°C.

As can be seen from Table 7.5, heater power was supplied to the HS also in the case of enhanced circulation test. In fact, the ultrasonic flowmeter was not yet installed along the NACIE loop. An estimation of the LBE flow rate under steady state condition, for both the NC and the GEC tests was made applying an energy balance. In Fig. 7.34, the trend of the HLM flow rate carried out for the test n.21 is reported.

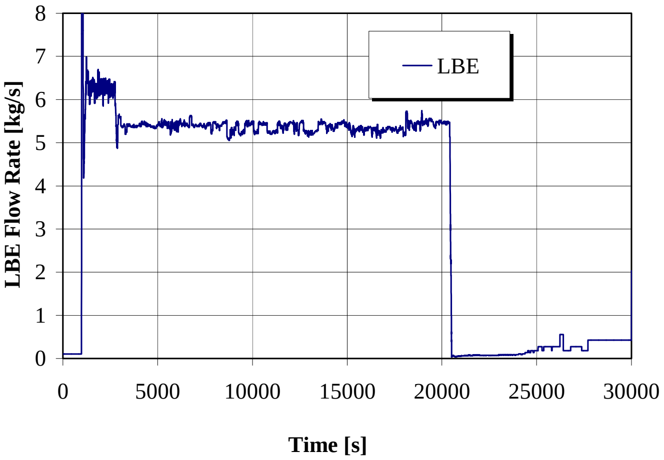

FIG. 7.34. Heavy liquid metal flow rate under natural circulation flow regime (test n.21).

Natural circulation tests were performed by supplying electrical power to the heater (activating the pin n.1) and circulating coolant in the secondary side of the heat exchanger. During the tests, no gas was injected in the riser, so, the only DF for fluid circulation in the loop results from thermal buoyancy.

After about 2000 s (see Fig.7.36), a steady state condition was obtained with an estimated flow rate of about 5.5 kg/s. In Fig. 7.36, the trend of the inlet and outlet temperature through the HS is reported, depicting the transients during the NC tests. For the same test, Fig. 7.36 presents the value of the Reynolds number and average lead-bismuth velocity through the HS. As can be noted, the LBE velocity during the NC tests is less than 0.25 m/s, and in steady state condition the Reynolds number is about 40 000. The cladding temperature trend of the active pin (pin n.1) on the matching surface between pin and spacer grid is depicted in Fig. 7.37 for the test 22. As can be noted, the temperature is quite uniform around the pin, and even if the test n.22 is quite severe, the maximum cladding temperature is quite below 550°C.

In Fig. 7.38, for the same test, the cladding temperature trend upstream and downstream of the spacer grid is shown, compared with the trend obtained on the matching surface. The hot spot factor clearly appears in this figure, the temperature of TC14 being higher by about 15°C than the upstream temperature TC16.

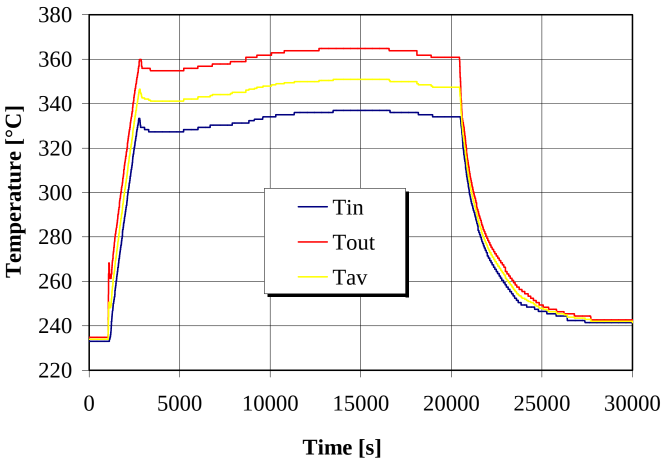

FIG. 7.35. Inlet and outlet temperature through the HS under a NC flow regime (test n.21).

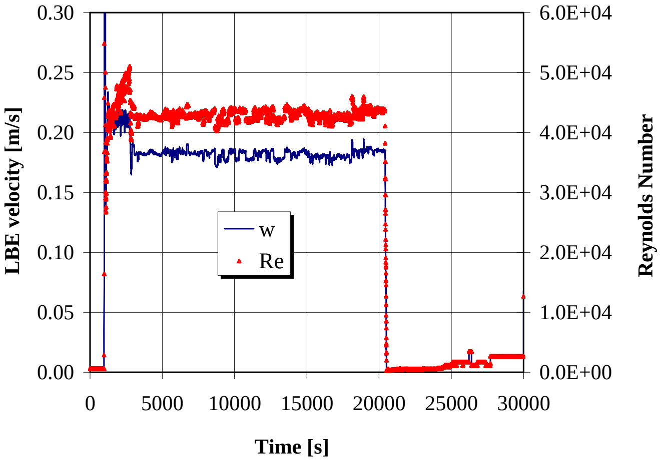

FIG. 7.36. LBE velocity and Reynolds number through the HS (test n.21).

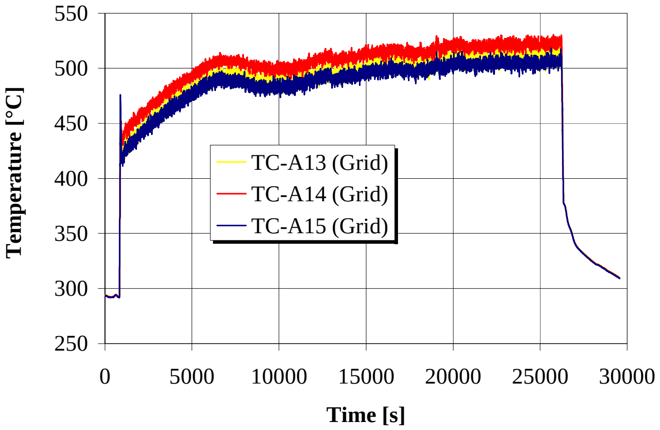

FIG. 7.37. Cladding temperature trend along the matching surface between active pin and spacer grid, NC test (test n.22).

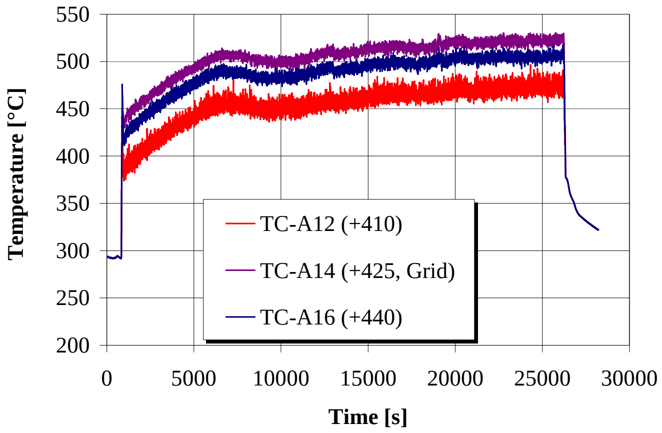

FIG. 7.38. Cladding temperature trend upstream and downstream the spacer grid, compared with the temperature along the matching surface, NC test n.22.

The hot spot factor due to the installation of the spacer grid clearly appears also in Fig. 7.39, where the cladding temperature trend of the active pin monitored in the lower end and in the upper end is compared with the thermocouple TC14. In this case, the difference between TC14 and TC17 is about 50°C.

Concerning the GEC tests, Fig. 7.40 reports the HLM flow rate trend compared with the gas injection flow rate, which promotes the LBE circulation along the loop. Gas enhanced circulation tests were performed by supplying electrical power to the heater (activating pin n.1), starting the argon injection and circulating coolant in the secondary side of the HX. During the tests, because argon is injected in the riser, the DF for fluid circulation in the loop results from void buoyancy in the riser.

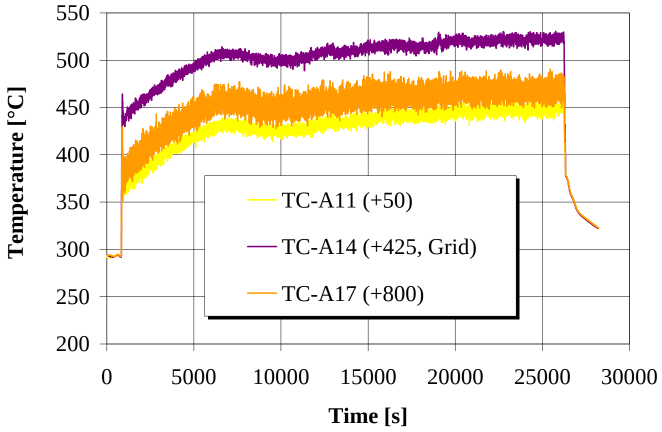

FIG. 7.39. Cladding temperature trend in the lower end and in the upper end of the pin, compared with the temperature along the matching surface with the spacer gird, NC test (test n.22).

As presented in Fig. 7.40, for the GEC tests, the LBE flow rate obtained is higher than the one obtained under natural circulation. With a gas injection of about 5 Nl/min, the liquid metal flow rate is about 13 kg/s.

In Fig. 7.41, the trend of the inlet and outlet temperature through the HS is reported, depicting the transients during the GEC tests, and highlighting that also in this case a steady state condition is obtained after about 2000 s.

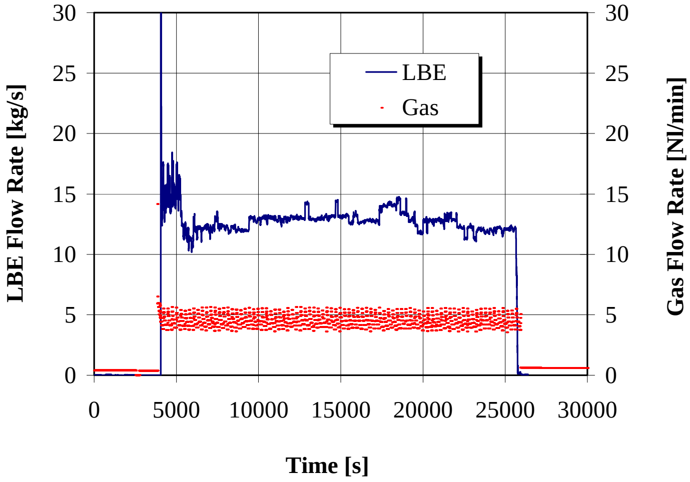

FIG. 7.40. HLM flow rate and gas injection flow rate for a GEC test (test n.12).

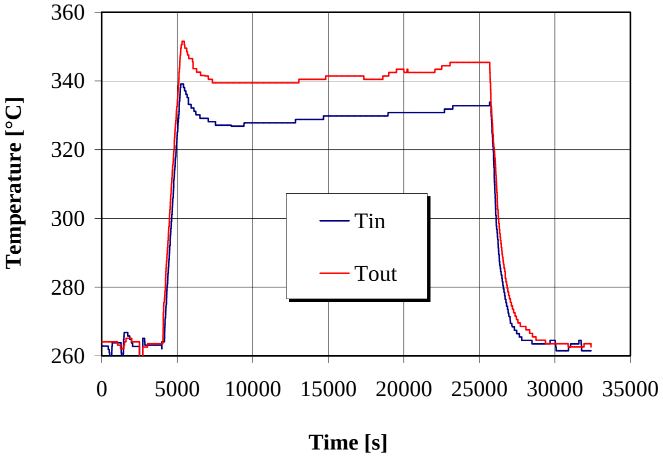

FIG. 7.41. Inlet and outlet temperature through the HS under a GEC flow regime (test n.12).

For the same test, Fig. 7.42 reports the value of the Reynolds number and average liquid metal velocity through the HS. As can be noted, the LBE velocity reaches a value of 0.45 m/s, against the 0.25 m/s obtained during the NC tests, and a Reynolds number of about 100 000, underlining the higher turbulent behaviour of the main stream line in the case of void buoyancy promoted flow.

For the GEC test n.9, Fig. 7.43 reports the cladding temperature trend of the active pin (pin n.1) on the matching surface between pin and spacer grid. In this case, the temperature around the pin is not as uniform as in the case of test n.22, and the thermocouple TC14 shows that an azimuthal hot spot factor appears.

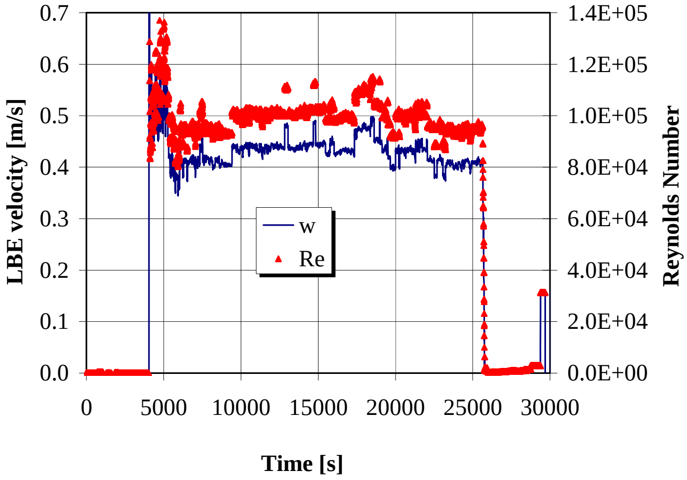

FIG. 7.42. LBE velocity and Reynolds number through the HS (test n.12).

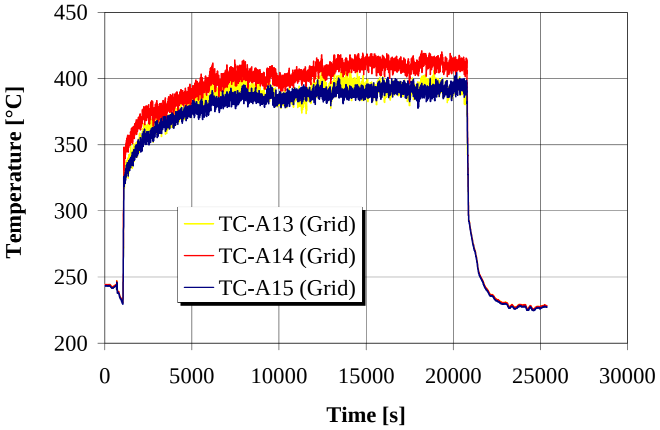

FIG. 7.43. Cladding temperature trend along the matching surface between active pin and spacer grid, GEC test (test n.9).

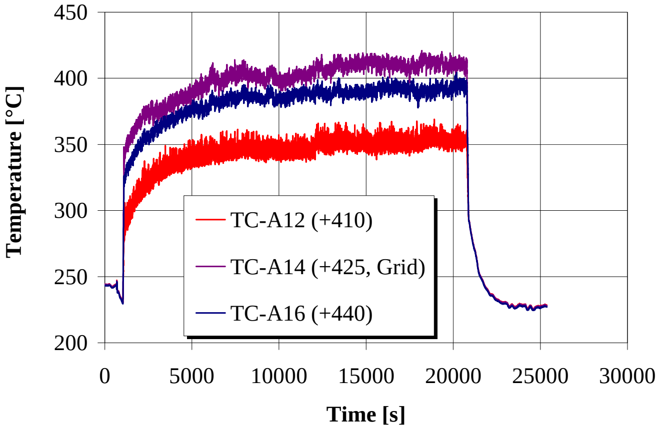

FIG. 7.44. Cladding temperature trend upstream and downstream the spacer grid, compared with the temperature along the matching surface, GEC test (test n.9).

Anyway, for the gas lift tests, the maximum temperature on the pin is well below 450°C, highlighting that the heat transfer coefficient between the liquid metal and the pin is really increased if compared with the NC tests.

Figure 7.44 shows the cladding temperature trend upstream and downstream of the spacer grid, compared with the trend obtained on the matching surface. Also for this test, the hot spot factor clearly appears, with the TC14 higher by about 15°C than the upstream temperature TC16.

Again, also in Fig. 7.45, the hot spot factor appears, and also in this case, the difference between TC14 and TC17 is about 50°C, as reported in Fig. 7.39.

So, for the experimental tests carried out on the NACIE loop, the magnitude of the hot spot factor seems quite independent from the turbulence and liquid metal velocity, at least in the investigated range.

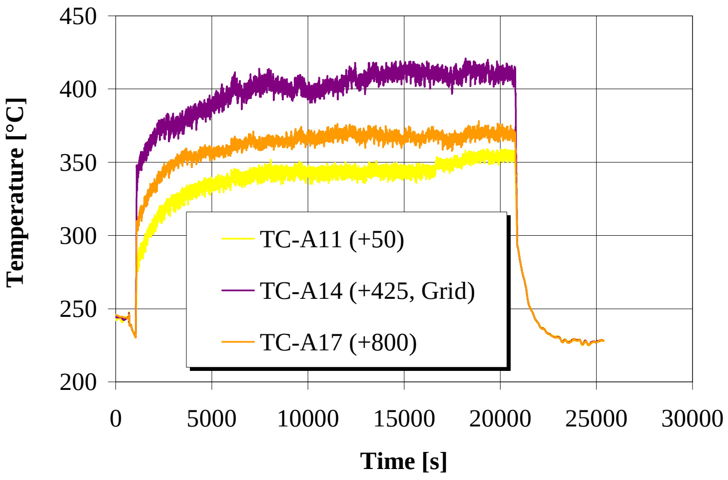

FIG. 7.45. Cladding temperature trend in the lower end and in the upper end of the pin, compared with the temperature along the matching surface with the spacer grid, GEC test (test n.9).

As reported, several experimental tests have been performed in the NACIE loop, testing different types of prototypical pins with high thermal performance (heat flux up to 1 MW/m^2) aiming to be adopted as fuel pin simulator in large scale experiments in a pool type configuration [7.31]. In the experimental campaign presented, a new simple bundle, well instrumented, has been installed in the NACIE loop, with the goal to qualify the thermal behaviour of the pins for future applications, and to obtain experimental data about NC and GEC in HLM loop.

Moreover, a rough estimation of the hot spot factor due to the installation of a home-made spacer grid along the heating length of the pins was performed.

The tests carried out allow to preliminarily address the phenomena related to the NC as well as the mixed convection in a HLM loop, and to establish a reference experiment for the benchmark of commercial codes when employed in the HLM loop.

7.8. PRESSURE DROP AND HEAT TRANSFER IN MOLTEN SALT (FLINAK) FLOW THROUGH 1.4 MM-DIAMETER CIRCULAR TUBE

7.8.1. Introduction

Flinak is a mixture of LiF, NaF and KF. The mole fraction of each salt is 46.5%, 11.5% and 59.1%, respectively, or 29.2%, 11.7% and 59.1% in mass. The objective of the present study was originally to investigate the thermohydraulic characteristics of the Flinak molten salt flow in a small channel of millimeter-range hydraulic diameter in order to provide the thermohydraulic data for designing a compact He-Flinak Intermediate Heat Exchanger (IHX) of Very High Temperature Reactor (VHTR). The melting point of this eutectic salt mixture is 454°C and the major physical properties are given in Table 7.6 [7.32].

TABLE 7.6. PHYSICAL PROPERTIES OF MOLTEN FLINAK AND HELIUM GAS AT 700°C (He at 7 MPa)

		Flinak	He
Melting point	°C	454	-
Density	kg/m^3	2020	4.818
Specific heat	kJ/kg K	1.88	5.19
Viscosity	*m*Pa·s	2.90	0.036
Thermal conductivity	W/m K	0.92	0.281

The millimeter-range diameter small channels are illustrated in Fig. 7.46. This plate was constructed using the concept of printed circuit heat exchanger (PCHE). Half-circular grooves of 1.2 mm diameter were chemically etched on a 2 mm thick plate of Inconel 600 and two etched plates were then diffusion-bonded. Such plates with small channels are used in constructing a compact HX.

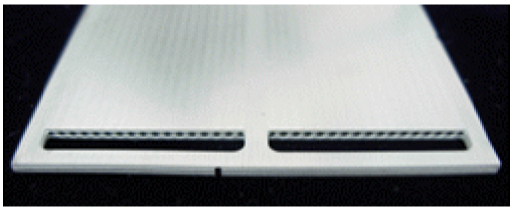

FIG. 7.46. Diffusion-bonded plate with chemically-etched small channels (d~1.2 mm).

7.8.2. Experimental apparatus

The Flinak is an eutectic mixture of LiF, NaF and KF, and the molten salt must be maintained at higher temperature than the melting point of 454°C to prevent even partial freezing near a cold wall. The handling and operation of the Flinak also requires an oxygen and humidity free environment since this high temperature molten salt is chemically unstable to water vapour and oxygen. The experimental setup and the procedure have been carried out with careful consideration of these characteristics of Flinak. The experimental apparatus consists of a molten salt loop and a high temperature gas loop as shown in Fig. 7.47.

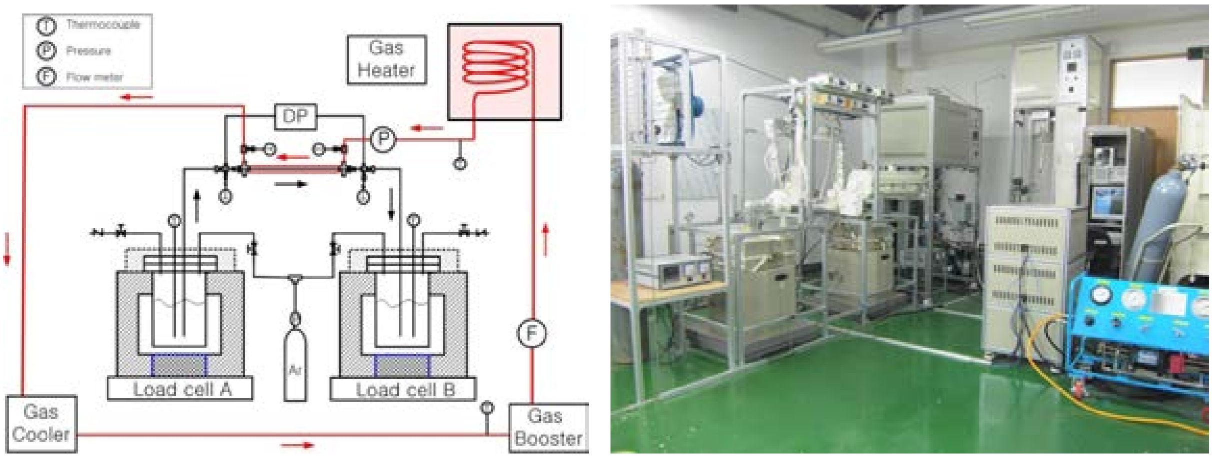

FIG. 7.47. A schematic diagram and photographic view of molten salt–gas heat exchange loop.

To avoid using a mechanical pump for high temperature salt flow, two crucible tanks made of Inconel 600 are used and a differential pressure across these two tanks causes the molten salt to flow from the high pressure tank (supplying tank) to the low pressure tank (receiving tank). All pipes for the molten salt flow are wrapped by electric heating jackets in order to maintain the pipe wall above the melting point of the salt. The flow rate of the molten salt is deduced from the weight change of a crucible measured by load cells.

A double pipe type HX using small diameter tubes was constructed for the heat exchange between the molten salt and the gas (helium or argon). The material of the tubes and tube fittings is Inconel 600. The outer and the inner diameters of the inner tube are 3.18 mm and 1.40 mm, and of the outer tube, 6.35 mm and 4.57 mm, respectively. The length of the test section is 500 mm. The molten salt flows through the inside of the inner tube and the gas flows through the annulus of 0.7 mm gap. Temperatures of the two heat exchanging fluids are measured at various points including the inlets and the outlets, as well as the pressure drop across the molten salt inlet and the outlet to obtain the flow and heat transfer characteristics of the molten salt flow. The temperatures are measured using exposed, Inconel-sheathed K-type thermocouples.

The gas loop is to provide high temperature gas flow of either helium or argon to the HX and it consists mainly of gas booster, coil-in-furnace gas heater, pressure regulator, coriolis-type flowmeter and a cooler. The gas loop is designed to operate at high pressure (<7 MPa) and high temperature (<950°C). All the temperature, pressure and flow rate data are monitored and recorded using the Labview system.

The three salts, LiF, NaF and KF, were first mixed in powder form according to the required mass fractions in a moisture free, inerted glovebox and the mixed powder was then loaded into a crucible placed in an electric furnace. The first melting of Flinak in powder form was successful according to the observed salt temperature as shown in Fig. 7.48. Thereafter, the first molten salt was solidified in the crucible and was re-melted for the next experimental run. The temperature trace shown in Fig. 7.48 is the typical temperature behaviour of the salt inside the crucible indicating the heating up and the melting. According to this temperature trace, the melting begins at ~460°C and is completed at ~490°C.

The molten salt flow rate was successfully measured by monitoring the weight changes of both crucibles placed on separate mass balances employing load cells. The mass change of

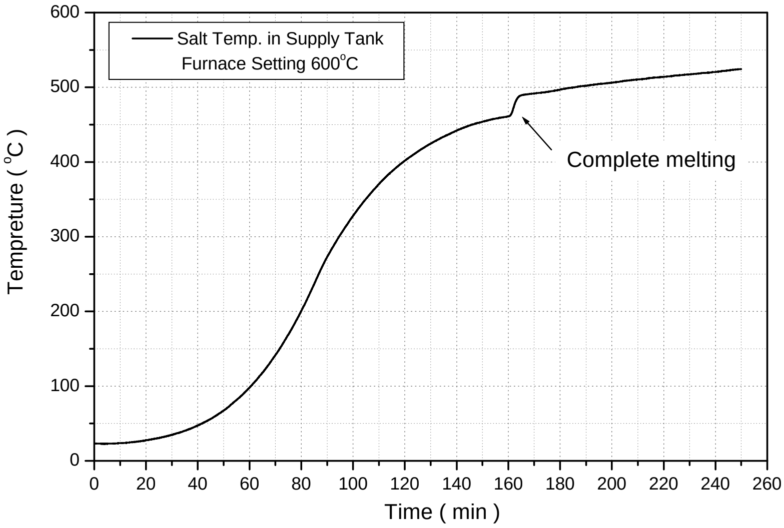

FIG. 7.48. Flinak temperature trace during melting.

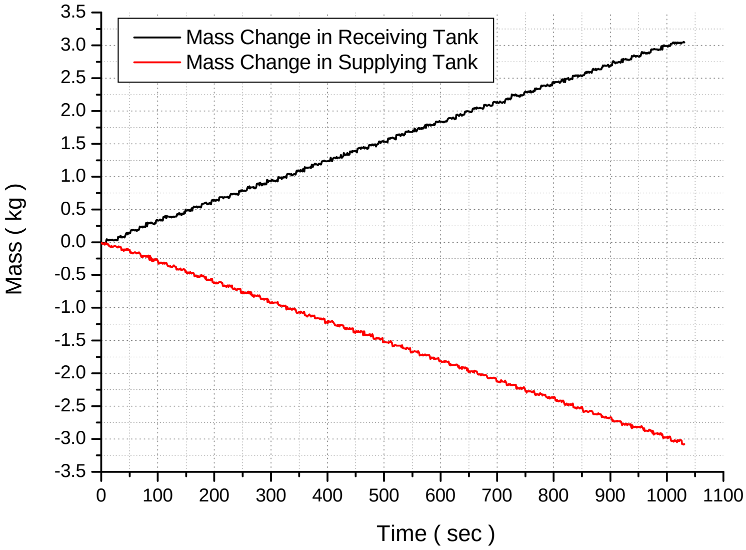

FIG. 7.49. Mass changes of supplying and receiving crucibles used for Flinak flow rate measurement.

the supplying tank was equal to the mass change of the receiving tank as shown in Fig.7.49. Although the flow rate was nearly constant throughout the test time as the differential pressure was held constant at a desired value, the mass balance data was best-fitted into a quadratic function of the mass change to get more accurate time dependent flow rates of the molten salt.

The range of the inlet temperature of the molten salt was limited by the melting point of the salt at the lower end and the available hot gas inlet temperature at the upper end. In this report of the data, argon gas was used for the heating gas and the inlet temperature ranges are 500–650°C for the molten salt and 620–665°C for the argon gas.

7.8.3. Results and discussion

7.8.3.1. Friction factor in laminar flow of Flinak

By applying a differential pressure in the range of 0.1–0.3 bar across the supplying tank and the receiving tank of the salt, the molten salt flow rates of 4.4–11.5 kg/h were obtained. This range of salt flow rates corresponds to the Re number range of 250–600 in the 1.4 mm ID test tube, indicating the salt flow is a laminar flow, as expected for small diameter tubes. The measurement of the pressure drop of the molten salt flow across the test section was often a problem due to an unexpected freezing of the salt inside the pressure guide tubes.

The correct measurement of pressure drop in the present experiment must include the hydrostatic head of the molten salt rising in the guide tube to the differential pressure transducer. The measurement of the height of the molten salt in the guide tube was possible by inserting a metered wire through the guide tube from the sensor side while the power to the heating jacket covering the guide tube was off temporarily to freeze the molten salt in the guide tube.

The measured pressure drop data for the Flinak was reduced to friction factors using the relation of pressure drop and the friction factor. The ORNL correlation for temperature dependent viscosity of the Flinak was used in this calculation [7.33].

$$\Delta P = f \frac{L}{d} \frac{G^2}{2\rho} \tag{7.41}$$

As shown in Fig. 7.50, the measured friction factor shows a good agreement with the analytical relation of 64/Re for laminar flow in circular tube [7.37], implying that the Flinak molten salt is a Newtonian fluid in small diameter channels.

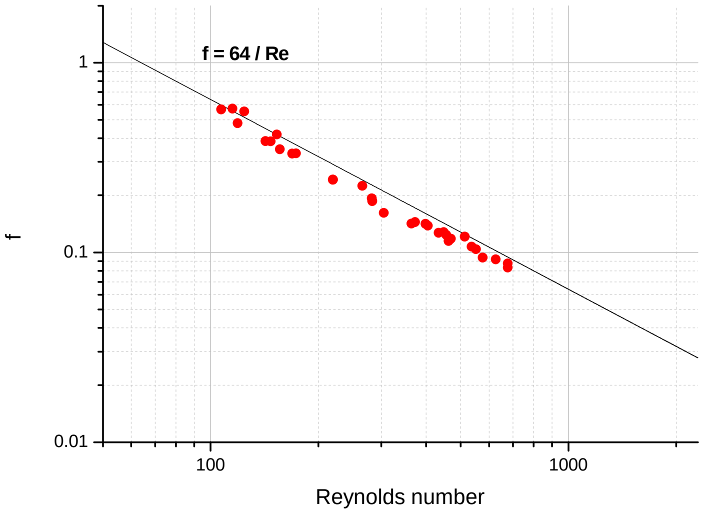

FIG. 7.50. Measured friction factors of Flinak flow in 1.4 mm inner diameter round tube and comparison with the theoretical laminar flow relation.

Viscosity data of Flinak are rare and uncertainty can be large as discussed in the ORNL report. There are two correlations available for the Flinak viscosity: the ORNL correlation [7.34] and the Oye correlation [7.35], [7.36]. The viscosity according to the ORNL correlation is 15% higher than the viscosity according to the Oye correlation over the temperature range of 600–650°C (Fig. 7.51).

ORNL correlation [7.34]:

$$\mu = 0.04\exp(4170/T), \qquad \mu:[mPa\cdot s],\ \ T:[K] \tag{7.42}$$

Oye correlation [7.35], [7.36]:

$$\mu = 1.633\exp(-2762.9T^{-1} + 3.1095\times10^{6}T^{-2}), \qquad \mu:[mPa\cdot s],\ \ T:[K] \tag{7.43}$$

Using the measured pressure drop of the laminar flow of Flinak, the viscosity can be calculated based on the analytical friction factor of f = 64/Re (Re = Gd/μ). The calculated viscosity is compared with the existing correlations in Fig. 7.51. The present data are close to the data of Torklep and Oye [7.36], but smaller by 20%. Based on the viscosity data obtained in the present experiment, a new correlation of viscosity of Flinak is proposed as follows:

$$\mu = 631\exp(-13490T^{-1} + 7.821\times10^{6}T^{-2}), \qquad \mu:[mPa\cdot s],\ \ T:[K] \tag{7.44}$$

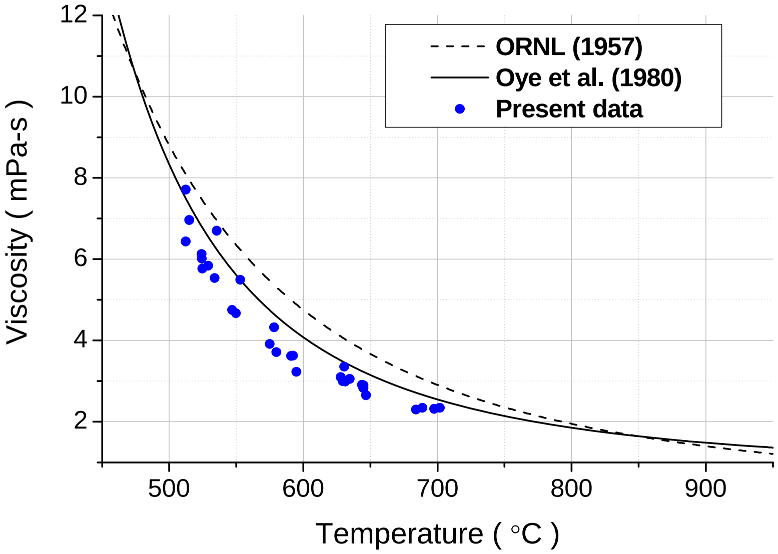

FIG. 7.51. Comparison of deduced viscosity from measured pressure drop and existing viscosity correlations for Flinak.

7.8.3.2. Heat transfer in laminar flow of Flinak

The heat transfer tests were run in the double-pipe type HX. The typical temperatures at both inlet and outlet of the two working fluids in the counter-flow direction are shown in Fig. 7.52. In the initial scoping tests, the heat loss from the hot gas to the surroundings was so large that the measured exit temperature of the hot gas was lower than the inlet temperature of the molten salt, although the test section was heavily insulated and wrapped with a heating jacket. The insulation has been further improved so that the heat loss was reduced and the measured temperatures were within the physically reasonable range as shown in Fig. 7.52. However, the heat loss from the hot gas was larger than the heat gain in the molten salt as shown in Fig. 7.53. The heat loss from the hot gas to the surroundings was too large to be ignored.

The heat balance of each fluid is calculated using the mass flow rate and the temperature rise or drop across the inlet and outlet.

$$q_{MS} = \dot{m}c_p(T_o - T_i)_{MS} \tag{7.45}$$

$$q_G = \dot{m}c_p(T_i - T_o)_G \tag{7.46}$$

It is noted that the molten salt flows through the inner tube so that the heat loss from the salt to the surroundings is negligibly small. Based on this condition, the actual heat transfer rate is assumed to be the molten salt side heat gain. The difference between the heat loss from the hot gas and the heat gain by the molten salt is the heat loss from the hot gas to the surroundings. As shown in Fig. 7.53, this heat loss is sizable enough to be considered in the heat transfer analysis for obtaining the heat transfer coefficient of the Flinak side.

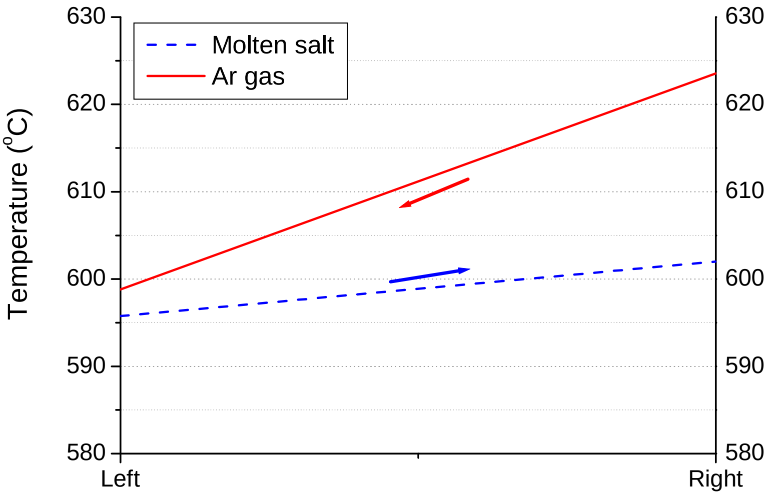

FIG. 7.52. Illustration of inlet and outlet temperatures in counter-flow HX.

If the heat loss to the surroundings is absent (or negligibly small) and the energy balance is met between the gain and the loss of the two fluids, the heat transfer rate can be written using the log-mean temperature difference. For the counter flow direction:

$$q = UA\Delta T_{LM} \tag{7.47}$$

$$\Delta T_{LM} = \frac{\Delta T_1 - \Delta T_2}{\ln(\Delta T_1 / \Delta T_2)} \tag{7.48}$$

$$\frac{1}{UA} = \frac{1}{(hA)_{MS}} + R_w + \frac{1}{(hA)_G} \tag{7.49}$$

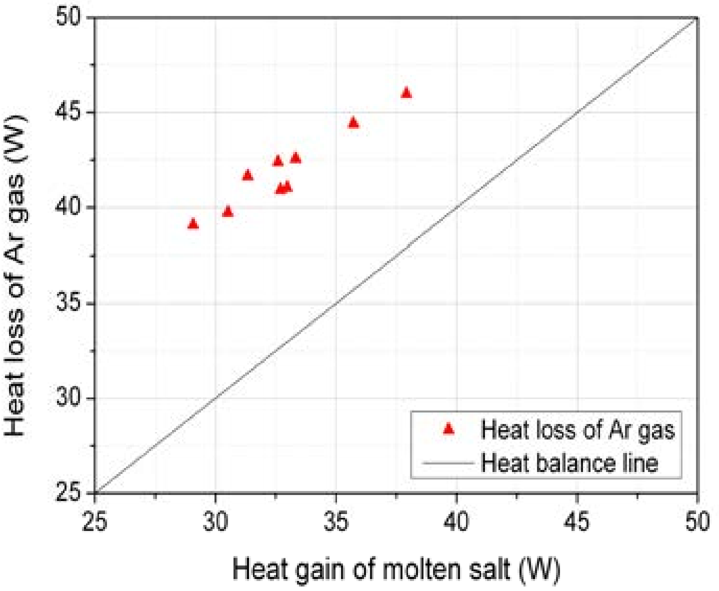

FIG. 7.53. Differences between heat gain and heat loss indicating the amount of energy loss to the surroundings.

Using the measured heat rate and the temperatures at the inlet and outlet and the dimensions of the tubes, the overall heat transfer coefficient, *UA*, can be calculated and from this value the molten salt side heat transfer coefficient can be calculated if the annulus-side heat transfer coefficient is known.

In case, however, that the heat loss to the surroundings is large, Eq. (7.47) can be modified to account for the heat loss. If the heat loss is assumed uniform across the HX, the heat balance equation for counter flow can be written for each fluid as:

$$dq = -\dot{m}_h c_{p,h} dT_h - dq_{loss} = -C_h dT_h - dq_{loss} \tag{7.50}$$

$$dq = -\dot{m}_c c_{p,c} dT_c = -C_c dT_c \tag{7.51}$$

Also the heat transfer rate can be written as:

$$dq = U(T_h - T_c)dA = U\Delta T dA \tag{7.52}$$

Combining Eqs (7.50, 7.51 and 7.52) results in a first-order differential equation for the temperature difference, ΔT:

$$\frac{d(\Delta T)}{dx} + P(\Delta T) = r$$

$$where, \ P = U(\pi d_o)\left(\frac{1}{C_h} - \frac{1}{C_c}\right), \quad r = -\frac{dq_{loss}}{C_h} \tag{7.53}$$

By solving Eq. (7.53), the relation between ΔT_1 and ΔT_2 can be obtained:

$$\Delta T_1 e^{-PL} = \Delta T_2 - \frac{r}{P}(1 - e^{-PL}) \tag{7.54}$$

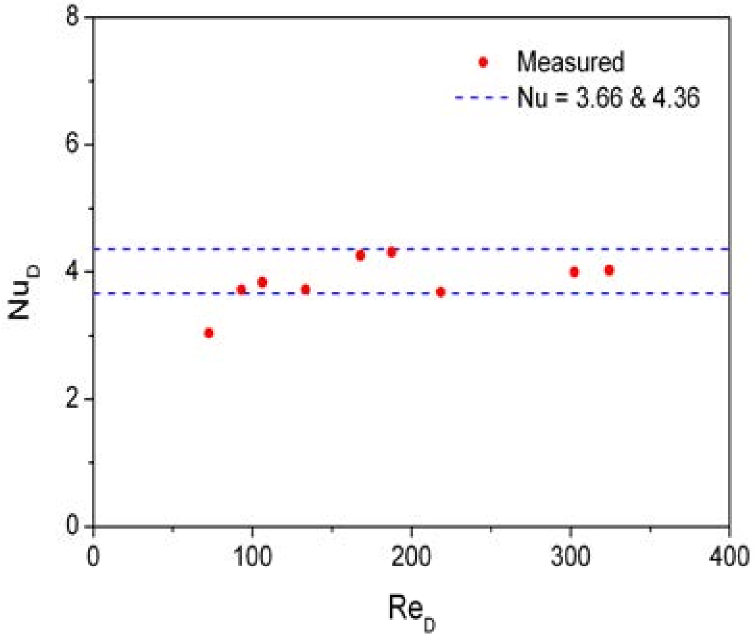

FIG. 7.54. Measured Nu numbers of Flinak flow in 1.4 mm inner diameter round tube.

The gas flow through the annulus was mostly turbulent flow in the present experiment. In general, the correlations of turbulent heat transfer coefficient for circular tubes can be applied also to an annulus but using the hydraulic diameter. In this analysis, the Gnielinski correlation [7.37] was used for the turbulent heat transfer coefficient in the annulus to obtain the heat transfer coefficient of the Flinak side. The calculated Nu numbers are plotted in Fig. 7.54. It is noted that the Nusselt number for the fully developed laminar flow in circular tubes is 3.66 for constant wall temperature and 4.36 for constant wall heat flux [7.37]. The comparison shows that the data generally lie within these theoretical values.

7.9. CONCLUSION

Experimental studies have been performed in test facilities for single phase NC flow in liquid metal loop “HANS”. Transient studies have also been performed in the same loop. A computer code is developed and steady state and transient analyses have been performed. Results show a good agreement between theoretical and experimental studies.

Experimental studies on enhanced circulation of HLM by gas injection have been performed in the ENEA LBE facility “CIRCE” located at CR Brasimone. The possibility of enhancing the LBE circulation by gas injection has been confirmed in the CIRCE facility.

Further, the experiments are performed in the NACIE loop, with the goal to qualify the thermal behaviour of the pins for future applications, and to obtain experimental data about NC and GEC in HLM loop.

The molten salt Flinak, a potential candidate as a working fluid for the intermediate heat transport loop of high temperature reactors such as VHTR, has been experimentally studied for its thermal and flow behaviour in a small channel of a compact HX. By using the pressure drop data in laminar flow, a correlation for the viscosity of Flinak was established. Also, it was found that the measured Nusselt number was in general agreement with the theoretical values, in the range between 3.66 and 4.36.

List of abbreviations and symbols to Chapter 7

A	Area (m^2)
C_p	Specific heat (J/kg-K)
Co	Courant number (dimensionless)
D, d	Diameter (m)
De	Equivalent diameter (m)
E	Emf (V)
F	Faraday constant, (C/mol)
ΔF	Free energy of formation, (J/K-mol)
f	Darcy friction factor (dimensionless)
G	Mass flux (kg/s-m^2)
Fo	Fourier number (dimensionless)
Gr_m	Modified Grashof number (dimensionless)
g	Acceleration due to gravity (m/s^2)
h	Heat transfer coefficient (W/m^2-K), or height (m)
H	Hydrostatic height (m)
k	Thermal conductivity (W/m) or local loss coefficient (dimensionless)
K	Concentrated loss coefficient
L, l	Length (m)
LT	Level meters
$\dot{m}$	Mass flow rate (kg/s)
NG	Geometrical parameter (dimensionless)
Nu	Nusselt number ($h_{in}d_{in}/K$)
p	Pressure (N/m^2)
p_0	Cover gas pressure (N/m^2)
Pe	Peclet number
PT	Pressure meters
q	Heat flux rate (W/m^2)
Q	Heat transfer rate (W)
R	Constant (Eq. Gas constant (J/K-mol)
R_w	Thermal resistance
S	Slip ratio
t	Time (seconds)
T	Temperature (^oC, K)
ΔT_{LM}	Log-mean temperature difference
T_o	Reference temperature (^oC)
U	Overall heat transfer coefficient (W/m^2K)
v	Velocity (m/s)
W	Mass flow rate (kg/s)
x	Length wise distance (m)
z	Height or curvilinear coordinate (m)

α	Thermal diffusivity in liquid (m^2/s) or void fraction
β	Thermal expansion coefficient (K^{-1})
φ	Interfacial friction factor
μ	Viscosity (m^2/s)
ρ	Density (kg/m^3)
ρ_o	Density at reference temperature (kg/m^3)
Δp	Pressure drop (N/m^2)
$\Delta \rho$	Density difference (kg/m^3)
Δx	Length difference (m)
Δz	Height difference (m)
χ	Flow quality

Subscripts

a	ambient
acc	acceleration
c	cold fluid
DF	driving force
f	fluid
fric	friction
g, G	gas
grav	gravity
h	heater or hot fluid
i	i^{th} node or inlet
in	inside
l	liquid
ln	logarithmic mean
m	average or mixture
max	maximum
min	minimum
MS	molten salt
n	n^{th} time step
o	outside, or outlet
r	riser
s	secondary side
ss	steady state
t	total
w	wall
1	inlet side of hot fluid
2	inlet side of cold fluid

REFERENCES TO CHAPTER 7

[7.1] CHENG, X., CAHALAN, J.E., FINCH, P.J., Safety analysis of an accelerator driven test facility, Nucl. Eng. Des. **229** (2004) 289–306.

[7.2] TAKAHASHI, M., et al., Study on Pb-Bi natural circulation phenomena, Prog. Nucl. Energy **47** 1-4 (2005) 553–560.

[7.3] MA, W., BUBELIS, E., KARBOJIAN, A., SEHGAL, B.R., CODDINGTON, P., Transient experiments from the thermal-hydraulic ADS lead bismuth loop (TALL) and comparative TRAC/AAA analysis, Nucl. Eng. Des. **236** (2006) 1422–1444.

[7.4] MA, W., KARBOJIAN, A., SEHGAL, B.R., Experimental study on natural circulation and its stability in a heavy liquid metal loop, Nucl. Eng. Des. **237** (2007) 1838–1847.

[7.5] LEE, I.S., SUH, K.Y., “Helios For Thermal-Hydraulic Behavior of Pb-Bi Cooled Fast Reactor Peacer”, Theoretical and Experimental Studies of Heavy Liquid Metal Thermal Hydraulics: Proc. Technical Meeting Karlsruhe, Germany, 28–31 October 2003, IAEA-TECDOC-1520, IAEA, Vienna (2006).

[7.6] TARANTINO, M., DE GRANDIS, S., BENAMATI, G., ORIOLO, F., Natural circulation in a liquid metal one-dimensional loop, J. Nucl. Mater. **376** 3 (2008) 409–414.

[7.7] COCCOLUTOA, G., et al., Heavy liquid metal natural circulation in a one-dimensional loop, Nucl. Eng. Des. **241** 5 (2011) 1301–1309.

[7.8] CHO, D.H., et al., “Direct Contact Heat Exchange Interfacial Phenomena for Liquid Metal Reactors: Part I-Heat Transfer”, Proc. ICONE10, Arlington, VA, United States of America (2002).

[7.9] TAKAHASHI, M., Study on Pb-Bi-Water direct contact boiling two-phase flow and heat transfer, Prog. Nucl. Energy **47** 1–4 (2005) 569–576.

[7.10] SATYAMURTHY, P., DIXIT, N.S., MUNSHI, P., “Void-Fraction Measurements in Two- Phase Nitrogen-Mercury Flows”, Theoretical and Experimental Studies of Heavy Liquid Metal Thermal Hydraulics: Proc. Technical Meeting Karlsruhe, Germany, 28–31 October 2003, IAEA-TECDOC-1520, IAEA, Vienna (2006).

[7.11] BENAMATI, G., et al., Experimental study on gas-injection enhanced circulation performed with the CIRCE facility, Nucl. Eng. Des. **237** 7 (2007) 768–777.

[7.12] WU, Q., SIENICHI, J.J., Stability analysis on single-phase natural circulation in Argonne lead loop facility, Nucl. Eng. Des. **224** (2003) 23–32.

[7.13] KUMAYEV, V.Y., LEBEZOV, A.A., ALEXEEV, V.V., “Development and application of MASKA-LM code for calculation of thermal hydraulics and mass transfer of lead cooled fast reactors”, Proc. NURETH-11, Avignon, France (2005).

[7.14] ABÁNADESA, A., PENA, A., Steady-state natural circulation analysis with computational fluid dynamic codes of a liquid metal-cooled accelerator driven system, Nucl. Eng. Des. **239** 2 (2009) 418–424.

[7.15] DAVIS, C.B., Thermal-hydraulic analyses of transients in an actinide burner reactor cooled by forced convection of lead–bismuth, Nucl. Eng. Des. **224** 2 (2003) 149–160.

[7.16] LEE, I.S., SUH, K.Y., Full-height thermal-hydraulic scaling analysis of Pb–Bi-cooled fast reactor PEACER, Nucl. Technology **155** 3 (2006) 265–281.

[7.17] DULERA, I.V., SINHA, R.K., High temperature reactors, J. Nucl. Mater. **383** 1–2 (2008) 183–188.

[7.18] VIJAYAN, P.K., et al., Investigations on the effect of heater and heat exchanger orientation on the steady state, transient and stability behaviour of single phase natural circulation in a rectangular loop, BARC/2001/E/034, 2001.

[7.19] JAISWAL, B.K., VIJAYAN, P.K., MAHESHWARI, N.K., BORGOHAIN, A., "Development of a computer code to study the staedy state and the transient behaviour of liquid metal natural circulation loop", 19th National and 8th ISHMT-ASME heat and mass transfer conference, JNTU Hyderabad, India (2008).

[7.20] VIJAYAN, P.K., Experimental observations on the general trends of the steady state and stability behaviour of single-phase natural circulation loops, Nucl. Eng. Des. **215** 1–2 (2002) 139–152.

[7.21] CINOTTI, L., "The Pb-Bi Cooled XADS Status of Development", II International Workshop on Materials for Hybrid Reactors and Related Technologies, ENEA Brasimone Research Centre, April 18–20, 2001.

[7.22] TURRONI, P., CINOTTI, L., CORSINI, G., MANSANI, L., "The CIRCE Facility", Proc. AccApp'01&ADTTA'01, Nuclear Application in the new Millennium, Reno, Nevada, United States of America, Nov. 11–15, 2001.

[7.23] AMBROSINI, W., et al., Testing and qualification of CIRCE instrumentation based on bubble tubes, J. Nucl. Mater. **335** (2004) 293–298.

[7.24] AGOSTINI, P., et al., "Testing and Qualification of CIRCE Venturi-Nozzle Flow Meter for Large Scale Experiments", Proc. 13th Int. Conf. on Nuclear Engineering, Beijing, China, May 16–20, 2005.

[7.25] IMBENI, V., MARTINI, C., MASINI, S., PALOMBARINI, G., "State of the art on physic-chemical properties of Lead and Lead-Bismuth", (in Italian), Istituto di Metallurgia, Università di Bologna, May 1999.

[7.26] LOCKHART, R.W., MARTINELLI, R.C., Proposed correlation of data for isothermal two-phase two-component flow in pipes, Chem. Eng. Prog. **45** (1949) 39.

[7.27] TODREAS, N.E., KAZIMI, M.S., Nuclear System I, Thermal Hydraulic Fundamentals, Taylor and Francis, New York (1989).

[7.28] AMBROSINI, W., FORASASSI, G., FORGIONE, N., ORIOLO, F., TARANTINO, M., "Natural and gas-injection enhanced circulation in a loop with variable friction", Int. Conf. Global Environment and Advanced Nuclear Power Plants, GENES4/ANP2003, September 15–19, 2003, Kyoto, Japan.

[7.29] AMBROSINI, W., FORASASSI, G., FORGIONE, N., ORIOLO, F., TARANTINO, M., Experimental study on combined natural and gas-injection enhanced circulation, Nucl. Eng. Des. **235** 10–12 (2005) 1179–1188.

[7.30] TARANTINO, M., Gas Enhanced Circulation Experiments On Heavy Liquid Metal System, Report ENEA HS-F-R-001 (2007).

[7.31] TARANTINO, M., et al., "Heavy liquid metal natural circulation in a one-dimensional loop", ICONE 17, Brussels, Belgium, July 12–16, 2009.

[7.32] DE ZWAAN, S. J., et al., Static design of a liquid-salt-cooled pebble bed reactor (LSPBR), Ann. Nucl. Energy **34** (2007) 83.

[7.33] WILLIAMS, D.F., TOTH, L.M., CLARNO, K.T., Assessment of Candidate Molten Salt Coolants for the Advanced High-Temperature Reactor, Oak Ridge National Laboratory Report ORNL/TM-2006/12, March (2006).

[7.34] COHEN, S.I., JONES, T.N., Viscosity Measurements on Molten Fluoride Mixtures, ORNL-2278, Oak Ridge National Laboratory, Oak Ridge, TN (1957).

[7.35] TORKLEP, K., OYE, H.A., An absolute oscillating-cylinder (or cup) viscometer for high temperatures, J. Phys. E: Sci. Instrum. **12** (1979) 875.

[7.36] TORKLEP, K., OYE, H.A., Viscosity of eutectic LiF-NaF-KF, J. Chem. Eng. Data **25** (1980) 16.

[7.37] INCROPERA, F.P., et al., Introduction to Heat Transfer, 5th ed., John Wiley and Sons (2007).

CHAPTER 8. DEVELOPMENT OF TOOLS FOR ON-LINE MONITORING AND CONTROL OF HLM COOLANT CHEMISTRY

8.1. INTRODUCTION

Lead and lead-alloys are considered as working fluids for advanced nuclear applications such as accelerator driven systems (ADS) [8.1] and Lead Fast Reactors (LFR) of GEN IV [8.2] due to their thermal and neutronic properties. The advantages of heavy liquid metals (HLMs) as a coolant in fast neutron nuclear systems are discussed in reference [8.3].

Concerns related to the use of HLM arise from the materials compatibility, in terms of corrosion and mechanical resistance. To avoid the dissolution of steel components in liquid-lead alloys, a protective oxide scale is formed on the steel surface by inserting a small amount of oxygen into the metallic melt [8.4], [8.5], [8.7]–[8.10]. The oxide scale hinders cation diffusion from the steel into the liquid metal and vice-versa. The chemical activity of oxygen in the lead alloy, however, is a critical parameter, because PbO precipitates if the activity is too high, and steel does not form a protective oxide layer if it is too low [8.6].

If we consider a liquid metal loop with temperature gradients like in ADS, the situation becomes more complicated because the oxygen partial pressure at which oxide formation occurs varies with temperature. Since in a liquid metal loop one has to operate with a constant concentration of oxygen, the relations between concentration, activity and partial pressure of oxygen have to be known.

In order to monitor and control the oxygen content of HLMs, oxygen sensors and oxygen control systems were developed.

8.2. HIGH TEMPERATURE OXYGEN SENSOR FOR LEAD-BISMUTH EUTECTIC

The use of the ionic conduction properties of some solid electrolytes, and in particular the Yttria-Stabilised-Zirconia (YSZ) based ceramic, allows making an electrochemical cell assembly for on-line measurement of dissolved oxygen in a liquid metal system in a wide concentration range. Several open literatures are available about the development and application of YSZ sensor for the dissolved oxygen measurement in LBE systems [8.11], [8.12].

8.2.1. Theory

The upper limit of the dissolved oxygen in LBE is defined as the concentration of oxygen required to form Fe_3O_4 protective oxide layer and the upper limit as the saturation level of oxygen at a particular temperature. The limits are obtained from the following two reactions taking place in LBE [8.13]:

$$Pb + O = PbO \tag{8.1}$$

$$3Fe + 4O = Fe_3O_4 \tag{8.2}$$

Using Henry's law, the limits of partial pressure of oxygen can be expressed, using Eqs (8.1, 8.2), as follows [8.13]:

$$\frac{1}{2}\Delta G_{Fe_3O_4} < RT\ln P_{O_2} < 2\Delta G_{PbO} - 2RT\ln a_{Pb} \qquad (8.3)$$

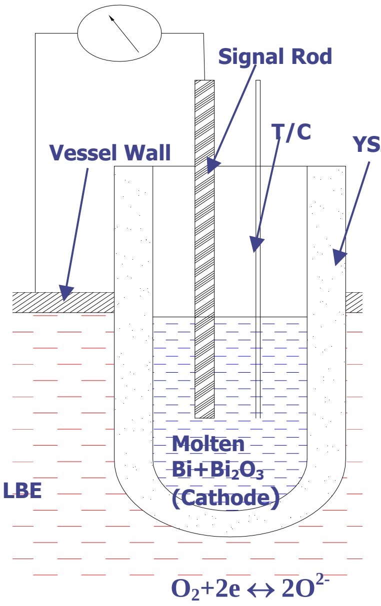

FIG. 8.1. YSZ oxygen sensor.

Figure 8.1 shows an oxygen sensor consisting of a one-end closed YSZ tube as solid electrolyte with Bi+Bi_2O_3 mixture as reference electrode. The molten lead alloy in which the tube is immersed serves as the other electrode. At high temperature (>300°C), the solid electrolyte membrane (i.e. YSZ) is porous to oxygen ion, an imbalance in the oxygen concentration between two electrodes will cause oxygen ion to migrate to equalize the concentrations on each side. Oxygen on the higher concentration side will 'pick up' two electrons to become ions, travel through the YSZ and re-form into a neutral molecule at lower oxygen concentration electrode surface where they will 'deposit' two electrons. The potential difference across the electrodes can be calculated from Nernst equation as [8.12]:

$$E = \frac{RT}{4F}\ln\frac{P_{O_2}{}'}{P_{O_2}} = \frac{1}{2}F\left(\frac{1}{3}\Delta G_{Bi_2O_3} - \Delta G_{PbO} - RT\ln a_{PbO} + RT\ln a_{Pb}\right) \qquad (8.4)$$

Where $P_{O_2}^{/}$ and P_{O_2} are the partial pressure of the dissolved oxygen in reference electrode and liquid metal, respectively.

For pure lead, a_{Pb} =1.0.

Using Eqs (8.3, 8.4) and referring Oxide Handbook [8.14] for ΔG's, the limits of the sensor voltage can be expressed as:

E_{max}= 8.123x10^{-5} T+0.4304 (Volts) (8.5)

$E_{min=}$-7.264x10^{-5} T+0.142 (Volts) (8.6)

8.2.2. Sensor construction and testing

An oxygen sensor is developed to measure dissolved oxygen level in lead. As shown in Fig. 8.1, the oxygen sensor consists of a one-end closed YSZ tube, fabricated in BARC. The tube is partially filled with laboratory grade $Bi+Bi_2O_3$ mixture, which is the reference electrode of the sensor. A molybdenum rod (signal rod, for electrical connection between molten reference electrode and vessel wall) and a SS sheathed thermocouple (for temperature measurement) are immersed in the mixture. The tube is sealed with a high temperature Teflon cap and a high temperature silicon sealant. The molten lead alloy in which the tube is immersed serves as the other electrode. A test set-up (Fig. 8.2) is made to test the oxygen sensor. The test set-up mainly consists of a SS vessel with oxygen sensor fittings, level sensor, thermocouples and gas inlet and outlet fittings. The sensor is inserted into the vessel through specially designed leaktight fitting, so that it is partially immersed inside the molten metal. Figure 8.3 shows the sensor before installation in the test set-up. The level sensor is a discrete type sensor.

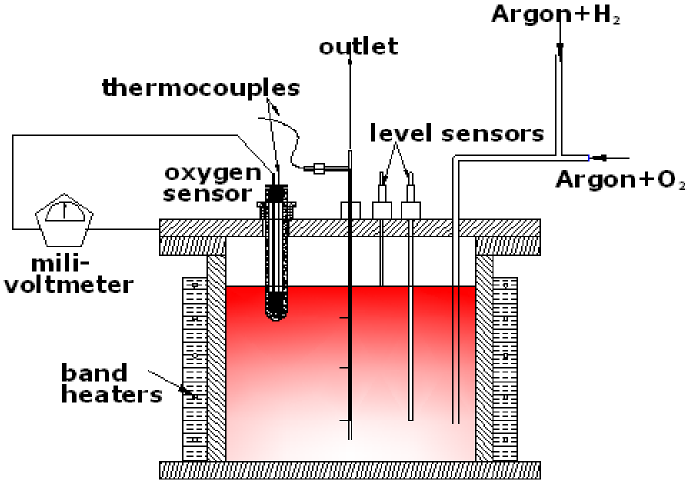

FIG. 8.2. Oxygen sensor test set-up.

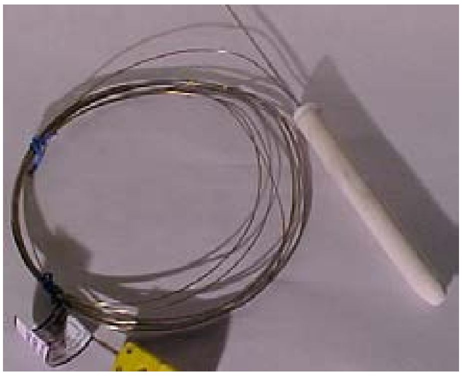

FIG. 8.3. Oxygen sensor.

When the level sensor tip touches the liquid metal level, the electrical circuit closes between the sensor tip and the vessel wall, and the indication is given by a LED. A high impedance milli-voltmeter is connected between the molybdenum rod and the test vessel body (Fig. 8.4) to measure the EMF generated across the tube wall, due to difference in oxygen concentration in reference electrode and molten metal. Since the vessel body is in contact with the molten metal, the EMF generated between reference electrode and molten metal will be sensed by the milli-voltmeter.

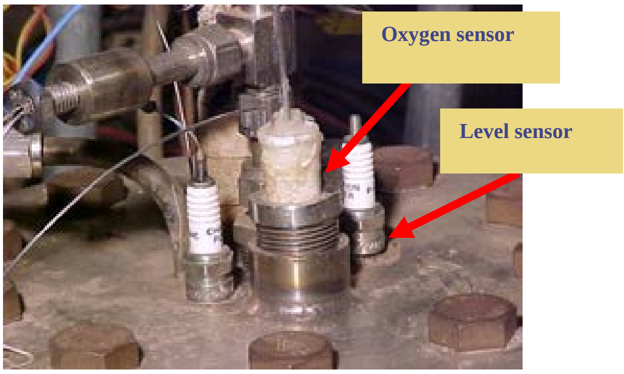

FIG. 8.4. View of the oxygen sensor with the test set-up.

The vessel is heated by high temperature ceramic band heaters. The heater power is controlled by dimmer-stat. The temperature of the liquid metal and the vessel surface is measured by SS316L sheathed thermocouples. The centre temperature of the vessel is measured and ensured that it is well above the melting point of the lead.

High purity argon gas is used as the cover gas of the liquid metal in the vessel to avoid oxidation of liquid metal at high temperature. Argon+H_2 gas is used as reducing gas to remove the excess dissolved oxygen in the vessel. A pressure gauge is used to monitor the gas pressure in the vessel and rotameters are used to measure the gas flow rates. The oxygen level in the molten lead is increased by bubbling with air and decreased by bubbling with H_2+argon gas.

8.2.3. Results and discussions

Figure 8.5 shows the predicted variation of EMF generated in the oxygen sensor with different temperature at different oxygen concentration (%wt) in LBE. The figure is derived from Eqs (8.4–8.6). From the figure, it can be seen that, if the EMF value of the sensor goes below 0.1 V, PbO oxide layer formation starts. If it goes above 0.4 V, the protective oxide layer on the metal surface becomes unstable, which may lead to corrosion. In terms of EMF, it can be inferred that, between 0.2 V and 0.4 V, the zone of operation is safe for all temperatures.

In the experimental studies, the molten lead is kept at constant temperature for few hours, to attain a uniform temperature. After that, air is injected in the lead to increase the oxygen partial pressure in the lead, which reduces the EMF in the sensor [8.11].

After some time, the oxygen concentration in the lead is reduced by introducing H_2+argon gas, which is indicated by increase in EMF values of the sensor. This process is repeated and similar trends of EMF values are found, as shown in Fig. 8.6. The maximum and minimum EMF in the sensor are found to be 0.45 V and 0.115 V, which are close to the E_{max} and E_{min} predicted by Eq. (8.5) and Eq. (8.6), respectively.

In the second test, the molten lead is cooled from 525°C to 450°C with high purity argon bubbled in the liquid metal. Fig. 8.7 shows the variation of EMF of the sensor with temperature. It can be seen that the EMF of the sensor reduces as per prediction from 525°C to 440°C.

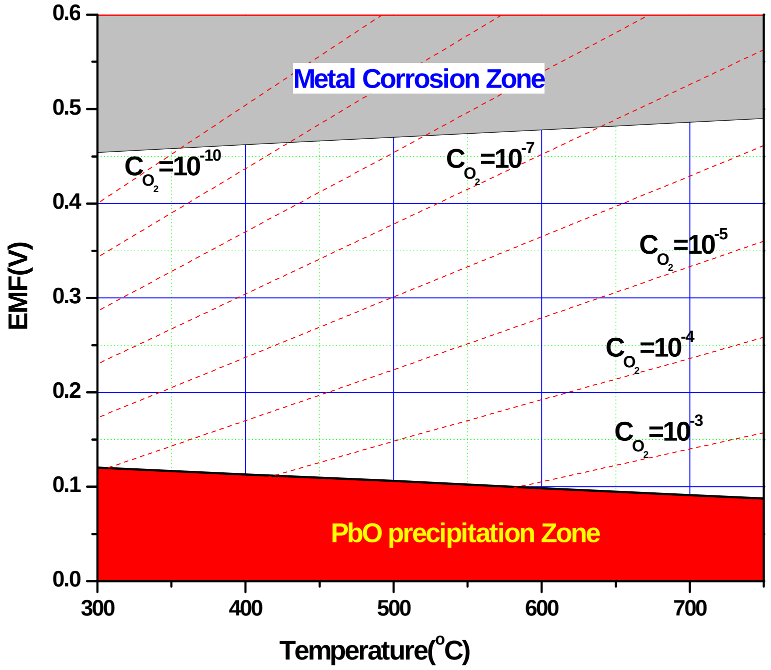

FIG. 8.5. Variation of EMF in the oxygen sensor with temperature, at different dissolved O_2 concentration (%wt) in LBE.

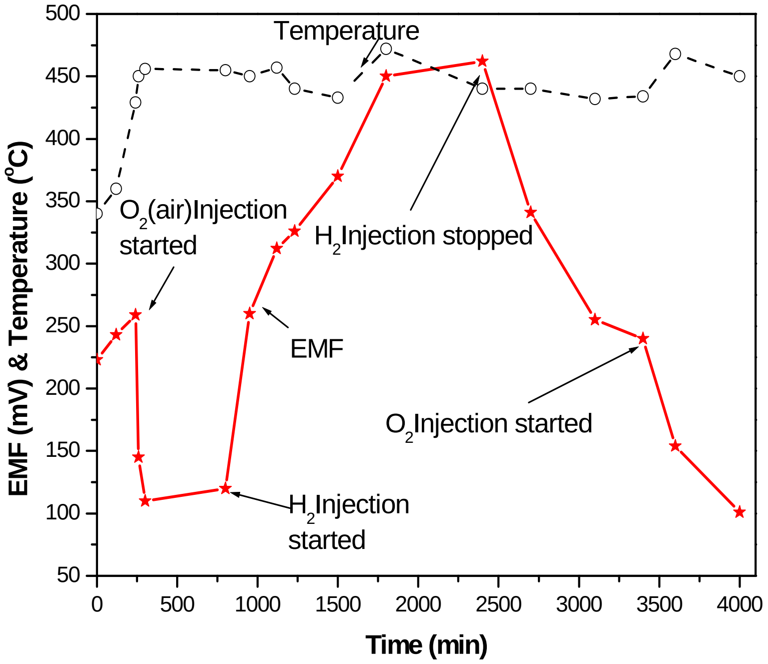

FIG. 8.6. Experimental results concerning the variation of EMF in the oxygen sensor with oxygen concentration in molten lead.

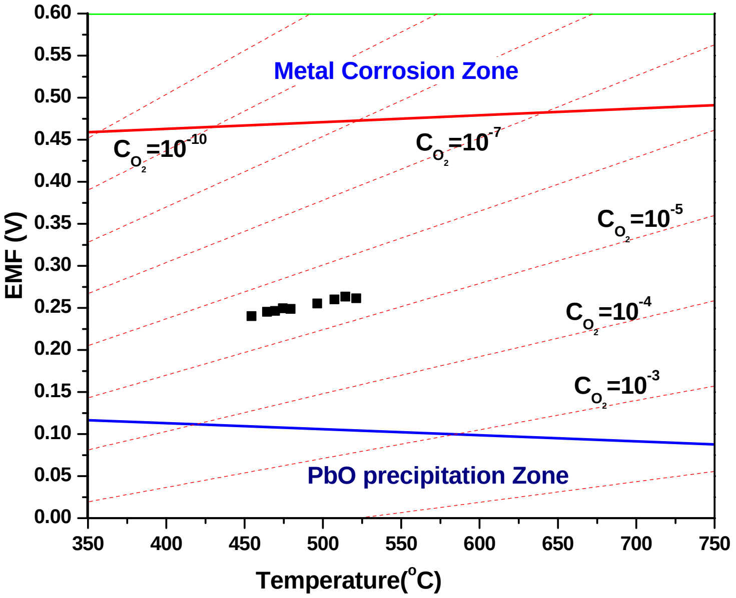

FIG. 8.7 Variation of EMF with temperature during pure argon gas bubbling.

8.2.4. Conclusions

The theoretical basis of the oxygen sensor for molten lead has been briefed. The construction and testing of an YSZ probe is described. The oxygen concentration in the liquid metal was varied and the response of the oxygen sensor in terms of EMF is studied. Accurate and fine control of dissolved oxygen control system is required to calibrate the oxygen sensor at different oxygen concentration levels.

8.3. DEVELOPMENT OF OXYGEN CONTROL PROCESS AND ASSESSMENT OF INSTRUMENTATION TECHNIQUES

The control of oxygen concentration in HLM is one of the key work areas in the frame of GenIV nuclear reactors technologies. During recent years, a huge amount of experiment work has been performed by several international laboratories in the field of oxygen sensing and control in HLM loops. All those successful experiments had the goal to implement a reliable method for an active control of the concentration of oxygen, in order to avoid system plugging. A new technological challenge comes when transferring this system to a pool type facility, where technological and safety requirements are completely different. This chapter describes the experimental activity, carried on in the frame of the DEMETRA EUROTRANS Programme [8.15], in the CIRCE facility at ENEA Brasimone, where three newly designed deeply immersed oxygen sensors, based on Bi_2O_3 electrochemical electrodes, were tested and validated.

The sensor under development is a device for control of oxygen content in Pb-Bi eutectic (as well as in molten Pb) and is designated for using in the CIRCE circulating test facility. Technical performances of the sensor are depicted in Table 8.1.

The results of investigations, conducted within the framework of several national and European programmes [8.16]–[8.18], demonstrated that the most acceptable method of control of oxygen in liquid Pb and Pb-Bi is the method based on use of the galvanic concentration cell (GCC) with solid electrolyte possessing ion-selective conductivity (relative to oxygen ions). With operating GCC, the thermodynamic activity of oxygen (a_0) in liquid metal converts to an electric signal. With known thermodynamic properties of GCC's reference electrode, the GCC's EMF can easily be calculated at high accuracy [8.19], [8.20]. If the reference electrode represents Bi and Bi_2O_3 mixture (the most probable reference electrode for sensor under development), the EMF is determined by the relations:

for liquid Pb $\quad E\ (\text{в}) = 0{,}131 - 1{,}5\cdot 10^{-5}\ T\ (1 + 6{,}61\ \ln a_0) \quad (8.7)$

for eutectic Pb-Bi. $\quad E\ (\text{в}) = 0{,}088 - 1{,}78\cdot 10^{-5}\ T - 9{,}907\cdot 10^{-5}\ T\ \ln a_0 \quad (8.8)$

A capsule-type sensor measuring thermodynamic activity of oxygen in liquid metal coolant, which is shown in Fig. 8.8, is used as basis for the sensor under development (see Table 8.1).

In the upper part of the sensor, a sealed lead-in (8) is positioned, where the potential terminal (6), isolating the internal cavity of sensor from the gas system of the test facility, is hermetically fixed. The sealed lead-in consists of an external sleeve and a co-axially placed internal electrode electrically insulated from the external sleeve by glass ceramics [8.20], [8.21]. The external sleeve of the sealed lead-in is welded to the sensor case (7). The sensor case is welded to the metallic shell of ceramic sensitive element (CSE) (1), connected to ceramic test tube (1) by means of high temperature glass ceramic (5). In the lower part of the internal cavity of the ceramic test tube, the reference electrode (the mixture of bismuth (2) and bismuth oxide (3): $Bi\text{-}Bi_2O_3$) is located.

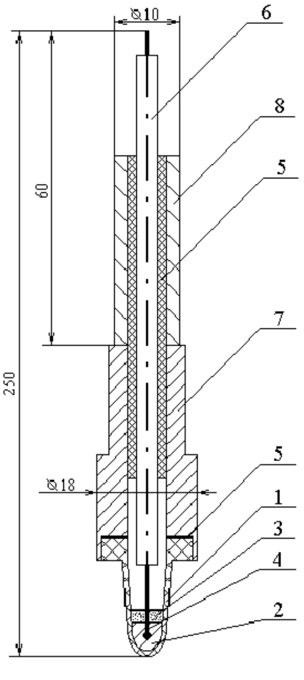

FIG. 8.8. Base design of oxygen TDA sensor: 1 — CSE; 2 — bismuth; 3 — bismuth oxide; 4 — electrode; 5 — glass ceramics; 6 — potential terminal; 7 — casing; 8 — sealed lead-in.

TABLE 8.1. BASIC TECHNICAL PERFORMANCE OF SENSOR

Measurement range of a_0		$1 \cdot 10^{-6}$–1
Maximum pressure of medium under investigation		0.5 MPa
Maximum flow velocity of Pb, Pb-Bi		1.0 m/s
Maximum rate of temperature variation of Pb, Pb-Bi		10°C/s
Range of temperature variation of fluid under investigation		350–650°C
Limits of permissible relative deviation from nominal static characteristic (NSC)		±10%
Maximum time required to achieve the operating conditions at first installing of sensor into fluid under investigation		10 h
Overall dimensions of sensor	length	3000 mm 4000 mm 8000 mm
	diameter	27 mm

An oxygen activity sensor should meet the following design requirements [8.11], [8.18], [8.23]:

- Sensor should be resistant to mechanical action and strong vibration.
- Sensor design and used structural materials should be stable to temperature variations whose amplitudes and variation rates meet the conditions of sensor locations on CIRCE test facility.
- Sensor design should provide its service ability under the condition of being permanently in liquid lead-bismuth within the given CIRCE test facility lifetime.
- Electric connectors of the sensor should provide non-trouble operation under the conditions of temperature, pressure and ambient humidity, meeting the requirements that are placed upon the environment of CIRCE operating areas.
- Sensor design should rule out ingress of liquid lead-bismuth into a room at accident failure of its ceramic components.

8.3.1. Justification of design of sensor under development

The basic specific feature of CIRCE circuit design is that the sensor must operate in liquid metal melt at large depths (up to 6 m).

First, the base option of the sensor (Fig. 8.8), updated for possible submergence at a depth up to 5 m in molten lead (lead-bismuth), was tested. Measurements were taken at oxygen thermodynamic activity TDA (Tetradecyl-ammonium in molten lead) in the range from a = 1, which corresponds to sensor’s EMF ≈ 120 mV, to $a = 10^{-4} \div 10^{-5}$, which corresponds to sensor’s EMF ≈ 420÷500 mV, at temperatures between 480 and 540°C.

Table 8.2 gives the parameters of liquid Pb as well as EMF values and corresponding TDA of reference sensors installed in test section. Listed are as well the EMF values and the corresponding TDA values of the oxygen sensor with a 5 m long immersed part as a function of depth of immersion.

TABLE 8.2. TEST SECTION REFERENCE SENSORS

L, m	T, °C	V, m/s	$E_{ref.\ sensor}$, mV	$A_{ref.\ sensor}$	E_6	a_6
1	470	0.25	117	1	120	1
2	470	0.25	119	1	113	-
3	480	0.25	120	1	102	-
4	480	0.25	132	0,8	91	-
5	480	0.25	140	0,5	83	-
1	480	0.25	148	0,4	141	0,4

Note: L: depth of immersion; T: temperature of the molten lead; V: velocity of the molten lead; $E_{ref.\ sensor}$: EMF of the reference sensor; $A_{ref.\ sensor}$: oxygen activity (TDA) of the reference sensor; E_6: EMF of the tested sensor; a_6: TDA of the tested sensor.

As evident from the data presented in the table, at a small depth of sensor submergence into melt (about 1 m), its readings are in fair agreement with the readings of reference sensors. However, as the depth of submergence into melt increases, the corresponding EMF values show a continuous strong decrease in respect to the reference values.

In this case, the absolute EMF value becomes less than the possible theoretical values (120÷116 mV) for Bi-Bi_2O_3 reference electrode, which is used in oxygen TDA sensors.

The reason why readings decrease is the reduction in the resistance of insulation of the potential terminal being inside the sensor body (Fig. 8.8).

To eliminate the loss of sensor signal, the following changes were introduced into the base model design:

- A new design using sealed lead-in based on special temperature stable 2-shell metallic cable was developed.
- A special system was developed to measure the sensor signal and form a guard potential equal to the level of the valid sensor signal on the intermediate shell of the potential terminal cable, to protect the valid sensor signal against loss.

In the process of further justification of sensor design, the geometric dimensions of separate components and sensors on the whole were refined, and requirements to materials used in the sensor were formulated.

The sensor can have several modifications differing in length of the immersed part and the presence (or absence) of reducer for welding. The general view of the refined oxygen sensor design for which working drawings have been developed is shown in Fig. 8.9.

The sensor under development consists of ceramic sensitive element (CSE) (5) (material — ZrO_2 Y_2O_3) as capsule with 12 mm outer diameter, 4–6 mm inner diameter and 15–20 mm length. The capsule is connected with metallic CSE casing (3) by means of high temperature sealant which is to provide an airtight strong and reliable connection. The metallic CSE casing (3) is welded to sensor body (4). There is a Bi-Bi_2O_3 reference electrode (where the predetermined partial pressure of oxygen is maintained) inside CSE. In the upper part of the sensor, a sealed lead-in (2) is located, which is welded to casing (4) and is designed to make the internal pool of sensor leaktight. Besides, the sealed leak-in is designed to prevent spill of

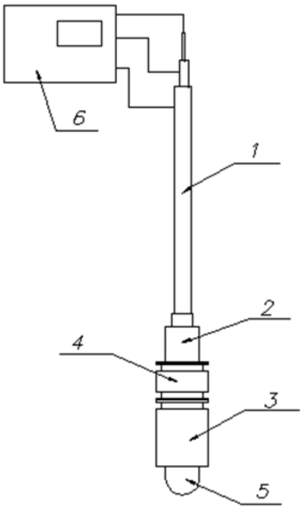

FIG. 8.9. Updated oxygen TDA sensor: 1 — two-shell potential terminal lead; 2 — sealed lead-in; 3 — metallic casing of ceramic sensitive element; 4 — adapter (transition part); 5 — ceramic sensitive element; 6 — measuring system with former of guarding potential.

alloy outside into operating areas in case of capsule failure. Two-shell potential terminal lead (1) implements electric contact between reference electrode (2) and measuring block (6) and protects valid signals of sensor from loss [8.24].

Hermetic sealing of the sensor installed in the closed loop test rig is planned to be achieved by using potential terminal cable by means of fluoroplastic seals in the ‘cold’ zone.

8.3.2. The work in the CIRCE facility

The sensors were installed and calibrated in the new section of the CIRCE pool facility. New software was installed and implemented, as shown in Figs 8.10 and 8.11.

The experimental campaign consisted essentially of two separated goals: the validation of the full system and the model of oxygen concentration in a large HLM pool. The screenshot of the acquisition system software is the confirmation of the accomplishment of both goals. The electrochemical sensor gave expected outputs: the CIRCE melt had never been treated, conditioned or modified, so it was expected to find a signal proportional to an almost oxygen saturated environment, i.e. around a value of 180 mV.

8.3.3. Conclusions

The challenge of manufacturing, validating and implementation of oxygen sensors in a pool device like CIRCE was a large technological issue. The goal of this work consisted in the engineering of the whole system, and it can be considered a good success. The next challenge will be the study of the sensors’ behaviour when coupled with chemistry active control systems.

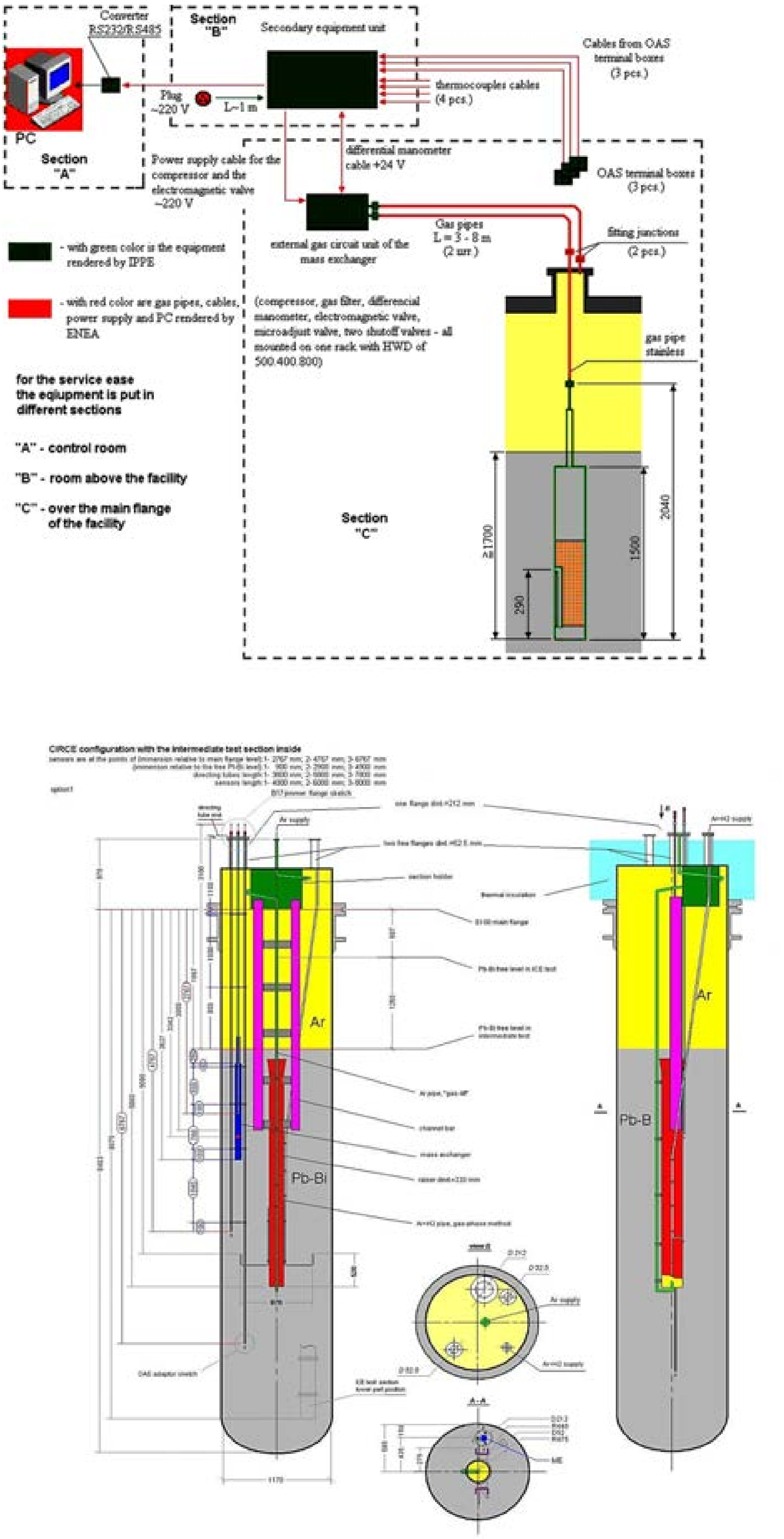

FIG. 8.10. System scheme and CIRCE set-up.

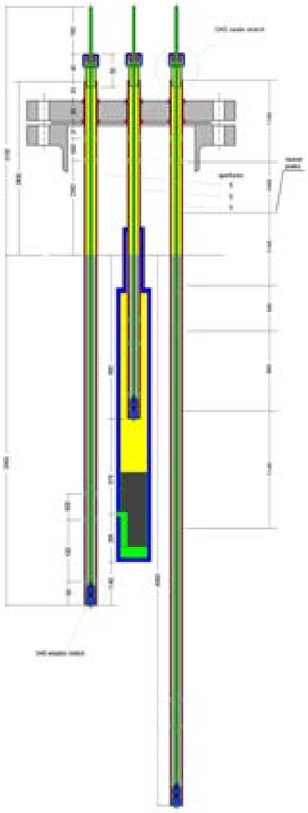

FIG. 8.11. Test section of the three CIRCE sensors.

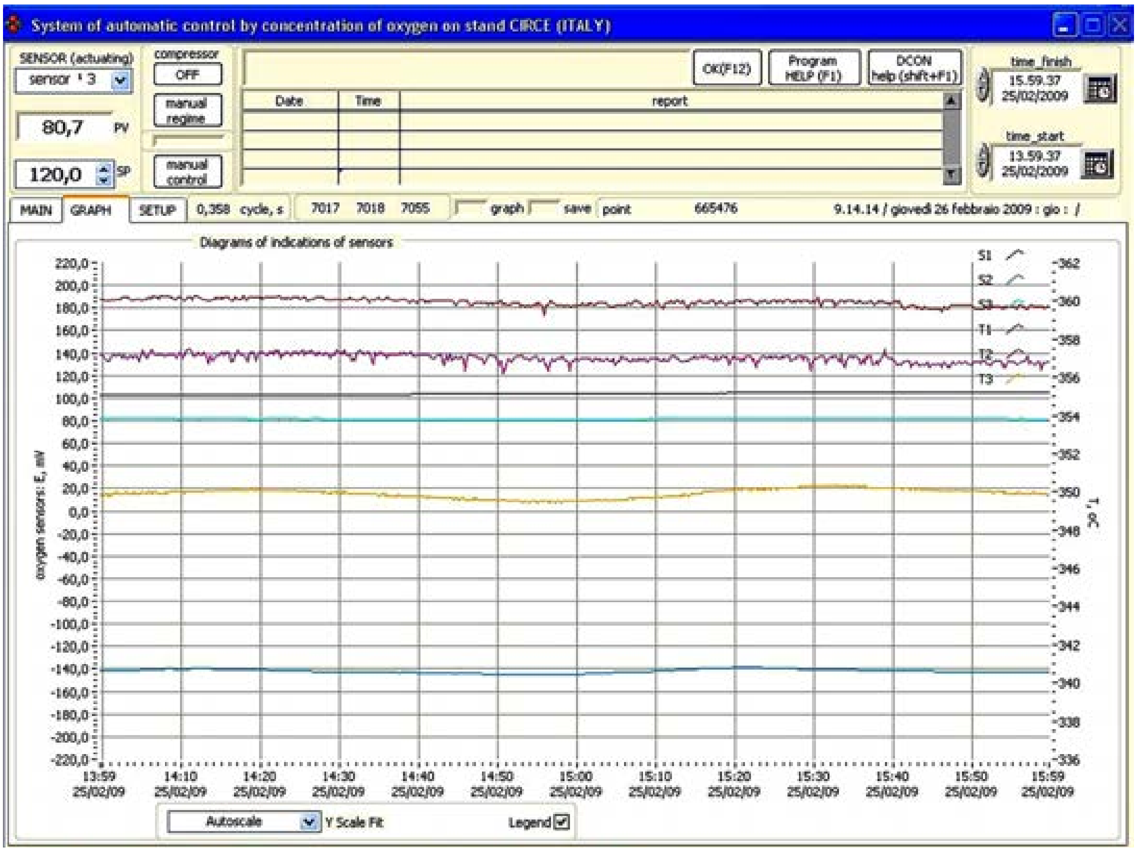

System of automatic control by concentration of oxygen on stand CIRCE (ITALY)

SENSOR (actuating): sensor ' 3

80,7 PV

120,0 SP

compressor: OFF

time_finish: 15.59.37 25/02/2009

time_start: 13.59.37 25/02/2009

0,358 cycle, s

7017 7018 7055

point 665476

9.14.14 / giovedì 26 febbraio 2009 : gio : /

FIG. 8.12. Screenshot of the three CIRCE sensors.

8.4. OXYGEN CONTROL IN LIQUID LEAD ALLOYS

8.4.1. The principle of oxygen control via the gas phase

The oxygen potential that is required to protect the steel surface by formation of stable oxide layers is established throughout the composition of the gas atmosphere above the liquid lead alloy.

It is not possible to use an oxygen/inert gas mixture, e.g. O_2/Ar, to control the oxygen concentration in the liquid metal because the oxygen partial pressure would be too low (<10^{-15} bar) to deliver the oxygen consumed by oxide scale formation on steel structures. Therefore, a mixture of H_2 and H_2O is used to control the concentration of oxygen in the liquid metal. It allows to carry a sufficient amount of oxygen at an oxygen partial pressure that corresponds to the stability conditions. The diagram in Fig. 8.13 demonstrates in which region the stable conditions exist and how they can be established. The ordinate shows the partial Gibbs energy of oxygen expressed by the oxygen partial pressure, the abscissa the temperature. The lines of constant H_2/H_2O ratios and those of constant oxygen partial pressures, P_{O2}, show the ratios which must be established in the gas phase to attain a certain oxygen partial pressure. Those lines intersect at absolute zero temperature, the P_{O2} lines at RT ln $P_{O2} = 0$ and the H_2/H_2O lines at RT ln $P_{O2} = 2\Delta_f G^o$ (H_2O). The important region with protective oxide scale formation is the one between the lines for PbO and Fe_3O_4/FeO in the temperature region of 200–650°C, which is relevant for loops with liquid $Pb_{45}Bi_{55}$ and Pb. The diagram also contains lines of constant oxygen concentration in Pb and the $Pb_{45}Bi_{55}$ melt in equilibrium with the corresponding oxygen partial pressure and H_2/ H_2O ratios. First ones end at the melting point. We note three different properties of the curves in Fig. 8.13. Gibbs energies are higher for oxygen in the $Pb_{45}Bi_{55}$ melt than for Pb at the same oxygen concentration. The slope of the concentration of oxygen with increasing temperature is steeper for the $Pb_{45}Bi_{55}$ melt than for Pb. The curve, for the partial Gibbs energy of oxygen in the saturated $Pb_{45}Bi_{55}$ melt, appears about 3 kJ/mol above that for the pure Pb melt.

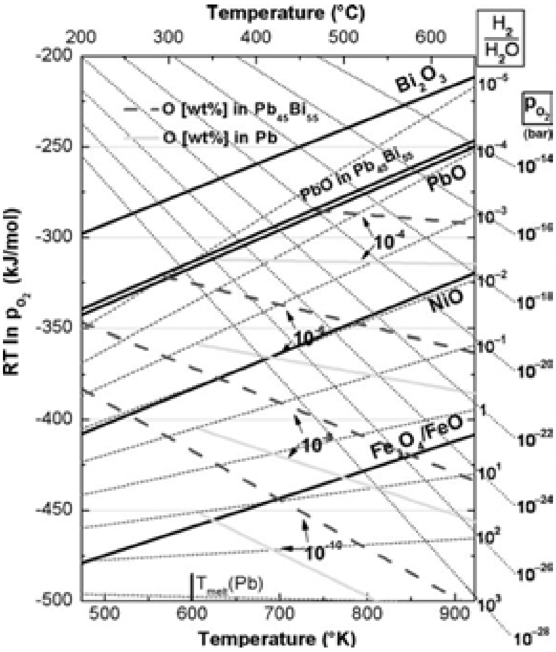

FIG. 8.13. *Ellingham–Richardson diagram containing oxides of steel components and of Bi and Pb. Lines of constant oxygen concentrations in Pb and the* $Pb_{45}Bi_{55}$ *melt indicate the stability regions of iron oxide without PbO precipitation in the temperature gradient of a loop.*

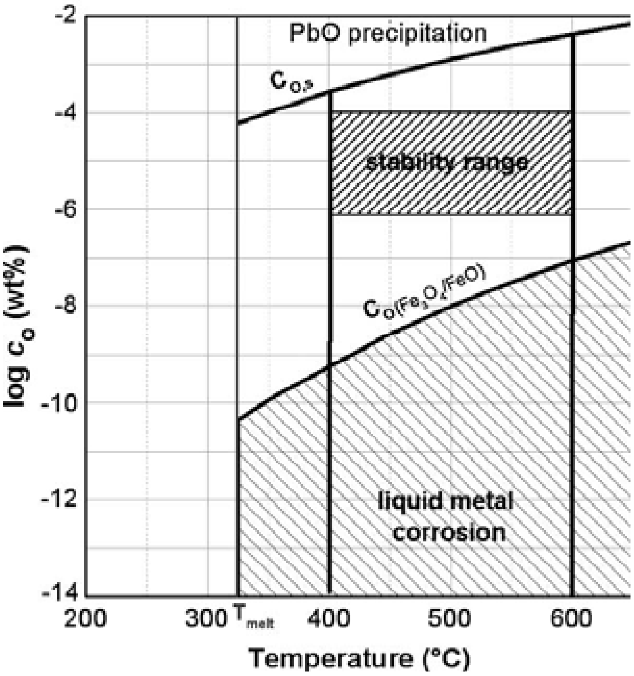

FIG. 8.14. Range between the solubility limit $c_{O,s}$ and the oxygen concentration at which decomposition of iron oxides takes place. The area between the curves indicates the concentrations for which stable conditions are expected in a loop with liquid Pb.

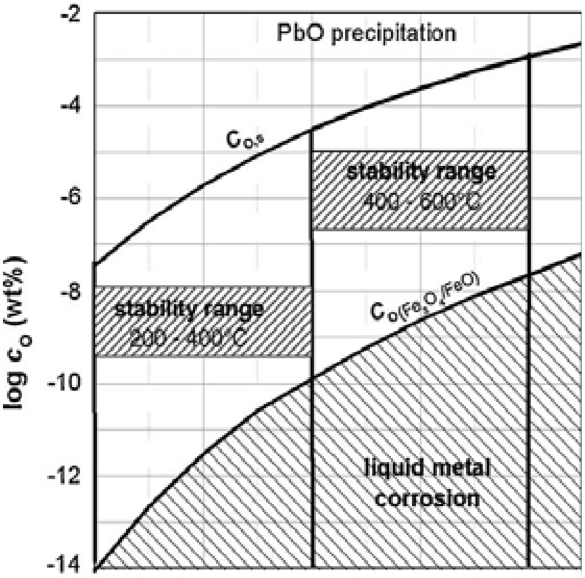

FIG. 8.15. Range between the solubility limit $c_{O,s}$ and the oxygen concentration at which decomposition of iron oxides takes place. The area between the curves indicates the concentrations for which stable conditions are expected in a loop with the $Pb_{45}Bi_{55}$ melt.

Since the liquid metal containing a defined oxygen concentration extends over regions with about 150 and 200°C temperature differences in a liquid metal loop, it is most convenient to use c_O-T diagrams for determination of the stability ranges of steel in Pb and the $Pb_{45}Bi_{55}$ melt. The first diagram (Fig. 8.14) shows the situation in a Pb loop over a temperature range from the melting point to 650°C. Two boundary curves enclose the limits of the stability range.

In case of the $Pb_{45}Bi_{55}$ melt, the curves differ from those for the Pb melt because of the different saturation concentrations and the contribution of ΔG^{xs} ($Pb_{45}Bi_{55}$). Fig. 8.15 shows the situation in a $Pb_{45}Bi_{55}$ melt in which the lowest loop temperature could be around 200°C.

8.4.2. Oxygen control system

The gases Ar and Ar/5%H_2 are mixed in an oxygen control system by two flow controllers to obtain the required hydrogen concentration in the cover gas (Fig. 8.16). The gas passes through a moisturizer, the water vapour pressure of which is controlled by a precision thermostat. The oxygen control by equilibration between gas phase and liquid metal in the reaction tube is sketched in the shaded area of Fig. 8.16. The incoming and outgoing gas is checked by a moisture sensor and finally by an oxygen partial pressure detector. The used moisture sensor is a dew point meter DEWMET SD from MICHELL®, the partial pressure detector a SGMT 1.1 from ZIROX®.

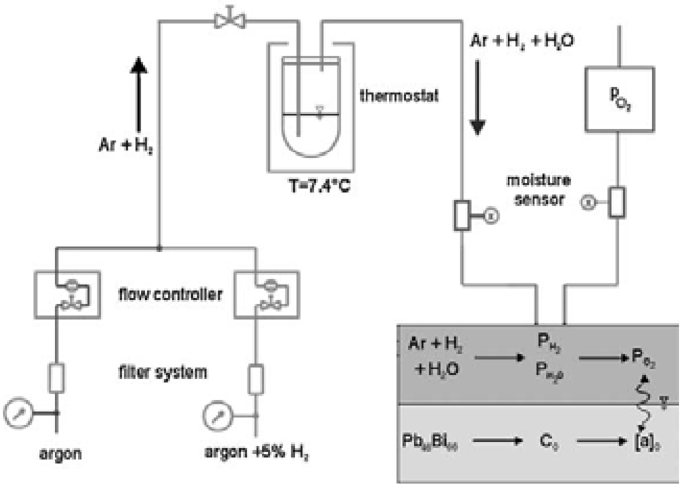

FIG. 8.16. Scheme of an oxygen control system with gas conditioning and control. The shaded areas show the equilibrium processes taking place between gas phase and the $Pb_{45}Bi_{55}$ melt.

On the principle described above, the oxygen control system was developed and built to control the oxygen concentration in the KALLA loops at KIT (Karlsruhe Institute of Technology, Germany). The oxygen control of 1000 l of $Pb_{45}Bi_{55}$ inventory is accomplished under flow conditions in this loop. The surface that is exposed to the control gas flow is about 0.14 m^2 at a temperature of 345°C. The timescale in which the equilibration of the oxygen activity between the gas phase and the liquid metal is reached in the loop is demonstrated in Fig. 8.17 by comparison of the EMF signals of the zirconia oxygen sensors in the gas phase and in the liquid metal. The oxygen activity in the $Pb_{45}Bi_{55}$ melt, represented by the EMF signal of the Pt/air oxygen meter in the lower curve, follows quite closely that of the oxygen partial pressure change in the gas phase. This latter one is depicted by the signal of the gas oxygen meter in the upper curve. It takes only about 5 h at 345°C to establish the new oxygen activity in $Pb_{45}Bi_{55}$ that corresponds to the new H_2/H_2O ratio of 0.25. The reverse process, i.e. the reduction of the activity to the initial value at a H_2/H_2O ratio of 2.5, took only about half of the time. The difference can be explained by considering the hydrogen that gets dissolved in the liquid metal. In any case, the experiment shows that the response of the oxygen activity

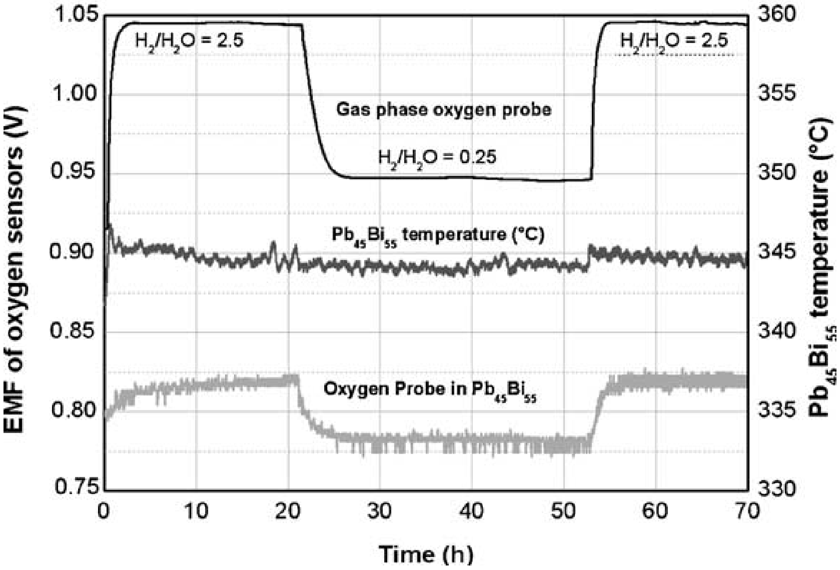

FIG. 8.17. Equilibration of oxygen activities between the gas phase and the $Pb_{45}Bi_{55}$ *melt in a liquid metal loop.*

in the liquid metal loop to changes in the gas phase is fast enough to allow an oxygen control via the gas phase also in large loops.

8.4.3. Conclusions

The oxygen control of $Pb_{45}Bi_{55}$ in loops was demonstrated. It was shown that equilibration between gas phase and liquid $Pb_{45}Bi_{55}$ is fast enough for the control of oxygen concentration in $Pb_{45}Bi_{55}$.

Calculation of Gibbs energies of oxygen as a function of its concentration in the liquid, eutectic $Pb_{45}Bi_{55}$ alloy reveals that two orders of magnitude higher oxygen partial pressures over the $Pb_{45}Bi_{55}$ melt than over the Pb melt must be established to achieve the same oxygen concentration in the alloy. When this function is used to calculate oxygen solubility data in eutectic $Pb_{45}Bi_{55}$, the agreement with data of the only known measurement is satisfactorily at temperatures above 500°C. Below 500°C, discrepancies get larger with decreasing temperatures. This has implications on experiments employing large temperature differences. Measurements of the oxygen solubility in eutectic $Pb_{45}Bi_{55}$ are necessary, especially for temperatures below 500°C [8.25].

List of abbreviations and symbols to Chapter 8

a, a_0	activity constant
E ,	EMF, Electromotive force, V
F	Faraday’s constant, C/mol
ΔG	Free energy of formation, [8.5], J/mol
P	Partial pressure, Pa
R	Gas constant, $JK^{-1}mol^{-1}$
T	Temperature, K

REFERENCES TO CHAPTER 8

[8.1] KNEBEL, U., et al., “European Research Programme for the Transmutation of High Level Nuclear Waste in an Accelerator Driven System”, Proc. FISA 2006, Luxembourg 13–16 March 2006.

[8.2] CINOTTI, L., et al., LFR Lead Fast Reactor, Proc. FISA 2006.

[8.3] OECD NUCLEAR ENERGY AGENCY, Handbook on Lead-Bismuth Eutectic Alloy and Lead Properties Material Compatibility, Thermal-hydraulics and Technologies, OECD/NEA Nuclear Science Committee, NEA No. 6195 (2007). http://www.oecd-nea.org/science/reports/2007/pdf/

[8.4] GROMOV, B.F., ORLOV, Y.I., MARTYNOV, P.N., GULEVSKI, V.A., Proc. Heavy Liquid Metal Coolants in Nuclear Technology, HLMC’98, October 5–9, 1998, Obninsk, Russian Federation (1999) 87.

[8.5] YACHMENYOV, G.S., et al., Proc. Heavy Liquid Metal Coolants in Nuclear Technology, HLMC’98, October 5–9, 1998, Obninsk, Russian Federation (1999) 133.

[8.6] MÜLLER, G., SCHUMACHER, G., ZIMMERMANN, F., J. Nucl. Mater. **278** 1 (2000) 85.

[8.7] SOLER, L., MARTIN, F.J., HERNANDEZ, F., GOMEZ-BRICENO, D., J. Nucl. Mater. **335** (2004) 174.

[8.8] MÜLLER, G., et al., J. Nucl. Mater. **335** (2004) 163.

[8.9] FAZIO, C., BENAMTI, G., MARTINI, C., PALOMBARINI, G., J. Nucl. Mater. **296** (2001) 243.

[8.10] MARTINELLI, L., DUFRENOV, T., JAAKOU, K., ROSANOV, A., BALBAUD-CELERIER, F., J. Nucl. Mater. **376** (2008) 282

[8.11] KONYS, J., MUSCHER, H., VOSS, Z, WEDEMEYER, O., J. Nucl. Mater. **335** (2004) 249–253.

[8.12] ZHANG, J., LI, N., Review of studies on fundamental issues in LBE corrosion, Los Alamos National Laboratory, Report No: LA-UR-04-0869, 2004.

[8.13] ORLOV, Y.I., The main impurities and their condition in the Pb-Bi coolant, Contract SSC RF IPPE/CEADRN-DER 5010 6 8 B049630, Substage 2.1, Obninsk (1998).

[8.14] SAMSONOV, G.V., (Ed.), The Oxide Handbook, 2nd Ed., IFI/Plenum, New York 1982.

[8.15] COCCOLUTO, G., et al., Proc. 17th Int. Conf. Nuclear Engineering, **1** (2009) 693.

[8.16] BHAT, N.P., BORGSTEDT, H.U., Fusion Technol. **21** (1992) 59.

[8.17] SHMATKO, B.A., RUSANOV, A.E., Mater. Sci. **36** (2000) 700.

[8.18] COUROUAU, J.-L., J. Nucl. Mater. **335** (2004) 259.

[8.19] KONYS, J., MUSCHER, H., VOSS, Z., WEDEMEYER, O., J. Nucl. Mater. **296** (2001) 294.

[8.20] FERNÁNDEZ, J.A., ABELLÀ, J., BARCELÓ, J., VICTORI, L., J. Nucl. Mater. **301** (2002) 52.

[8.21] COUROUAU, J.-L., et al., J. Nucl. Mater. **301** (2002) 59.

[8.22] COUROUAU, J.-L., DELOFFRE, P., ADRIANO, R., J. Phys. IV France **12** (2002) Pr8/141.

[8.23] COLOMINAS, S., ABELLÀ, J., VICTORI, L., J. Nucl. Mater. **335** (2004) 260.

[8.24] ASKADULLIN, R.SH., et al., Development of Oxygen Sensors, Systems of Control of Oxygen Content in Lead Coolants for Test Loops and Facilities, ITSC Project No. 3020, Final Report, Institute for Physics and Power Engineering (IPPE), Obninsk, Russian Federation (2007).

[8.25] MULLER, G., HEINZEL, A., SCHUMACHER, G., WEISENBURGER, A., J. Nucl. Mater. **321** (2003) 256.

CHAPTER 9. COMPONENTS FOR SERVICE IN INTIMATE CONTACT WITH HEAVY LIQUID METALS

9.1. INTRODUCTION

A lead-cooled nuclear reactor is one of the systems to be deployed in the future. Concerns related to the use of lead and lead alloys arise from the materials compatibility, in terms of corrosion and mechanical resistance.

The reference structural materials selected for the Heavy Liquid Metal (HLM) cooled systems are 9Cr ferritic-martensitic (F/M) steels for core components and heat exchanger and the austenitic steel AISI 316L for vessel and in-vessel structures.

Ti3SiC2, a ternary compound, was selected as one of the most promising candidate material for pump impeller and bearings, because it combines some of the most attractive properties of ceramics with those of metals.

The design of a prototypical DHR heat exchanger has been carried out in the frame of the R&D activities for the development of a lead fast reactor, meeting the GEN IV requirements.

9.2. IMPROVING THE CORROSION RESISTANCE AND CREEP STRENGTH OF STEELS EXPOSED TO HEAVY LIQUID METALS BY SURFACE MODIFICATION USING PULSED E-BEAMS

In case of steels, dissolution of metallic components into the lead alloy, extensive oxide scale growth and reduced mechanical resistance are major challenges for such systems [9.1]. Previous studies showed that the corrosion mechanism of the structural steels in Pb-Bi eutectic melt is affected by several parameters, such as oxygen activity in the liquid metal and temperature [9.2]–[9.10]. Oxide scales formed on steels act as diffusion barriers for cations and anions and provide the best protection against dissolution attack. Below 500°C and with appropriate oxygen activity in LBE, dissolution of steel elements in the liquid metal can be minimized or suppressed through the formation of a protective oxide scale on the steel surface. At temperatures above 500°C, austenitic steels (316 type) suffer from severe dissolution attack, while 9 Cr martensitic steels form thick oxide scales, which hinder heat transfer from the fuel pins and which may break off and eventually lead to blocking of the coolant channel. Therefore, above 500°C, steels have to be protected by stable and thin oxide scales.

Besides the described corrosion problems, the negative influence of LBE or lead on the mechanical properties was also reported [9.11], [9.12]. Liquid metal embrittlement (LME) and stress corrosion cracking are investigated and still under debate by different groups. During creep-to-rupture experiments at high stress levels, a significant influence of the LBE, namely at 550°C, on the T91 in original state was reported [9.13].

Alloying steel in the near surface region with strong oxide formers like aluminium (Al) combines protection against dissolution with slowly growing oxide scales. Alumina scales, which grow very slowly due to low diffusion coefficients of cations and anions, are formed on a steel surface. The required amount of Al depends on temperature, oxygen content and chromium concentration. FeCrAlY coating, modified using pulsed electron beams (GESA treatment), is the surface protection method used at Karlsruhe Institute of Technology (KIT) to obtain the required aluminium concentrations in the near surface region [9.14]. The alloyed area should be limited to the near surface region due to the negative influence of Al on the mechanical strength of the steels. Mechanical properties of steels were not influenced by the surface modification treatment, as proven during low cycle fatigue and pressurized tube experiments [9.15], [9.16].

9.2.1. Materials and experimental work

Materials

The ‘T91’ steel has been selected as one of the candidate materials for neutron spallation target of accelerator driven systems (ADSs) and core components of lead cooled fast reactors (LFRs) because of its good mechanical strength and irradiation resistance in a fast neutron or a spallation spectrum.

The T91 steel is a modified 9Cr steel with additions of Nb and V, to increase the mechanical strength, especially at higher temperatures. Before the tests, T91 has been normalized at 1050°C for 30 min and air quenched, followed by tempering at 770°C for 1 h.

The Al surface-alloyed specimens were produced in a two step process: deposition of the Al containing layer; and post-treatment using pulsed electron beams (GESA process).

Surface modification process

The GESA facilities are designed and constructed together with Efremov Institute of Electrophysical Apparatus (EIEA), St. Petersburg, and are widely explored at KIT and EIEA. Presently, GESA treatment of Al-alloy coatings is the favourite process at KIT (Karlsruhe Institute of Technology, Germany).

The GESA (Gepulste ElektronStrahl Anlagen) process uses pulsed electron beams [9.17] with a kinetic energy in the range of 50±400 keV, a beam power density up to 6 MW/cm^2 at the target and a pulse duration up to 40 μs. The energy density adsorbed at the target is up to 80 J/cm^2, which is sufficient to melt metallic materials adiabatically up to a depth of 50 μm. Due to the high cooling rate ($\sim 10^7$ K/s), very fine grained structures develop during the solidification of the molten surface layer. This is a suitable basis for the formation of protective oxide scales with good adhesion.

The above described surface modification process is mainly considered for cladding tubes. Therefore, a special GESA facility with a cylindrical cathode was designed (Fig. 9.1). This facility allows the treatment of an entire tube of about 30 cm length with a single pulse.

FIG. 9.1. GESA facility with a cylindrical cathode.

The first step of the surface modification process consists in thermal spraying the FeCrAlY powder, with modified low pressure plasma spraying (LPPS) process, to obtain layers with an average thickness of about 30µm. During the second step, the deposited layer plus some micrometers of the steel surface are melted using pulsed e-beams generated by GESA facility, in order to obtain a metallic bonded surface layer or a surface graded material. A subsequent heat treatment at 400°C in air for 2 h is performed for releasing residual stresses. Images of the Al surface-alloyed samples, after LPPS coating and after GESA treatment, are shown in Figs 9.2(a) and (b), respectively. The GESA treatment makes the surface smooth, removes the pores, creates a metallic interface, but leads to a reduction in Al content mainly due to evaporation.

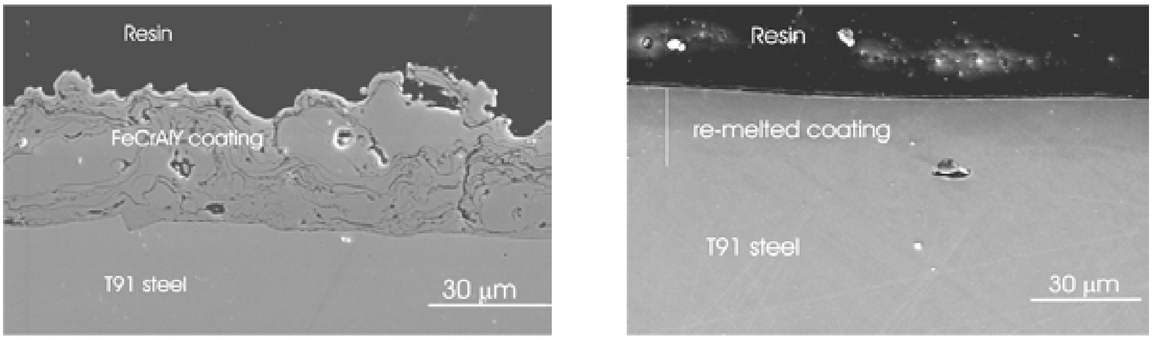

(a) (b)

FIG. 9.2. SEM cross-sections images of T91 with as sprayed FeCrAlY coating showing a rough, porous layer (a) and, after GESA treatment, a smooth metallic bonded layer (b).

Corrosion and mechanical test facilities

The COSTA (COrrosion in STagnant liquid lead Alloys) facility at the KALLA laboratories of the KIT is employed for running corrosion tests in molten lead/lead alloys with control of temperature and oxygen content. The facility consists in furnaces, made of quartz tubes, having independent gas supply systems, aimed to control the atmosphere inside the furnaces. According to the thermodynamic considerations, detailed in [9.18], the desired oxygen concentration in the molten metal/alloy is achieved through the thermodynamic equilibrium between gas and liquid phase.

The multiple zones heating system allows temperature profile homogeneity in the furnaces, where thermocouples, connected to control units, are allocated along the quartz tubes. Additional details on the design and the functioning of the COSTA facility can be found in [9.19]. Corrosion tests consist in dipping specimens into molten LBE (about 150 g) contained in ceramic crucibles, placed in the COSTA furnaces; they could be performed at temperatures varying from 450°C up to 750°C and oxygen concentrations in the liquid PbBi from 10^{-8} to 10^{-4} wt%.

The creep tests in uni-axial mode were performed in a heavy liquid metals loop, especially designed for mechanical tests like LCF and creep-to-rupture. The creep tests in lead or LBE were conducted in a loop set-up that contained four separated vessels, each one to host up to two samples mounted in a capsule with its own loading system. Two specimens were simultaneously tested, at two different stress levels, and extracted together from the melt. These facilities allow specimens testing under a wide range of conditions: temperatures from 400°C to 700°C, flow velocities from stagnant up to turbulent flow, oxygen concentrations from 10^{-8} wt% up to saturation level, isothermal and non-isothermal conditions.

Creep tests in air were performed using a vertical tensile testing machine equipped with a resistive furnace.

9.2.2. Results and discussion

Corrosion tests

Corrosion tests in static and flowing LBE covered the temperature range from 400 to 650°C and were performed on samples with and without surface modification. The oxygen concentration of LBE was 10^{-6} and 10^{-8} wt% in order to allow the formation of protective oxide scale on the steel surface.

After 2000 h of exposure to LBE at 550°C and 10^{-6} wt% oxygen concentration, the samples made out of T91 without surface modification showed thick oxide scale with multilayer morphology, consisting in magnetite (outer part), Fe-Cr-based spinel (middle) and an internal oxidation zone (inner part) (Fig. 9.3(a)).

Al surface-alloyed T91 specimens, using GESA process, were also exposed for 2000 h to LBE with 10^{-6} wt% oxygen at 480°C, 550°C and 600°C. Even at higher temperature (600°C), there is only a very thin alumina scale (<1 μm) on top of the surface (Fig. 9.3(b)) [9.15].

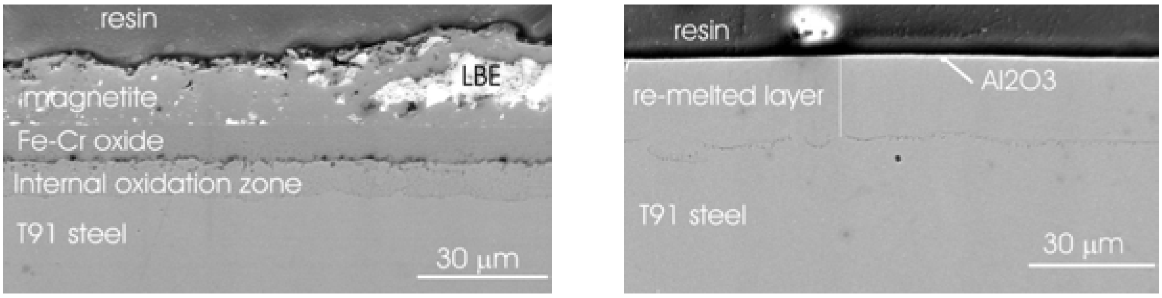

(a) (b)

FIG. 9.3. SEM of the cross-section of original T91 specimen (a) and of Al surface-alloyed T91 specimen (b) after exposure to LBE (550°C, 10^{-6}wt% oxygen).

Creep tests

Uni-axial creep-to-rupture tests were performed on original T91 steel, in air and in flowing lead-bismuth eutectic melts (550°C, 10^{-6} wt.% oxygen, flow rate of 0.5 m/s), at stress levels of 140, 160, 180, 200 and 220 MPa [9.13].

Compared with specimens tested in air, the specimens tested in liquid metal show: (i) an increase of the strain and the strain rate; (ii) a decrease of the time-to-rupture; (iii) a rapid transition into the third stage of creep at high stress (above 180 MPa) (Fig. 9.4). For all the applied stresses, the secondary creep rate is significantly lower for the specimens tested in air than for those tested in LBE, as depicted in Fig. 9.5. The fitted curves for LBE and air were finally taken to calculate the ratio of the 2nd creep rates of specimens tested in LBE and in air (Table 9.1).The influence of LBE on the creep strength is clearly stress-dependent. At 200 MPa, the creep is about 53 times faster in LBE than in air; at 140 MPa, this ratio drops to 27.

Fractographic analysis was performed in order to determine the main macroscopic and microscopic features of the broken specimens. The specimens tested in air show necking regions and cup-and-cone fracture surfaces. The fracture surfaces consist of many microvoids and of dimples, a morphology specific to ductile-type fracture surfaces. The oxide scale has an inhomogeneous aspect: an outer region with cracks and tendency to spall and an inner region, continuous and adherent to the steel surface. It was assumed that the brittle oxide layers crack under the applied loads, but the cracks stop at the steel–oxide interface and do not affect the steel substrate [9.13].

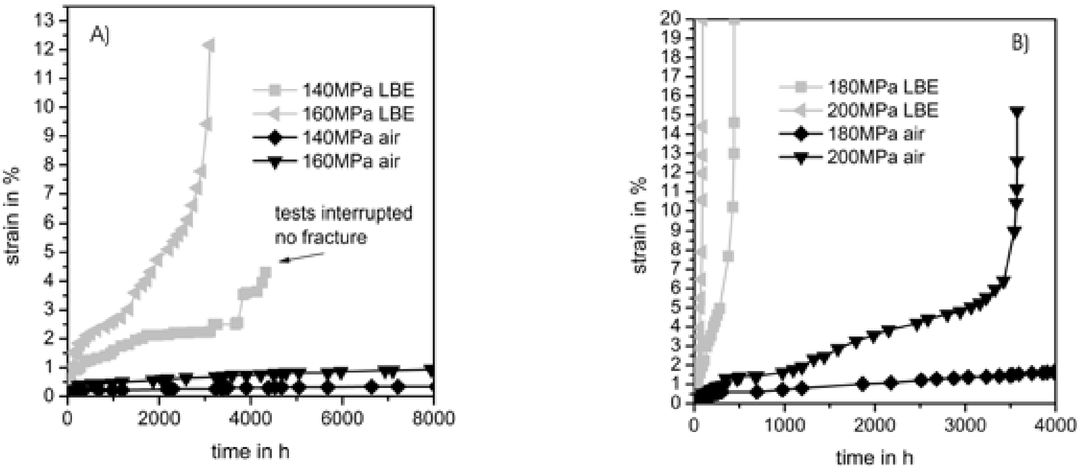

(a) (b)

FIG. 9.4. Comparison of creep-to-rupture diagrams of T91 in LBE and in air at 550°C (a) 140 and 160 MPa, (b) 180 and 200 MPa.

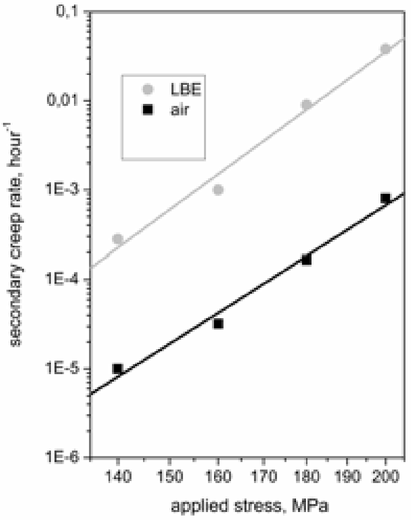

FIG. 9.5. Comparison of secondary creep rate of T91 tested at 550°C in air and LBE.

TABLE 9.1. RATIO OF 2ND CREEP RATES FOR T91 TESTED IN AIR AND LBE, AT 550°C

Stress [MPa]	Ratio of 2nd creep rates, LBE/air
140	27
160	35
180	44
200	53

All T91 specimens exposed to LBE show necking regions. Multiple microcracks in the oxide scale were observed on the lateral surfaces of the specimens (Fig. 9.6). The density, width, depth and orientation of these microcracks depend on the applied load and on the distance from the fracture surfaces. The number, width and depth of these microcracks decrease with increasing distance from the fracture surfaces, because the deformation of the samples decreases also in these regions.

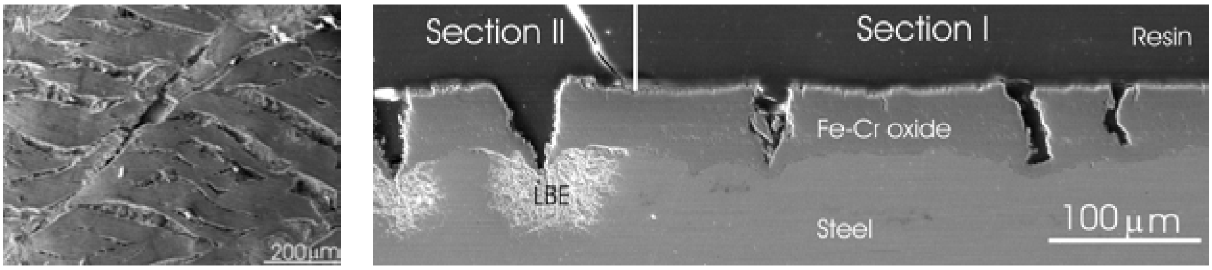

(a) (b)

FIG. 9.6. (a) Microcracks on the lateral surface of the specimen tested with 180MPa and (b) microcracks observed in the sample exposed to 160 MPa far from fracture surface (section I) and at the beginning of the necking region (section II).

The examinations of the cross-sections by scanning electron microscopy (SEM) combined with energy dispersive X-ray spectroscopy (EDX) have revealed that all samples exhibit an oxide scale with multilayer morphology: an outer magnetite layer, an inner Fe–Cr spinel-type oxide layer and an innermost internal oxidation zone (IOZ) with Cr-depleted grains (4–6 wt.%). The magnetite layer tends to spall off and the entire scale lost adherence and was removed in many parts of the necking regions (especially close to the fracture surface). The multilayered oxide scales show many microcracks. The cracks, observed in the oxide scales, are initiated in the external sublayer and either stop at the interface between the two sublayers or cross also into the internal sublayer. The microcracks, located far from the fracture surface (low strain), are blocked by a renewed scale (section I in Fig. 9.6(b)). But the tips of the microcracks, located close to the fracture surface (in the highly deformed region of the neck), show LBE penetration into regions with porosities and along grains boundaries, leading to dissolution attack (section II in Fig. 9.6(b)).

The analysis of the creep test results revealed several important surface phenomena, which lead to different behaviours of the specimens tested in lead-bismuth eutectic melts, compared with the specimens tested in air: (i) oxide scale breaking and crack propagation; (ii) liquid–metal–steel interaction at the crack tips; (iii) dissolution of steel components. The weight, with which these phenomena influence the specimen behaviour during creep-to-rupture tests in lead-bismuth eutectic melts, depends on the value of the applied stress, which, in turn, determines the exposure times. At high stress, and therefore high strain, the crack propagation process is mostly controlled by the reduction of the surface energy due to Pb and Bi adsorption on the steel surface [9.20]. At low stress (140 and 160 MPa) and low strain, this process is delayed due to the competing mechanism of healing the oxide scale cracks.

The Al surface-alloyed specimens, using the GESA process, were tested in LBE and air. The tests in air, performed at 200 and 220 MPa, show an increase in creep-to-rupture strength of the surface-alloyed material, which might be a result of the increased hardness of the outer layer. The surface-alloyed (GESA) specimens exhibit, at both loads, significantly later breaking, compared with samples made out of original T91 (Fig. 9.7(a)). At 220 MPa, the surface-alloyed specimen survived for more than 2000 h, while the T91 in original state ruptured already after less than 1000 h. The creep-to-rupture test of the GESA specimen at 200 MPa was stopped after more than 10 000 h with a strain of 2.6%. The T91 original ruptured after 3500 h. In addition to the rupture times, the strain rates are also lower for the surface-alloyed specimens, compared to the non-modified ones. The alloyed surface forms an alumina scale that is very thin (<1µm) and seems to be very ductile (Fig. 9.7(b)).

The Al surface-alloyed specimens, exposed to LBE (550°C, 10^{-6} wt% oxygen), were creep tested at 160, 180, 200 and 220 MPa. The experiments at 160 and 180 MPa were interrupted after 2590 h and those with 200 and 220 MPa were conducted until break of the specimen. The strain-time curves of the experiments are plotted together with the respective curves of the T91 original in air and LBE (Fig. 9.8(a)). At lower stresses, none of the strain curves reaches the 3rd creep stage — all are still in the 2nd creep phase. The strain of the surface-alloyed specimens tested in LBE is slightly higher for low stress than the one of original T91 tested in air. At higher stress, all three phases of creep can be recognized. Up to a strain of about 3.5%, the behaviours of T91+GESA tested in LBE and of original T91 tested in air with a load of 200 MPa are almost identical. With increasing exposure time, the creep in LBE is accelerated. At higher load of 220 MPa (not depicted), this difference is less pronounced and the creep-to-rupture time is only slightly smaller in the specimen tested in LBE.

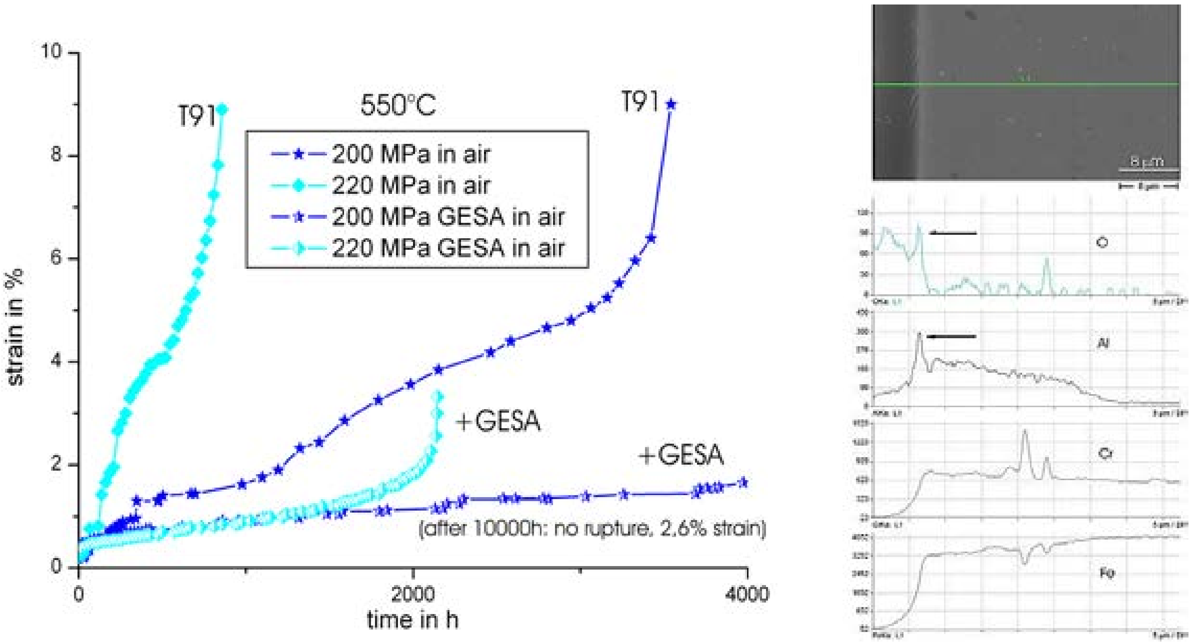

(a) (b)

FIG. 9.7. (a) Comparison of strain versus time for GESA surface-alloyed T91 with original T91 tests in air at 550°C; (b) SEM of cross-section and EDX elemental line scan of surface-alloyed T91 after creep test at 200 MPa showing the thin Al-oxide scale not exhibiting cracks.

Due to imperfections in the surface coating and alloying process, the Al content was not homogeneously high enough to guarantee the formation all over the specimens of a protective alumina scale. Parts of the specimens, up to 40%, exhibit normal oxidation with the formation of Fe-Cr spinel-type oxide and magnetite. The cross-section clearly showed the cracking of the magnetite layer and the penetration of the LBE (Fig. 9.9(a)). Regions with thin alumina scale do not crack in the lower strain regions (Section I), and only in the necking region with the highest strain (Section II), cracks could be observed (Fig. 9.9(b)). However, such cracks were never penetrated or filled with LBE. For this reason, the Al surface-alloyed specimens, obtained after pulsed electron beam treatment, show strain, 2nd creep rates (Fig. 9.8(b)) and creep-to-rupture times, at 550°C in LBE, comparable to original T91 exposed in air. The difference is mainly attributed to the non-perfect alloying of specimen surface.

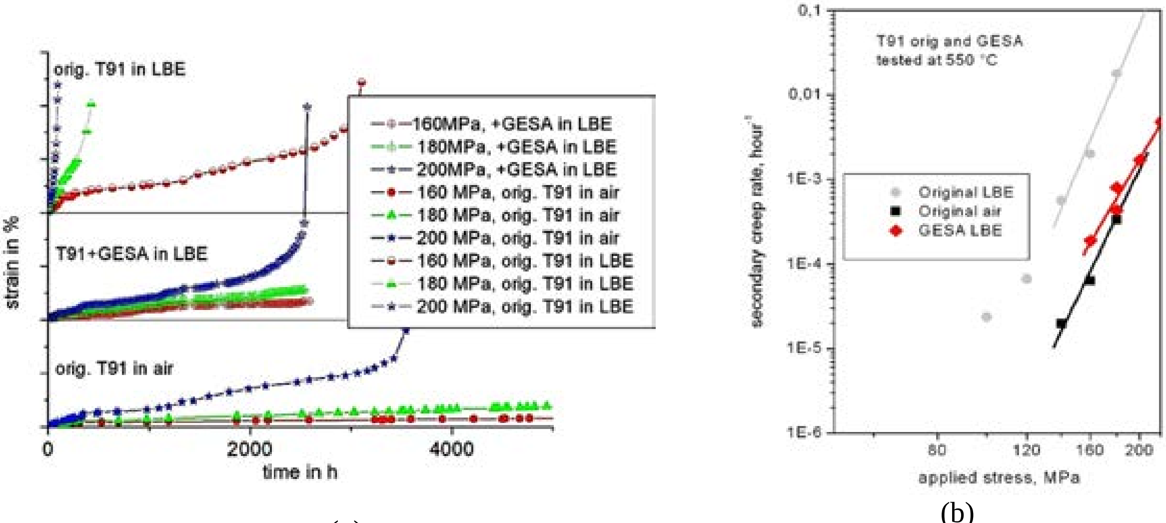

(a) (b)

FIG. 9.8. (a) Strain versus time of original T91 creep tested in air, and original and GESA treated T91 specimen tested in LBE; (b) Secondary creep rates versus applied stress (MPa) of original T91 in air and LBE and of GESA surface-alloyed T91 in LBE (original T91 and GESA tested at 550°C).

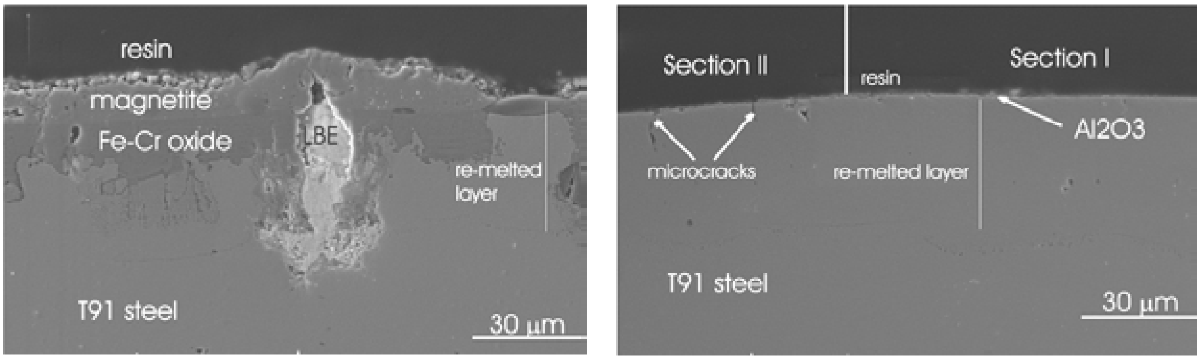

(a) (b)

FIG. 9.9. SEM of cross-section of surface-alloyed T91, at the onset of the necking region, after creep test in LBE at 550°C with 200 MPa load: (a) region with less Al and thicker multilayered oxide scale having LBE filled cracks; (b) region with high Al content with thin non-visible scale and only tiny cracks.

9.2.3. Conclusions

The alloying of steel surface with aluminium using microsecond-pulsed intense electron beams was developed and optimized in order to be used for improving the corrosion resistance and creep strength of steels, exposed to liquid Pb and Pb-Bi eutectic. The procedure consists in two steps: (i) coating the steel surface with an Al-containing alloy layer; and (ii) melting the coating layer and the steel surface layer using intense pulsed electron beam.

Using the mentioned procedure, the corrosion resistance and creep strength of the F/M 9Cr ‘‘T91” steel, exposed to Pb and Pb-Bi eutectic with different oxygen concentrations and under different temperatures, were considerably improved due to the formation of a thin alumina layer, whose thickness is lower than 1 µm for all the tested temperatures and durations. This slowly growing alumina layer acts as an anticorrosion barrier and is less susceptible to crack formation and, therefore, to lead alloy enhanced creep.

First indications on the tolerable creep strain were evaluated. However, further detailed experiments would be required at higher operating temperatures, which are expected usually in pure Pb-cooled systems.

9.3. IDENTIFICATION AND TESTING OF THE MOST PROMISING ALLOYS AS CANDIDATE MATERIAL FOR PUMP IMPELLER

One of the main issues regarding the design of LFR is the corrosion-erosion behaviour of materials in contact with high temperature and high velocity lead, such as pump impeller and bearing materials. Those materials will worked in lead at about 480°C with a velocity relative to impeller blade in the magnitude of 10 m/s. Ti_3SiC_2, a ternary compound, was selected as one of the most promising candidate material, because it combines some of the most attractive properties of ceramics with those of metals.

This material was already applied in industry, but more effort is needed to qualify its performance when compared with candidate structural stainless steel available in Europe. With the purpose of evaluating the corrosion resistance of Ti_3SiC_2, a preliminary screening test was carried out at ENEA Brasimone in flowing lead under oxidation conditions (oxygen concentration of about 10^{-6} wt% in the melt), with an average temperature of 500°C and a flow velocity of about 1 m/s.

Traditional steels (austenitic steels, ferritic-martensitic steels) cannot be used as materials for pump impeller, due to their high corrosion-erosion rate in flowing lead at temperatures higher than 400°C and lead velocity magnitude of 10 m/s [9.21]. In fact, the pump impeller has to work in contact with lead at high relative velocity, higher than 10m/s, and the hydrostatic bearing will be working at very high lead relative velocity. The synergy between the corrosion-erosion phenomena on the materials in contact with high temperature and high velocity lead required developing new kinds of materials as composite materials.

A set of new materials need to be developed and tested with the aim to investigate and identify the most promising candidates for further validation at larger scale in the frame of European or national programmes.

Ti_3SiC_2 is one of the candidate materials; its main advantages over the other composite materials are:

- very easy to machine;
- easy to form using different techniques such as pressing, slip casting and injection molding.

Some experimental tests in pure lead and in lead-bismuth, static and flowing lead were performed in the past for about 1000 h at different operative conditions and their results are available in literature [9.22], [9.23].

TABLE 9.2. THERMOPHYSICS PROPERTIES OF TI$_3$SIC$_2$

Physical and electrical properties		
Density	g/cm^3	4-5
Electrical conductivity at RT	Ohm^{-1} m^{-1}	2-4.5 × 10^6
Thermal properties		
CTE	K^{-1}	8–12 × 10^{-6}
Thermal conductivity at RT	W/m K	30–45
Thermal conductivity at 1200°C	W/m K	25–35
Service temperature, Air	°C	1000–1400
Service temperature, inert or vacuum	°C	1400–1800
Mechanical properties		
Elastic modulus	GPa	270–320
Hardness	Vickers	400–600
Tensile strength at RT (brittle)	MPa	100–200
Tensile strength at 1200°C (ductile)	MPa	20–40
Flexure strength at RT (brittle)	MPa	250–400
Flexure strength at 1200°C (ductile)	MPa	50–100
Compressive strength at RT (brittle)	MPa	700–1100
Compressive strength at 1200°C (ductile)	MPa	200–500
Fracture toughness, K_{IC}	MPa m$^{1/2}$	6–9
Thermal shock, ΔT_C (100 µm grain size)	°C	1200–1400
Thermal shock, ΔT_C (5 µm grain size)	°C	500–700

Ti_3SiC_2 was chosen because it combines the best properties of metal and ceramics [9.25], [9.26]. It is a ternary compound belonging to $M_{n+1}AX_n$-phases (n = 1, 2 or 3) [9.27], that can be considered as a nano-laminar composite, with a layered microstructure where mono-atomic Si-element sheets are interleaved with Ti_3C_2-layers (see Fig. 9.10).

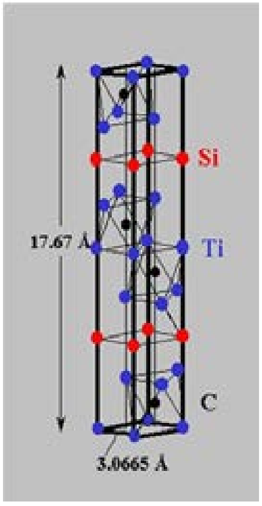

FIG. 9.10. Ti_3SiC_2 crystal structure [9.24].

The Ti_3SiC_2 is the most well studied MAX phase to date. Polycrystalline samples of Ti_3SiC_2 are brittle at room temperature as any other ceramic, but single crystals are ductile. This is because Ti_3SiC_2 deforms by the formation of so-called ‘kink bands’. Kink bands are formed when edge dislocations are generated in a crystal and then set to move in two directions opposite each other. At higher deformation stresses or higher temperatures, the dislocation walls bounding the kinks apparently separate and become mobile [9.28]. It is the coalescence of several such walls that eventually produces a kink boundary; two kink boundaries constitute a kink band. It seems that the production and annihilation of kink bands is a fully reversible process, where the dislocation walls remain attached. Instead, the production and annihilation of kink bands, which have mobile dislocation walls, is an irreversible process. The behaviour of kinks bands into material permits to contain and confine damage to small areas preventing/limiting crack propagation through the material. An initiated crack cannot propagate beyond the kink boundaries which become containers of damage. This damage behaviour, high damping capability, is typical of kinking non-linear elastic (KNE) solids, so described because they deform non-linearly but elastically by the formation of dislocation-based kink bands. MAX phase is also characterized by this behaviour. It is a particular characteristic that clearly distinguishes Ti_3SiC_2 from traditional brittle ceramics. Ti_3SiC_2 is also insensitive to thermal shock.

Ti_3SiC_2, like its corresponding binary carbides and nitrides, is elastically stiff, has relatively low thermal expansion coefficients, good thermal and electrical conductivities, and is resistant to chemical attack (see Table 9.2).

At higher temperatures, it goes through a brittle-to ductile transition. It is in addition readily machinable, as confirmed by samples realization with a block of material, and it can even be plasma sprayed to form a coherent coating [9.29], [9.30].

To verify the corrosion-erosion behaviour of the material, a preliminary corrosion test was performed in a lead loop called CHEOPE III [9.21]. The as-received material was machined in 10 cylindrical specimens with 10 mm diameter, 33.4 mm length and 0.2 Ra surface roughness. One specimen was degreased and its chemical composition was analysed by EDX (Fig. 9.11).

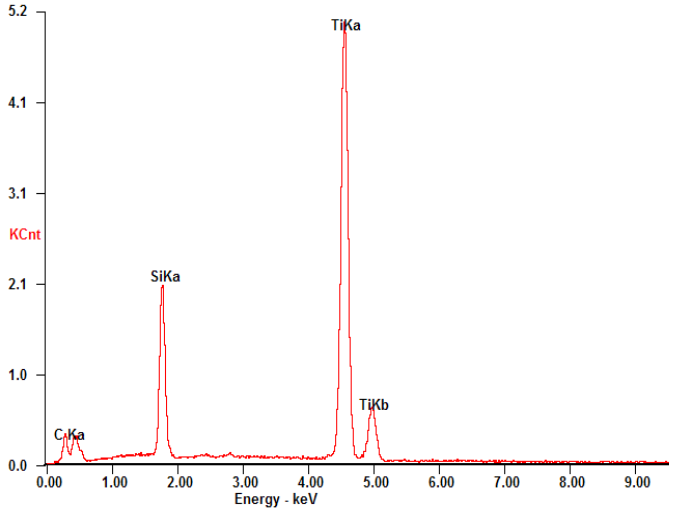

Element	*Wt %*	*At %*
C K	13	35
SiK	13	15
TiK	73	49

FIG. 9.11. Atomic analysis of not exposed Ti_3SiC_2 sample by EDX in the bulk of the sample.

The other nine specimens were measured, degreased and weighted before being placed inside the test section, shown in Fig. 9.12. In this configuration, the liquid metal flows from the bottom, through the test section and goes out from the top. The test section is constituted by three sections in AISI 316, each one containing three tubes with three specimens each. The Ti_3SiC_2 specimens were placed together by fixing their ends with pins.

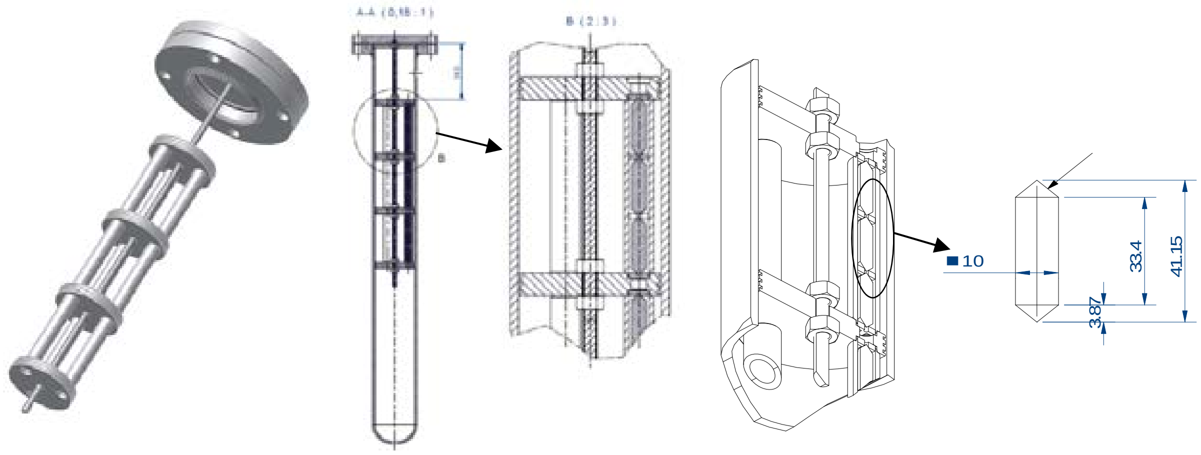

FIG. 9.12. 3-D view and a detail of CHEOPE III test section; detail of one sample.

The test was performed at relevant LFR operative conditions:

- ⇒ The temperature inside the test section was 500°C.
- ⇒ The average velocity of lead was about 1 m/s.
- ⇒ The oxygen concentration in lead was maintained at a constant value 10^{-6} wt% by means of an oxygen control system and gas mixture injections (Ar-H_2) inside the test section during the test [9.31].

The monitoring of the oxygen concentration was performed by means of an ENEA’s oxygen sensor installed in the upper part of the test section [9.31].

The total duration of the test was 2000 h. After exposure to lead, three specimens were cut and polished for cross-section examination by Scanning Electron Microscopy (SEM). The chemical composition of the bulk materials at one micron from the boundary layer was analysed. The other six samples were immersed in a cleaning solution (CH_3COOH : H_2O_2 : C_2H_5OH = 1:1:1) at room temperature to remove the adherent lead. The procedure was repeated three times until no weight change was observed. Specimens were then cleaned and dried for weight measurement.

Table 9.3 shows the weight change for six of the nine specimens tested in CHEOPE III loop. It is possible to observe a low increase of weight for each specimen. The value of mass gain is about 0.05g (47g/m^2) per specimen.

TABLE 9.3. CHANGE OF WEIGHT OF SIX SPECIMENS IN Ti_3SiC_2 AFTER THE EXPOSING TO LEAD AT 500°C FOR 2000 h

Sample PM	Material	Ø (mm)	L (mm)	Weight pre (g)	Weight post (g)	Δp (g)	Δp_s (g m^{-2})
1	Ti_3SiC_2	9.96	33.5	11.5442	11.5989	0,054	51,49
2	Ti_3SiC_2	9.97	33.5	11.5645	11.6152	0,050	47,68
3	Ti_3SiC_2	9.96	33.5	11.5322	11.5939	0,061	58,16
4	Ti_3SiC_2	9.96	33.5	11.5769	11.6332	0,056	53,40
5	Ti_3SiC_2	9.95	33.5	11.5324	11.5958	0,063	60,07
6	Ti_3SiC_2	9.93	33.5	11.5712	11.6247	0,053	50,54

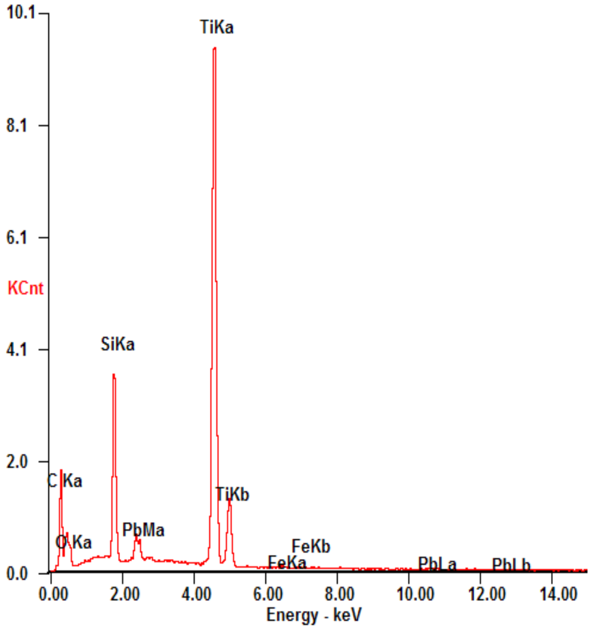

Element	**Wt %**	**At %**
C K	27	55
O K	06	09
SiK	09	07
TiK	51	26
FeK	00	00
PbL	04	00

FIG. 9.13. Atomic analysis of exposed sample PM 08907 in pure lead at 500°C for 2000 h, 1 µm from boundary layer.

On the basis of EDX analysis on the other three specimens, it is possible to observe the presence of oxygen in the first micron from the boundary. This can suggest the formation of a superficial oxide layer on each specimen.

No deep lead penetration into the Ti_3SiC_2 matrix has been observed in the EDX micrographics in the analysed area (Fig. 9.13). Only some lead inclusions were observed in the outer region of the material due to the surface porosity (Figs 9.14 and 9.15), but the lead penetration is limited to the first micron. Even big open porosities (20–30 µm) in communication with the surface porosities have not shown the presence of lead (Fig. 9.16).

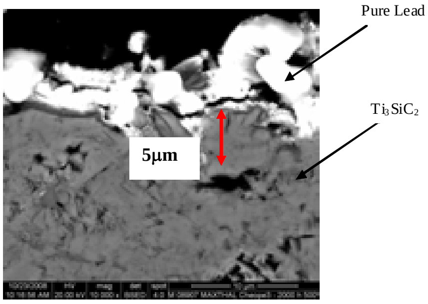

FIG. 9.14. Micrograph of Ti_3SiC_2 specimen (PM08907), 10 μm scale. Exposure time in lead 2000 h, T: 500°C.

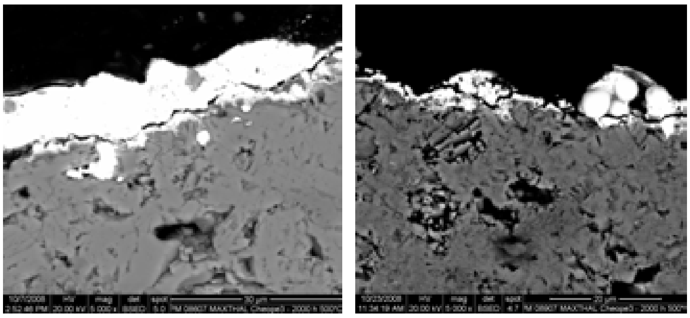

FIG. 9.15. Micrograph of Ti_3SiC_2 specimens (PM08607 and PM 08907), 30 and 20 μm scale, respectively. Exposure time in lead 2000 h, T: 500°C.

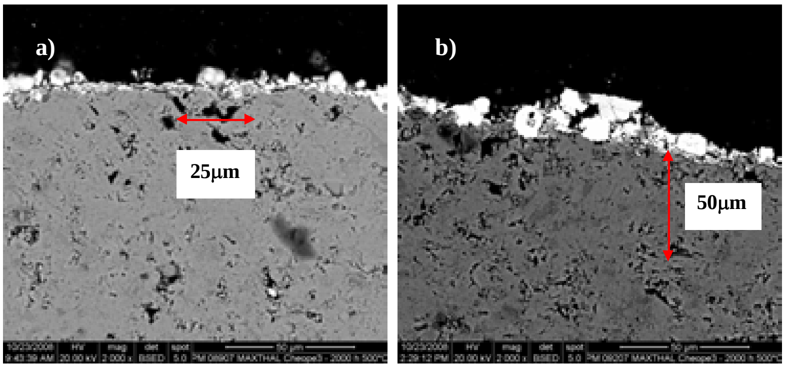

FIG. 9.16. SEM micrograph of Ti_3SiC_2 specimens (PM08907 and 09207), 50 μm scale. Exposure time in lead 2000 h, T: 500°C. a) Open porosity size is in the range of 1–30 μm; b) No lead penetration is observed in the bulk.

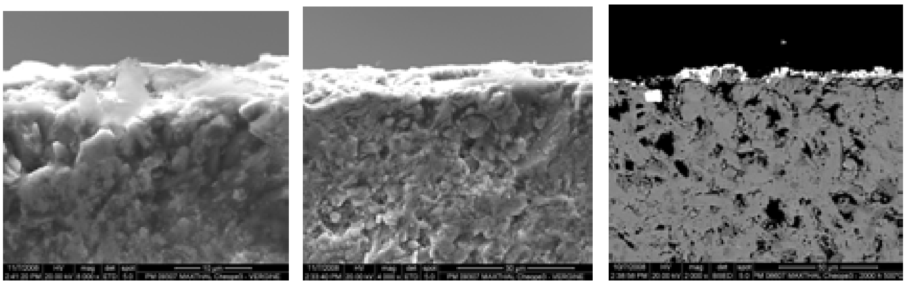

FIG. 9.17. Micrograph of Ti_3SiC_2 specimens: on the two photos on the left, the specimen (PM09307) not exposed in lead and, on the right photo, the specimen (PM08607) exposed in lead for 2000 h.

No corrosion of the materials by the lead can be observed; the surface does not show relevant shape change, only some roughness along the surface of the samples. Lead does not appear to stick to the surface of Ti_3SiC_2 specimens in any of the analysed areas (Fig. 9.17).

TABLE 9.4. EXPERIMENTAL RESULTS CARRIED OUT COMPARED WITH THE RESULTS AVAILABLE IN LITERATURE [9.22], [9.23]

Material	Test	Main Parameters	Results
Ti_3SiC_2 (supplied by 3-ONE-2 LLC)	Corrosion test in flowing lead (M. Utili et al., 2008)	lead velocity: ~1 m/s Oxygen concentration (wt.%):~10^{-6} Temperature: 500°C Time exposure: 2000 h	- no lead penetration into material matrix - no trace of corrosion - lead penetration only into superficial pores - no dissolution of material in lead
Ti_3SiC_2 (supplied by 3-ONE-2 LLC)	Corrosion test in stagnant lead-bismuth (M. Takahashi, 2008 [9.23]	Oxygen concentration (wt.%):~$5\cdot10^{-6}$ Temperature: 700°C Time exposure: 1000 h	- no penetration of LBE into Ti_3SiC_2 matrix - no trace of corrosion - no penetration into superficial pores of the composite
Ti_3SiC_2 (supplied by 3-ONE-2 LLC)	Corrosion test in lead with natural convection (L.A. Barnes, 2007 [9.22])	Oxygen concentration: was reduced by gas-handling system, no value was measured Temperature: 650 and 800°C Time exposure: 1000 h	- no corrosion - little interaction between the lead and the ceramic, either along the cut or original surfaces

In Table 9.4, the experimental results carried out in this test have been compared with the results performed in literature. It should be noted that all tests carried out are preliminary tests, due to the fact that Ti_3SiC_2 has been studied for nuclear application only recently. On the base of these experimental results, it is possible to observe:

- the high corrosion resistance behaviour of Ti_3SiC_2 at high temperature, that is showed by the experimental results carried out from L.A. Barnes; it is constant also in flowing lead (1 m/s) at 500°C;
- no penetration of lead alloy inside the Ti_3SiC_2 matrix has been observed at 1000°C in stagnant condition, at 500°C in flowing lead and at 650°C in lead with natural circulation.

The low increase of weight for the specimen is due probably to the formation of a thin superficial oxide layer.

This hypothesis is accredited due to the constant increase of weight for each sample, $47 g/m^2$, and to the presence of oxygen in the first micron from the boundary (10% At), which could suggest the formation of an oxide scale consisting mainly of TiO_2, mainly in the rutile phase.

The formation of an outer rutile layer agrees well with descriptions of the oxidation behaviour of Ti_3SiC_2 at high temperatures in air at 10^{-6} %wt and with Ti oxidation at low oxygen partial pressures (Ellingham Richardson diagram).

An inner layer, consisting of amorphous SiO_2 and fine crystalline TiO_2, could not be confirmed because of the thin formation of the oxide layer. Only preliminary evaluation can be done on the erosion behaviour of material, due to low lead velocity of the screening test.
On the basis of the analysis carried out on the exposure specimens, it is possible to conclude:

- Ti_3SiC_2 exhibits a good corrosion resistance in flowing lead.
- The positive mass gain of 0.05g (47g/m^2) for each specimen and the presence of oxygen (10 At%) in the first micron from the boundary of the Ti_3SiC_2 after the exposure to lead suggest the formation of a thin oxide layer.
- No dissolution of Ti_3SiC_2 has been observed in the three specimens analysed by SEM.
- No pure lead penetration inside the Ti_3SiC_2 matrix through open porosities after first microns has been observed.

The results from this preliminary experimental qualification of Ti_3SiC_2 suggest that it could be a good candidate material for some applications in the primary circuit of a lead cooled fast reactor. Ti_3SiC_2 could be even a potential material for the pump impeller and bearing of mechanical pumps which work in lead. The erosion characterization of Ti_3SiC_2 compound, at high relative lead speed by a dedicated facility, could be envisaged with the aim to better evaluate its applications.

9.4. DESIGN AND ASSESSMENT OF HEAT EXCHANGERS FOR DECAY HEAT REMOVAL (DHR) SYSTEMS IN HLM REACTORS

The design of a prototypical DHR heat exchanger has been carried out in the frame of the R&D activities for the development of a lead fast reactor meeting the GENIV requirements. This component is particularly critical in the pool configuration under study; in fact, the secondary system is not a safety-grade system and additional more reliable systems are necessary to meet the safety objectives depicted in Generation IV rules. Furthermore, in case of excessive amount of steam detected in the cover gas following a SGTR (Steam Generator Tube Rupture) event, because of the impossibility to immediately distinguish the failed SG, all steam and feed water lines will be simultaneously depressurized and hence made unavailable for the DHR function.

One of the options analysed for a large power reactor is the installation of additional loops equipped with coolers immersed in the primary coolant pool, a safety-grade DHR system able to operate with water (W-DHR) or water and/or air (WA-DHR). A prototype of W-DHR has been designed and manufactured to be installed and tested into the CIRCE large scale facility in the frame of the ICE (Integral Circulation Experiment) activity [9.32], [9.33].

The prototype consists of a dip cooler tube bundle made of 91 bayonet tubes, with a thermal duty of about 1 MW. The bayonet consists of three concentric tubes (Fig. 9.18). The inner tube is fed by low pressure water (2.5 bar) that evaporates in the annulus between the inner and the intermediate tube. The annular space between the intermediate and the outer tube is filled with He gas at pressure higher than the lead pressure. The continuous monitoring of the pressure in a common gas plenum allows to promptly detect a leakage of helium. Moreover, this configuration concentrates most of the thermal gradient between boiling water and lead in the gas layer, thus avoiding both risk of lead freezing and excessive thermal stresses in the walls.

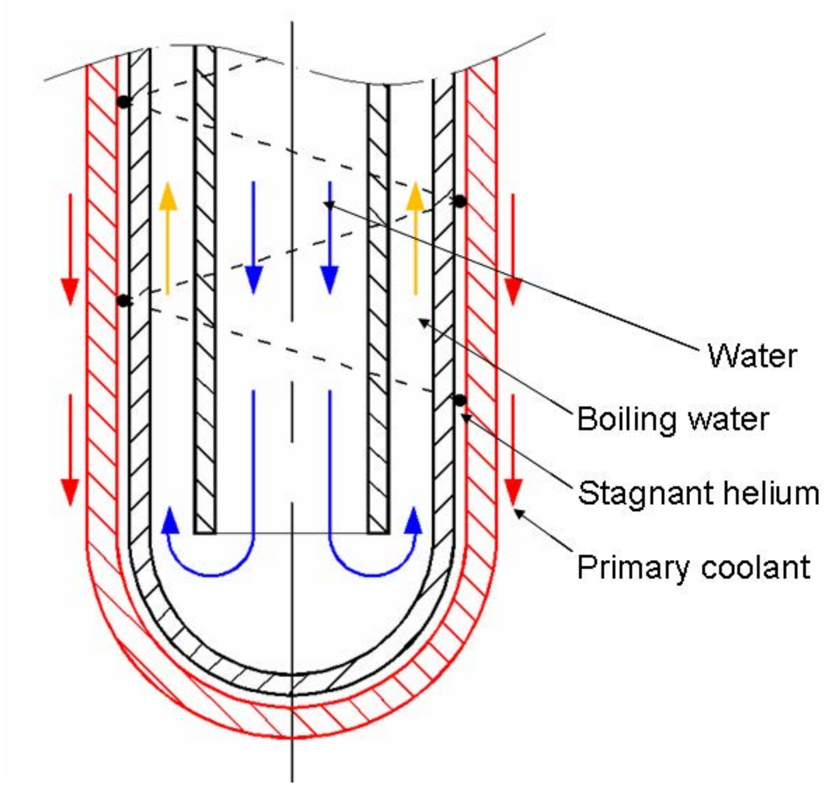

FIG. 9.18. Bayonet scheme adopted for the W-DHR prototype.

In the frame of EUROTRANS, Domain DEMETRA "Development and assessment of structural materials and heavy liquid Metal technologies for Transmutation systems", ENEA assumed the commitment to perform an integral experiment with the aim to reproduce the thermohydraulic behaviour of a relevant part of the primary system of a HLM cooled nuclear reactor in a pool configuration.

For this aim, ENEA designed and implemented the ICE activity [9.32], [9.33], with the objective to obtain information about different topics such as:

- the thermohydraulics behaviour of a HLM pool system by the analysis of the coupling between an appropriate heat source and a cold sink placed inside;
- characterization of representative components (i.e. prototypal heat exchangers, W-DHR) for the LFR/ADS concepts;
- operational and accidental transients;
- transition from the forced to the natural circulation flow regime;
- qualification of a chemistry control system for HLM pool.

Moreover, the ICE activity will allow establishing a reference experiment for the benchmark of commercial codes when employed in HLM pool systems.

The ICE activity has been designed to be implemented on the CIRCE facility [9.32].

The ICE test section [9.33] was designed to reproduce, as close as possible, the thermo-hydraulic behaviour of LFR/ADS primary systems.

The main experimental parameters characterizing the ICE experiments are reported in Table 9.5.

TABLE 9.5. OVERVIEW OF THE EXPERIMENTAL PARAMETERS ADOPTED FOR THE ICE ACTIVITY

Coolant	LBE
Primary loop circulation	Gas lift technique
Fuel assembly lattice	Hexagonal
Fuel assembly type	Wrapper
Fuel assembly spacer	Grid
Fuel pin diameter (D) [mm]	8.2
Pitch to diameter ratio (P/D)	1.8
Fuel heat flux q’’ [W/cm^2]	100
Fuel power density q’’’ [W/cm^3]	488
Average velocity fuel pin region [m/s]	1
Fuel pin active length [mm]	1000
T_{in}/T_{out} core [°C]	300/400
T_{HS}/L_{act} [°C/m]	100
Fuel pin cladding material	AISI 316L
Secondary coolant	Low pressure boiling water

As can be noted for the ICE test section, a P/D ratio value of 1.8 is adopted to reduce the overall pressure drop along the primary flow path, still preserving the main characteristics of the heat source and allowing performing the tests with the available pumping system (gas-lift technique).

The ICE test section, to be placed inside the CIRCE main vessel (S100), consists of the following main components, as depicted in Figs 9.19 and 9.20.

⇒ Downcomer: it is the volume between the test section and the main vessel which allows the hydrodynamic connection between the outlet section of the HX with the inlet section of the feeding conduit.

⇒ Feeding conduit: it is the inlet pipe of the test section which allows the hydrodynamic development of the upward primary flow rate towards the flowmeter.

⇒ Flowmeter: it is a Venturi-Nozzle flowmeter; bubble tubes [9.34]–[9.38] are adopted to measure the pressure gradient along the throat of the Venturi pipe. The flowmeter is directly connected to the heat source, without bypass, allowing measuring directly the primary flow rate through the pin bundle.

⇒ Fuel pin simulator (FPS): it is a mechanical structure needed to take on the HS. It is connected to the flowmeter in the lower section and to the insulation volume in the upper section by the coupling flange. The coupling flange assures the sealing, avoiding that the insulation volume be flooded by LBE. In the upper section, the FPS is hydraulically linked to the fitting volume, assuring the continuity of the main flow path.

⇒ Fitting volume: it is placed in the middle part of the test section, allowing the hydraulic connection between the HS and the riser.

⇒ Riser: it is a pipe which connects the fitting volume with the separator. In the lower section, a nozzle is installed to allow the argon injection.

⇒ Separator: it is a volume needed to connect the riser with the HX. It allows the separation between the LBE, which flows downward into the HX, and the argon flowing in the test section cover gas through the free level. Moreover, the separator assures that the overall LBE flow rate flows directly into HX (shell side) before falling down in the downcomer.

⇒ Heat exchanger: it constitutes the heat sink of the system. In order to promote the natural circulation along the primary flow path, it is installed in the upper part of the test section.

⇒ Dead volume: it is a component made of two concentric pipes. The inner pipe is connected by bolted junctions, to the FPS (by the coupling flange) and to the cover head. The volume inside the inner pipe is called insulation volume. The outer pipe is welded to the inner pipe at the lower end by a flange which allows a bolted connection between the dead volume and the fitting volume; it spans up to the cover gas, above the free level. The annulus between the inner and the outer pipe, kept melt-free by design, is linked to the cover gas and partially filled by thermal insulation material in order to reduce the radial heat flux towards the insulation volume.

⇒ Insulation volume: it encloses the power supply rods feeding the heat source (HS). Due to the self-heating by Joule effect of the power supply rods, an insulation volume cooling system (IVCS) has been foreseen, with a thermal duty of 40 kW. To achieve this result, a thin shell surrounding the power supply rods (see Fig. 9.21) is inserted into the insulation volume; it spans from the coupling flange up to the cover head. The shell is hydraulically linked to the insulation volume at the bottom. Air is injected from the top in the annulus between the inner pipe and the shell; it flows downward and enters inside the shell at the bottom. Flowing upwards, it cools the power supply rods. The IVCS is designed to assure a maximum room temperature less than 200°C.

The HS is coupled with the test section by an appropriate mechanical structure. The HS and the mechanical structure which surrounds it make up the so-called Fuel Pin Simulator (FPS).

The ICE heat source consists of a pin bundle made by electrical heaters with a nominal thermal power of 800 kW (total power of 925 kW); it has been designed to achieve a difference temperature through the HS of 100°C, a fuel power density of 500 W/cm^3 and an average liquid metal velocity of 1 m/s, in accordance with the reference values adopted for the LFR/ADS concepts.

The ICE HS consists of 37 pins placed in a wrapped hexagonal lattice with a pitch to diameter ratio of 1.8 (see Fig. 9.22). Each pin has an outer diameter of 8.2 mm, a power of about 25 kW and a wall heat flux of 1 MW/m^2. The selected active length is 1000 mm and the adopted cladding material is AISI 316L. To get an average LBE velocity of 1 m/s, a flow rate of 60 kg/s is needed through the HS.

Along the HS, three spacer grids (see Fig. 9.22) are placed, aiming to assure the relative position of the pins inside the bundle, improve the mixing of the coolant and guarantee a uniform and constant subchannel cross-section during the tests.

One of the main challenges addressed during the implementation of the ICE test section was the design of the spacer grids (see Fig. 9.22) and lower grid assembly in order to reduce as practicable as possible the pressure losses through these components.

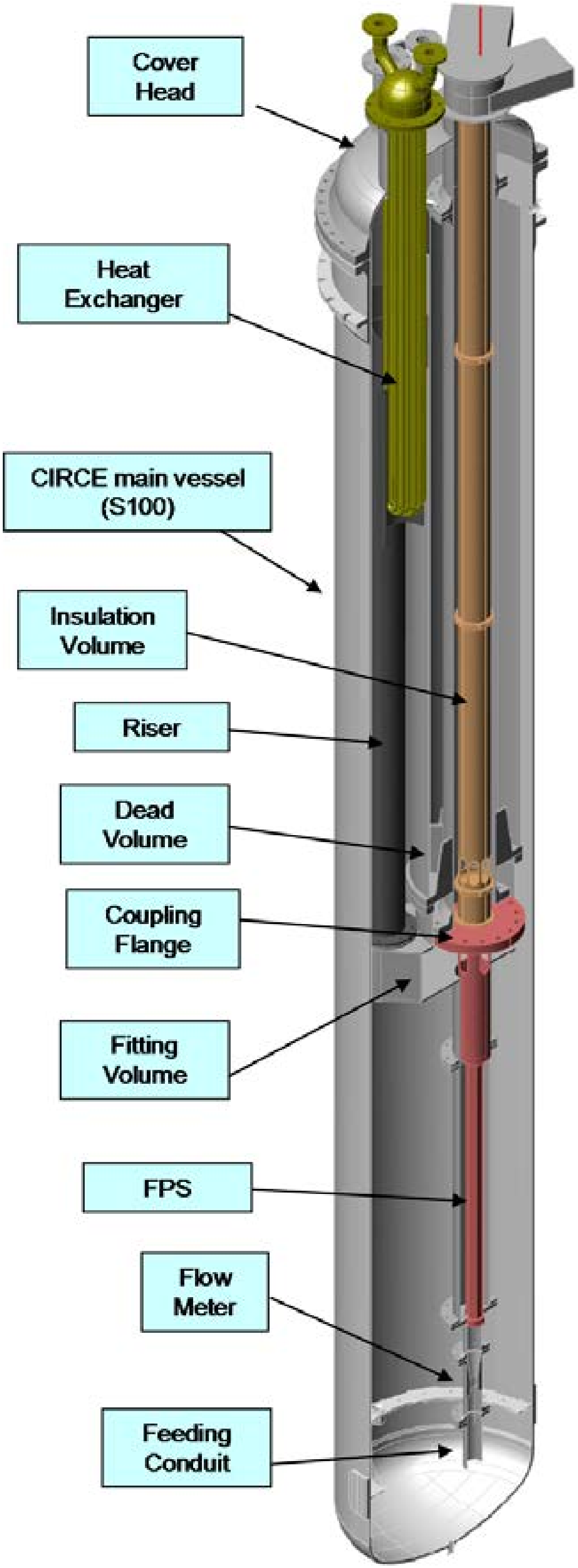

FIG. 9.19. ICE test section overview.

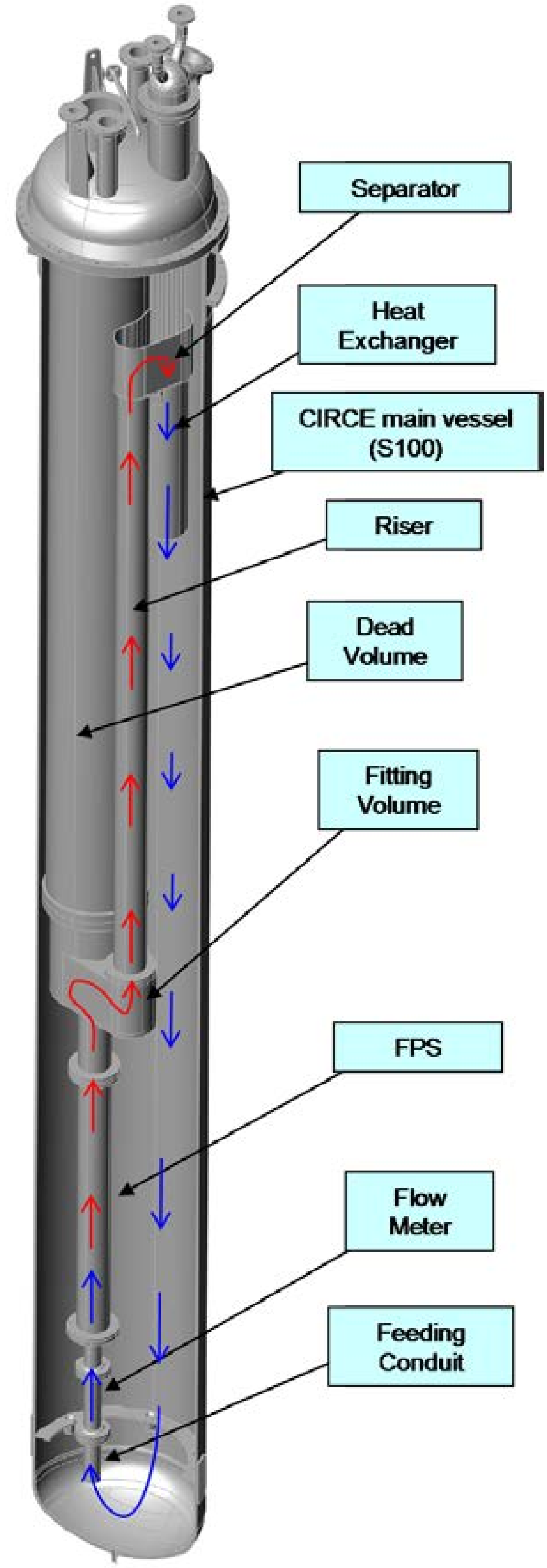

FIG. 9.20. ICE primary flow path overview.

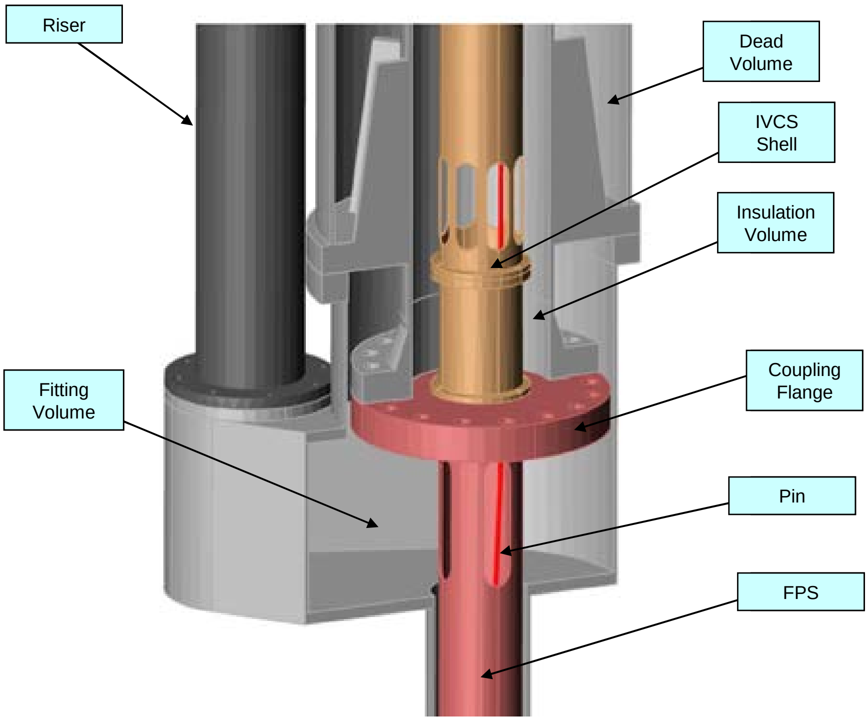

FIG. 9.21. Details of the insulation volume and of the coupling flange.

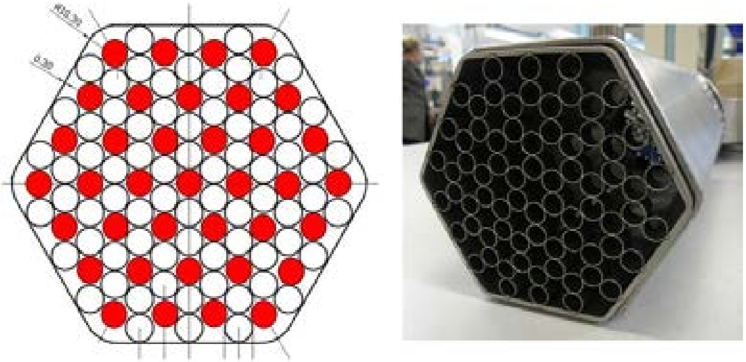

FIG. 9.22. Cross-section of the ICE heat source and a view of the adopted spacer grid.

To obtain these results, the design of the components followed a step by step process. A preliminary sketch was defined, an analytical calculation performed [9.33] and, after two or more iterations, a final calculation of the pressure loss factor was made by a CFD tool. From the simulations carried out, a friction loss factor of 0.24 has been estimated for the spacer grid, and a value of 2.54 has been estimated for the lower grid. The results obtained by the CFD simulations for the spacer grid are quite in agreement with the analytical simulations performed by ENEA [9.33], where a pressure loss factor of 0.18 (about 33% lower) has been estimated.

A larger difference exists between the simulations and analytical calculations performed for the lower grid. For this component, a value of 1.42 has been analytically estimated. This larger difference between the two different approaches is probably due to the fact, in the analytical calculation, also the entrance effect, that the LBE stream undergoes flowing from the feeding conduit into the hexagonal wrapper. As reported in [9.33], the total pressure loss factor (referred to the overall flow path) estimated for the ICE test section is 6.6, and so, the overall pressure drop along the flow path is equal to 34 kPa.

So, for the ICE activity, a pitch to diameter ratio of 1.8 allows obtaining an overall pressure drop along the flow path of 34 kPa, and the integral tests can be performed adopting the gas lift pumping system already available (maximum pressure head 40 kPa), without the need to install mechanical pumps. Moreover, the P/D ratio value selected for the ICE activity has not compromised the implementation of the integral test, allowing to accomplish the scheduled goals. For the ICE activity, the cold sink consists of a cooling water circuit, a LBE low pressure boiling water shell HX, interconnecting piping and steam vent piping to discharge steam into the atmosphere.

In particular, the HX is made of 91 bayonet tubes. The bayonet consists of three concentric tubes (see Fig. 9.18), the outer two of which have the bottom end sealed. The water flows downward in the inner pipes, and then upward in the annulus between the inner and the intermediate pipes. In the annulus, vaporization takes place. The annulus between the middle and the outer pipes is filled by pressurized helium (4.5 bar). All annuli are interconnected to form a common gas plenum, the pressure of which is continuously monitored. A leakage from either wall of any of the outer tubes is promptly detected because of depressurization of the common helium gas plenum. The two outer tubes are mechanically and thermally decoupled. This configuration allows localizing the most part of the thermal gradient, between lead and boiling water across the gas layer, avoiding both risk of lead freezing and excessive thermal stresses across the tube walls during steady state operation and transients.

For the ICE activity, the test matrix reported in Table 9.6 was defined with the scope to achieve the objectives above described. The experimental campaign has been completed in the first part of 2009 and the experimental data are presently being analysed.

TABLE 9.6. TEST MATRIX FOR ICE ACTIVITY

	Test A: Steady state circulation	Test B: Steady state circulation	Test C: Transient condition Loss of cold sink	Test D: Transient condition Loss of pumping system
Conditions / parameters	Isothermal conditions (350°C) No thermal power	T LBE: 350°C DT assembly: 100°C Full thermal power	Nominal conditions Time of thermal power shutdown	Nominal conditions Thermal power Local pressure drop
Key measurements	Dp distribution	Dp through FPS Tin, Tout in the FPS Tin, Tout in the HX	Cladding temperature LBE temperature Tin, Tout in the FPS	Cladding temperature LBE temperature LBE flow rate under natural circulation regime
Objectives	Fluid-dynamic characterization	To verify the coupling of the FPS and the HX To evaluate the HTC (assembly) and the global HTC (HX) To validate nodalization parameters for hydraulic system codes	To compare the system behaviour under transient with the computer code simulations	To study the transition from forced to natural circulation To characterize the natural circulation flow regime To compare the system behaviour under transient with the computer code simulations

9.5. CONCLUSIONS

The alloying of steel surface with aluminum, using microsecond-pulsed intense electron beams, was developed and optimized in order to be used for improving the corrosion resistance and creep strength of steels, exposed to liquid Pb and Pb-Bi eutectic.

The corrosion resistance and the creep strength of the T91, F/M steel, exposed to Pb and Pb-Bi eutectic with different oxygen concentrations and under different temperatures, were considerably improved due to the formation of a thin alumina layer. This slowly growing alumina layer acts as an anticorrosion barrier and is less susceptible to crack formation and therefore to lead alloy enhanced creep.

The ternary compound, Ti_3SiC_2, was selected as one of the most promising candidate material for pump impeller and bearing materials, because it combines some of the most attractive properties of ceramics with those of metals. After the preliminary screening test, performed in melted lead, one may conclude that this ternary compound exhibits good corrosion resistance due to the formation of thin and protective TiO_2 layer at the surface.

A prototypical decay heat removal (DHR) system, in HLM pool-type reactors, has been proposed. The prototype cooler is made of 91 bayonet tubes, which consist of three concentric tubes, containing water, helium and HLM, respectively. This configuration avoids the risk of local freezing and excessive stresses in the walls. Monitoring of the gas pressure allows the detection of leakages.

REFERENCES TO CHAPTER 9

[9.1] OECD NUCLEAR ENERGY AGENCY, Handbook on Lead-Bismuth Eutectic Alloy and Lead Properties Material Compatibility, Thermal-hydraulics and Technologies, OECD/NEA Nuclear Science Committee, NEA No. 6195 (2007). http://www.oecd-nea.org/science/reports/2007/pdf/ (Chapter 4).

[9.2] SOLER, L., MARTIN, F.J., HERNANDEZ, F., GOMEZ-BRICENO, D., J. Nucl. Mater. **335** (2004) 174.

[9.3] MÜLLER, G., et al., J. Nucl. Mater. **335** (2004) 163.

[9.4] FAZIO, C., BENAMTI, G., MARTINI, C., PALOMBARINI, G., J. Nucl. Mater. **296** (2001) 243.

[9.5] MÜLLER, G., SCHUMACHER, G., ZIMMERMANN, F., J. Nucl. Mater. **278** (2000) 85.

[9.6] GLASBRENNER, H., KONYS, J., MUELLER, G., RUSANOV, A., J. Nucl. Mater. **296** (2001) 237.

[9.7] BENAMATI, G., FAZIO, C., PIANKOVA, H., RUSANOV, A., J. Nucl. Mater. **301** (2002).

[9.8] DELOFFRE, PH., TERLAIN, A., BARBIER, F., J. Nucl. Mater. **301** (2002) 35.

[9.9] MÜLLER, G., et al., J. Nucl. Mater. **301** (2002) 40.

[9.10] BALLINGER, R., LIM, J., LOEWEN, E., Proceedings of the 11th International Conference on Nuclear Engineering, Tokyo (2003), No. ICONE11-36531.

[9.11] LEGRIS, A., NICAISE, G., VOGT, J.-B., FOCT, J., J. Nucl. Mater. **301** (2002) 70.

[9.12] VOGT, J-B., NICAISE, G., LEGRIS, A., FOCT, J., J. Phys. IV France **12** (2002) 8.

[9.13] JIANU, A., et al., J. Nucl. Mater. **394** (2009) 102–108.

[9.14] HEINZEL, A., et al., “Cladding tubes made of ferritic/martensitic or austenitic steel for nuclear fuel elements/fuels and method for subsequently treating a FeCrAl protective layer thereon that is suited for high temperatures”, Patent: EP 1 896 627 B1 (2006).

[9.15] WEISENBURGER, A., et al., J. Nucl. Mater. **377** (2008) 261–267.

[9.16] WEISENBURGER, A., et al., J. Nucl. Mater. **376** (2008) 274–281.

[9.17] ENGELKO, V., YATSENK, B., MUELLER, G., BLUHM, H., Vacuum **62** (2001), 211.

[9.18] MÜLLER, G., et al., J. Nucl. Mater. **335** (2004) 163–168

[9.19] MÜLLER, G., SCHUMACHER, G., ZIMMERMAN, F., J. Nucl. Mater. **278** (2000) 85–95.

[9.20] STOLOFF, N.S., JOHNSTON, T.L., Acta Metallurgica **11** (1963) 251.

[9.21] GESSI, A., BENAMATI, G., UTILI, M., “Nuclear application steels compatibility with flowing Pb”, Proc. Int. Conf. on EUROCORR 2008, 7–11 September 2008, Edinburgh, Scotland.

[9.22] BARNES, L.A., DIETZ RAGO, N.L., LEIBOWITZ, L., J. Nucl. Mater. **373** (2008) 424–428.

[9.23] RIVAI, A.K., TAKAHASHI, M., Prog. Nucl. Energy **50** (2008) 560–566.

[9.24] www.3one2.come, 3-ONE-2 LLC data sheet.

[9.25] KERO, I., Ti3SiC2 Synthesis by Powder Metallurgical Methods, Lulea University of Technology Department of Applied Physics and Mechanical Engineering Division of Engineering Materials, ISSN: I402-I757, 2007.

[9.26] BARSOUM, M.W., RADOVIC, M., “Mechanical Properties of the MAX Phases”, Encyclopaedia of Materials: Science and Technology, Elsevier Science, (2004).

[9.27] BARSOUM, M.W., EL-RAGHY, T., American Scientist **89** (2001) 336–345.

[9.28] ZHOU, A.G., FRACZKIEWICZ, M., Acta Materialia **54** (2006) 5261–5270.

[9.29] HOGBERG, H., HULTMAN, L., Surface and Coatings Technology **193** (2005) 6.

[9.30] KHALID RIVA, A., TAKAHASHI, M., Prog. Nucl. Energy **50** (2008) 560–566.

[9.31] FOLETTI, C., GESSI, A., BENAMATI, G., J. Nucl. Mater. **376** (2008) 386–391.

[9.32] TURRONI, P., CINOTTI, L., CORSINI, G., MANSANI, L., “The CIRCE Facility”, AccApp’01&ADTTA’01, Nuclear Application in the New Millennium, Reno (Nevada, United States of America), November 11–15, 2001.

[9.33] TARANTINO, M., SCADDOZZO, G., Test Specifications of the Integral Circulation Experiments, Report ENEA ET-F-S-001, Deliverable D. 4.15, DM4 DEMETRA, IP-EUROTRANS, 2006.

[9.34] BENAMATI, G., FOLETTI, C., FORGIONE, N., ORIOLO, F., SCADDOZZO, G., TARANTINO, M., Nucl. Eng. Des. **237** 7 (2007) 768–777.

[9.35] TARANTINO, M., Gas Enhanced Circulation Experiments On Heavy Liquid Metal System, Report ENEA HS-F-R-001 (2007).

[9.36] CINOTTI, L., “The Pb-Bi Cooled XADS Status of Development”, II International Workshop on Materials for Hybrid Reactors and Related Technologies, ENEA Brasimone Research Centre, April 18–20, 2001.

[9.37] BENAMATI, G., BERTACCI, G., ELMI, N., SCADDOZZO, G., Report on Gas Enhanced Circulation Experiments and Final Analysis (TECLA D41), ENEA HS-A-R-016 (2005).

[9.38] AMBROSINI, W., FORASASSI, F., FORGIONE, N., ORIOLO, F., TARANTINO, M., Experimental study on combined natural and gas-injection enhanced circulation, Nucl. Eng. Des. **235** 10–12 (2005) 1179–1188.

ABBREVIATIONS

ADS	accelerator driven system
AHTR	advanced high temperature reactor
BARC	Bhabha Atomic Research Centre
CEFR	China Experiment Fast Reactor
CFD	computational fluid dynamics
CFX	Commercial CFD code
CIRCE	Large scale facility at ENEA
COSTA	CORrosion in STagnant liquid lead Alloys facility
CRT	Chiu-Rohsenow-Todreas model
CSE	ceramic sensitive element
DHR	decay heat removal
DNS	direct numerical simulation
DOF	degree of freedom
EDX	energy dispersion X-ray
ELSY	European Lead-cooled SYstem
EMF	electromotive force
FLUENT	Commercial CFD code
FPS	fuel pin simulator
GCC	galvanic concentration cell
GESA	Gepulste Elektron Strahl Anlage (Pulsed electron beam facility)
HELIOS	Heavy Eutectic liquid metal Loop for Integral test of Operability and Safety of PEACER (Republic of Korea)
HLM	heavy liquid metal
ICE	integral circulation experiment
IP	integrated project
KALLA	KArlsruhe Liquid metal Laboratory at KIT
KIT	Karlsruhe Institute of Technology, Germany
KNE	kinking non-linear elastic
KTH	Royal Institute of Technology, Stockholm, Sweden
LACANES	lead-alloy cooled advanced nuclear energy system
LBE	lead-bismuth eutectic
LES	large eddy simulation
LFR	lead cooled fast reactor
LME	liquid metal embrittlement
LPPS	low pressure plasma spraying
MAX	ternary carbides with the general formula $\mathbf{M}_{n+1}\mathbf{AX}_n$, where $n = 1–3$, **M** is an early transition metal, **A** is an A-group element (mostly IIIA and IVA), and **X** is C and/or N
MSR	molten salt reactor
RANS	Reynolds Average Navier Stokes (modelling)
SA	Sub-assembly
SEM	scanning electron microscopy
SEM/EDX	scanning electron microscopy combined with energy dispersive X-ray spectroscopy
SFR	sodium cooled fast reactor
TDA	TetraDecyl-Ammonium (oxygen sensor)
VHTR	very high temperature reactor
YSZ	Yttria-Stabilised-Zirconia

CONTRIBUTORS TO DRAFTING AND REVIEW

Bang, K.-H.	Korea Maritime University, Republic of Korea
Bilbao Y Leon, S.	International Atomic Energy Agency
Jianu, A.	Karlsruhe Institute of Technology (KIT), Germany
Kim, S.B.	International Atomic Energy Agency
Maheshwari, N.K.	Bhabha Atomic Research Centre (BARC), India
Meloni, P.	ENEA UTFISSM, Italy
Meyer, L.	International Atomic Energy Agency
Monti, S.	International Atomic Energy Agency
Souza Dos Santos, R.	Institute of Nuclear Engineering (IEN/CNEN), Brazil
Xu, Yijun	China Institute of Atomic Energy (CIAE), China

No. 22

IAEA
International Atomic Energy Agency

Where to order IAEA publications

In the following countries IAEA publications may be purchased from the sources listed below, or from major local booksellers. Payment may be made in local currency or with UNESCO coupons.

AUSTRALIA
DA Information Services, 648 Whitehorse Road, MITCHAM 3132
Telephone: +61 3 9210 7777 • Fax: +61 3 9210 7788
Email: service@dadirect.com.au • Web site: http://www.dadirect.com.au

BELGIUM
Jean de Lannoy, avenue du Roi 202, B-1190 Brussels
Telephone: +32 2 538 43 08 • Fax: +32 2 538 08 41
Email: jean.de.lannoy@infoboard.be • Web site: http://www.jean-de-lannoy.be

CANADA
Bernan Associates, 4501 Forbes Blvd, Suite 200, Lanham, MD 20706-4346, USA
Telephone: 1-800-865-3457 • Fax: 1-800-865-3450
Email: customercare@bernan.com • Web site: http://www.bernan.com

Renouf Publishing Company Ltd., 1-5369 Canotek Rd., Ottawa, Ontario, K1J 9J3
Telephone: +613 745 2665 • Fax: +613 745 7660
Email: order.dept@renoufbooks.com • Web site: http://www.renoufbooks.com

CHINA
IAEA Publications in Chinese: China Nuclear Energy Industry Corporation, Translation Section, P.O. Box 2103, Beijing

CZECH REPUBLIC
Suweco CZ, S.R.O., Klecakova 347, 180 21 Praha 9
Telephone: +420 26603 5364 • Fax: +420 28482 1646
Email: nakup@suweco.cz • Web site: http://www.suweco.cz

FINLAND
Akateeminen Kirjakauppa, PO BOX 128 (Keskuskatu 1), FIN-00101 Helsinki
Telephone: +358 9 121 41 • Fax: +358 9 121 4450
Email: akatilaus@akateeminen.com • Web site: http://www.akateeminen.com

FRANCE
Form-Edit, 5, rue Janssen, P.O. Box 25, F-75921 Paris Cedex 19
Telephone: +33 1 42 01 49 49 • Fax: +33 1 42 01 90 90
Email: formedit@formedit.fr • Web site: http://www. formedit.fr

Lavoisier SAS, 145 rue de Provigny, 94236 Cachan Cedex
Telephone: + 33 1 47 40 67 02 • Fax +33 1 47 40 67 02
Email: romuald.verrier@lavoisier.fr • Web site: http://www.lavoisier.fr

GERMANY
UNO-Verlag, Vertriebs- und Verlags GmbH, Am Hofgarten 10, D-53113 Bonn
Telephone: + 49 228 94 90 20 • Fax: +49 228 94 90 20 or +49 228 94 90 222
Email: bestellung@uno-verlag.de • Web site: http://www.uno-verlag.de

HUNGARY
Librotrade Ltd., Book Import, P.O. Box 126, H-1656 Budapest
Telephone: +36 1 257 7777 • Fax: +36 1 257 7472 • Email: books@librotrade.hu

INDIA
Allied Publishers Group, 1st Floor, Dubash House, 15, J. N. Heredia Marg, Ballard Estate, Mumbai 400 001,
Telephone: +91 22 22617926/27 • Fax: +91 22 22617928
Email: alliedpl@vsnl.com • Web site: http://www.alliedpublishers.com

Bookwell, 2/72, Nirankari Colony, Delhi 110009
Telephone: +91 11 23268786, +91 11 23257264 • Fax: +91 11 23281315
Email: bookwell@vsnl.net

ITALY
Libreria Scientifica Dott. Lucio di Biasio “AEIOU”, Via Coronelli 6, I-20146 Milan
Telephone: +39 02 48 95 45 52 or 48 95 45 62 • Fax: +39 02 48 95 45 48
Email: info@libreriaaeiou.eu • Website: www.libreriaaeiou.eu

JAPAN
Maruzen Company Ltd, 1-9-18, Kaigan, Minato-ku, Tokyo, 105-0022
Telephone: +81 3 6367 6079 • Fax: +81 3 6367 6207
Email: journal@maruzen.co.jp • Web site: http://www.maruzen.co.jp

REPUBLIC OF KOREA
KINS Inc., Information Business Dept. Samho Bldg. 2nd Floor, 275-1 Yang Jae-dong SeoCho-G, Seoul 137-130
Telephone: +02 589 1740 • Fax: +02 589 1746 • Web site: http://www.kins.re.kr

NETHERLANDS
De Lindeboom Internationale Publicaties B.V., M.A. de Ruyterstraat 20A, NL-7482 BZ Haaksbergen
Telephone: +31 (0) 53 5740004 • Fax: +31 (0) 53 5729296
Email: books@delindeboom.com • Web site: http://www.delindeboom.com

Martinus Nijhoff International, Koraalrood 50, P.O. Box 1853, 2700 CZ Zoetermeer
Telephone: +31 793 684 400 • Fax: +31 793 615 698
Email: info@nijhoff.nl • Web site: http://www.nijhoff.nl

Swets and Zeitlinger b.v., P.O. Box 830, 2160 SZ Lisse
Telephone: +31 252 435 111 • Fax: +31 252 415 888
Email: infoho@swets.nl • Web site: http://www.swets.nl

NEW ZEALAND
DA Information Services, 648 Whitehorse Road, MITCHAM 3132, Australia
Telephone: +61 3 9210 7777 • Fax: +61 3 9210 7788
Email: service@dadirect.com.au • Web site: http://www.dadirect.com.au

SLOVENIA
Cankarjeva Zalozba d.d., Kopitarjeva 2, SI-1512 Ljubljana
Telephone: +386 1 432 31 44 • Fax: +386 1 230 14 35
Email: import.books@cankarjeva-z.si • Web site: http://www.cankarjeva-z.si/uvoz

SPAIN
Díaz de Santos, S.A., c/ Juan Bravo, 3A, E-28006 Madrid
Telephone: +34 91 781 94 80 • Fax: +34 91 575 55 63
Email: compras@diazdesantos.es, carmela@diazdesantos.es, barcelona@diazdesantos.es, julio@diazdesantos.es
Web site: http://www.diazdesantos.es

UNITED KINGDOM
The Stationery Office Ltd, International Sales Agency, PO Box 29, Norwich, NR3 1 GN
Telephone (orders): +44 870 600 5552 • (enquiries): +44 207 873 8372 • Fax: +44 207 873 8203
Email (orders): book.orders@tso.co.uk • (enquiries): book.enquiries@tso.co.uk • Web site: http://www.tso.co.uk

On-line orders
DELTA Int. Book Wholesalers Ltd., 39 Alexandra Road, Addlestone, Surrey, KT15 2PQ
Email: info@profbooks.com • Web site: http://www.profbooks.com

Books on the Environment
Earthprint Ltd., P.O. Box 119, Stevenage SG1 4TP
Telephone: +44 1438748111 • Fax: +44 1438748844
Email: orders@earthprint.com • Web site: http://www.earthprint.com

UNITED NATIONS
Dept. I004, Room DC2-0853, First Avenue at 46th Street, New York, N.Y. 10017, USA
(UN) Telephone: +800 253-9646 or +212 963-8302 • Fax: +212 963-3489
Email: publications@un.org • Web site: http://www.un.org

UNITED STATES OF AMERICA
Bernan Associates, 4501 Forbes Blvd., Suite 200, Lanham, MD 20706-4346
Telephone: 1-800-865-3457 • Fax: 1-800-865-3450
Email: customercare@bernan.com · Web site: http://www.bernan.com

Renouf Publishing Company Ltd., 812 Proctor Ave., Ogdensburg, NY, 13669
Telephone: +888 551 7470 (toll-free) • Fax: +888 568 8546 (toll-free)
Email: order.dept@renoufbooks.com • Web site: http://www.renoufbooks.com

Orders and requests for information may also be addressed directly to:

Marketing and Sales Unit, International Atomic Energy Agency
Vienna International Centre, PO Box 100, 1400 Vienna, Austria
Telephone: +43 1 2600 22529 (or 22530) • Fax: +43 1 2600 29302
Email: sales.publications@iaea.org • Web site: http://www.iaea.org/books

13-11221

INTERNATIONAL ATOMIC ENERGY AGENCY
VIENNA
ISBN 978–92–0–139910–6
ISSN 1011–4289